THESIS

SWELL, STIFFNESS AND STRENGTH OF EXPANSIVE SOIL-RUBBER (ESR) MIXTURES AT VARIOUS SCALES: EFFECT OF SPECIMEN AND RUBBER PARTICLE SIZES

Submitted by

Lance C. Heyer

Department of Civil and Environmental Engineering

In partial fulfillment of the requirements

For the Degree of Master of Science

Colorado State University

Fort Collins, Colorado

Summer 2012

Master's Committee:

Advisor: J. Antonio H. Carraro

Charles D. Shackelford
Gregory Butters

ABSTRACT

SWELL, STIFFNESS AND STRENGTH OF EXPANSIVE SOIL-RUBBER (ESR) MIXTURES AT VARIOUS SCALES: EFFECT OF SPECIMEN AND RUBBER PARTICLE SIZES

Expansive soils and stockpiled scrap tires present unique constructability and environmental challenges to the Front Range of Northern Colorado, respectively. Swell, stiffness and strength parameters of expansive soil-rubber (ESR) mixtures were systematically evaluated in the laboratory under one-dimensional and axisymmetric boundary conditions. ESR mixtures tested contained highly plastic, swelling clay from the Pierre shale formation and scrap tire rubber (STR) with nominal maximum particle sizes equal to approximately 6.7 or 19.0 mm. Compaction parameters were determined using standard Proctor compaction procedures (ASTM D698). Mixtures were compacted to relative compaction levels equal to 90, 95 or 100% and water contents varying by ± 2% around the optimum water content. Rubber contents used were equal to 0, 10 or 20%. Specimen and rubber particle sizes were also studied to assess differences in mechanical behavior of 6.7- and 19.0-mm ESR mixtures tested in one-dimensional compression employing three specimen sizes (small-scale, large-scale and field-scale) and in undrained axisymmetric compression employing two specimen sizes (small-scale and large-scale).

Swell-compression results indicated the swell percent and swell pressure of specimens subjected to one-dimensional compression with lateral confinement were most impacted by initial water content, followed by relative compaction and rubber content. Compressibility parameters, including the constrained and elastic moduli, are most impacted by rubber content, followed by relative compaction and initial water content. Small-scale one-dimensional specimens demonstrated a minimal increase in swelling and insignificant variations in compressibility in comparison to large-scale one-dimensional and field-scale specimens. ESR specimens subjected to axisymmetric boundary conditions exhibited volumetric swell during flushing and back pressure saturation and swelling magnitudes were similar for nominal rubber particle sizes equal to 6.7 and 19.0 mm. Normal compression line parameters, λ_{cs} and κ_{cs}, were equal to 0.10 and 0.05, and 0.11 and 0.04 for large-scale 6.7- and 19.0-mm ESR specimens, respectively. Critical state parameters, M_{cs}, Γ_{cs}, and λ_{cs}, were equal to 1.20, 2.23 and 0.14, and 1.04, 2.15 and 0.13 for large-scale 6.7- and 19.0-mm ESR specimens, respectively. Scalability results indicate similar swell, stiffness and strength of ESR mixtures compacted to various specimen sizes with the inclusion of either 6.7- or 19.0-mm scrap tire rubber particles. Results indicate reasonable predictions of the mechanical behavior of ESR mixtures including tire chips can be made using conventional laboratory specimen sizes and testing techniques employing similar host expansive soils and rubber contents used to create ESR mixtures including granulated rubber.

AWKNOWLEDGEMENTS

Firstly and foremost, the author would like to thank his advisor, Dr Antonio Carraro, for his expertise, wisdom, and guidance during graduate coursework, research, and the preparation of this manuscript. Gratitude is extended toward committee members, Dr Shackelford and Dr Butters, for their support and knowledge in soil mechanics.

The author would like to especially acknowledge his wife, Mary Beth, for her love, encouragement, and understanding during graduate studies and research at Colorado State University. Her attitude towards pursuing a master's degree was very beneficial. The author's parents, Lindsay and Julie, and brothers, Joshua, Andrew and Seth were also a crucial element in the completion successful of graduate work.

Thanks are provided to the author's mentor, Dan Overton, for his instrumental role in the author's choice of geotechnical engineering as a career path and his encouragement and recommendation to pursue graduate studies. Special thanks are extended to industry professionals Tom Chapel and Mae Benvenga for their support and advice regarding graduate school.

Finally, thanks is extended to the Colorado Department of Public Health and Environment (CDPHE) for partial funding of graduate studies, and the two local scrap tire rubber manufacturers, Front Range Tire Recycle, Inc. and Caliber, Inc., for providing materials used in the presented field and laboratory analyses.

TABLE OF CONTENTS

Page

LIST OF TABLES

LIST OF FIGURES

LIST OF SYMBOLS

A ..... Activity
A ..... Skempton's Pore Water Pressure Coefficient
A_C ..... Cross Sectional Area
A_{C0} ..... Initial Cross Sectional Area
A_{Cc} ..... Corrected Cross Sectional Area
A_{Ccs} ..... Corrected Cross Sectional Area at the End of Testing
A_{Cf} ..... Cross Sectional Area at Failure
A_{cs} ..... Skempton's Pore Water Pressure Coefficient at Critical State
B ..... Skempton's Pore Water Pressure Coefficient
c_v ..... Coefficient of Consolidation
C_c ..... Compression Index
C_r ..... Recompression Index
C_R ..... Relative Compaction
C_{RI} ..... Initial Relative Compaction (Prior to Flushing or Inundation)
d_0 ..... Diameter of the Specimen at the End of Consolidation
d_{im} ..... Initial Membrane Diameter
d_R ..... Nominal Rubber Particle Diameter
e ..... Void Ratio
E ..... Elastic or Young's Modulus
E_i ..... Initial Membrane Tangent Modulus
G ..... Shear Modulus
i ..... Hydraulic Gradient
I_P ..... Plasticity Index
G_s ..... Specific Gravity
m_v ..... Modulus of Volume Compressibility
m_{vr} ..... Modulus of Volume Recompressibility
M ..... Constrained Modulus
M_{cs} ..... Slope of the Critical State Line in the $p' - q$ Plane
M_{csmax} ..... Maximum Slope of the Critical State Line in the $p' - q$ Plane
p' ..... Mean Effective Stress
p'_0 ..... Mean Effective Stress after Isotropic Compression
p_{0m} ..... Initial Confining Pressure
p'_{cs} ..... Mean Effective Stress at Critical State
p'_p ..... Peak Mean Effective Stress
q ..... Deviatoric Stress
q_{cs} ..... Deviatoric Stress at Critical State
R_0 ..... Over-Consolidation Ratio
RC ..... Rubber Content
$S_{\%}$ ..... Swell Percent
t ..... Time
u ..... Pore Water Pressure
Δu ..... Pore Water Pressure Change
Δu_{cs} ..... Pore Water Pressure Change at Critical State

Δu_{max} ..... Maximum Pore Water Pressure Change
V_e ..... Excitation Voltage
V_s ..... Sensor Voltage
V_{ESR} ..... Total Volume of an Expansive Soil Rubber Mixture
w ..... Water Content
w_I ..... Initial Water Content (Prior to Flushing or Inundation)
w_L ..... Liquid Limit
w_{opt} ..... Optimum Water Content
w_P ..... Plastic Limit
W_r ..... Weight of Rubber
W_x ..... Weight of Solids
ε_a ..... Axial Strain
ε_{acs} ..... Axial Strain at Critical State
ε_{af} ..... Axial Strain at Failure
ε_{ap} ..... Axial Strain at M_{csmax}
ε_r ..... Radial Strain
ε_v ..... Volumetric Strain
ε_z ..... Vertical Strain
Γ_{cs} ..... v Value for the Intercept of the CSL at p' = 1kPa
ϕ ..... Mobilized Friction Angle
ϕ_c ..... Critical State Friction Angle
ϕ_p ..... Peak Friction Angle
κ_{cs} ..... Slope of the URL in the $\ln(p') - v$ Plane
λ_{cs} ..... Slope of the NCL and CSL in the $\ln(p') - v$ Plane
Λ_s ..... Plastic Volumetric Strain Ratio
v ..... Specific Volume
ν_p ..... Poisson's Ratio
v_κ ..... Specific Volume Value of the URL at p' = 1 kPa
v_κ ..... Specific Volume Value of the NCL at p' = 1 kPa
σ ..... Total Stress
σ' ..... Effective Stress
σ'_1 ..... Major Principal Stress
σ'_3 ..... Minor Principal Stress
σ_a ..... Axial Stress
σ_r ..... Radial Stress
$\Delta\sigma_r$ ..... Difference in Radial Stress
σ'_r ..... Effective Radial Stress
σ'_z ..... Effective Vertical Stress
σ'_{zs} ..... Swell Pressure
γ_d ..... Dry Unit Weight
γ_{dmax} ..... Maximum Dry Unit Weight
γ_s ..... Soil Matrix Unit Weight

LIST OF ACRONYMS

ASTM ..... American Society for Testing and Materials
CEC ..... Cation Exchange Capacity
CDPHE ..... Colorado Department of Public Health and Environment
COV ..... Coefficient of Variation
CS ..... Critical State
CSL ..... Critical State Line
CSU ..... Colorado State University
ERC ..... Engineering Research Center
ESR ..... Expansive Soil and Rubber
ESTS ..... Expansive Soils Test Site
FSSM ..... Field Scale Swell-Monitoring
ICU ..... Isotropically Consolidated Undrained
LSTX ..... Large-Scale Triaxial
LSC ..... Large-Scale One-Dimensional Swell-Compression
LVDT ..... Linear Variable Differential Transformer
NCL ..... Normal Compression Line
OC ..... Over Consolidated
OCR ..... Over Consolidation Ratio
PDF ..... Powder Diffraction File
SC ..... Swell-Compression
SSC ..... Small-Scale One-Dimensional Swell-Compression
STR ..... Scrap Tire Rubber
SSTX ..... Small-Scale Triaxial
TX ..... Triaxial
URL ..... Unloading Reloading Line
XRD ..... X-Ray Diffraction

CHAPTER 1: INTRODUCTION

1.1 Problem Statement

Expansive soils are distinctive in that significant volume change consistently occurs with the addition or subtraction of liquids with high surface tension, most commonly water, from a representative matrix. Engineering when expansive soils are present is difficult and can lead to severe damage to structures such as buildings and pavements if performed incorrectly. Road and structural subgrade materials can also be weakened during expansion and contraction cycles causing cracking and fracturing, further damaging overlying structures. The majority of expansive soils can be classified as montmoillonite-rich clays, over-consolidated clays and shales (Nelson and Miller 1992). From a practical standpoint, monetary losses from damages related to expansive soils have been reported to be as high as $13 billion dollars per year (Puppala and Cerato 2009). This figure omits situations where a more conservative design criterion was necessary and successfully used to mitigate the swell potential of expansive material.

Due to the potential problems posed by expansive soils, it has become common practice in academia and practice to develop stabilization techniques. A common form of stabilization includes the addition of chemical and or physical additives. Chemical additives are mixed with expansive soils in order to decrease overall swell response. Traditional chemical stabilization approaches considered over the past 60 years fall primarily into three categories: lime, Portland cement, and fly ash (Petry and Little 2002). Physical stabilization techniques include mixing non-expansive material to an expansive

soil in order to minimize expansive response (Johnson 1979, Dickson et al. 1990, Ikizler et al. 2009, Perko 2009, Dunham-Friel and Carraro 2011). Recently, scrap tire rubber has been investigated as a potential additive to reduce swelling behavior and stabilize expansive soil (Seda et al. 2007).

Scrap tire rubber (STR) disposal has become a problem of increasing concern, especially in Colorado. The United States leads the world in tire consumption, with an estimated 290 million scrap tires generated annually (USEPA 2008). Many of the recycled tires are stockpiled in Colorado where 61.7 million tires are currently stockpiled and 6.7 million addition tires are added to stockpiles yearly (CDPHE 2009). Due to these staggering figures, end-use markets for recycled tire rubber should be considered high priority (CDPHE 2009).

In order to determine potential applications for expansive soil-rubber (ESR) mixtures further research must be conducted regarding the scalability of swell, stiffness and strength parameters of interest. Generally, compacted materials are designed with strength and stiffness as the predominant elements of concern when supporting road base and structural elements. In order to reach the desired strength and stiffness a minimum dry unit weight (γ_d) and specified range of water content (w) is typically specified in backfill applications (Daniel and Benson 1990). By defining an acceptable zone baseline compaction parameters are provided. Varying γ_d and w within the acceptable zone can have dramatic effects on strength and stiffness parameters. Therefore, it is necessary to

quantify strength and stiffness parameters of ESR mixtures based on different relative compactions (C_R) , w and rubber contents (RC).

Finally, being able to evaluate strength and stiffness parameters of ESR mixtures for varying scrap tire rubber sizes is essential. Utilization of ESR mixtures to limit volume changes in expansive soils and create another end use market for scrap tire rubber is an ultimate goal of previous and current research. In order to implement ESR technology it is paramount to understand if specimen and nominal maximum rubber particle size (d_R) has a significant effect on parameters calculated from one-dimensional swell-compression and undrained triaxial tests. If scaling is a factor, the ability to define parameters appropriately for engineering use will be necessary for the implementation of this technology.

1.2 Research Objectives

The main objective of this study is to systematically evaluate the mechanical response of ESR mixtures using both advanced laboratory testing, and large-scale field testing. This study will compare remolded ESR specimens in order to better understand how specimen and nominal maximum rubber particle diameter (d_R) affect swell, stiffness and strength. Throughout the research state parameters including relative compaction (C_R), water content (w), rubber content (RC) and d_R will be varied under relatively well controlled ranges in order to determine the effects each parameter independently has on the swell, stiffness and strength of specimens subjected to one-dimensional swell-compression and undrained monotonic shearing under axisymmetric stress conditions.

The specific objectives of this study were to:

1) Develop a method of specimen preparation that yields a desired C_R, w and RC for one-dimensional swell-compression specimens, field-scale swell-monitoring plots and axisymmetric compression specimens tested throughout this study;
2) Completely characterize the effects that C_R, w and RC have on the mechanical response of ESR mixtures tested in small-scale one-dimensional swell-compression tests;
3) Define the effects that w and d_R have on the mechanical response ESR mixtures tested in large-scale one-dimensional swell-compression tests;
4) Monitor large scale field plots and characterize the effect d_R has on the swell response;
5) Determine the effect specimen size has on the one-dimensional mechanical response of ESR mixtures;
6) Identify the effect that d_R and specimen size have on the mechanical response of ESR mixture tested in undrained, static, monotonic, axisymmetric compression.

1.3 Research Scope

This study focuses on the mechanical response of ESR sample mixtures tested in one-dimensional swell-compression, field-scale swell-monitoring, and undrained monotonic shearing under axisymmetric stress conditions. An expansive material was extracted from a local geotechnical research site utilized by Colorado State University (CSU) to study expansive soils. Expansive soil and rubber were mixed together in order to investigate the effects manufactured scrap tire rubber has on swell-compression, and

shear strength results. Two nominal rubber particle diameters (d_R) were utilized in this study, 6.7-mm granulated rubber and 19.0-mm tire chips, with different levels of manufacturing and impurities. Twenty-seven different specimens were tested in small-scale laboratory swell-compression apparatuses with variations in initial C_R, w, and initial RC. Six different specimens were tested in large-scale laboratory swell-compression testing with variations in d_R and w. Three field plots were monitored for swelling behavior with variations in the d_R. Finally, six specimens were tested to determine shear strength and critical state parameters of ESR specimens in undrained monotonic shearing under axisymmetric stress conditions with variations in the target mean effective stress (p') after isotropic compression and d_R.

1.4 Manuscript Organization

This manuscript contains six additional chapters covering the mechanical response of ESR mixtures. Chapter 2 includes a literature review presenting an overview of expansive soils, potential hazards expansive soils pose to infrastructure, research related to the expansive soil and expansive-soil and rubber (ESR) mixtures, problems scrap tire rubber can pose if stored in large facilities exposed to the environment and a brief overview of the work that has currently been completed regarding ESR mixtures. Chapter 3 examines the conceptual framework used to analyze gathered results. Chapter 4 explains the experimental program including materials utilized, index testing, compaction parameters, and testing procedures. The results obtained throughout the experimental program developed to fully investigate the mechanical response of ESR mixtures are presented in Chapter 5. Chapter 6 is devoted to explaining the results

obtained throughout this research. Finally, Chapter 7 draws conclusions based on the results and provides recommendations for future research. Appendices cover additional information including instrumentation calibration and additional figures supporting results.

CHAPTER 2: LITERATURE REVIEW

2.1 Background

Expansive soils can cause significant damage to light building and pavement structures due to deformations significantly greater than elastic deformations predicted by classical elastic or plastic theory (Nelson and Miller 1992). Expansive soils can be mapped based on their swell potential, Figures 2.1 and 2.2. According to Figures 2.1 and 2.2, provided by the Colorado Land Use Commission and USGS, respectively, Northern Colorado is located in the Sothern Rocky Mountain physiographic province. The Southern Rocky Mountain physiographic province contains significant areas of highly expansive material. In fact, many highly expansive soil deposits found in the United States are located throughout the Midwest. Research presented in this thesis was conducted at Colorado State University (CSU) located in Fort Collins, Colorado. Material used in the study was collected from the Engineering Research Center (ERC), approximately 5 miles west of the universities' main campus, and as explained later has been found to be highly expansive.

Generally, the severity of expansion in swelling soils is explained though swell potential and swell pressure. Swelling potential can be defined as the relative capacity for the expansion (Nelson and Miller 1992) or increase in volume when an element of soil is inundated with a wetting fluid, typically water. Swell potential depends on a variety of environmental conditions including, but not limited to, overburden stress, seasonal and climatic variations and, in reconstituted material, compaction effort. Expansion results

from a disturbance in the internal stress equilibrium due to a change in the soil water system. Swell pressure is the vertical load necessary to limit volume change when an element of soil is inundated (Nelson and Miller 1992).

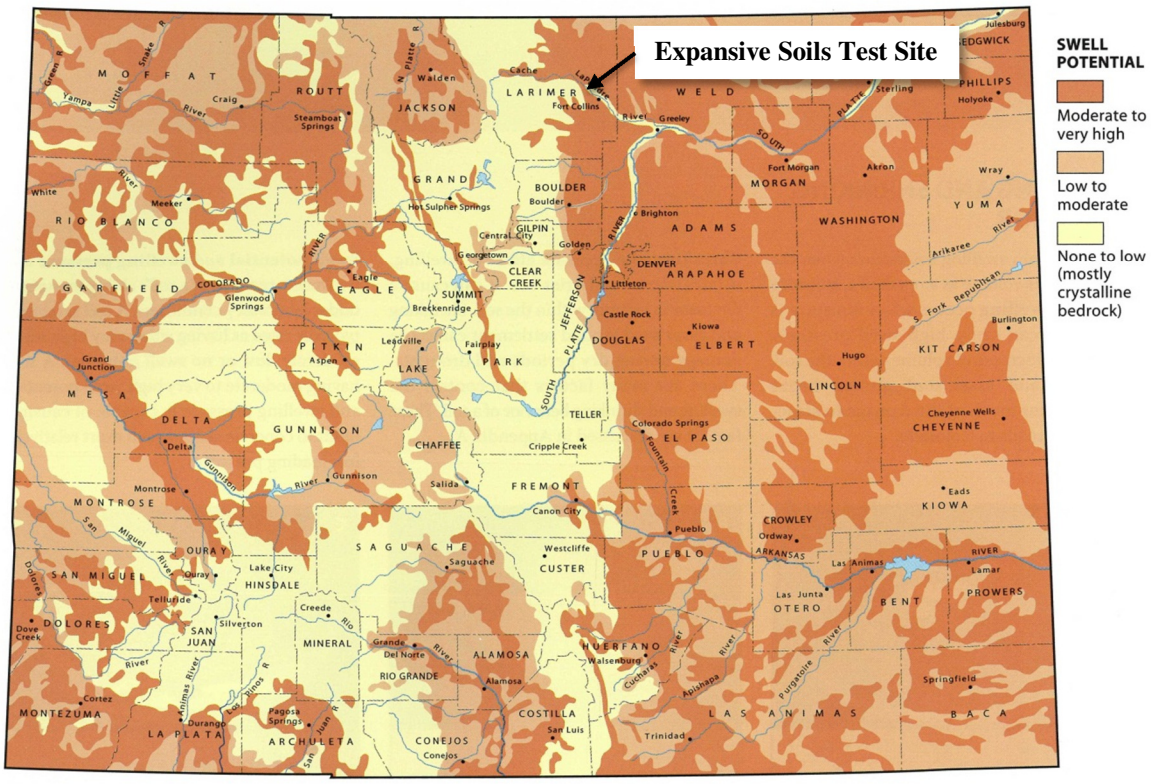

Figure 2.1 Generalized distribuiton of swelling soil and bedrock in Colorado (after the Colorado Land Use Commission)

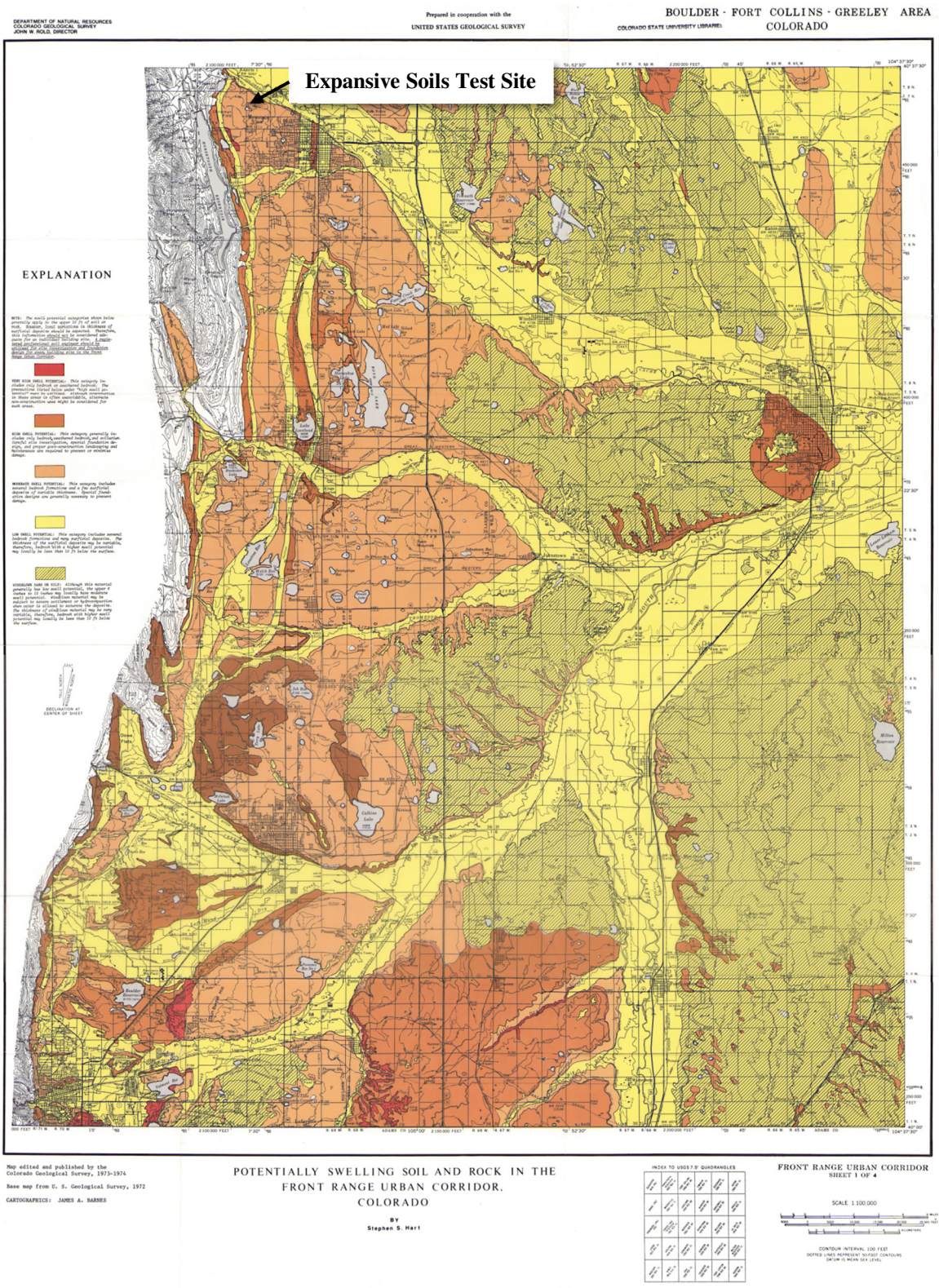

Figure 2.2 Potentially swelling soil and rock in the Front Range urban corridor, Colorado. Swell potential severity by color reference decreases in the following order from very high to low: red (very high), dark orange (high), light orange (moderate) and yellow (low) (after Hart 1974).

2.2 Clay Mineralogy

Clay particle formation mechanisms control the behavior of expansive soils. Definitions for clay particles can be based on particle size and mineralogical composition. Individual clay particles encompass sizes smaller than 2 μm. Definitions involving mineralogical make-up are slightly more complex involving discussion of phyllosilicate and alluminosilicate minerals. Phyllosilicate and alluminosilicate minerals are the basic building blocks of clay particles Clay structures differ according to the orientation of these two building blocks.

Expansive soils throughout the Midwest include significant amounts of montmorillonite; the primary component of bentonic clays, a 2:1 phyllosilicate and a dioctahedral smectite. 2:1 phyllosilicates are comprised of two silica tetrahedrons surrounding an aluminum octahedron. Tetrahedral and octahedral structures are used to describe the general orientation of the various crystalline lattices comprising clay particles (see Figure 2.2). Tetrahedrons are commonly filled with silica, while octahedrons are commonly filled with aluminum. Dioctahdral smectites contain numerous subspecies, including montmorillonite, distinguished by the principle location of the layer charge (Essington et al. 2004).

During the formation of clay particles isomorphic substitution can occur in both the aluminum octahedron and the silica tetrahedron. In montmorillonite it is common for the isomorphic substitution to take place in the aluminum octahedron, and for magnesium to replace the aluminum in the crystal lattice. An ideal half unit cell formula for

montmorillonite is $Na_{0.4}(Al_{1.6}Mg_{0.4})Si_{0.4}O_{10}(OH)_2$. 0.4 Mg^{2+} atoms commonly substitute for Al^{3+} atoms in the octahedral layer, resulting in a net negative charge within the clay lattice. Therefore, an ideal montmorillonite half unit cell contains a layer charge of 0.4. A half unit cell layer charge of 0.4 is between 0.2 and 0.6; the range of 2:1 phyllosilicates (Essington et al. 2004). A representative illustration of two montmorillonite sheets can be seen in Figure 2.3.

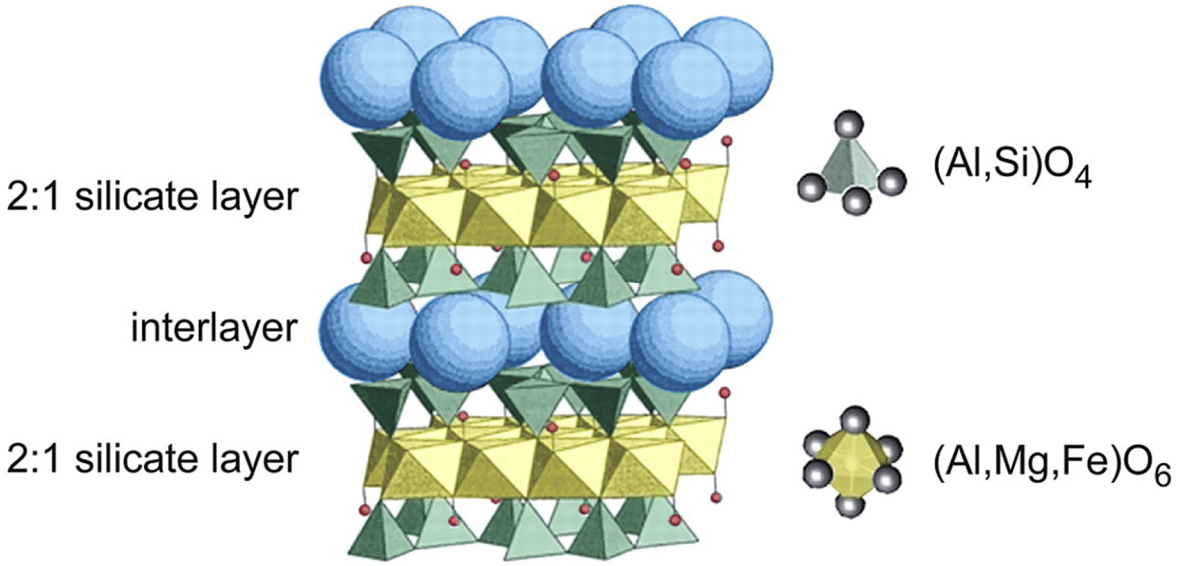

Figure 2.3 Structure of Montmorillonite (Mineralogical Society of America, 2009)

The net negative charge of montmorillonite is balanced by exchangeable cations which collect around the negative surface of the clay particle. Positive cations enter the diffuse double layer balancing the negatively charged clay surface (Bohn et al. 1985). Common exchangeable cations include Na^+, K^+, Ca^{2+}, and Mg^{2+} (Essington et al. 2004). The swelling process is induced when these interlayers become hydrated through the attraction of the positive cations and polar water molecules. The size and charge of cations present in the diffuse double layer control the limits of expansion. Na^+ causes the

largest interlayer expansion in comparison to K^+, Ca^{2+}, and Mg^{2+}. Sodium is the most common exchangeable cation found in the diffuse double layer of montmorillonite particles in the Midwest. The bulk of sodium bentionite used in various applications worldwide is mined in the northern Great Plains (Knechtel and Patterson 1962), which includes the northern Colorado region.

2.3 Geologic Origin of the Pierre Shale Soil Deposit

The ERC Expansive Soils Test Site, where expansive soils used throughout the present research were collected, is located within the Colorado Piedomont section of the Great Plains Physiographic Province. The Colorado Piedomont is a broad erosional basin separating the Sothern Rocky Mountains from the High Plains, was formed during the late Tertiary and early Quaternary eras, and consists primarily of over consolidated sandstone, limestone, and clay-shale strata (Braddock et al. 1990). The ERC is situated approximately 100 feet above the contact between the Smoky Hill Shale Member of the Biobrara Formations and the lower Gammon Ferrunginous member of the Pierre Shale Formation. More accurately, the ERC is located approximately 5 to 15 feet above the contact between the Gammon Ferrunginous and the Sharon Springs members of the Pierre Shale (Scott and Cobban, 1986).

The Gammon Ferrunginous and Sharon Springs members of the Pierre shale consist of dark grey to greyish back, hard, platy shale approximately 7 m thick, and an overlying ironstone unit of olive grey, non-calcareous, hard platy shale approximately 20 m thick

(Abshire 2002). The grey platy shale concentrations weather to tan or orange, and interbedded orange bentonite layers ranging in thickness from 15 to 150 mm occur in both Gammon Ferrunginous and Sharon Springs members (Scott and Cobban, 1986). Orange bentonite seams occur more often in the Sharon Springs deposit in comparison to the Gammon Ferrunginous deposit. A diagram resenting time and rock stratigraphic sequences is provided and a cross-section presenting the subsurface lithology below the ERC expansive soil testing site is presented in Appendix E.

2.4 Techniques for Stabilizing Expansive Soils

Due to the harmful nature and difficult design criterion related to expansive soils, techniques have been developed to stabilize their shrink-swell characteristics. Stabilization techniques can be divided up into two primary categories; physical stabilization and chemical admixtures. In practice it is important to take into account effectiveness, economy and ease of implementation before choosing a stabilization technique (Nelson and Miller 1992). Stabilization methods are used to alter the chemical and or physical behavior of the expansive material. The following sections will describe several physical and chemical stabilization techniques commonly employed in expansive material.

2.4.1 Physical Stabilization Methods

Structures commonly and negatively impacted by expansive soils are foundations and light structural elements. Light structural elements and foundations typically require small displacements and high stiffness. When building such elements on expansive soils,

foundation elements can be altered to account for the expansive consequences. Due to a relatively rigid design criterion in comparison to other geotechnical applications, the discussions in this section will be limited to stabilization techniques aimed specifically at foundations and light structural elements.

Foundation alternatives generally exhibit one of two possible goals; (1) complete isolation of the structure from soil movements or (2) a rigid foundation with the ability to withstand differential foundation movements (Nelson and Miller 1992). Common categories of foundation alternatives for expansive soils include shallow foundations, reinforced and stiffened slabs, thick reinforced mat, or beam on pier (Johnson 1979). Significant swelling potential of expansive soils along the Front Range usually prevents using strengthened foundation elements as the singular method to mitigate expansion. Common practice in areas of significant expansion includes the placement of structures as small as residential homes on a foundation involving helical piles (Perko 2009). In worst case scenarios, piers are drilled past expansive soil layers and keyed into bedrock in order to ensure a high level of stability (Perko 2009). Foundation alternatives can be used in combination with other physical and chemical stabilization methods to ensure stability in cases where high levels of expansion are expected.

Sources of swelling in expansive soils derive directly from an increase in water content within the soil matrix. Therefore, by controlling moisture variations expansion can be limited. It is virtually impossible to completely control the seasonal moisture variations under structural elements; however it is reasonable in certain situations to limit variations

to control the rate and magnitude of expansion (Nelson and Miller 1992). Generally the top 3 to 6 m of soil will experience large variations in water content in comparison to lower depths and cycles of water content variation can range from one to ten years (Porter 1977; Nelson and Edgar 1978; Goode 1982). Common practice to mitigate moisture variations involves drains. However, in expansive soil generally permeability is low and soils suction is high, therefore, vertical drains have been used with limited effectiveness (Nelson and Miller 1992). Other forms of moisture variation alleviation include barriers. Although barriers do not completely eliminate moisture variations, more uniform heave patterns develop with their installation and seasonal variations have been limited successfully (Goode 1982).

Another basic technique applied to reduce shrink swell characteristics encountered in expansive soils involves pre-wetting or ponding prior to construction. Caveats to this technique involve soil strength and stability. The moisture content and the overall strength and stability of the soil have an inverse relationship (Dickson et al. 1990). In other words when the moisture content of an expansive soil increases the strength decreases, resulting in significantly lower bearing capacities. Other problems relating to pre-wetting derive from comparatively low hydraulic conductivities. The amount of time needed to adequately pre-wet an expansive soil can potentially be excessive, further discouraging the use of this technique. In certain applications, for example backfill, where strength and time constraints are of secondary concern pre-wetting can be employed successfully (Nelson and Miller 1992).

Swelling can be prevented using surcharge loads in excess of the swell pressure. This technique is often referred to as preloading. Preloading is typically utilized for soils with moderate swell characteristics. It is generally not ideal to use excessive amounts of fill to mitigate swell, especially considering that some expansive materials can have swell pressures as high as 480 kPa (Puppala and Musenda 2000).

Similar to any situation with problematic soils removal and replacement is always an option. Removal and replacement involves substituting a soil with more advantageous properties for one that is difficult to design for, or cannot meet design requirements. Factors affecting the potential of using this technology include depth of removal, amount of soil needing replacement, location, and cost of fill (Nelson and Miller 1992). Practicality of utilizing this technique is assessable on a site to site basis. If non-expansive fill is not readily available, and or transport costs cannot be justified, expansive soil can be disturbed and compacted to a less dense state, or higher water content, to mitigate swell potential. One such study performed by Kasangake and Towhata examined the excavation and water treatment of expansive material before subsequent compaction. The authors found that wet compaction did initially decrease swelling potential, but eventually the benefits were lost when subjection to cyclic wetting and drying followed (Kasangake and Towhata 2009).

Physical displacement of expansive material in lieu of non-expansive material can be used to decrease the amount and severity of swell characteristics. An emerging stabilization technique involves adding sand to expansive soil deposits (Mowafy et al.

1985; Basma et al. 1998; Sridharan and Gurtug 2004; Hudyma and Avar 2006; Rao et al. 2006; Mishra et al. 2008; and Ikizler et al. 2009). Ikizler et al. 2009 successfully reduced the swell pressure of pure bentonite from 422 to 274 kPa when increasing the sand content from 0 to 80%, a reduction of nearly 50%. Results by aforementioned researchers display a liner decrease in swell percent and pressure with increasing sand content.

Another common replacement material studied is discrete and randomly oriented fiber reinforcement (Kumar et al. 2007; Punthutaecha et al. 2006; Abdi et al. 2008; and Viswanadham et al. 2009). Research employing fiber reinforcement to stabilize cohesive material have shown several benefits including a reduction swelling characteristics and tension cracking during seasonal variations in water content. For the purpose of this manuscript the discussion will be limited to fiber reinforcement to mitigate swelling characteristics. Punthutaecha et al. (2006) found that a fiber dosage level of 0.2% produced the highest improvement in swell mitigation, where higher contents had decreasing levels of improvement, attributed partically to poor compaction at high fiber dosages. A fiber dosage level of 0.2% enabled the reduction of swell by almost half. Abdi et al. (2008) found a reduction in the compression and swelling upon unloading when employing various contents of polypropylene fibers. Finally Viswanadham et al. (2009) reported an increased effectiveness in heave reduction with shorter fiber employment at similar fiber to rubber ratios. An optimal fiber length of approximately 20 mm was most effective in swell reduction; reducing swell by 60%. In all studies

randomly distributed fibers had a positive effect in reducing the swelling potential of expansive material.

Numerous studies have also been performed, and are currently being conducted, at Colorado State University regarding the use of scrap tire rubber (STR) in place of more traditional geomaterials to mitigate swell in expansive soil deposits (Seda et al. 2007; Dunham-Friel and Carraro 2011; Wiechert et al. 2011). These studies have been successful in reducing swell potential in compacted mixtures mined from expansive soil deposits along the Front Range. A complete discussion on the effect of STR on swell potential will be provided later in Chapter 2.

2.4.2 Chemical Stabilization Methods

Lime has been widely studied as an additive to minimize swell potential and stabilize expansive materials. Lime has been cited as one of the oldest chemical agents in stabilization techniques, and has been shown to improve compaction plasticity, workability, swell potential, strength, stress-strain behavior, fatigue, and durability (Bashar et al. 2003). With the addition of lime several important mechanisms devolve increasing stability: (1) reduction in the thickness of the diffuse double layer; (2) flocculation of clay particles; (3) increased internal friction angle; and (4) reduction in plasticity (Rodgers and Glendinning 2000). The long term stabilization of lime treated materials depends on the development of pozzolanic reaction products. A major class of pozzolanic reaction products formed in lime stabilized soil is calcium-silicate-hydrates (CSH) (Harvey et al. 2010). Lime stabilization studies performed by Harvey et al. (2010)

found that the highest number of CSH reactions formed at lime contents slightly higher than 3-8% in a soil with high montmorillonite content. Another study conducted by Bashar et al. (2003) found that by adding lime the resilient modulus, or recoverable deformation upon repetitive loading, of a typical subgrade can be increased by 3 to 10 times when treated with lime. Of specific interest when stabilizing with lime is the effect of pulverization. Bozbey and Garaisayev (2009) found: (1) lime pulverization quality to have a direct impact on the ability to achievable stabilization at maximum stress levels; (2) when using poorly pulverized lime longer curing times may be necessary; and (3) there are environmental benefits of using lime over importing granular material. Similar to other chemical admixture stabilization techniques success varies depending on the character of the soil, the type and length of curing, and the method and quality of construction (Bell 1996).

Fly ash has displayed effectiveness in stabilizing expansive soils. Fly ash forms as a byproduct during coal combustion in power plants. Stabilization mechanisms include pozzolanic reactions and cation exchange due to an adequate array of divalent and trivalent cations provided by fly ash (Cokca 2001). Fly ash is generally divided into three classes based on its chemical and physical constituents; Class C, Class F, and Class N (ASTM C618). Class C fly ash is produced from the buring of lignite and subbituminous coal, while class F is formed by the burning of antharacite or bituminous coal. Generally, Class C is considered more pozzolanic and self-cementing in nature in comparison to Class F fly ash primarily due to a higher percentage of free lime (USEPA 2005). Off-specification fly ash, or Class N, has also been studied as a potential stabilizer in ESR

mixtures (Wiechert et al. 2011). Wiechert et al. (2011) established the promotion and development of pozzolanic reactions with Class N fly ash after seven days of curing. Results also indicated an improvement in unconfined compressive strength (UCS) using Class N similar to Class C fly ash in ESR mixtures. Cokca (2001) found an increasing reduction in the swell potential of an expansive soil with increasing fly ash curing time, prompting the use of fly ash stabilization when time constraints are less stringent. Taking Cokca's further, Nalbantonğlu (2004) found and inverse relationship between fly ash content and the curing time in achieving similar swell pressures in expansive material. Finally, Zha et al. (2008) found reductions in swell potential and swell pressure with mixtures of expansive soil, lime and fly ash as the pozzolanic constituent contents increased.

Cement is another pozzolanic material considered in stabilization. Similar to lime stabilization, cement stabilization develops due to the reactions between aluminate hydration products and the soil matrix (Croft 1967). The mixing of cement and expansive material reduces plasticity, lessens the potential for volume change, and increases shear strength (Chen 1988). Al-Rawas et al. (2005) compared the effectiveness of lime and cement on stabilization of an expansive soil from Oman. Specifically studied was the effect of different amounts of lime and cement had on index properties and swelling potential. Results concluded that other than a slight increase in the plasticity index at low quantities (3% by dry weight) of pozzolanic material, as the quantity of pozzolanic material increased (up to 9% by dry weight) plasticity, swell percent, and swell pressure were reduced. It can be concluded from results displayed by Al-Rawas et

al. (2005) that lime was much more effective in reducing swell percent and swell pressure in comparison to cement for expansive soils near Oman. Other research by Basma et al. (1998) found that by mixing cement into expansive soils in small quantities (3-9% by dry weight) swelling characteristics can effectively minimized. Cement is generally not as effective as lime in stabilizing materials with a high affinity for water. Highly expansive materials have such a high affinity for water that cement often does not hydrate enough to completely promote pozzolanic reactions. Therefore, cement is usually preferred when soils are not lime reactive (Mitchell and Raad, 1973). From an economic standpoint the material and implementation costs of both lime and cement are similar so the overall treatment costs can be similar (Nelson and Miller 1992).

A comparative analysis of various additives used in the stabilization of expansive soils has been performed by Al-Rawas et al. (2002). The four pozzolanic additives investigated were cement by-past dust (CBPD), copper slag, slag cement, and granulated blast furnace slag (GBFS). In regards to plasticity Al-Rawas et al. found CBPD, slag cement, and GBFS increased the plasticity index slightly at low contents (3%) while having little effect at higher contents (9%). Only GBFS showed ability to reduce swell pressure at low content (3%) while all materials except for copper slag were able to reduce the swell pressure at higher contents (9%). Finally, CBPD, slag cement, and GBFS were able to reduce swell percent at contents as low as 3%. For the specific expansive soil tested by Al-Rawas, there seems to be a threshold of swell percent reduction near 3% where additional amounts of additive do little to affect the swell

percent. Copper slag was unable to reduce the swell percent and actually increased the swell pressure and swell percent over the range tested (3-9% by dry weight).

2.5 Scrap Tire Rubber in Colorado

Colorado is currently the leading state in stockpiled scrap tires. In 2008, an estimated 55 million waste tires were inventoried at stockpiles in the state of Colorado, and it is estimated that an additional 6.7 million waste tires were added to those stock piles by the end of 2009, bringing the total to 61.7 million tires (CDPHE 2009). The majority of those tires were produced within the state, while approximately 430,000 of them were imported from other states. Recycling techniques in the state of Colorado found end-use-markets for 79% of the generated waste tires in applications including tire-derived fuel, alternative daily covers for landfills, resale tires, baled, ground rubber, civil engineering applications. Figure 2.4 captures the primary end use markets utilized in 2009.

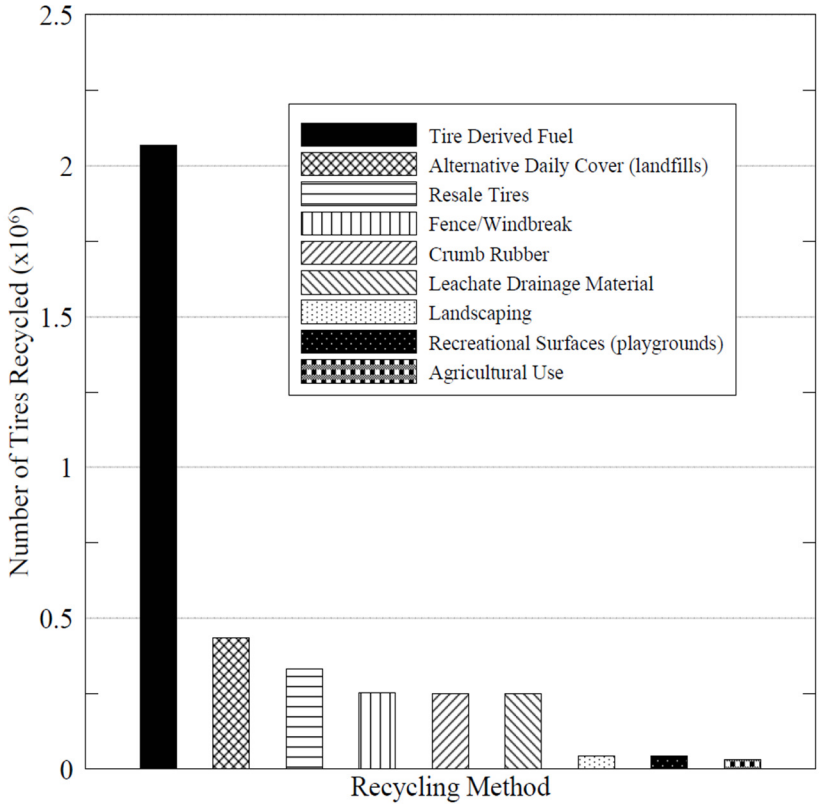

Figure 2.4 End-use-markets utilizing produced scrap tires in the state of Colorado in 2009 (after CDPHE 2009)

The majority of scrap tires are being utilized, however, the remaining 21% of tires not utilized continue to add to the current stockpile of approximately 50 million tires (CDHPE 2009). Although Colorado has a large number of stored tires, its relative legislation is lacking in comparison to other states regarding correct disposal, and recycling. For instance, Colorado does not have a funding source generated from the disposal or storage of used tires (CDHPE 2009). Also, Colorado is lacking in landfill restrictions, and processor regulations (Jang et al. 2008), creating more substantial need to produce additional end-use-markets for tire disposal.

2.5.1 Current End-Use-Markets for STR

Applications and uses for STR have been of major concern due to potential health and safety dilemmas; as described below. Perhaps the most promising end-use-market for STR is tire derived fuel. Approximately 56% of recycled scrap tires in Colorado were utilized as fuel in 2009 (CDPHE 2009), by far the largest contributor to the recycling effort. Specific studies have been conducted to determine pyrolysis and combustion of STR (Williams et al. 1990; Laresogiti et al. 2004; and Juma et al. 2006). In 2009 civil engineering applications provided only 25% of the total end-use market for STR (2009). Civil engineering studies involved grinding down STR to a powder like material, and using the powered rubber to sorb contaminants. Research has shown the ability powered rubber to adsorb more than twice its weight in oil, and a positive affinity in sorbing other problematic contaminants from water bodies and the subsoil (Gunasekara et al. 2000; Chapman et al. 2006; and Lin et al. 2008). STR has been employed successfully in distinct civil engineering applications including road subgrades, backfill and embankment media, and as sorbtive media (Benson 1995; Bernal et al. 1996; Tweedie et al. 1998; Dickson et al. 2001; Pierce and Blackwell 2003; Salgado and Yoon 2003; Park et al. 2003; Recycling Research Institute 2004; Wolfe et al. 2004; Youwai and Bergado 2004; Humphrey 2005; and Edincliler 2007). In 2009 85% of STR tires were recycled, in comparison to 1990 where only 11% found end-use-markets. Although end-use-markets and recycling techniques have improved dramatically, the number of impounded waste tires is still significant. Recycling percentages for scrap tire rubber have increased from 2004 to 2009, as shown in Figure 2.5.

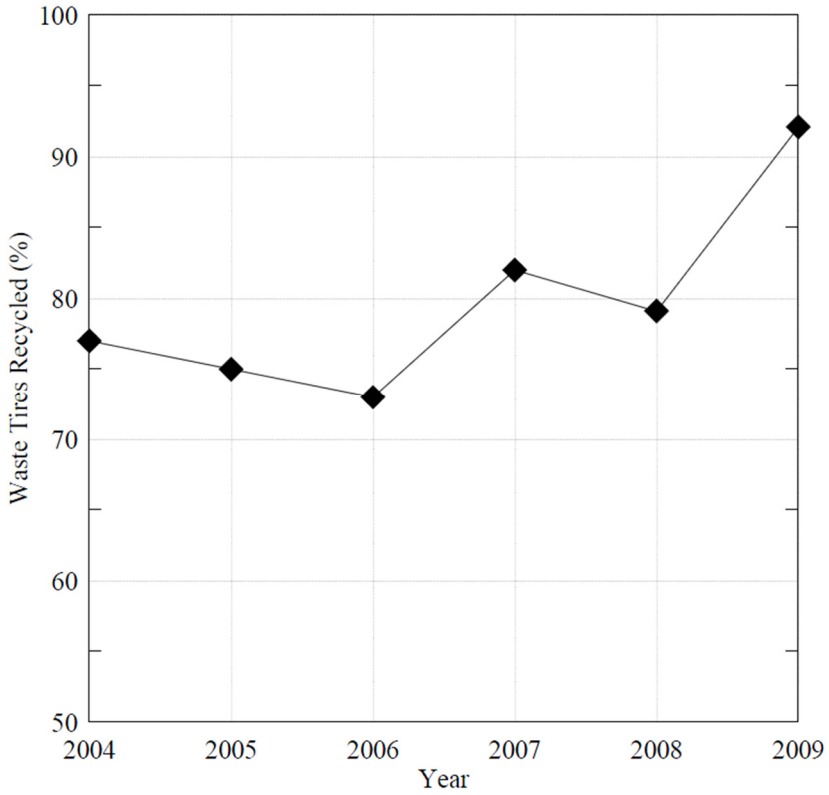

Figrue 2.5 Annual recycling percentage for STR in Colorado based on the number of recycled scrap tires divided by the total number or produced scrap tires (after CDPHE 2009)

ASTM D6270 has been designated for testing physical properties, design considerations, construction practices, and leachate generation potential of STR and STR and sand mixtures. Although D6270 contains valuable information, documentation and testing criterion of ESR mixtures are lacking, and must be addressed.

2.5.2 Environmental Concerns of STR Stockpiles

Three major environmental concerns arise from large STR stockpiles. Firstly, improperly stored tires can be breeding grounds for disease-carrying insects and rodents; specifically mosquitoes. Due to the shape and relative impermeability of discarded tires, water can be held for long periods of time creating moist environments ideal for mosquito larva

development (Jang et al. 1998). Mosquitoes have long been identified as vectors of disease, and enhanced breeding is concerning.

Secondly, pollution, risk to human life, and the need for extensive extinguishing resources can result from fires in STR stockpiles. STR contains highly volatile carbon contents and heating values on the order of 33-35MJ/kg, making STR ideal for energy production and large scale combustion (Juma et al. 2006). On average, discarded tires present a void space of approximately 75%, making fires difficult to quench because of a large initial oxygen supply. Once initiated fires cause the release of air pollution through toxic gas emissions, and solid water pollutants during the release of pyrolytic oil which mixes with extinguishing water and can be carried offsite (Jang et al. 1998). Tire fire by-products may cause the contamination of surface and subsurface regions. Figure 2.6, below, shows a large fire in Stanislaus County, California. The tires were ignited by a lighting strike. The ignited tires took 30 days to extinguish and caused a significant amount of air and water pollution, costing approximately 3.5 million dollars in damage and cleanup costs (USEPA 1999).

Figure 2.6 Waste tire rubber stockpile fire in Stanislaus County, California fire, 1999 (USEPA 1999)

Another famous case history resulting from the ignition of STR occurred in a geographic region similar to this research; Central Colorado. A substantial number of scrap tires (between 400,000 and 450,000) shredded were used to construct an embankment on a section of interstate highway (FWHA 2008). After construction, STR behind the retaining wall experienced combustion problems. Preliminary assessments indicate that the combustion process was initiated by heat released either by the presence of organic solids, microbial degradation, the oxidation of exposed steel reinforcing wire, or microbes consuming liquid petroleum potentially spilled on the tires (FWHA 2008). The STR fire in Colorado helped lead to many of the regulations and restrictions adopted and practiced today.

In a two year study conducted by FEMA from 1996 to 1997, STR fires were reported in many other geographic regions of the United States including Washington, Maryland,

New York, Kentucky, and Arizona (FEMA 1998). The source of ignition for the fires included pyrolysis, arson, open-flame heaters, and undetermined or suspicious sources. Due to difficulties in extinguishing tire fires, extinguishing methods included: excavation, foam, and dirt smothering. Case histories included burn durations of anywhere from 3 days to 5 months. In all cases the fires were not intentionally ignited and little to no preplanning was conducted for any of the sites (FEMA 1998).

Lastly, concern has been raised regarding the leaching of heavy metals from STR with the potential of contaminating groundwater (Edil 2004). Polynuclear aromatic hydrocarbons (PAHs) and volatile organic compounds (VOCs) have been found to leach from STR stockpiles in excess of drinking water standards (Miller and Chadik 1993). Researchers have found toluene, carbon disulfide, and methyl ethyl ketone (Rubber Manufacturers Association 2004) as well as zinc, barium, iron and manganese (Grefe 1989) in STR leachate. A comprehensive summary of several leaching procedures performed by various researchers on tire chips can be viewed in Table 2.1. Mixing STR with various soils may or may not decrease the amount of leached contaminants, and would depend on the sorbtion capacity of the soil and the hydraulic conductivity of the mixture.

Table 2.1 Compounds leached from typical tire chips (after Tatlisoz et al. 1996)

Compound	Concentration limits based on tire chip mass			Reported concentrations based on tire chip mass				
	TCLP[1] [mg/kg]	USEPA's RMCLs[2] [mg/kg]	WI PALs[2] [mg/kg]	Grefe[3] (1989) [mg/kg]	RMA[3] (1990) [mg/kg]	MPCA (1990) [mg/kg]	Miller & Chadik[4] (1993) [mg/kg]	Park et al. (2003) [mg/kg]
As	25.9	0.06	6.15×10^{-3}		-		0.02	
Ba	518.0	2.27	0.25	0.55	0.1	1.08		0.37
Cd	5.18	6.15×10^{-3}	1.23×10^{-3}		-	0.27		
Cr	25.9	0.15	6.15×10^{-3}		0.008	0.51		0.019
Pb	25.9	0.025	6.15×10^{-3}	0.075	0.003	0.92		0.14
Fe		0.37	0.18	1.15		1081		
Mn		0.06	0.03	1.5				
Zn		6.15	3.1	3.15		50.3	5.02	1.13
Se	5.18	0.055	1.23×10^{-3}			0.44		0.05
Hg	1.03	3.7×10^{-3}	2.5×10^{-3}		7.2×10^{-5}			
NO_2^-/NO_3^-		1.23	2.46	1.85				
Toluene	33.79	2.46	84.3×10^{-3}		0.034		0.28	
Carbon disulfide	332.64				0.012			
Phenol	332.64		1.23×10^{-3}		0.01			
Benzene	0.36	6.15×10^{-3}	0.08×10^{-3}		-		0.63	

[1]TCLP are converted to mass of compound per kg of tire chips assuming that 100 g of tire chips with a specific gravity of 1.22 is used. (volume of extractor = 600 mL; mass of solid = 100 g for inorganics and 25 g for volatile organics)
[2]RMCLs and Wisconsin PALs of 1.22 (1 mg/L = 1.22 mg/kg of tire chips)
[3]The liquid concentrations are converted to mass of compound per kg of tire chips based on the given quantities of tire chips and liquid used in the study.
[4]Concentrations for compounds are taken from approximately 16 hour readings which are usually the highest concentrations achieved during the test. The liquid concentrations are converted to mass of compound per kg of tire chips based on the given quantities of tire chips and liquid used in the study.
[5]Concentrations for compounds are the final concentration reached in 800 days. The liquid concentrations are converted to mass of compound per kg of tire chips based on the given quantities of tire chips and liquid used in the study.

2.5.3 Economic Impacts of STR Refinement

STR research to date has focused primarily on smaller, more refined STR particles that are easily manageable in most conventional geotechnical testing apparatuses (Sections 2.6 and 2.7). The potential economic impacts of using a less refined STR with larger nominal particles and greater impurities could yield more interest into the implementation of ESR mixtures for various applications. Table 2.2 presents the various STR costs ($/kg) for various refinement options. The costs in Table 2.2 were provided by Front Range Tire, Inc., the local STR manufacturer that provided one of the two nominal rubber particle sizes used in this study.

Table 2.2 Impact of manufactured nominal rubber particle diameter and removal of steel reinforcement on scrap tire rubber costs in dollars/kg and dollars/ton. Data issued from Front Range Tire Recycle, Inc.

Nominal Rubber Particle Diameter (mm)	Steel Reinforcement Removed (yes/no)	Cost ($/kg)	Cost ($/ton)
50.8	No	$ 0.04	$ 35.00
38.1	No	$ 0.05	$ 45.00
19.1	**No**	**$ 0.07**	**$ 65.00**
19.1	Yes	$ 0.49	$ 440.00
12.7	Yes	$ 0.49	$ 440.00
6.7	**Yes**	**$ 0.49**	**$ 440.00**
<6.7	Yes	$ 0.49	$ 440.00

As presented in Table 2.2, the cost of STR increases significantly with increasing refinement. The largest increase in STR refinement cost occurs due to the removal of steel reinforcement. For an identical nominal particle diameter, removal of steel reinforcement increases the unit cost of STR by approximately seven times. The unit cost for nominal rubber particle sizes smaller than or equal to 19.1 mm (1 inch) is

identical. Also, nominal rubber particle sizes smaller than 19.1 mm do not have the option of including steel reinforcement to buffer potential costs. The potential cost relief from not removing steel reinforcement during the refinement process could be very significant, depending on the size of project and amount of ESR employed.

2.6 Sand-Rubber-Mixtures

Preliminary research on recycling waste tire rubber through soil-rubber-mixtures began with the addition of STR to sand. Sand-rubber-mixtures were investigated with the intention of reducing problematic scrap tire rubber stockpiles though highway embankments (Bosscher er al. 1997; and Heimdahl and Drushcher 1999), lightweight fill (Lee et al. 1999; and Zornberg et al. 2004), backfill for retaining walls (Garga and O'Shaughnessy 2000), drainage systems (Nagasaka et al. 1996; and Lee et al. 2005) and liquefaction resistance (Promputthangkoon and Hyde 2008). Researchers have concluded unique properties of sand rubber mixtures, including but not limited to, high compressibility, low density, high internal angle of friction, and low void ratio (Edil and Bosscher 1994; Foose et al. 1996; Youwai 2003; Zornberg et al. 2004; Bergado et al. 2005; Pamukcu and Akbulut 2006; Lee et al. 2007; Kim and Santamarina 2008; and Lee et al. 2010). Properties of sand-rubber-mixtures including compressibility, stiffness, and strength will be investigated further in the following sections.

2.6.1 Effect of Rubber on Compressibility

Tire rubber grains are dissimilar to sand grains in individual grain stiffness and mass density (Patil et al. 2008) yielding sand-rubber matrix compressibility values much larger

in comparison to isolated sand. Refined STR products, referred to as tire shreds, have displayed isolated compressibility values of 25 to 47% axial strain upon vertical stress applications of 20 to 700 kPa (Warith and Rao 2005). Kim and Santamarina (2008) studied deformation characteristics of tire shred-sand mixtures and found trends displaying and increase in compressibility and expansion upon unloading with and increasing rubber content by dry weight (*RC*). In fact, vertical strains were nearly 20 times greater in isolated tire rubber in comparison to isolated sand at an applied vertical stress (σ'_z) of 500 kPa. Constrained modulus (C_M), or deformation occurring in confined compression (Hunt 2005), values decreased in excess of 10 times over *RC* ranges of 0 to 100% for applied vertical stresses of approximately 10 to 1000 kPa. Finally, swelling indices upon unloading became increasingly greater and less log-liner versus an applied vertical stress with increasing *RC*.

Results of research performed by Kim and Santamarina (2008) are supported by other researchers in relation to overall matrix compressibility of sand-rubber mixtures. For example Lee et al. (2007) found a decrease in vertical strain with increasing sand fraction for applied vertical stresses of 2 to 800 kPa. Lee et al. (2007) also plotted C_M versus applied effective stress and found results similar to Figure X. C_M was log-log linear when plotted versus effective stress, and held values ranging from approximately 0.1 to 2 MPa for rubber alone to approximately 5 to 50 MPa for sand alone over a range of σ'_z of 15 to 500 kPa.

Of particular interest to this manuscript, Lee et al. (2010) studied the effect of size ratio (or the ratio of the average diameter of rubber particles to the average diameter of sand particles) on compressibility. The two size ratios investigated were 4.7 and 0.5, or average rubber particle diameters of 3.375 and 0.363 mm respectively. Similar trends were observed for both size ratios; increasing strain with increasing *RC* for respective σ'_z. Deformations of isolated rubber particles were 30 to 40 times greater in comparison to isolated sand. However, larger deformations were seen with smaller in comparison to rubber particle sizes at similar *RC*. The trend was attributed to the increasing angularity and irregularity of rubber particles as rubber particle size decreases. For *RC* values similar to those studied in this manuscript ($\leq 20\%$) normalized strains were found to be almost identical for both sand fractions. Finally, similar to both Kim and Santamarina (2008) and Lee et al. (2007) C_M increased log-log linearly with an increase in σ'_z. Also, C_M decreased for decreasing *RC* at respective σ'_z. Bounds of the constrained modulus were similar to both Kim and Santamarina (2008) and Lee et al. (2007). Figure 2.7 displays the constrained modulus versus applied effective stress for size ratios of 4.7 and 0.5.

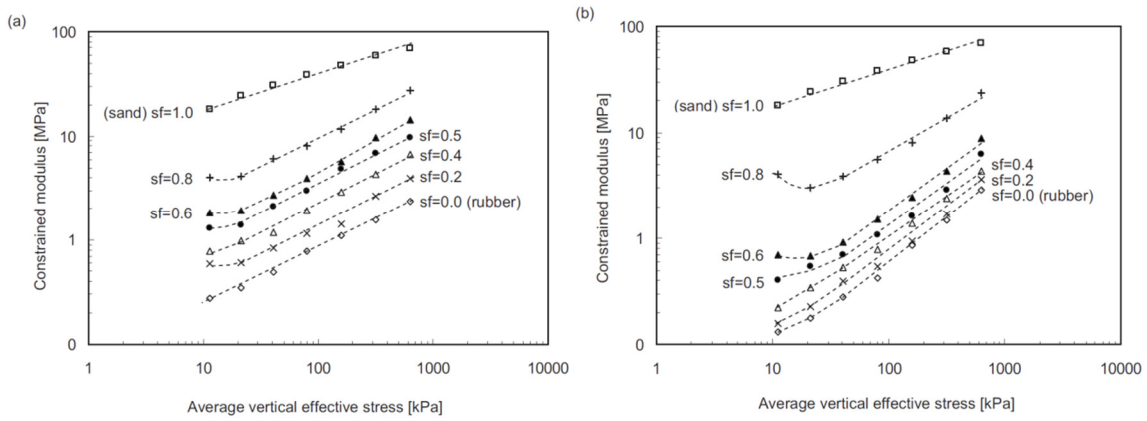

Figure 2.7 Constrained modulus (M) versus applied effective stress (σ'_z) for sand-rubber mixtures with: (a) size ratio of 4.7; and (b) size ratio of 0.5. The sand fractions (= 1 - rubber content) are denoted on the right side of both figures (after Lee et al. 2010)

2.6.2 Effect of Rubber on Small and Large Strain Stiffness

The deformation of granular materials is controlled by the relative motion between particles as a result of sliding or rolling and distortion of individual particles (Lamb and Whitman 1979). These mechanisms are virtually always linked, and have been widely studied in stiff, rigid granular materials. Due to the significantly lower stiffness of rubber particles sand-rubber matrix stiffness generally varies significantly in comparison to isolated granular materials (Lee et al. 2007). Several researchers have studied the small and large strain stiffness of sand-rubber mixtures at varying *RC* (Lee et al. 2007, Kim and Santamarina 2008 and Lee et al. 2010).

Small strain stiffness is generally described at axial strains between 0.0001 and 0.001% (Atkinson 2000). Bender element testing to measure the shear wave velocity is typically employed to estimate the small strain stiffness of soil media (Shirley and Hampton 1977). Lee et al. (2007), Kim and Santamarina (2008) and Lee et al. (2010) exercised bender

element testing on sand rubber mixtures of various *RC*, and in the case of Lee et al. (2010) at two size ratios. Lee et al. (2007) observed a threshold value of the shear modulus (G_{max}) at a *RC* of 40% (by dry weight), where less rubber does not have a significant impact on the stiffness. At a *RC* of 40%, the sand matrix controls still controls the stiffness of the mixture at small strains, but at higher values of *RC* a significant decrease in G_{max} is evident. Similar to the results by Lee et al. (2007), Kim and Santamarina (2008) found the sand skeleton to control small strain behavior at a rubber volume (V_{rubber}) (by dry weight) < 30%, while the rubber skeleton prevails at V_{rubber} > 60%. Intermediate mixtures exhibit transitional effects controlled by both sand and rubber particles. Finally, Lee et al. (2010) found a sudden rise in G_{max} at a *SF* of 40 to 60%, regardless of nominal rubber particles size, yielding the conclusion that rubber particle size has only a small effect on the small strain stiffness of sand-rubber-mixtures. For all research described above, G_{max} displayed log-log linear results with increasing mean effective stress.

Large strain stiffness of sand-rubber-mixtures was studied in triaxial compression by Youwai and Bergado (2003) and Zornberg et al. (2004). Youwai and Bergado (2003) studied shredded rubber tire-sand mixtures at mixing ratios of 40:60 and 50:50. In comparing triaxial compression data for the two mixing ratios it is clear that at large strain values the rubber tire-sand-mixtures at mixing ratio of 50:50 is less stiff. Zornberg et al. (2004) studied the shear stress mobilized at 5% axial strain for mixtures with varying tire shred contents, Figure 2.8. As shown, the sample with an *RC* of 38.3% mobilized the most shear stress at 5% axial strain, for applied normal stresses of 0 to 100

kPa. Samples with *RC* values above and below this threshold exhibit less mobilized shear stress at 5% axial strain for the same range of normal stresses. At an applied normal stress of 200 kPa, the difference in mobilized shear stress at 5% axial strain for *RC* values of 5 to 38.3% is small and controlled by an *RC* of 10%.

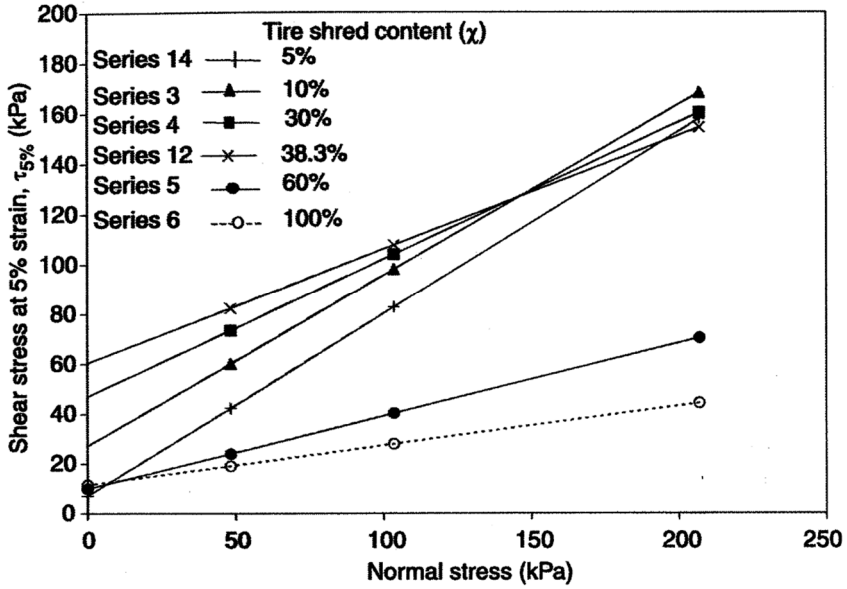

Figure 2.8 Shear stress mobilized at 5% axial strain for varying tire shred contents in sand-rubber mixtures (after Zornberg et al. 2004)

2.6.3 Effect of Rubber on Peak and Critical State Shear Strength

The peak and residual strength of sand-rubber-mixtures have been studied by many researchers (Section 2.5) and the results are generally agreeable between studies; therefore, only the results of Youwai and Bergado (2003) and Zornberg et al. (2004) will be discussed in detail. Specimens tested by Youwai and Bergado (2003) displayed strain hardening behavior, and increasing friction angles with both increasing mean effective stress and *RC* for tire shred-sand mixing ratios of 30:70, 40:60 and 50:50. For a mixing ratio of 20:80 specimens exhibited strain softening behavior beyond approximately 8%

distortional strain. Peak and residual friction angles were similar at rubber tire-sand mixing ratios of 20:80, 30:70 and 40:60 and residual friction angles were approximately 10% below peak friction angles for mean effective stresses of 50, 100 and 200 kPa. Triaxial compression testing by Zornberg et al. (2004) yielded strain hardening behavior for *RC* values of 0 to 80%. In comparison to Youwai and Bergado (2003), Zornberg et al. (2004) studied a wider range of *RC* values and two different initial relative densities. According to research by Zornberg et al. (2004) the influence of tire shred content on the behavior of sand-rubber-mixtures is significant. Peak shear strengths were not reached at axial strains as high as 15% for mixtures with *RC* above 30%. The internal friction angle increased with *RC* up to approximately 30%, upon which increasing tire content decreased shear strength.

2.7 Expansive Soil Rubber Mixtures

The combination of expansive-soil-rubber (ESR) mixtures form a newly developed technology employed to stabilize expansive material. ESR mixtures use principles similar to that of stabilization with the addition of sand; as expansive material is replaced with non-expansive material swelling becomes less severe through replacement and dilution. The primary research on ESR mixtures has been performed at Colorado State University in Fort Collins, Colorado. Specific areas of ESR mixtures have been examined including mitigation of swell potential (Seda et al. 2007), shear strength and stiffness of ESR mixtures (Dunham-Friel and Carraro 2011) and stiffness improvement of ESR mixtures using fly ash (Wiechert et al. 2011). The following sections will cover the findings in the preceding documents in addition to other findings in soil rubber

mixtures. Numerous studies have been explored regarding ESR mixtures including topics such as strength, stiffness, compressibility and hydraulic conductivity. Topics relevant to the work presented in this study will be covered in detail. Due to the limited amount of research on ESR mixtures, non-expansive clay-rubber-mixtures will also be discussed where pertinent.

2.7.1 Effect of Rubber on Compressibility and Swell Response

Al-Tabbaa and Aravinthan (1998) studied mitigation of swelling characteristics using tire shreds as part of a larger study. Rubber particles employed were between 1 to 4 and 4 to 8 mm in nominal rubber particle diameter, and *RC* ranged between 6 and 15%. Water and paraffin with both used as inundation fluids to examine the differences in swell behavior and permeability for landfill applications. As displayed in Figure 2.9, the amount of swell decreases with increasing *RC* while an inverse trend is shown for swell pressure which decreases with decreasing *RC* for gravimetric water content (*w*) ranges of 16 to 22%. Peak swell response and maximum swell pressures were observed at a *w* of 18% for specimens inundated with water. Differing trends can be seen for specimens inundated with paraffin. Specimens inundated with paraffin increased in swell percent with increasing *RC* for *w* from 16 to 22%, and increased in swell pressure with increasing *RC* for *w* from 18 to 22%. Peak swell response and maximum swell pressures were also observed at a *w* of 18% for specimens inundated with paraffin.

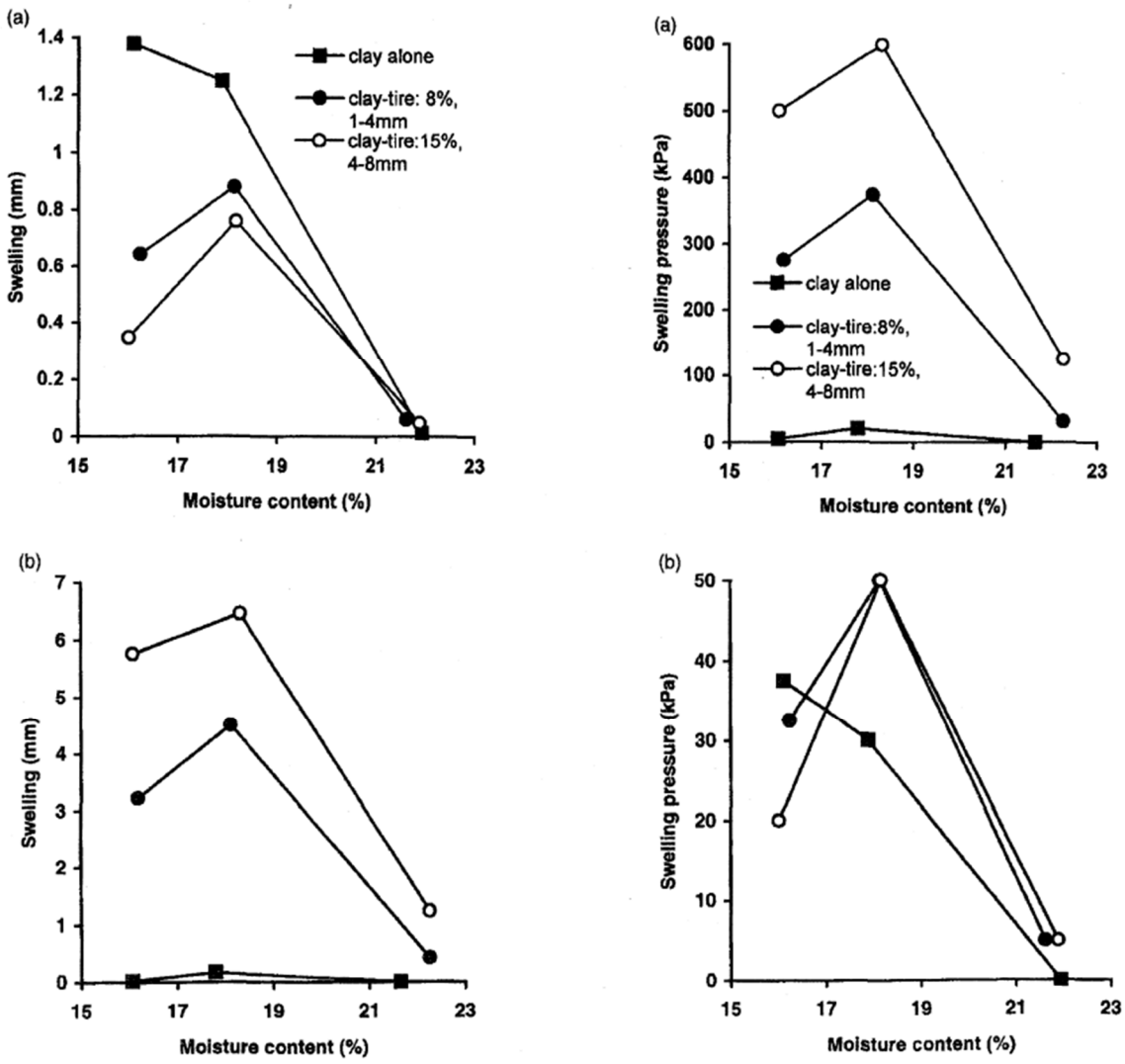

Figure 2.9 Swell response with varying initial water content (w_i) and rubber content *RC* for (a) samples inundated with de-ionized water and (b) samples inundated with paraffin (after Al-Tabbaa and Aravinthan 1998)

Seda et al. (2007) first explored the possibility of adding another STR refining product, granulated rubber, particles to expansive soils specifically for the purpose of mitigating swell. A complete discussion of rubber particle size termeology is provided in section 2.7.2. Using a typical expansive soil found along the Front Range of Colorado Seda et al. (2007) compared mechanical properties of isolated expansive soil and an ESR mixture with an *RC* of 20% (by dry weight). Seda et al. (2007) investigated the effect of

granulated rubber on index properties, compaction, and one-dimensional swell-consolidation response. Conclusions of research by Seda et al. (2007) included: (1) similar plasticity indices for the isolated soil and the ESR mixture; (2) standard proctor density testing (ASTM D698) on both the isolated soil and the ESR mixture provided similar optimum water contents and a decrease in the maximum dry unit weight for the ESR mixture; and (3) the ESR mixture provided a significant decrease in both the swell percent and swell pressure by reducing overall compressibility when tested in a one dimensional swell-consolidation apparatus (ASTM D4546).

Expanding on Seda et al.'s work Patil et al. looked into the specific mechanisms of compressibility variations for expansive soil stabilized with both sand and granulated rubber. Specifically, grain stiffness and elastic properties were analyzed using moist tamping and complementary discrete element method simulations. Major conclusions from Patil et al.'s research include: (1) swell mitigation increases as both the sand and *RC* increase; (2) stiff sand grains are more efficient in mitigating swell in comparison to flexible granulated rubber grains; (3) isolated heterogeneous regions of both water content and density exist more prevalently in ESR mixtures in comparison to sand and expansive soil mixtures; (4) the extent with which an additive mitigates swell is related to its ability to sustain shear contact forces upon expansion; and (5) stiff sand grans enable the locking of shear forces translating to a decrease in contact sliding, opposed to flexible rubber grains which allow the release of shear forces translating to an increase in contact sliding.

Dumham-Friel and Carraro (2011), and Wiechert et al. (2011) both examined isotropic swell response of ESR mixtures during triaxial testing. Dumham-Friel and Carraro (2011) found a decrease in isotropic swell from 6.5% to 2.3% when comparing a host soil to an ESR mixture at 20% *RC*. Wiechert et al. (2011) tested ESR mixtures with the addition of fly ash. Results from Wiechert et al. (2011) displayed a decrease in volume, or contraction, during inundation or up to 3.8% when including fly ash in the mixture. The lack of swell is explained by the inclusion of fly ash which results in the development of particle bonding, restricting the movement of soil particles within the matrix and fly ash induced cation exchange reducing the host soil's high affinity towards water. Swell response was not the primary focus of the two aforementioned researchers, as discussed later in the manuscript.

2.7.2 Effect of Rubber on Small and Large Strain Stiffness

As alluded to previously, rubber particles have much lower stiffness in comparison to soil particles (Lee et al. 2007). Numerous studies exhibit reduced stiffness when adding rubber to fine grained material (Edil and Bosscher 1994; Foose et al. 1996; Al-Tabbaa and Aravinthan 1998; Garga and O'Shaughnessy 2000; Pupuala and Musenda 2000; Cetin et al. 2006; Őzkul and Baykal 2007; Seda et al. 2007; Promputthangkoon and Hyde 2008; Dunham-Friel and Carraro 2011; Patil et al. 2011; and Wiechert et al. 2011). Edil and Bosscher (1994) concluded that soil-rubber mixtures exhibit significant initial compression under load, as high as 40% of the initial thickness, and once compressed behave like an elastic material with very little stiffness. Also, Edil and Bosscher (1994) found that the resilient modulus decreased 1.2 orders of magnitude over a bulk stress

range of 50 to 700 kPa. Resilient modulus testing is common practice in pavement engineering, where vehicular loads will be applied to a soil matrix repetitively, and has particular implications for research presented in this manuscript due to the potential applications of ESR mixtures. Al-Tabbaa and Aravinthan et al. (1998) found initial stiffness to be approximately one half and similar strain to failure values comparing ESR mixtures at 6 to 10 % *RC* to host material in UCS testing. Also, increasingly prolonged strain ranges over which the maximum stress value was retained were evident with increasing *RC*.

Dumham-Friel and Carraro (2011), and Wiechert et al. (2011) have both studied the stiffness of ESR mixtures thoroughly. Dumham-Friel found stiffness reductions when including STR in an expansive soil mixture of 12 to 58% for mean effective stress values ranging from 50 to 200 kPa. Bender element testing was conducted in order to determine small-strain stiffness. Results revealed a reduction in G_{max} of 44 to 63% at an *RC* range of 0 to 20%. Shear wave velocities, and therefore G_{max} decreased uniformly as *RC* increased irrespective of *p'*. Also, G_{max} exhibited a greater increase when plotted against *p'* for decreasing *RC* values. At typical vertical strains considered in foundation design, around 0.4%, a RC of 10 and 20% produced a reduction in the stiffness of 65 and 45% respectively. At large strains (in excess of 1%) differences in the secant young's modulus (*E*), another measure of stiffness, are less pronounced for differences in *RC*, *w* and *p'*. In fact, the discrepancy in *E* between the host expansive material employed and *RC* values of 10% and 20% decreases with increasing strain values. In general, the

results of Dumham-Friel and Carraro (2011) display that as *RC* values increase so does the strain to mobilize equal amounts of shear strength.

Expanding upon Dumham-Friel's research, Wiechert et al. investigated the small and large stiffness response of ESR mixtures with the inclusion of Class C and off-specification fly ash. Wiechert's results indicate that the stiffness of ESR mixtures is improved substantially with the addition of fly ash to the matrix. In fact, G_{max} at small strain levels increased by one to one and a half times when comparing specimens with similar levels of *RC* with and without fly ash. Fly ash curing time also played a pivotal role in initial stiffness, increasing G_{max} by approximately 20% for similar fly ash types, *RC* and *p'*.

Stiffness degradation at both small and large strain testing based on research by Dumham-Friel and Carraro (2011) can be viewed Figure 2.10. Figure 2.10 displays the decreasing small strain stiffness for increasing *RC*. Shown is the less pronounced degradation in stiffness at large strains, greater than 1%.

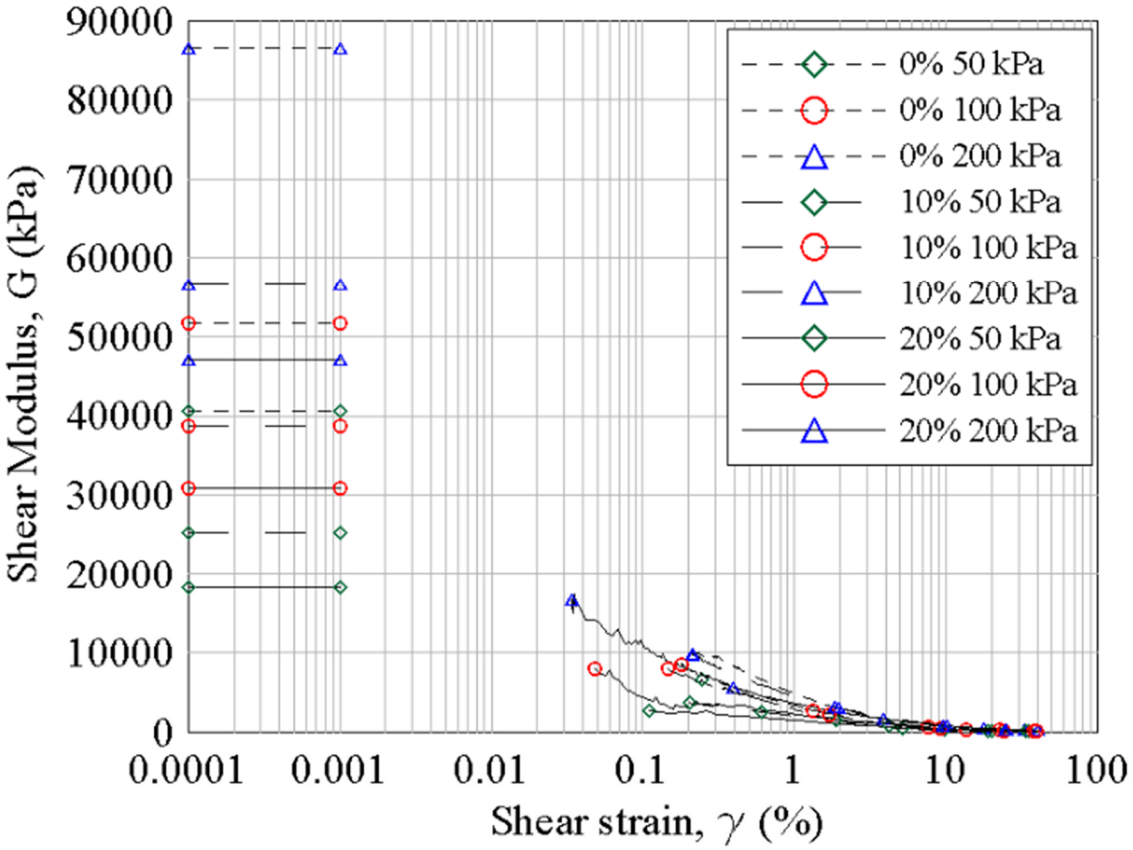

Figure 2.10 Stiffness degradation at small and large strains for expansive soil-rubber (ESR) mixtures (after Dunham-Friel and Carraro 2011)

2.7.3 Effect of Rubber on Peak and Critical State Shear Strength

The effects of rubber on peak and residual shear strength when mixed with fine grained material has been studied (Al-Tabbaa and Arvinthan 1998, Cetin et al. 2006, Őzkul and Baykal 2006, Akbulut et al. 2007 and Őzkul and Baykal 2007). Al-Tabbaa and Arvinthan (1998) displayed a reduction in peak shear strength of approximately 200 kPa when testing clay mixed with 6 to 10%, 1 to 8 mm tire rubber in UCS testing. Through a series of consolidated undrained (CU) triaxial and direct shear tests on clay tire mixtures Cetin et al. (2006) was able to show: (1) an increase in apparent cohesion with increasing *RC* of up to 40%; (2) decreasing vertical strains and volume changes during shearing for

an increase in *RC*; and (3) mixtures up to 20% coarse and 30% fine grained rubber can be used in situations where low weight and high strengths are desirable. Őzkul and Baykal (2006) and Akbulut et al. (2007) both found increasing UCS values as the inclusion tire fibers increased for *RC* up to 10% and 2% by dry weight, respectively.

Most consistent with the research presented in this manuscript are results by Dumham-Friel and Carraro (2011) and Wiechert et al. (2011). Dumham-Friel and Carraro (2011) found an increase in overall shear strength, decreasing peak friction angles, and increasing critical state friction angles with an increase in *RC*. Peak friction angles decreased from 46.8° to 42.6°, and critical state friction angles increased from 33.4° to 40.3° for host materials and 6.7 mm, 20% *RC*, ESR mixtures, respectively. Wiechert et al. (2011) found an increase in the UCS of ESR mixtures with the inclusion of fly ash at 20% *RC*. With the addition of fly ash a slight increase in critical state friction angles were observed; increasing from 29.5° to between 31.0° and 32.4° depending on the type of fly ash employed. As explained by Wiechert et al. (2011), once the pozzolanic soil-soil and soil-rubber bonds are broken (at low strain levels) fly ash no longer promotes an increase in shear strength. Therefore, the main advantage of using fly ash is seen at low strain levels, where additional shear strength is mobilized due to the pozzolanic reactions.

2.8 Scalability and Particle Size Effects

Economically, ESR mixtures become more feasible to employ as scrap tires become less refined, less homogeneous and larger in average particle diameter. The majority of testing on soil-rubber mixtures have employed well refined, uniform rubber particles with

minimal impurities (steel reinforcement for example). In order to determine how more economically savvy rubber constituents will behave in field scale ESR mixtures larger, less homogeneous rubber particle effects must be investigated. Also, to fully link the work presented later in this manuscript with previous studies general protocol for scaling soil laboratory testing, particle size effects of tire derived aggregate, and field scale testing on stabilized expansive material will be presented.

2.8.1 Scalability of Fine-Coarse Grained Media Mixtures

As the largest nominal particle diameter increases, so must laboratory testing techniques and the testing apparatus (Aghaei et al. 2010). For example, when testing rockfill materials several common modeling techniques are available to scale down particle diameters: (1) the scaling technique (Zeller and Wullimann 1957); (2) the parallel gradation technique (Lowe 1964); (3) the generation of quadratic grain-curve technique (Fumagalli 1969); and (4) the replacement technique (Frost 1973). Generally, the parallel gradation technique is regarded as the most successful and representative method to scale soil laboratory testing (Ramamurthy and Gupta 1986). Although scaling techniques work well for primarily coarse grained media containing few fines, these techniques cannot be employed when the fines content reaches substantial levels, similar to ESR mixtures.

Clayey soils containing various amounts of coarse grained media have been studied extensively. For example, Holtz and Willard (1956) may have been the first to examine shear strength of clayey soils including various contents of gravel from 0 to 65%. Results indicated that as the gravel content increases, so does the shear strength of clay-gravel

mixtures. Other researchers have also studied the effects of gravel on the shear strength of clay soils (Patwardhan et al. 1970; Donaghe and Torrey 1994; Vallego and Mawby 2000; Jafari and Shafiee 2004; and Vallejo and Lobo-Guerrero 2004). Mixtures of sand and fine grained material have also been studied (Miller and Sowers 1957; Graham et al 1989; and Tan et al. 1994). According to the aforementioned research the following variations in soil parameters can be expected with an increase in coarse material to a fine matrix: (1) decrease in plasticity; (2) increase in small and large strain stiffness; (3) increase in pore water pressure generation in the clay matrix during shearing; (4) increase in overall shear strength at all strains examined; (5) increase in permeability; and (6) increase in heterogeneities of effective stresses in the clay matrix.

Research in lacking regarding the scalability of coarse fine mixtures, specifically when the coarse fraction is highly elastic and compressible. The primary mechanisms controlling shear resistance in rockfill materials are interlocking between particles and particle breakage (Budhu 2011). The primary mechanisms controlling shear resistance in fine grained materials are frictional, including interlocking between particles. Therefore, alternative techniques must be designed in scaling rubber particles due to grain size characteristics and relative prominence of shearing mechanisms.

2.8.2 Particle Size Effects of Tire Derived Aggregate

Recycled tire rubber is grouped into various classifications based on average particle size; 305 to 50 mm rubber particles are classified as tire shreds, 12 to 50 mm rubber particles are classified as tire chips, and rubber particles smaller than 12 mm are classified as

granulated rubber (Strenk et al. 2007). Recycled tire rubber is often referred to as tire derived aggregate. Variability and scale dependency of tire derived aggregate has been studied effectively. According to Strenk et al (2007) shear strength and compressive parameters of various scrap tire rubber sizes have considerably large variations. Figure 2.11 displays a culmination of research performed on tire derived aggregate. Table 2.3 covers a statistical analysis of pertinent compressive and shear strength parameters of various rubber particle sizes, independent of manufacturing techniques.

Table 2.3 Statistical data for various geotechnical parameters of tire derived aggregate (after Strenk et al. 2007)

	Statistical properties				
Property	Data set size (n)	Range (Min.–Max.)	Mean ($\bar{x}$)	Standard deviation (σ)	COV ($\sigma/\bar{x}$) (%)
γ (kN/m^3)	**22**	**4.71–6.41**	**5.79**	**0.5**	**8**
Granulated rubber	4	4.95–5.88	5.48	0.4	7
Tire chips	8	5.13–6.41	5.91	0.4	7
Tire shreds	10	4.71–6.30	5.83	0.5	9
c (kPa)[a]	**15**	**3.3–25.4**	**13.8**	**7.4**	**54**
Granulated rubber	1	21.6	21.6	0	0
Tire chips	7	3.3–25.4	17.2	8.1	47
Tire shreds	7	4.3–13.2	9.3	3.6	38
ϕ (degrees)[b]	**23**	**6–39**	**21.8**[c]	**8.5**	**39**
Granulated rubber	6	6–32	18.8[c]	8.7	46
Tire chips	9	11–38	19.1	8.0	42
Tire shreds	8	19–39	27.0	6.2	23
M_{sec} (kPa)	**17**	**130–485**	**280**	**95**	**34**
Granulated rubber	—	—	—	—	—
Tire chips	7	253–485	354	76	22
Tire shreds	10	130–373	229	70	31
$C_{\alpha\varepsilon}$	**14**	**0.0038–0.0128**	**0.0070**	**0.0021**	**30**
Granulated rubber	—	—	—	—	—
Tire chips	7	0.0051–0.0090	0.0068	0.0011	16
Tire shreds	7	0.0038–0.00128	0.0071	0.0028	39

Note: COV=coefficient of variation.

[a]Cohesion values reported for normal stresses <100 kPa.

[b]Majority of friction angle values reported at normal stress <100 kPa. One data point (granulated rubber, ϕ=6°) from Masad et al. (1996) was evaluated at 150–350 kPa.

[c]Excluding Masad et al. (1996), total $\bar{x}$, σ, and COV change by +3, −6, and −9%; granulated rubber $\bar{x}$, σ, and COV change by +14, −17, and −27%.

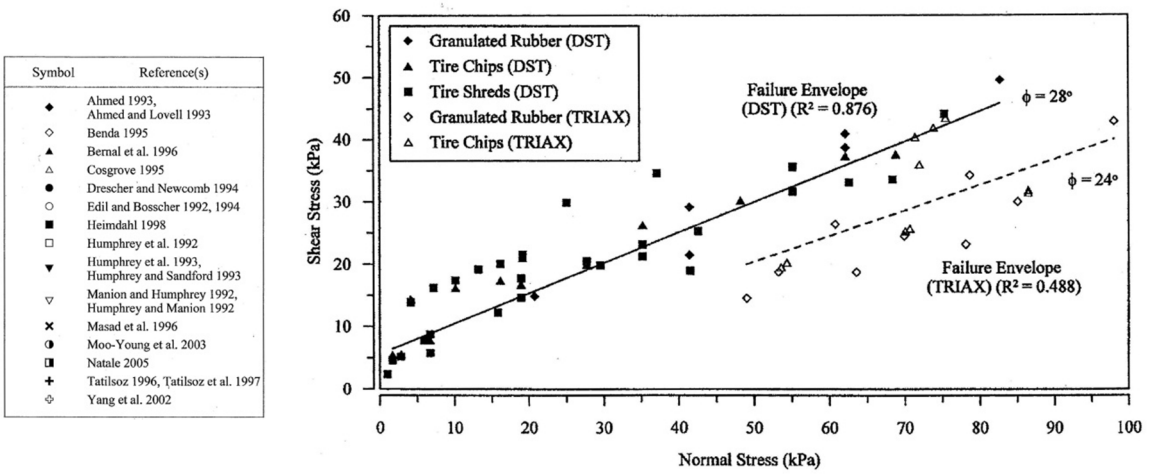

Figure 2.11 Direct shear and triaxial testing data for various tire derived aggregate sizes (after Strenk et al. 2007)

As presented in Figure 2.11 and Table 2.3, extensive variability exists between the compressive and shear strength parameters of differing sized tire derived aggregate tested in both direct shear and triaxial compression. Al-Tabbaa et al. (1997) studied the effect of rubber particle size in soil-tire mixtures. The research was performed on rubber particle sizes ranging from 1 to 12 mm, and UCS testing yielded consistent UCS results at 10% rubber content (by dry weight) for all particle sizes investigated. Bergado et al. (2005) displays triaxial results on a specific tire rubber particle size mixed with sand, Figure 2.12, and conclude that shear strength parameters are similar for various tire chips.

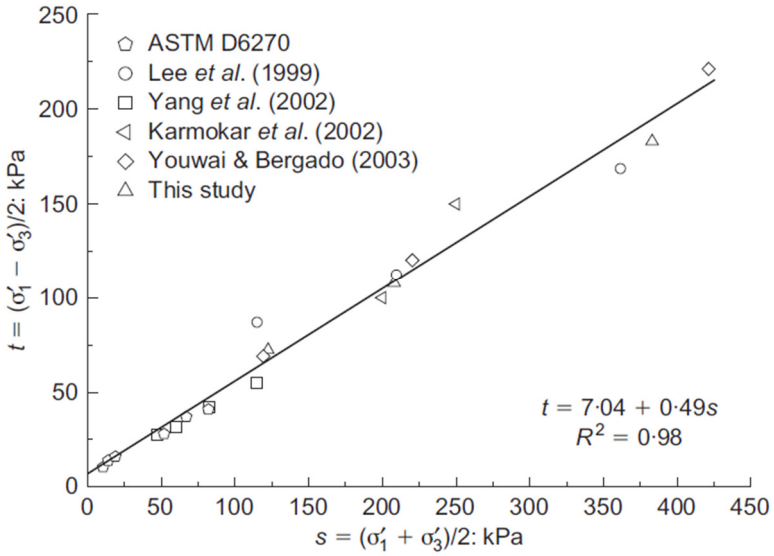

Figure 2.12 Shear strength from triaxial compression tests on tire chips (after Bergado et al. 2004)

According to Figure 2.12, it is conclusive that rubber particles of similar size provide similar shear strength characteristics independent of processing and refining techniques in sand-rubber mixtures. The limited rubber particle size range examined by Al-Tabbaa et al. (2007) yields the opportunity to define the affects additional rubber particle sizes have on soil rubber mixtures. Compressive and strength testing on various rubber particle sizes in ESR mixtures is absent from literature.

2.8.3 Field Scale Experiments on Expansive Material

The ability to fully quantify the response of a stabilized expansive material in various size testing protocols is an important for the potential applicability of ESR mixtures, especially when particle size considerations are of interest. Expansive soils have been studied at a field scale to: (1) monitor heave and swell pressure (Tang et al. 2009; Abduljauwad et al. 1998; and Mersi et al. 1994); (2) survey swell response due to

seasonal variations in water content over a period of several years (Tang et al. 2009; and Fityus et al. 2004); (3) study the effects of total heave of a slab-on-grade system (Yoshida et al. 1983); and (4) address to performance of various chemical stabilizers (Pappala et al. 2007). Important conclusions from previous field scale research relating to this research are: (1) on average, chemical admixtures were able to reduce vertical compression upon loading by more than half (Puppala et al. 2007); (2) heave measurements indicated that blast furnace slag was the most successful in controlling swell, followed by cement, fly ash-cement, and lime-fiber treated soils (Puppala et al. 2007); (3) the majority of recognized swell is generally limited to the top 0.5 m of expansive material (Tang et al. 2009 and Fityus et al. 2004); and (4) matric suction and initial water content play pivotal roles on swell potential and swell pressure experienced in reconstituted expansive soils under strip loads (Yoshida et al. 1983).

Field scale testing involving mixing coarse media, especially non-rigid rubber-like particles, with fine grained mixtures to monitor stability and swelling characteristics is generally lacking from research. The isolated instance of studying ESR mixtures in a field plot setting was performed at CSU as part of a larger study (Dunham-Friel 2009). Research from the field component of the study by Dunham-Friel (2009) has yet to be published in literature. The major conclusions from the research were: (1) using survey equipment is not an accurate enough measurement system to monitor the small strains due to swell expansion in field plots, (2) locally-available, compacted, non-expansive material does not provide adequate means of confining the base and lateral components of field plots to limit swelling behavior to a one-dimensional vertical response upon

inundation, and (3) compaction of expansive soil and associated ESR mixtures is feasible with the correct compaction equipment. The ability to compact ESR mixtures in a field scale scenario is displayed in Figure 2.13 (CDPHE 2011). A roller pass as indicated in Figure 2.13 is defined as a single pass for a single direction (not back and forth) of the roller compactor over the entire plot area at a rate slow enough to simulate a static, monotonic compaction effect. A roller pass as discussed in Chapters 4, 5 and 6 includes an identical definition. The three major conclusions from this field study were instrumental in controlling compaction, the selection of field equipment and monitoring devices, and the decision to continue researching ESR field scale plots.

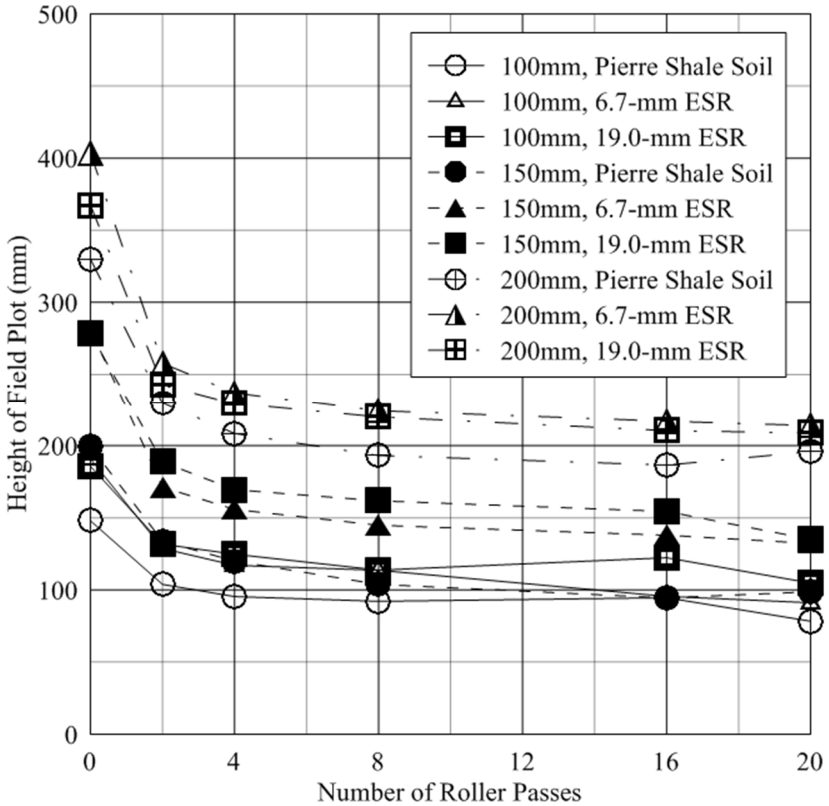

Figure 2.13 Vertical height of expansive-soil rubber (ESR) field plots versus the number of roller passes with a 73.4-kN C-433 vibratory roller (CDPHE 2011)

CHAPTER 3: CONCEPTUAL FRAMEWORK

3.1 Critical State Soil Mechanics

The critical state model (CSM) was selected as the basic framework to characterize the mechanical behavior of ESR specimens tested in one-dimensional swell-compression, isotropic swell-compression, and axisymmetric monotonic compression. A systematic and rigorous testing program, analyzed in a proper framework, will provide a better indication of the effects the initial state parameters including the relative compaction (C_R), water content (w) and rubber content (RC), the nominal maximum rubber particle diameter (d_R) and specimen size have on the mechanical response of ESR mixtures. In general critical state (CS) describes a unique surface upon which a respective soil will sustain a constant flow condition (Budhu 2011). During axisymmetric compression specimens reach a CS condition when additional shearing results in constant shear stress, effective confining stress and pore water pressure change or equilibrium in the stress state (Schofield and Wroth 1968), or $\delta q/\delta\varepsilon_a = \delta p'/\delta\varepsilon_a = \delta\Delta u/\delta\varepsilon_a = 0$. The CSM was introduced by Schofield and Wroth (1968) in the text *Critical State Soil Mechanics*, through the Granta-gravel rigid-plastic model and Cam-clay elastic-plastic model. A basic CS failure surface defined by a locus of points in specific volume (v) – mean effective stress (p') and mean effective stress (p') – deviatoric stress (q) space can be described for soils reaching CS or a purely plastic yielding phase (Salgado 2008), as displayed in Figure 3.1. Definitions of v, p', and q will be presented in subsequent sections of Chapter 3. Traditional soil mechanics adapted through Mohr-Columb framework was realized insufficient to describe purely plastic, CS soil behavior thus establishing the need for a

more rigorous and complete method to characterize soil response at large distortions (Schofield and Wroth 1968).

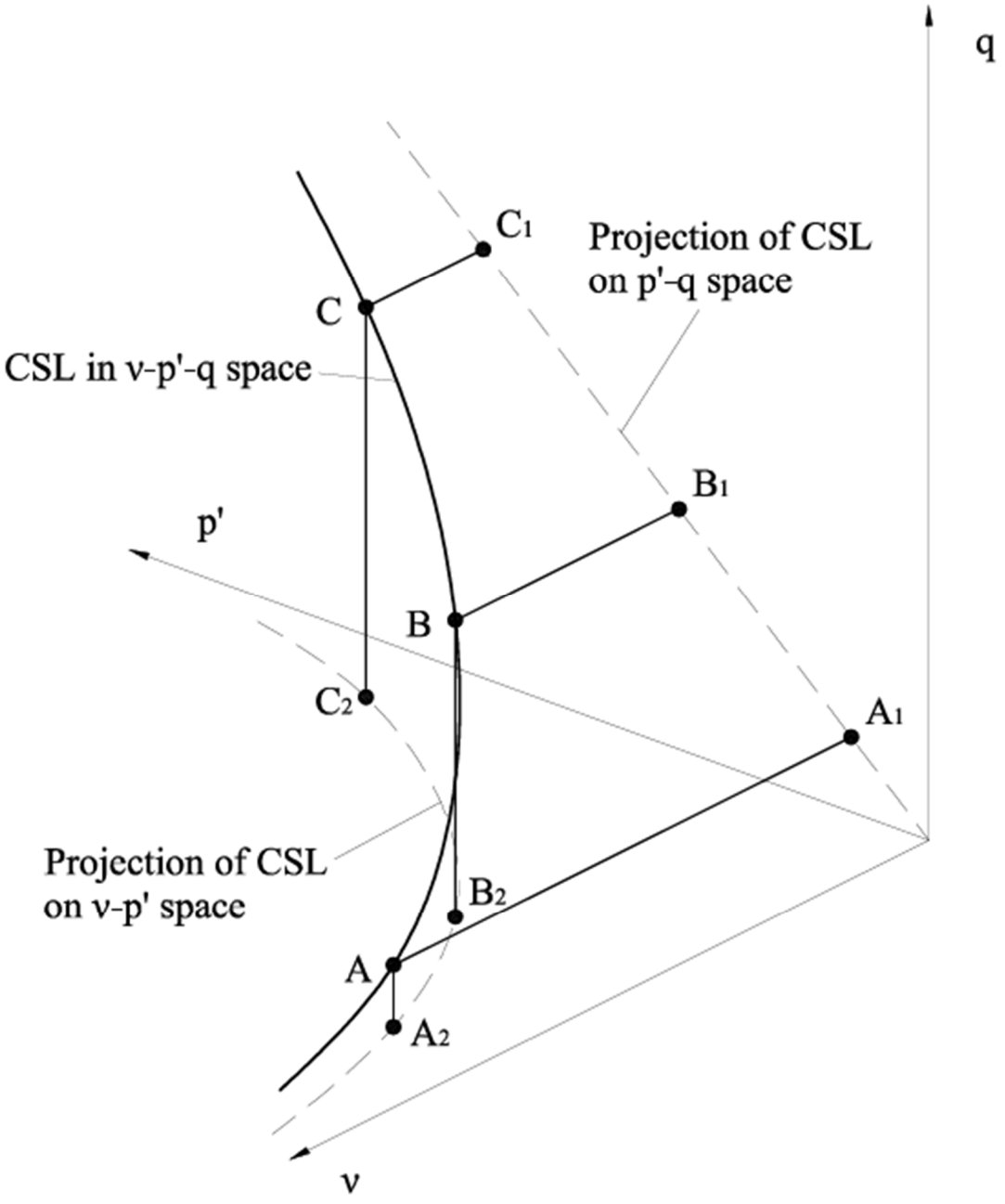

Figure 3.1 Critical state line (CSL) in $v - p' - q$ space with projections in $v - p'$ and $p' - q$ space (modified after Salgado 2008)

3.2 Yielding and Plasticity

In order to fully develop the CSM, a discussion involving yielding and elasticity is necessary. Similar to other materials tested in compression or extension, soils strain elastically until deformations become large enough to dissipate energy and produce irrecoverable or plastic strains (Atkinson, 2000). Once straining has exceeded the elastic range, typically referred to as the elastic yield surface (Schofield and Wroth 1968), an elastic-plastic range is produced where soils behave both elastically and plastically. During elastic-plastic yielding a material may harden or soften (compress or dilate) depending on solid particle orientations and localized material states, but only a limited amount of deformation realized during loading is recoverable upon unloading. Hardening refers to an increase in yield stress over a range of strains while softening refers to a decrease in yield stress over a range of strains (Atkinson 2000). Loose or "wet" specimens harden, while dense or "dry" specimens soften (Schofield and Wroth 1968), as presented in Figure 3.2. If the soil state prior to axisymmetric compression is looser than the CSL, the effective soil structure will be unable to support the application of stresses resulting in an increase in pore water pressures (wet). If the soil prior to axisymmetric compression represents a state denser than the CSL, the effective soil structure will expand and dilate during deformation (dry). The relative terms "wet" and "dry" refer to volume change during deformation resulting in a decreasing or increasing pore volume during drained loading or an increase or decrease in pore water pressure during undrained loading, respectively. In general lightly over-consolidated (OC) materials behave loosely and heavily OC materials behave densely (Atkinson 2000). When soils are axisymmetrically compressed under a single controlled volume

(undrained), a tendency toward a denser or less dense (dilative) state can be determined by the relative pore water pressure change (Δu). The decree of over-consolidation, referred to as the over-consolidation ratio (OCR), is the ratio of the current effective stress of a soil element divided by its maximum past effective stress.

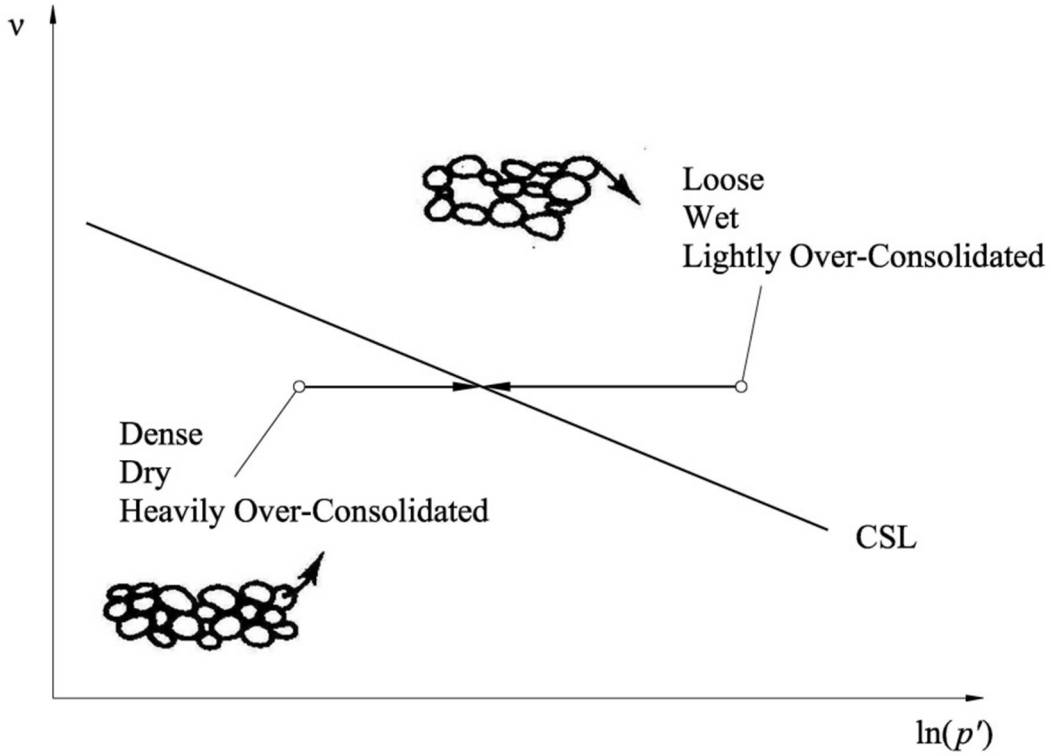

Figure 3.2 Initial soil states and corresponding stress paths to the critical state line (CSL) in the ln(p') - v plane during undrained axisymmetric compression (modified after Atkinson 2000)

Yield surfaces can take on a variety of meanings depending on specific aspects of soil behavior desired as presented in Figure 3.3. No-tension fracture, Hvorslev rupture, and cam clay yielding represent the limiting states of a soil element based on stress history (OCR) and stress state (p' and q) (Powrie 2004). Hvorslev rupture describes an increase in strength closely tied to a decrease in density producing an increase in dilation (Salgado

2008). Common yield surfaces discussed in soil mechanics include the elastic yield surface and critical state yield surface (Muir Wood 1990). Research presented in this thesis is focused on the critical state yield surface or the yield surface producing purely plastic or completely irrecoverable deformations (Muir Wood 1990), although various yielding states during axisymmetric compression including phase transformation and undrained instability are discussed in Chapter 6 (Murthy et al. 2007). CS for a specific material is unique in that at significant enough distortion the mechanical behavior is independent of initial density, sample preparation and the shear rate and is only dependent on the inherent nature of the material (Oquendo et al. 2010). CS is typically reached at strains greater than 10%, although some materials have required strains in excess of 50% (Atkinson 2000). Strains at which CS conditions are obtained during axisymmetric compression depend on the boundary conditions imposed and the soil state. As discussed in subsequent chapters, a feasible goal of 30 % axial strain (ε_a) was induced for undrained axisymmetric compression testing performed in the present research due to limitations in the triaxial apparatus.

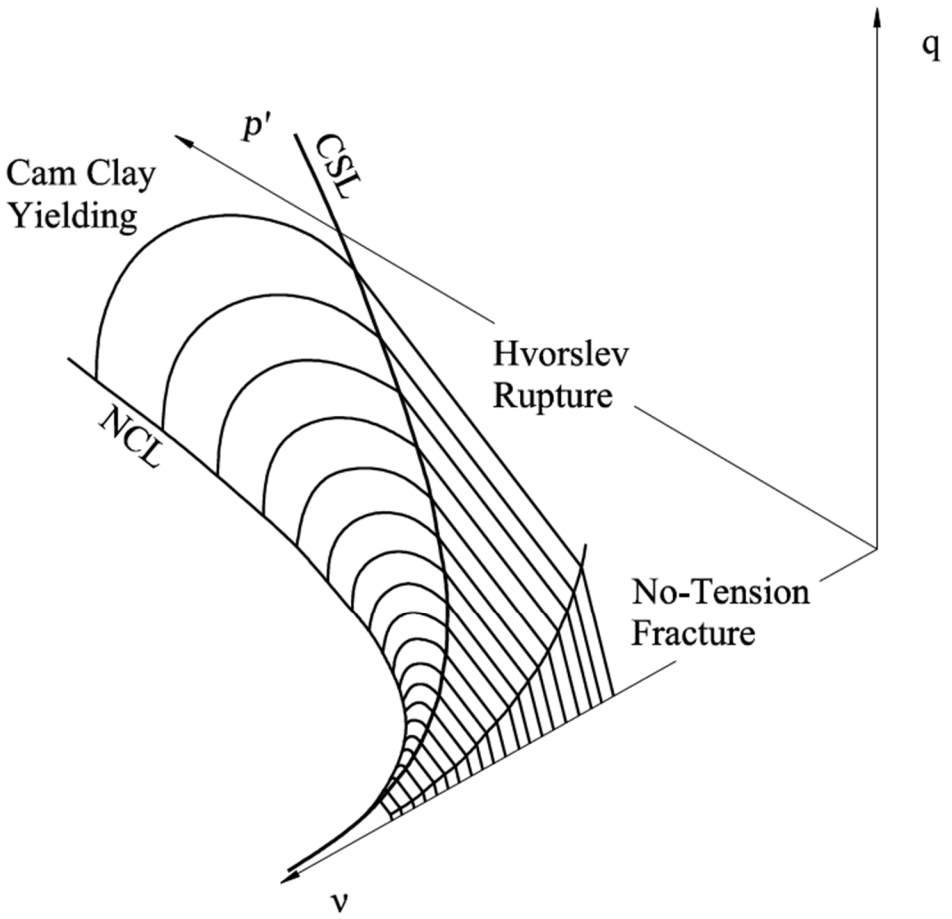

Figure 3.3 Limiting states and various yield surfaces at failure for soil samples in $v - p' - q$ space (modified after Muir Wood 1990)

3.3 One-Dimensional Compression

3.3.1 Swell-Compression Testing

One-dimensional swell-compression was used to define soil behavior and mechanical response in under applied effective vertical stresses (σ'_z) with lateral restraint or confinement (Figure 3.4). The complete dissipation of pore water prior to subsequent loadings is reflected in the nomenclature used to describe the loading sequence. Swell-compression testing is a unique type of one-dimensional compression, where expansive material is given the chance to swell under a selected level of σ'_z, typically referred to as

the seating pressure, prior to subsequent increases in σ'_z. In saturated soils, compression describes the process of dissipating positive pore pressure changes immediately following a change in the stress state of the soil matrix until an eventual equilibrium state is obtained in which pore pressures changes relative to the initial pore pressure state (Δu) no longer exist (Muir Wood 2009). Positive pore pressures changes due to alterations in the stress state are driven through the soil matrix by differential pressure gradients and, if dissipated, increase the overall effective stress of the soil matrix. For swell-compression testing performed on ESR mixtures, additional compression is recognized through distortion of individual rubber particles (Lee et al. 2007). However, in comparison to a soil water continuum, individual rubber particles (similar to those used in this study) are relatively incompressible. A complete discussion of rubber particle compressibility is outside of the scope of this research, and the reader is directed elsewhere (Lee et al. 2007; and Patil et al. 2011).

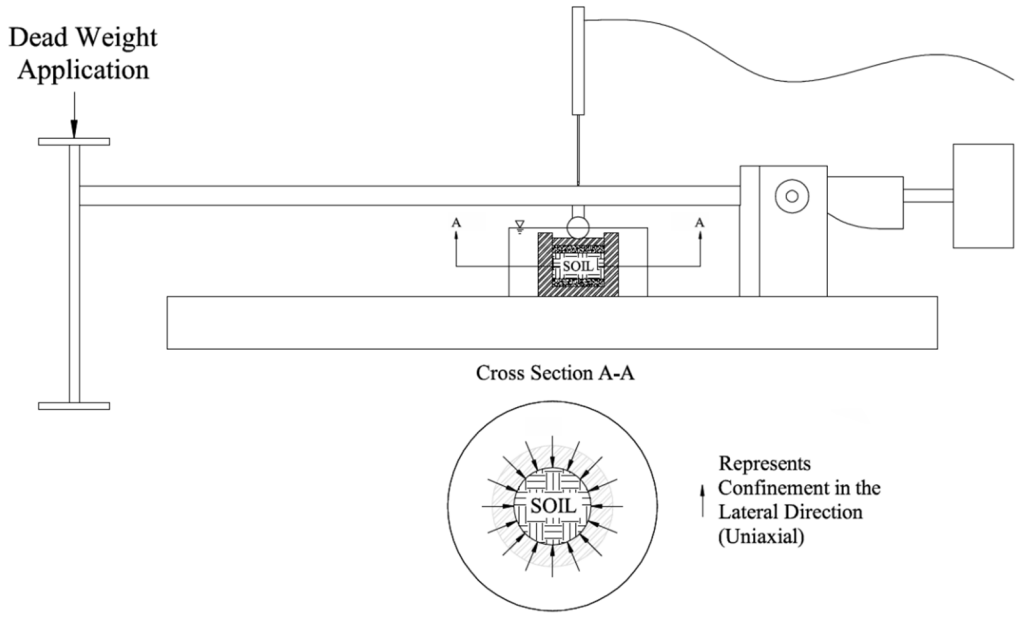

Figure 3.4 Small-scale one-dimensional swell-compression apparatus used in the present study including lateral confinement

One-dimensional compression testing is common practice in industry, and can represent cases of increasing σ'_z coupled with negligible lateral stress variations (Atkinson 2000). Swell-compression testing is typically performed on expansive fine-grained material where deformations are governed by changes in the pore structure and not individual particle distortion and reorientation (Budhu 2011). Through swell-compression testing it is possible to simulate and understand the mechanical response of soil media coupled with changes in σ_z and the degree of saturation. Displayed in Figure 3.5 is an idealized swell-compression curve presenting parameters pertinent to results presented in this manuscript.

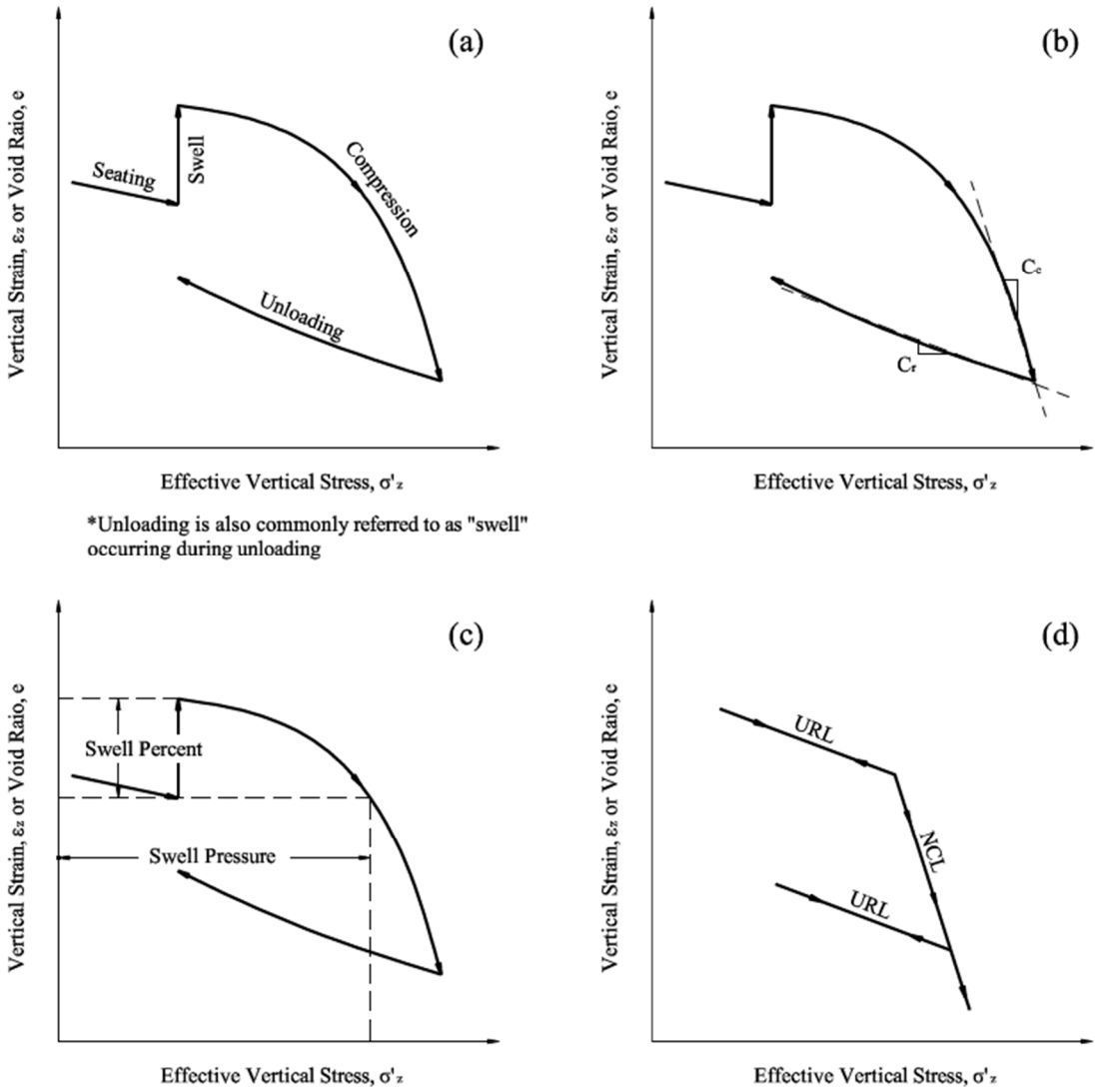

Figure 3.5 An idealized swell-compression curve for an expansive material including: (a) basic nomenclature used throughout this manuscript; (b) compression and recompression indices; (c) swell percent and swell pressure; and (d) idealized unloading and reloading lines (URL) and normal compression line (NCL) (modified after Nelson and Miller 1992 and Budhu 2011)

3.2.2 Swell-Compression Parameters

Swell-compression testing results are typically plotted on axes of vertical strain (ε_z) or void ratio (e) and σ'_z. The σ'_z axis is typically plotted on a log scale, due to the large variation in vertical stress application. In a one-dimensional swell-compression scenario,

a direct correlation between vertical strain and void ratio can be derived assuming that individual soil grains and water molecules are incompressible and all volume changes result from pore fluid entering or exiting the soil matrix. The most fundamental mechanical approach employing a stress-strain relationship was selected for the presentation of one-dimensional swell-compression results. Therefore, the duration of this manuscript will discuss one-dimensional response in terms of changes in vertical strain. Figure 3.6 presents the typical loading schedule used during swell-compression testing and in calculating Equation 3.1 through Equation 3.8.

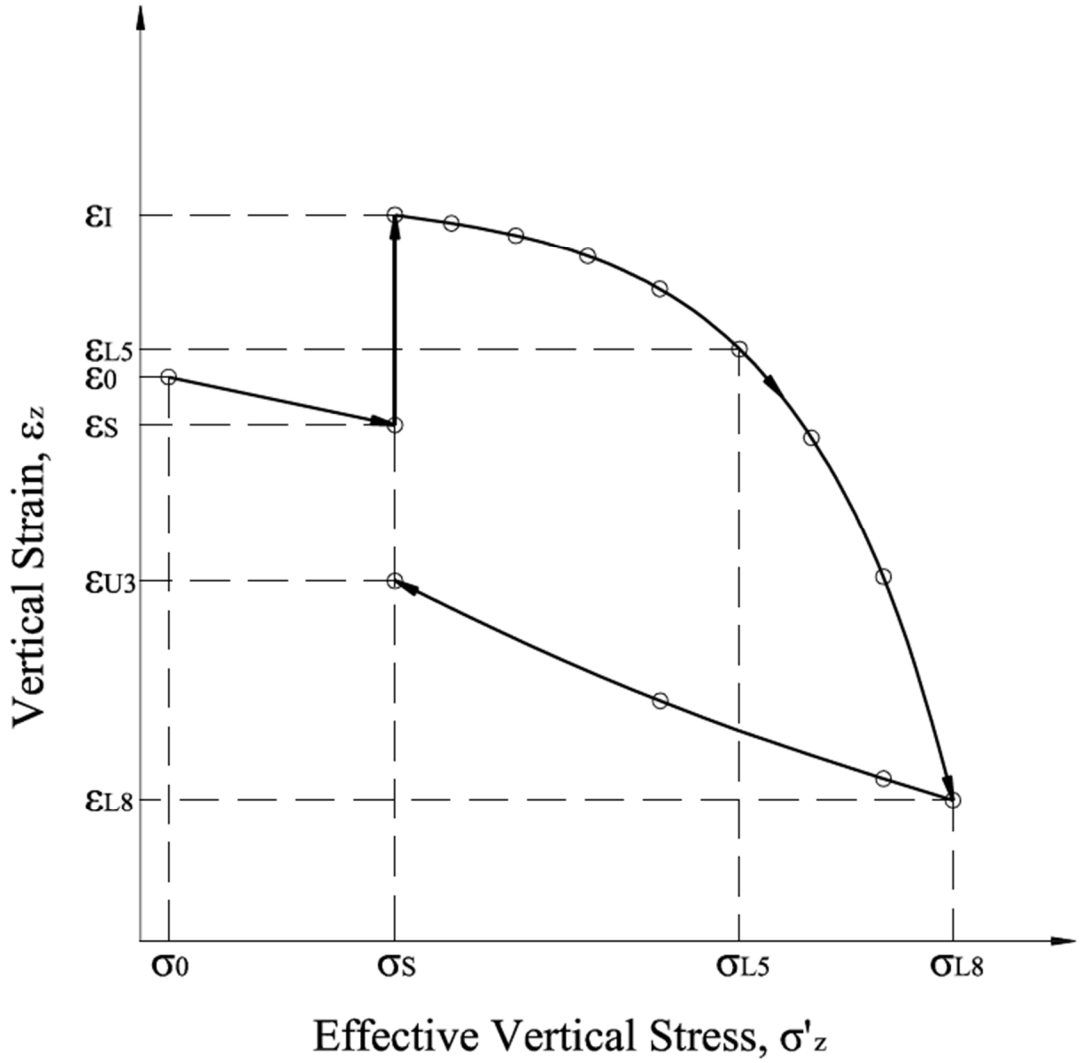

Figure 3.6 Typical loading schedule used in one-dimensional swell-compression indicating stress-strain relationships during loading and unloading used in determining equations 2 through 9. Each point on the curve represents a stage where: (1) additional vertical stress was applied; (2) inundation with water occurred; or (3) vertical stress was removed.

As presented in Figure 3.4 (c), swell percent ($S_{\%}$) and swell pressure (σ'_{zs}) are immediately available from one-dimensional swell-compression results plotted on axes of ε_z and σ'_z. The swell percent is defined as the difference in ε_z upon inundation under a selected seating load. The swell pressure is defined as the necessary to re-compresses a

specimen to a volume equal to its volume after completion of the seating load (Figure 3.5). In all cases σ'_{zs} was recognized between specific σ'_z, therefore σ'_{zs} was interpolated assuming a log-linear trend between σ_z values. $S_{\%}$ and σ'_{zs} are defined in equations 3.1 and 3.2:

$$S_{\%} = \varepsilon_I - \varepsilon_S \tag{3.1}$$

$$\sigma'_{zs} = \sigma_z^* \tag{3.2}$$

where ε_I represents the vertical strain after inundation, ε_S represents strain after seating, and σ_z^* represents the applied vertical stress necessary to obtain the swell pressure.

During compression the soil particles and pore fluid (typically water) are idealized as relatively incompressible. Therefore, matrix compressibility results from a decrease in pore volume, or void ratio, when Δu is relieved through drainage mechanisms and dissipation. Referring to Figure 3.4 (d), soils follow the normal compression line (NCL) when σ'_z exceed past maximum vertical stress, and follow the unloading reloading line (URL) at σ'_z less than the past maximum vertical stress (Budhu 2011). Two common compressibility values are present in one-dimensional compression testing including the compression index (C_c) and recompression index (C_r), as presented in Figure 3.4 (b). C_c is the log-linear slope of the NCL. C_r is the log-linear slope of the URL. C_c and C_r are defined in the following expressions:

$$C_c = \frac{e_{L8} - e_{L5}}{\log\left(\frac{\sigma_{L8}}{\sigma_{L5}}\right)} \tag{3.3}$$

$$C_r = \frac{e_{L8} - e_{U3}}{\log\left(\frac{\sigma_{L8}}{\sigma_{U3}}\right)} \tag{3.4}$$

where e_{L5} and e_{L8} are two successive void ratio measurements on the normal compression line (NCL), σ_{L5} and σ_{L8} are two successive applied vertical stresses on the NCL, e_{L8} and e_{U3} are two successive void ratio measurements on the unloading reloading line (URL), and σ_{U3} and σ_{L8} are two successive applied vertical stresses on the URL.

Further expressions relating to the compressibility of soils can be derived from a one-dimensional compression curve including the modulus of volume compressibility (m_v) the modulus of volume recompressibility (m_{vr}) the constrained modulus (M) and the elastic modulus (E). The moduli of volume compressibility and recompressibility define the linear slope of the NCL and URL, respectively, when employing axes of ε_z, and σ_z. The constrained and elastic moduli are reciprocal relationships of m_v and m_{vr}, respectively. Compressibility expressions are defined in equations 3.5 through 3.8:

$$m_v = \frac{\varepsilon_{L8} - \varepsilon_{L5}}{\sigma'_{L8} - \sigma'_{L5}} \tag{3.5}$$

$$m_{vr} = \frac{\varepsilon_{L8} - \varepsilon_{U3}}{\sigma'_{L8} - \sigma'_{U3}} \tag{3.6}$$

$$M = \frac{1}{m_v} \tag{3.7}$$

$$E = \frac{1}{m_{vr}} \tag{3.8}$$

where ε_{L5} and ε_{L8} are two successive strain measurements on the NCL.

Compressibility expressions are used interchangeably throughout literature, but there is a drive to revert to a more rigorous stress-strain mechanistic approach through presented results. Fundamental expressions for compressibility include *M* and *E* and are commonly used in mechanics (Beer et al. 2009). Expressions for compressibility presented in the following chapters will be used interchangeably depend on the appropriate expression for the present discussion.

3.4 One-Dimensional Consolidation

Swell-compression curves (Figure 3.5) are generated from a compilation of daily reading curves typically plotted on axes of displacement or vertical strain versus the logarithm of time (*t*), as shown in Figure 3.7 (a). The displacement can be normalized to reflect the amount of dissipated pore water (U_z), Figure 3.7 (b), assuming the completion of consolidation at the end of primary consolidation.

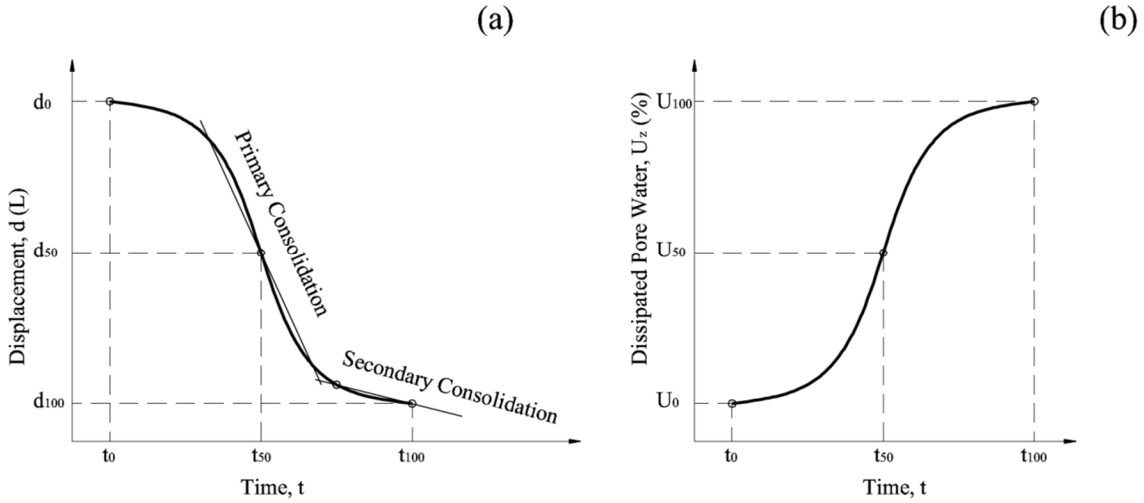

Figure 3.7 Daily reading curve for one-dimensional consolidation testing employing vertical axes of (a) displacement and (b) dissipated pore water (modified after Budhu 2011)

Recording reading with time allows for the calculation of two parameters commonly reported for the one-dimensional consolidation of soils; the coefficient of consolidation (c_v) and the permeability (k). Time rate of consolidation theory is governed by the following equation:

$$c_v \frac{\partial^2 u}{\partial z^2} = \frac{\partial u}{\partial t} \tag{3.9}$$

where c_v represents the coefficient of consolidation, u represents the pore water pressure, z represents the height or depth of the specimen and t represents time. The differential equation 3.9 can be resolved using Fourier Series, although it is typically solved using two approximate relationships (Budhu 2011):

$$T_v = \frac{\pi}{4}\left(\frac{U_z}{100}\right)^2 \qquad \text{for Uz} \leq 60\% \tag{3.10}$$

$$T_v = 1.781 - 0.933\log(100 - U_z) \qquad \text{for Uz} \geq 60\% \qquad (3.11)$$

where T_v is referred to as the time factor. Using the above relationships to solve for T_v allows for an estimation for the coefficient of consolidation:

$$T_v = \frac{c_v t}{\left(H_{dr}\right)^2} \qquad (3.12)$$

where H_{dr} is the drainage distance. Combining c_v and m_v allows for an approximation of the hydraulic conductivity (k) (Lamb and Whitman 1969) through equation 3.13:

$$k = c_v m_v \gamma_w \qquad (3.13)$$

where γ_w indicates the unit weight of water.

3.5 Axisymmetric Compression

Perhaps the most rigorous and fundamental apparatus used to determine shear strength parameters and stress-strain behavior of soils is the triaxial apparatus (Buhdu 2011). In triaxial testing, cylindrical specimens are subjected to two stress components: radial (σ_r) and axial (σ_a). Specimens can fail in extension or compression by increasing or decreasing radial or axial stresses, respectively (Muir Wood 1990). Axisymmetric refers to the symmetric application of forces about the axis of cylindrical specimens both radially and axially (Budhu 2011). Figure 3.8 displays a generic triaxial apparatus,

similar to the one employed in this study, specifically highlighting the total stress components: σ_r and σ_a.

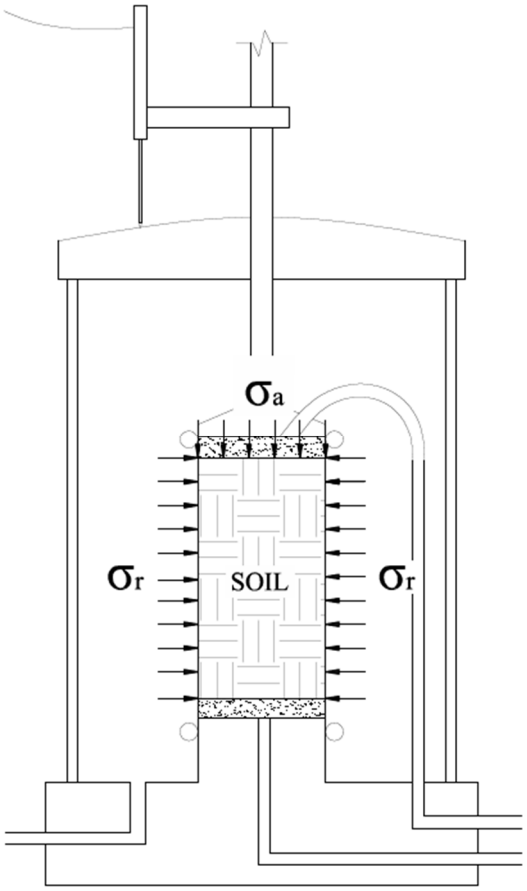

Figure 3.8 Generic triaxial apparatus highlighting the total stress components σ_r and σ_a used to back pressure saturate, isotropically compress, and axisymmetrically compress under undrained conditions (modified after Muir-Wood 1990)

Results of axisymmetric compression testing are typically projected onto two planes: the effective stress plane and the compression plane (Muir-Wood 1990), as presented in Figure 3.1. The compression plane is typically semi-logrithmic, employing axes of specific volume (v), and the natural log of mean effective stress ($\ln(p')$). The effective

stress plane is typically linear employing axes of p' and the deviatoric stress (q). The soil state parameters v, p' and q provide a unique insight into specimens behavior at any point during the axisymmetric compression process. The stress state within a soil specimen, normalized in the three principle stress application directions, for effective and total stress components, is presented in terms of q and p', respectively. The density of the specimen is expressed by v (Salgado 2008). Stress and density are two typical and examples of soil state variables significantly impacting mechanical behavior (Salgado 2008). The soil state parameters v, p' and q are defined in equations 3.14 through 3.16, respectively.

$$v = 1 + e \tag{3.14}$$

$$p' = \frac{\sigma'_1 + \sigma'_2 + \sigma'_3}{3} = \frac{\sigma'_1 + 2\sigma'_3}{3} = \frac{\sigma'_a + 2\sigma'_r}{3} \tag{3.15}$$

$$q = \sigma_1 - \sigma_3 = \sigma_a - \sigma_r \tag{3.16}$$

where e represents the void ratio, σ'_1, σ'_2, and σ'_3, represent the effective stress in three principal directions: axially and laterally, respectively. In triaxial compression stress applications are controlled axially and radially, therefore the lateral components of stress are in equilibrium.

Axisymmetric conditions govern soil response in the traditional triaxial apparatus. Friction angles (ϕ) can be determined from the effective major and minor principle stresses as presented on the Mohr's circle of stress:

$$\sin(\phi) = \frac{\frac{\sigma'_1}{\sigma'_3} - 1}{\frac{\sigma'_1}{\sigma'_3} + 1} \tag{3.17}$$

where σ'_1 is the major principal stress and σ'_3 is the minor principal stress. Equation 3.17 was used to estimate both peak (ϕ_p) and critical state (ϕ_{cs}) friction angles presented in this manuscript.

3.3.1 Isotropic Consolidation

During each isotropic consolidation step (increase in p') total dissipated pore water is measured. The percentage of dissipated pore water is typically plotted versus time using the equation 3.18:

$$U_z = \left(1 - \frac{\Delta u}{u_0}\right) \cdot 100 \tag{3.18}$$

where Δu is the pore water change at any time after the initiation of isotropic consolidation and u_0 is the pore water pressure change at t = 0. Similar to one-dimensional testing, the time required to dissipate a certain percentage of Δu (U_z) can be

employed to determine c_v and m_v using equations 3.19 through 3.23 (Rowe 1959), respectively:

$$c_{vi} = \frac{T_v \left(H_{dr}\right)^2}{t} \tag{3.19}$$

$$m_{vi} = \frac{\Delta e \cdot 1000}{\Delta p' \cdot (1 + e_{BPS})} \tag{3.20}$$

where eBPS is the void ratio after back pressure saturation and before consolidation, Δe and Δp' are the changes in void ratio and mean effective stress, respectively, during the step of consolidation being considered. Equations 21 through 23 are used to estimate c_v and m_v:

$$c_v = c_{vi} f_{cv} \tag{3.21}$$

$$f_{cv} = \frac{1}{1 - B(1 - A)(1 - K_0)} \tag{3.22}$$

$$m_v = \frac{2}{3} m_{vi} \tag{3.23}$$

where c_v and m_v are the K_0 coefficient of consolidation and the K_0 coefficient of volume change, respectively, and A and B are Skempton's pore water pressure parameters

(Skepmpton 1954) at critical state and after back pressure saturation, respectively. Assuming a normally consolidated soil (remolded specimens) and a friction angle of approximately 30° (Dunham-Friel 2009), equation 3.24 can be used to estimate K_0 as 0.5 (Budhu 2011):

$$K_0 = 1 - \sin(\phi) \tag{3.24}$$

Finally, the hydraulic conductivity can be estimated using c_v and m_v as indicated in equation 3.25:

$$k_v = c_v m_v \tag{3.25}$$

3.3.2 Undrained Compression

All triaxial testing presented in this manuscript was performed under isotropically compressed undrained loading conditions. Samples were isotropically consolidated to a specific level of p' prior to axisymmetric compression. The primary differences between drained and undrained loading are that during undrained loading: (1) pore water pressure changes are not allowed to dissipate and, therefore can be both positive or negative; (2) volume change is restricted; (3) total applied stresses and excess pore water pressures are measured; and (4) the restriction of volume change eliminates the possibility of shearing-induced consolidation, dilation, or other specimen deformation mechanisms (Budhu 2011). Traditionally, undrained compression is performed on fine grained soils with low permeability values, and is popular because of test completion speed (Budhu 2011).

However, undrained loading may also apply to coarse grained soils subjected to fast loading rates, such as seismic and cyclic loads (Salgado 2008). For most fine-grained material scenarios, pore water pressures equilibrate more rapidly in undrained loading in comparison to volume change and pore drainage required in drained loading. Idealized isotropically compressed undrained triaxial data is presented in Figure 3.9.

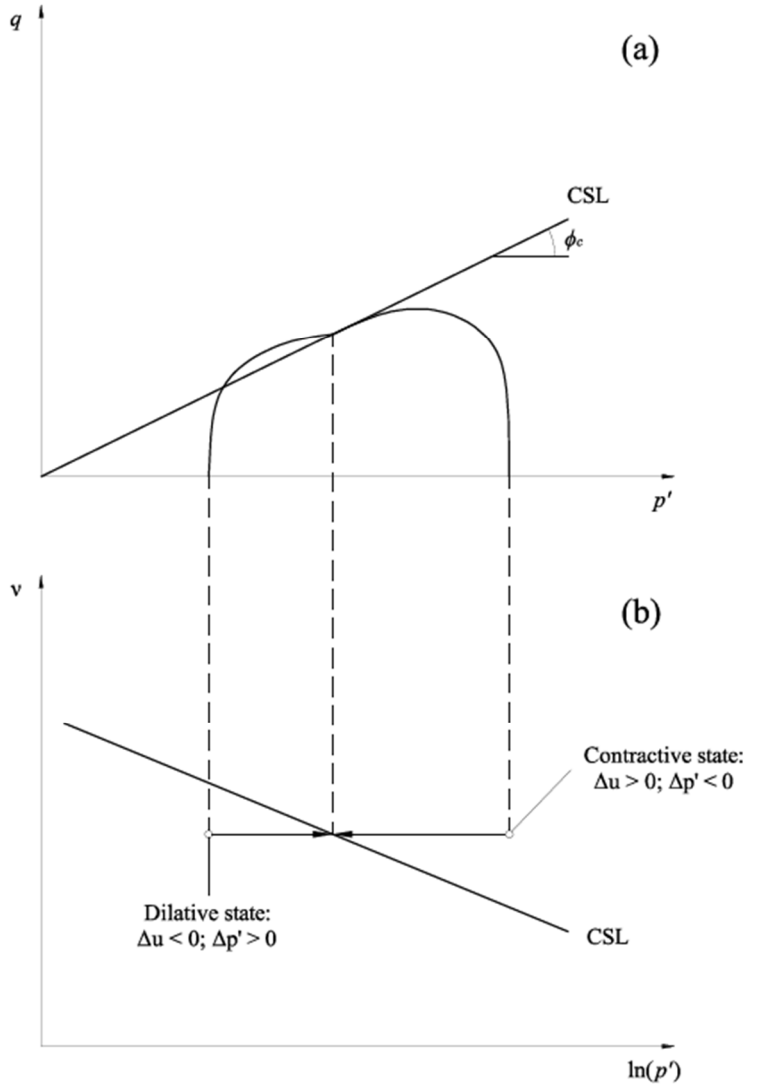

Figure 3.9 Idealized stress paths in (a) $p' - q$ and (b) $\ln(p') - v$ corresponding to the undrained strength of fully contractive and fully dilative materials in consolidated undrained triaxial tests (modified after Salgado 2008)

Stress paths and soil behavior during compression are important topics presented in Figure 3.7. A material consolidated isotropically to a state looser than critical state will initially exhibit contractive behavior while a material consolidated isotropically to a state more dense than critical state will exhibit dilative behavior upon an increase in applied total stress (Salgado 2008). Typically specimens exhibit both contractive and dilative behavior during compression when carried to critical state. Stress paths will be discussed in detail in Chapter 5 during the presentation of results. Three previous studies investigating fine grained material-rubber mixtures in a critical state framework are present in literature (Ozkul and Baykal 2007; Dunham-Friel and Carraro 2011; and Weichert et al. 2011) For additional information relating to these studies, the reader is directed to Chapter 2.

Undrained triaxial data is typically plotted on axes of q and $\varepsilon_{a,}$ Δu and ε_a, q and p', and v and p'. Critical state and general soil behavior can be adequately defined when presented on the previously mentioned axes.

3.3.3 Critical State Soil Parameters

The CSM, as presented in Section 3.1 and Figure 3.1, is typically projected onto two dimensional planes referred to as the compression plane and effective stress plane employing axes of $\ln(p') - v$ and $p' - q$, respectively. Figure 3.6 displays the important aspects of the CSM for conventional triaxial testing.

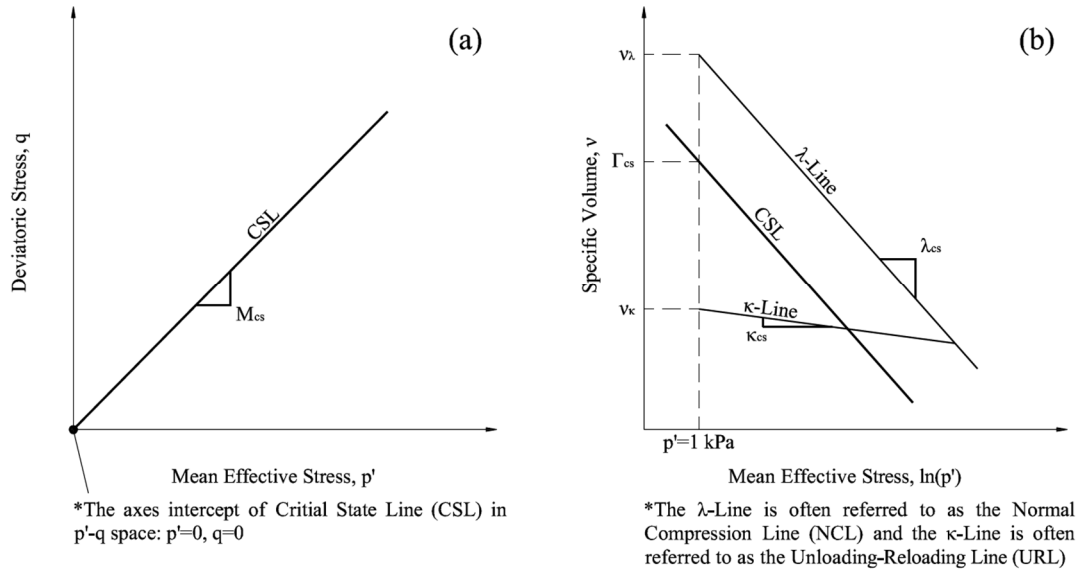

Figure 3.10 Critical state line projections in (a) $p' - q$ space and (b) $\ln(p') - v$ space (modified after Schofield and Wroth 1968)

As presented in Figure 3.10, the normal compression line (NCL), or λ-line, represents the path followed by specimens that have exceeded their past maximum mean effective stress and are no longer over consolidated (OCR = 1). The unloading reloading line (URL), or κ–line, represents the path followed by specimens that have yet to reach their past maximum mean effective stress and are over consolidated (OCR>1). The NCL and URL are followed semi-logarithmically in the compression plane during isotropic compression, similar to specimens tested in one-dimensional compression. Log-linear slopes of the NCL and URL are given by λ_{cs} and κ_{cs}, respectively. Equations 3.26 and 3.27 define λ_{cs} and κ_{cs} respectively:

$$\lambda_{cs} = \frac{v_2 - v_1}{\log\left(\frac{p'_2}{p'_1}\right)} \tag{3.26}$$

$$\kappa_{cs} = \frac{v_4 - v_3}{\log\left(\frac{p'_3}{p'_4}\right)} \tag{3.27}$$

where the subscripts 1 and 2 represent two successive points on the NCL and the subscripts 3 and 4 represent two successive points on the URL (Muir-Wood 1990).

Further developing equations 3.26 and 3.27 in the semi-logarithmic compression ln(p') – v plane, as presented in Figure 3.10 (b), yield representations of both the NCL and URL as presented in equations 3.28 and 3.29, respectively:

$$v = v_\lambda - \lambda_{cs} \cdot \ln(p') \tag{3.28}$$

$$v = v_\kappa - \kappa_{cs} \cdot \ln(p') \tag{3.29}$$

where v_λ represents the specific volume of a normally consolidated specimen at p' = 1 kPa and v_κ represents the specific volume of an over consolidated specimen at p' = 1 kPa.

As discussed in Sections 3.1 and 3.2, critical state defines a condition of plastic yielding or a condition of constant shear stress, constant confining stress, and constant Δu during continued axisymmetric compression of a soil specimen. The intrinsic critical state parameters λ_{cs}, Γ_{cs}, κ_{cs} and M_{cs} are defined by Equations 3.30 and 3.31:

$$v = \lambda_{cs} \cdot \ln(p') + \Gamma_{cs} \tag{3.30}$$

$$q = M_{cs} \cdot p' \tag{3.31}$$

where Γ_{cs} represents the specific volume of a specimen reaching critical state at p' = 1 kPa and M_{cs} represents the linear slope of the CSL in the effective stress plane (Muir-Wood 1990).

In defining the NCL and CSL the slope of both semi-logarithmic relationships, λ_{cs}, is idealized as equal. Experimental evidence (Bishop and Henkel 1957; Roscoe, Schofield, and Wroth 1958; and Parry 1958) suggests that the semi-logarithmic slope of both the NCL and CSL can be assumed as reasonably straight and parallel in the semi-logarithmic compression plane over a reasonable range of p'.

The critical state friction angle can be estimated a using a variety of criterion and parameters (Salgado 2008). The critical state friction angle (ϕ_{cs}) for a given soil specimen is simply the friction angle at a critical state condition. In order to provide a more rigorous estimate of ϕ_{cs} the critical state parameter M_{cs} was utilized to estimate ϕ_{cs} from multiple specimens isotropically compressed to varying levels of p':

$$\sin(\phi_{cs}) = \frac{3M_{cs}}{6 + M_{cs}} \tag{3.32}$$

It is convenient, especially when testing relatively elastic soil specimens, to have a method of relating plastic and elastic compressibility values. Therefore, the plastic volumetric strain ratio, Λ, (Schofield and Wroth 1968) is introduced in equation 3.32:

$$\Lambda = \frac{\lambda_{cs} - \kappa_{cs}}{\lambda_{cs}} = \frac{C_c - C_r}{C_c} \tag{3.33}$$

The plastic volume strain ratio depends in large part upon the over consolidation ratio of the specimen tested. The over consolidation ration, R_0, defined in terms of the mean effective stress (often referred to as the preconsolidation ratio) is defined as (Budhu 2011):

$$R_o = \frac{p'_c}{p'_0} \tag{3.34}$$

where p'_c is the preconsolidation stress and p'_0 is the initial mean effective stress.

Combining equations 3.32 and 3.33 yields an expression for the critical state mean effective stress, p'_{cs} (Budhu 2011):

$$\frac{p'_{cs}}{p'_0} = \left(\frac{R_0}{2}\right)^{\Lambda} \tag{3.35}$$

Using isotropic or one-dimensional compression data, along with the knowledge of stress history and more specifically the preconsolidation ratio of a soil element allows for the determination of p'_{cs} which can also lead to estimations of the CSL and ϕ_{cs}.

3.3.4 Stiffness

Of specific importance to the research and implementation of ESR mixtures is the topic of stiffness. Stiffness is an indication of how a soil matrix will behave when subjected to specific loading conditions (Muir Wood 2009). Stiffer soils deform less when subjected to loads in comparison to less stiff soils. ESR mixtures have unique stiffness parameters, specifically at low strains, due to the relatively high deformability values of individualized STR particles. Due to the inclusion of STR, stiffness of ESR mixtures reported in literature has been reduced by 15 to 55% with the addition of 20% STR (Dunham-Friel 2011).

Common expressions used to quantify stiffness are the Young's or elastic modulus (E), Poisson's ratio (v_p), and shear modulus (G) (Budhu 2011). In simple mechanics v_p is defined as the ratio of the change in lateral strain to the change in vertical strain when applying a vertical stress. Due to difficulties in measuring lateral strains during conventional triaxial testing, v_p is usually estimated by E and G:

$$G = \frac{E}{2(1+v_p)} \tag{3.36}$$

One-dimensional or isotropic compression testing can provide an estimate for E and bender element testing, not conducted in this research, allows for the calculation of G (Dunham-Friel 2009). It is important to distinguish specific volume from Poisson's ratio which are often identical symbolically in literature. The determination method of the shear modulus varies depending on the strain range of interest, Figure 3.11. Stiffness discussed in this manuscript focuses on large strains where conventional soil testing is sufficient.

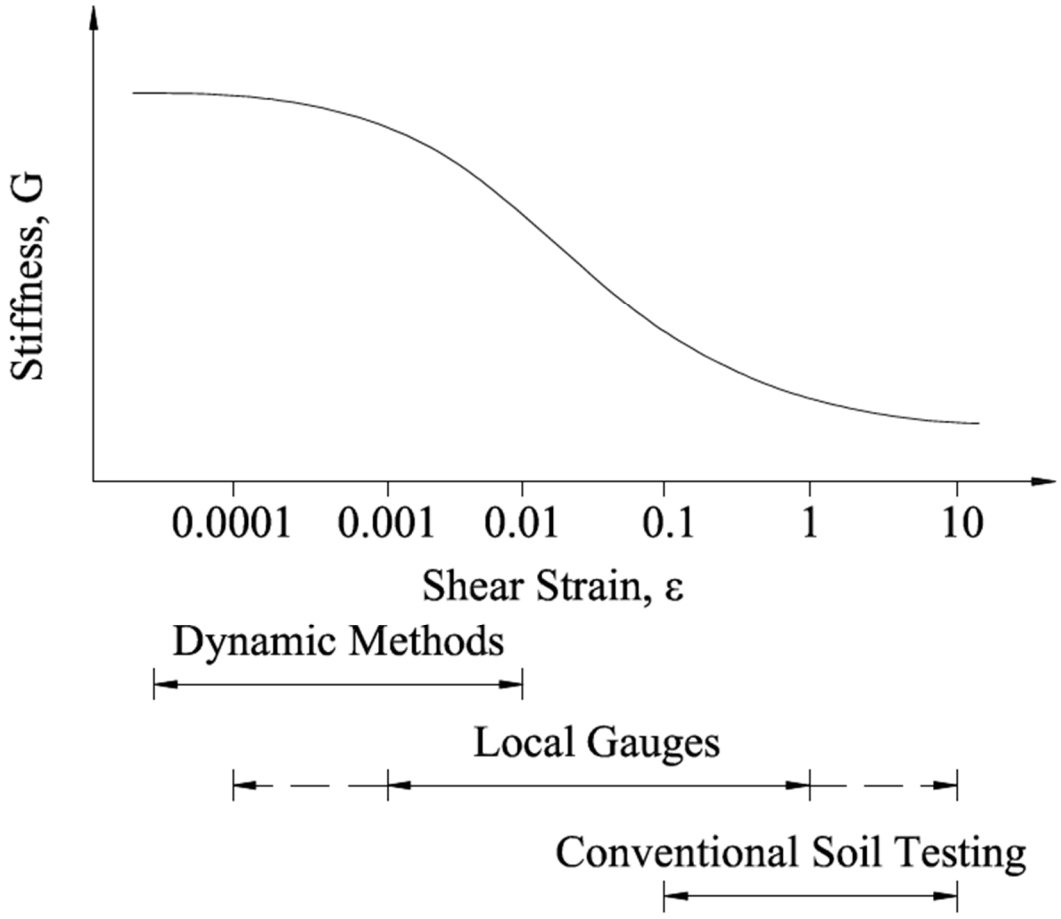

Figure 3.11 Shear modulus degradation with increasing shear strain and measureable ranges of the shear modulus for various methods (modified after Atkinson 2000)

CHAPTER 4: EXPERIMENTAL PROGRAM

4.1 Materials

Materials utilized in this research include a local expansive soil and two locally manufactured STR products. The expansive soil was removed from a location approximately 5.6 km (3.5 miles) northwest of the main campus of Colorado State University (CSU), near the Engineering Research Center (ERC) and referred to as the Expansive Soils Test Site (ESTS). The approximate location of the undisturbed expansive soil site prior to excavation is shown in Figures 4.1 and 4.2. Figure 4.2 depicts a more accurate representation of the test site where field plots were constructed and monitored for swell and the location from where Pierre shale expansive soil was removed. Recent field research on expansive soils by CSU is also included in Figure 4.2. The soil was mined from the Pierre shale deposit, known to be expansive in nature (Durkee 2000; Abshire 2002; Nelson et al. 2006) at depths of 0.5 to 2 m below the ground surface. Materials used in this study are shown in Figure 4.3.

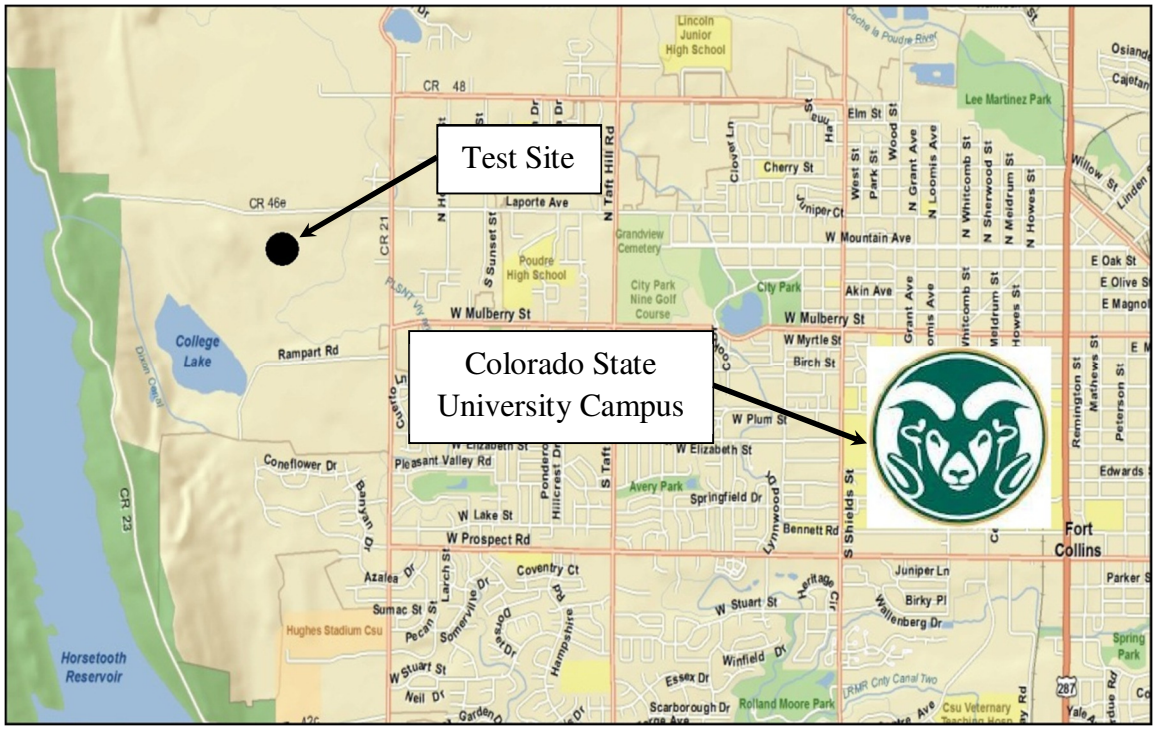

Figure 4.1 Location of test pit used to collect host Pierre shale expansive soil used in this study in relation to the Colorado State University main campus. Locations are approximate and the figure is not to scale.

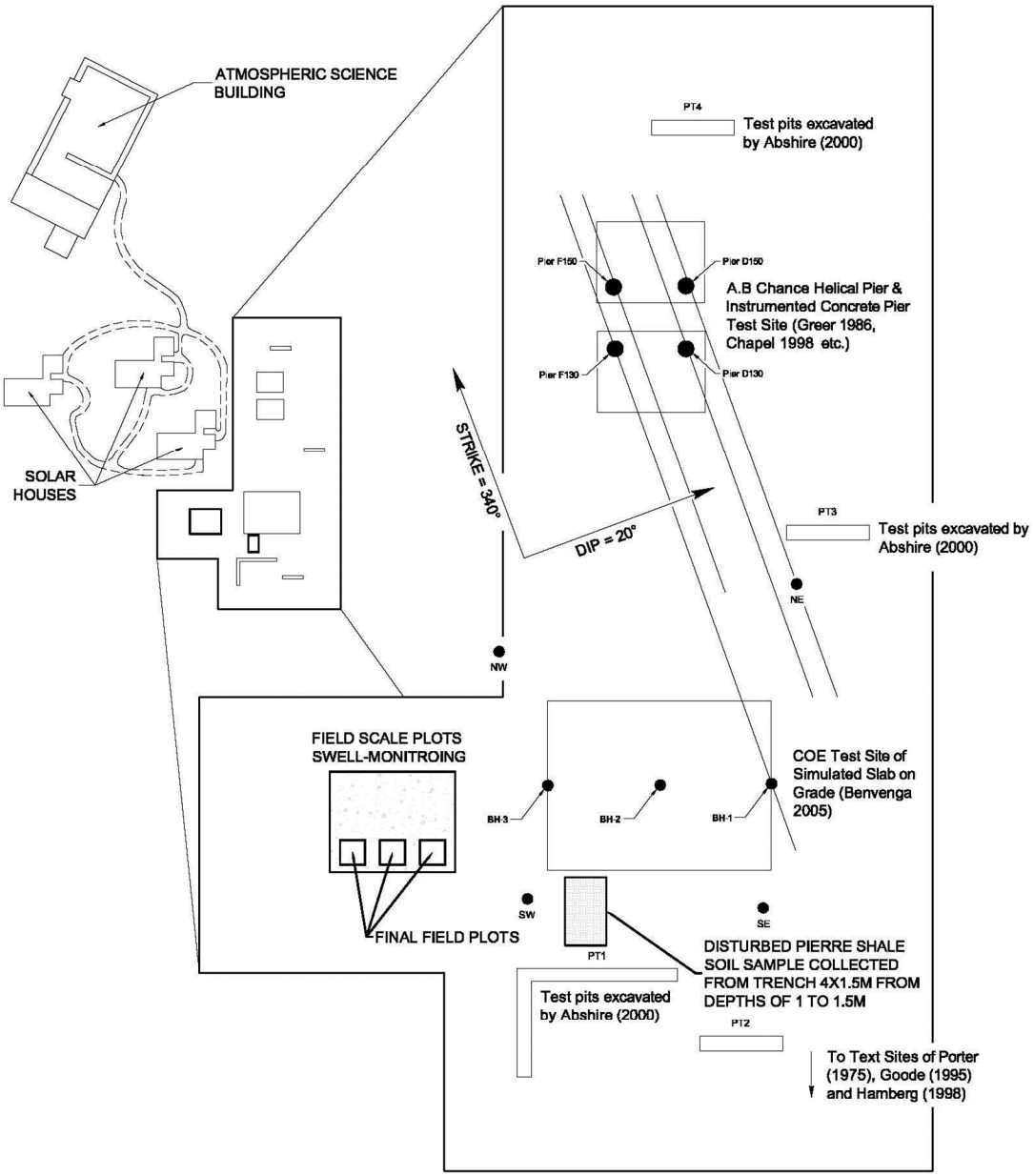

Figure 4.2 Expansive soil test site (ESTS) showing recent work on expansive soils by Colorado State University (after Abshire 2002). Locations are approximate and the figure is not drawn to scale.

Scrap tire rubber utilized in this study was supplied and processed or manufactured by two separate companies located in the northern and central parts of Colorado. 19.0-mm tire chips were provided by Front Range Tire Recycle, Inc., located in Salida, Colorado. 6.7-mm granulated rubber was provided by Caliber, Inc., located in Commerce City, Colorado. Processing of granulated rubber is much more elaborate in comparison to tire chips, including the removal of impurities such as steel reinforcement and other fiber-like reinforcements. Both materials are representative of each STR type, as per ASTM D6270, and are shown in Figure 4.3

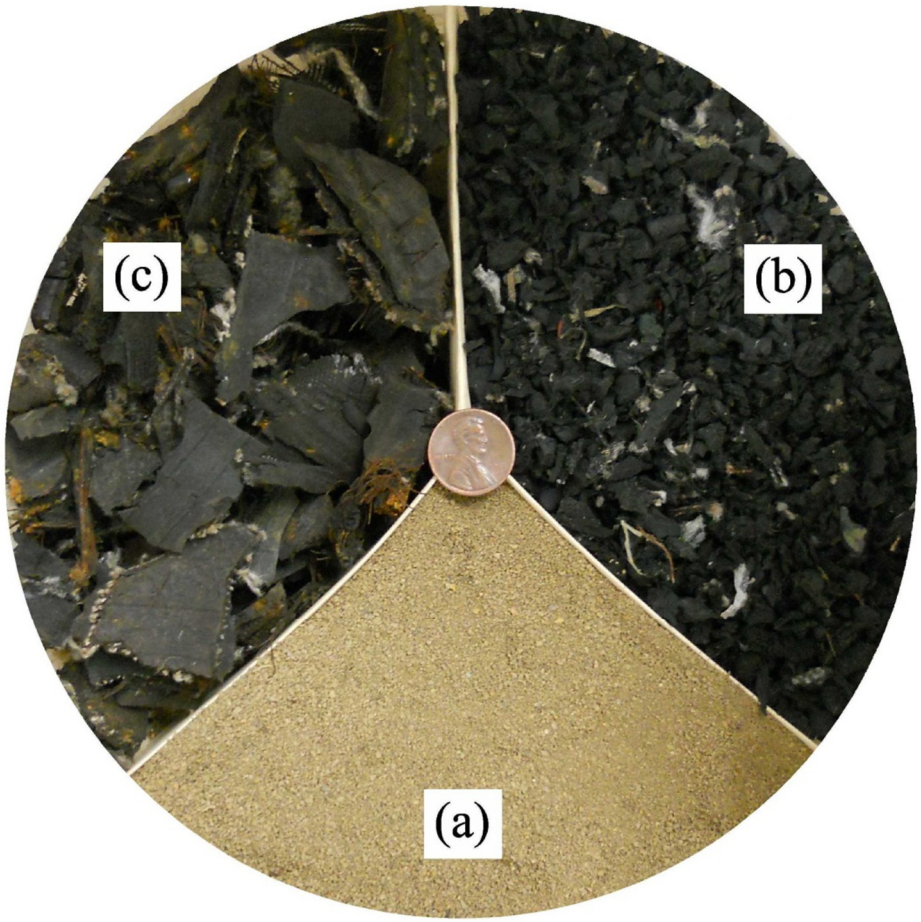

Figure 4.3 The three primary geo-materials used throughout this study including (a) Pierre shale expansive soil (b) 6.7-mm granulated rubber and (c) 19-mm tire chips

The materials employed in this study were specifically selected to represent an expansive soil unique to northern Colorado and typical STR available locally along the Front Range. This study addressed the local need for expansive soil swell mitigation in applications tolerable to stiffness reduction and the environmentally friendly use of STR in civil engineering applications.

4.1.1 Scrap Tire Rubber

As discussed previously, the STR materials employed were provided by two STR manufacturers from Northern Colorado. Basic characteristics of STR in terms of d_R and specific gravity (G_s) are presented in Table 4.1.

Table 4.1 Specific gravity and typical nominal rubber particle size range of scrap tire rubber

STR Type	Specific Gravity, G_s		Nominal Particle Size Range, d_R (mm)	
	Current Research	Reference	Current Research	Reference
Granulated Rubber	1.13	1.10[(1)]	2.0-19.0	0.5-12.0[(3)]
Tire Chips	1.42	1.18[(2)]	15.9-31.8	12.0-50.0[(3)]

(1) Manion and Humphery (1992)
(2) Bressette (1984)
(3) ASTM D6270

As shown in Table 4.1 the STR utilized in this study is representative of STR employed in various other studies. Deviations in G_s for granulated rubber and tire chips used in studies (1) and (2) from the ones used in this study are 0.03 and 0.24, respectively. Specific gravity values may provide a good indication of how much steel reinforcement was actually removed during the manufacturing process. Ranges of d_R for both

granulated rubber and tire chips are within typical values for each material (ASTM D6270).

4.1.2 Expansive soil

As presented in Chapter 2, the northern Colorado Front Range area contains significant quantities of expansive soil. Although swell potential varies significantly in different regions of the Front Range, the expansive soil selected for this research closely resembles typical expansive material from the area. CSU has been studying expansive soils since approximately 1977 (Porter 1977; Goode 1982; Hamberg 1985; Reichler 1997; Seda 2007; and Dunham-Friel 2009). The expansive soil employed in this study is consistent with expansive soils used in other previous studies conducted at CSU. A comparison of basic soil characteristics for the various studies is presented in Table 4.2.

As shown in Table 4.2, the expansive soil utilized throughout this study closely resembles local expansive soils from the Front Range used by previous researchers at CSU. The grain sizes and index properties compare closely and indicate similar classifications among soils listed in Table 4.2. In addition, compaction parameters are also similar to previous research. The close resemblance of expansive soils will further strengthen comparisons made to one-dimensional compression and axisymmetric compression results discussed in the following sections, particularly comparisons to previous research presented by Seda et al. (2007) and Dunham-Friel (2009).

Table 4.2 Comparison of basic grain size, index and compaction parameters for local expansive soils collected from the Front Range geographic area and used for research at Colorado State University since 1977

Reference	Grain Sizes			Index Properties				Soil Classification	Compaction Parameters[2]	
	Sand (%)	Silt (%)	Clay (%)	w_L (%)	w_P (%)	I_P (%)	G_S		γ_{dmax} (kN/m^3)	w_{opt} (%)
Current Research	1	42	57	55	23	32	2.65	CH	16.4	19.8
Dumham-Friel (2009)	2	48	50	56	22	34	2.72	CH	16.5	21.5
Seda (2007)	5	53	42	52	18	34	2.81	CH	16.5	21.5
Reichler (1997)[1]	—			55-64	18-23	32-46	—	CH	—	—
Hamberg (1985)	48		52	—	—	23	—	CL	—	—
Goode (1982)	—	90-100		52	25	14	2.74	CH	—	—
Porter (1977)[1]	—	97-100		37-68	19-35	15-46	2.67-2.76	CL-CH	17.5	16.8

[1] Several samples were collected from the same general location and employed in testing

[2] Based on standard Proctor compaction tesitng (ASTM D698)

4.1.3 Particle Size Distributions

Displayed in Figure 4.4 are the particle size distributions for Pierre shale residual soil, 6.7-mm granulated rubber, and 19.0-mm tire chips. Gradation and hydrometer tests were performed in accordance with ASTM D422. Pierre shale residual soil contains 98.8% fine sized particles, 42.1% of which are silt, and 56.7% of which are clay. 6.7-mm granulated rubber can be classified as poorly graded sand and 19.0-mm tire chips can be classified as poorly graded gravel, according to ASTM D2487. Gradation testing on isolated rubber indicated very narrow ranges of particle sizes, demonstrating adequate processing techniques. Although a large percentage of smaller particles for the 19.0-mm tire chips were not present, impurities such as steel reinforcement accounted for the majority of smaller particle sizes.

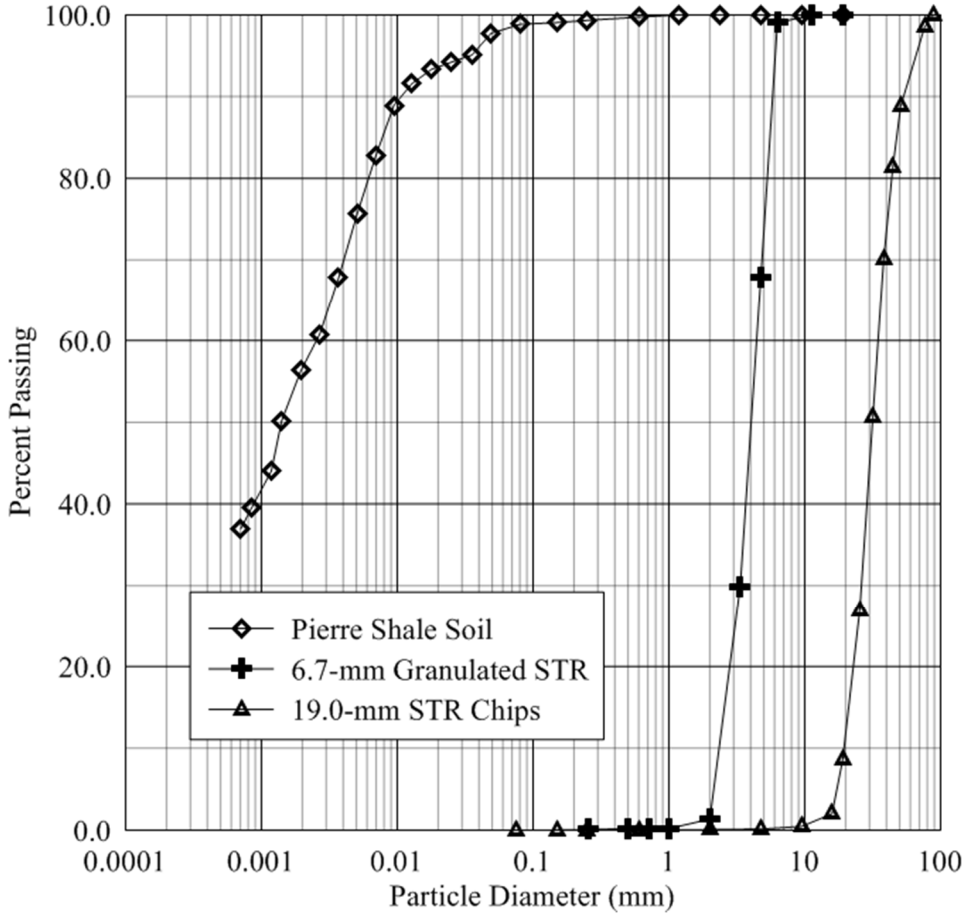

Figure 4.4 Particle size distributions for the three primary geo-materials utilized throughout this research determined in accordance with ASTM D422

4.1.4 Index Properties

Atterberg limits determined in accordance with ASTM D4318 indicated that the Pierre shale residual soil is highly plastic with a liquid limit (w_L) of 55 percent, a plastic limit (w_P) of 23 percent, and a plasticity index (I_P) of 32 percent. Pierre shale soil is classified as highly plastic fat clay according to the Unified Soil Classification System (ASTM D2487). Atterberg limits were not determined for ESR mixtures, but as previous research (Seda et al. 2007) indicates increasing *RC* of an ESR mixture correlates with slight increases in plasticity. Increases in plasticity were not sufficient to alter the material classification, over the ranges of *RC* studied (Seda et al. 2007). The activity (*A*)

(or the ratio of the plasticity index to the fines content) of Pierre shale expansive soil is 0.32.

Specific gravity, G_s, tests were conducted in accordance with ASTM D854 and performed on Pierre shale residual soil, ESR mixtures, and STR. Specific gravity results are summarized in Table 4.3.

Table 4.3 Specific gravity results for Pierre shale residual soil and ESR mixtures used in this study

Material	Nominal Rubber Particle Size (mm)	Rubber Content (%)	Specific Gravity, G_s
Pierre Shale Soil	–	0	2.65
10% 6.7-mm ESR	6.7	10	2.26
20% 6.7-mm ESR	6.7	20	2.10
20% 19.0-mm ESR	19.0	20	2.19
6.7-mm STR	6.7	100	1.13
19.0-mm STR	19.0	100	1.42

As shown the rubber content has an inverse relationship with specific gravity. Also, as the nominal rubber particle diameter increases, so does the specific gravity as shown in the bottom two rows of Table 4.3. The increase in G_s with d_R is likely due to a significant discrepancy in the amount of steel reinforcing fragments remaining in the 19.0-mm STR after refinement in comparison to the 6.7-mm STR which was relatively free of impurities.

4.1.5 Mineralogical Composition

The mineralogical composition of Pierre shale residual expansive soil employed throughout this study was determined using x-ray diffraction (XRD) analysis. One sample was ground into a fine powder and shipped to H&M Analytical Services for review. According to H&M Analytical Services the powder was inserted into a Panalytical X'Pert Pro diffractometer. Copper radiation was employed at 45KV/40mA, and the sample was scanned over a range of 3 to 90 degrees with a step size of 0.01576 degrees. Once scanned, peak intensities were compared with results published by the International Centre for Diffraction Data to identify mineralogical phases. A total of nine phases were identified in varying quantities, as shown in Table 4.4. All phases include a high level of confidence with the exception of Jadeite. A high level of confidence represents a good correlation between peak values of the collected diffraction pattern and the Powder Diffraction File published by the International Centre for Diffraction Data with over 700,000 entries. Identification figures used in the determination of mineralogical phases can be viewed in Appendix C.

Table 4.4 XRD mineralogical composition of Pierre shale residual expansive soil used in this study

Mineral	Quantitative Phase Analysis (wt %)	Structural Fomula
Quartz	45.8	SiO_2
Muscovite	43.4	$K_2(Al_2O_3)_3(SiO_2)_6(OH)_2$
Chlorite	4.0	$Al_6Si_4O_{10}(OH)_8$
Albite	3.3	$NaAlSi_3O_8$
Gyrolite	1.6	$Ca_4(Si_6O_{15})(OH)_2 \cdot 3H_2O$
Calcite	1.1	$CaCO_3$
Jadeite	0.5	$NaAlSi_2O_6$
Bassanite	0.2	$2CaSO_4 \cdot H_2O$
Rutile	0.1	TiO_2

Of the minerals discovered, quartz and muscovite (a member of the mica family) are often common in high quantities in expansive soils, specifically the Pierre shale geological formation (Nicolas and Bamburak 2009). Muscovite species are a subgroup of mica, have a layer charge of approximately one, and are non-swelling (Essington 2004). Layer charges indicate the relative affinity a specific mineral has for oppositely charged cations and anions. Chlorite is also generally stable and non-expansive (Essington 2004). Albite is a plagioclase feldspar with free substitution of Ca^{2+} for Na^{+} and Al^{3+} for Si^{4+} creating a discontinuous solid solution (Essignton 2004). The lack of expansive minerals in the XRD study is likely due to an unrepresentative and relatively small (0.3 g) selected sample used in the XRD testing methods. One previous researcher studied the mineralogical composition of the Pierre Shale soil deposit near the ERC expansive soils test site and determined that approximately 70 % of the clay fraction is highly expansive smectite mineral (Miller 1996). Several previous researchers indicated high CEC for Na^{+} and Ca^{2+} cations (Miller 1996; Porter 1977; and Hamberg 1985) used

in their studies, pointing toward the potential indication of large smectite quantities. All three researchers utilized expansive soil collected from an area near the expansive soils test site. A more elaborate explanation discussing the influence of testing methods and specimen size on XRD analyses is located in Appendix C.

4.1.6 Scanning Electron Microscopy (SEM)

Scanning Electron Microscopy (SEM) was performed on both Pierre shale expansive soil and 6.7-mm STR. Analyses were performed prior to this research as part of a larger study (Seda et al. 2007), but have yet to be included in a publication. Two different magnifications were used for each material; 3300 and 7500. SEM images for both materials can be seen in Figure 4.5. As shown in Figure 4.4 (a) Pierre shale expansive soil consists of flat plate-like clay particles, while in Figure 4.4 (b) 6.7-mm granulated STR consists primarily of smoother particle surfaces and edges. Isolated particles for 6.7-mm STR are much larger in comparison to Pierre shale soil. The isolated areas of rough edges seen in (b2) are attributed to the refining process where impurities are removed and STR is shredded to a desired size. The microstructure and interface between rubber and soil particles will be discussed later in this manuscript.

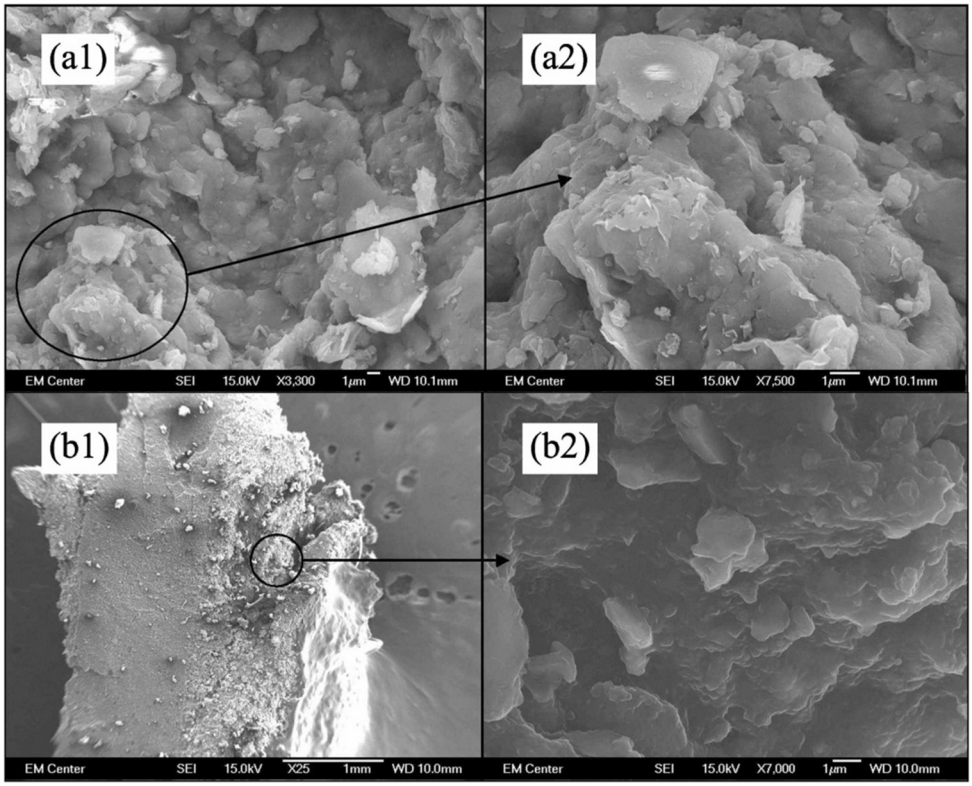

Figure 4.5 Scanning electron microscopy images for (a) Pierre shale expansive soil (b) 6.7-mm granulated STR at (1) 3300 and (2) 7500 times magnification

4.1.7 Compaction Parameters

Analyses presented in this thesis are in large part influenced by compaction parameters. Relative compaction values are based on standard Proctor compaction testing in accordance with ASTM D698. According to ASTM D6270, the dry density of TDA and TDA-soil mixtures with less than 30% retained on the 19.0-mm sieve can be determined in accordance with ASTM D698 and ASTM D1557. Compaction testing focused on samples comprised of Pierre shale residual expansive soil with the addition of 0, 10, or 20% rubber by dry weight. Compaction parameters were studied for Pierre shale expansive soil, 10 and 20% 6.7-mm ESR mixtures, and 20% 19.0-mm ESR mixture. C_R values displayed in the following chapters and sections compare dry densities of identical

expansive soil and STR contents and ESR mixtures types. Compaction results are presented in Figure 4.6, with corresponding maximum dry densities and optimum water contents systematically determined from a third order polynomial trend line of the following form (Howell et al., 1997):

$$\gamma_{dmax} = A \cdot w_{opt}^{\ 3} + B \cdot w_{opt}^{\ 2} + C \cdot w_{opt} + D \qquad (4.1)$$

where γ_{dmax} (kg/m^3) is the maximum dry unit weight; w_{opt} (%) is the optimum water content; and A, B, C, and D are constants related to the fitting process. Third-order polynomial fitting results are shown in Table 4.5. Zero air voids trends are drawn for each material type, associated with proctor curves by line type, and shown in Figure 4.6.

Table 4.5 Standard Proctor compaction results for Pierre shale residual soil and expansive soil-rubber mixtures used in this study

Sample Type	γ_{dmax} (kN/m^3)	w_{opt} (%)
Pierre Shale Soil	16.4	19.8%
10% 6.7-mm ESR	15.0	19.5%
20% 6.7-mm ESR	14.0	18.6%
20% 19.0-mm ESR	14.8	18.5%

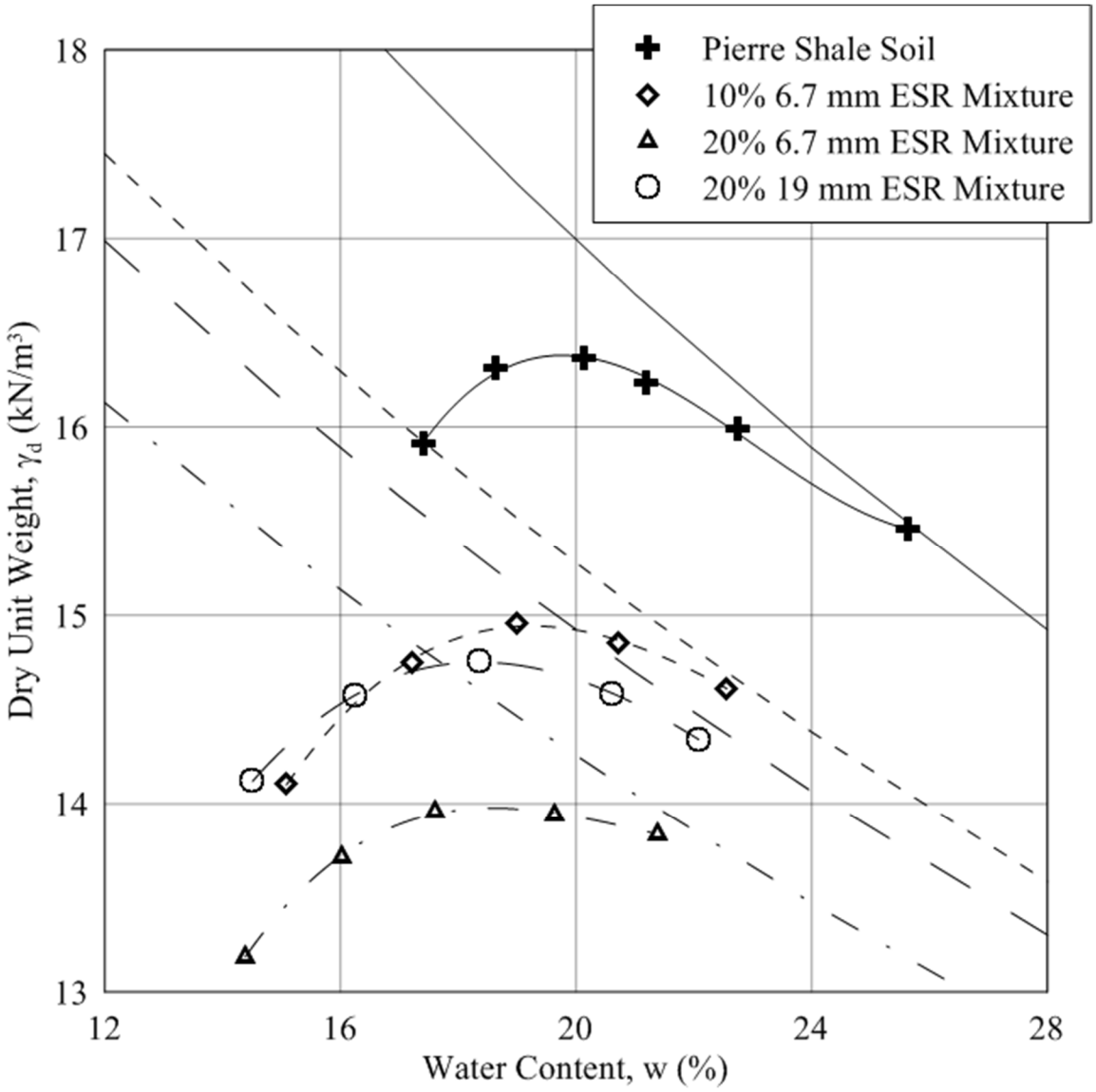

Figure 4.6 Standard Proctor compaction results for Pierre shale soil and ESR mixtures used in this study determined in accordance with ASTM D698

Dry unit weight values decrease by 1 and 1.4 kN/m^3 for each 10% *RC* increase of 6.7-mm granulated rubber studied with respect to Pierre shale soil. The 19.0-mm tire chips had a less significant effect on γ_{dmax} in comparison to 6.7-mm granulated rubber, decreasing γ_{dmax} by approximately 1.6kN/m^3. Due to differences in refinement and additional impurities such as steel reinforcement, a unit volume of 19.0-mm tire chips is better

formed and therefore heavier than a corresponding unit volume of 6.7-mm granulated rubber (Table 4.5). In addition, the more uniform and less concentrated 6.7-mm granulated rubber dissipated the Standard compaction hammer blow energy better than then 19.0-mm tire chips. The w at which γ_{dmax} was realized (for standard Proctor compaction energy) was affected significantly less in comparison to γ_{dmax} over the changes in nominal rubber particle diameter and RC studied. A general trend of decreasing optimum water content with increasing RC can be seen for both 6.7- and 19.0-mm ESR mixtures. The decreasing optimum water content is likely a result of the replacement of soil volume with STR and the significant differences in wetting and absorption characteristics of rubber particles and expansive soil particles.

4.2 Experimental Methods

4.2.1 Specimen Preparation

Specimens tested in both one-dimensional swell-compression and axisymmetric compression testing were compacted to target relative compaction, water content, and rubber content values based on standard compaction values (Section 4.1.7). Relative compaction is defined as follows:

$$C_R = \frac{\gamma_d}{\gamma_{d\max}} \tag{4.2}$$

where C_R denotes relative compaction (%); γ_d denotes the dry unit weight (kN/m^3) and; γ_{dmax} denotes the maximum dry unit weight (kN/m^3) relative to a specified compaction effort (in this case, the value obtained from Standard Proctor compaction energy).

Rubber content is defined as follows:

$$RC = \frac{W_r}{W_r + W_s} \tag{4.3}$$

where RC is the rubber content (%); W_r is the dry weight of rubber; and W_s is the dry weight of soil. Research presented in this manuscript defines RC using dry weights due to the differences in compressibility of soil particles and rubber particles. The benefit of defining RC using dry weights is the invariance in RC with differences in specimen volume due to applied stresses.

Initially, Pierre shale residual soil was processed over a 4.75-mm sieve (#4 standard sieve) to remove conglomerates of material formed during wetting and drying cycles in the field and for consistency with standard Proctor compaction testing (see method A ASTM D698). After processing, expansive soil was mixed with appropriate amounts of rubber and de-aired, de-ionized water in order to achieve a desired w and RC post compaction. Upon mixing, ESR specimen layers were allowed to cure in individual sealed containers in a humidity room for 24 hrs to ensure homogeneous water contents throughout each layer. After curing, ESR specimens were compacted to target lift thicknesses based on specimen geometry. Specimen compaction was performed by first selecting a target layer thicknesses based on the largest nominal particle size, constrained specimen dimensions, and target compaction parameters. Uniform distributions of rubber throughout each specimen were achieved by isolating and mixing each specimen layer separately, as explained in Section 5.1. Specific layer thicknesses for individual tests will be discussed in subsequent sections.

4.2.2 Specimen Geometry

Lift thicknesses employed when compacting specimens in multiple layers are constrained to a minimum thickness of the maximum particle size. Compaction testing according to ASTM D698 employs a minimum lift thickness of two times the maximum particle size. It has become common in fill operations to employ lift thicknesses of at least 1.5 times the maximum particle size (Schlegel and Stangl 1987 and Gue and Liew 2001). Lift thicknesses employed in this study ranged from 1.4 to 3.3 times the maximum particle diameter. Individual layers were investigated for C_R, w, and RC uniformity and to ensure overall specimen homogeneity, as discussed in Section 5.1. Initial state parameters C_R, w, and RC were also measured for each specimen to determine discrepancies between target and actual tested state parameters.

4.2.3 One-Dimensional Swell-Compression

Laboratory swell-compression testing was performed at two different scales in order to fully quantify the effect of specimen size and rubber particle size on one-dimensional swell-compression parameters. In addition to increasing overall specimen size, larger specimens allowed for the inclusion of larger individual rubber particles. All tests were monitored with displacement transducers to analyze displacements and ensure steady state conditions. Specimen specifications for all three geometries are included in Table 4.6.

Table 4.6 Specimen geometries and target initial state parameters used in small- and large-scale one-dimensional swell-compression testing and field-scale swell-monitoring

Test Type	Geometry			Test Criteria			
	Volume (m^3)	Height (mm)	Lift Thickness (mm)	Rubber Particle Size (mm)	C_R	RC	w *
Small-Scale (SSC)	6.03E-05	19	9.50	6.7	90, 95, 100	0, 10, 20	dry, optimum, wet
Large-Scale (LSC)	7.40E-02	152	51	6.7,19.0	95	20	dry, optimum, wet
Large-Scale (FSSM)	1.89E-01	102	102	6.7, 19.0	95	0, 20	optimum

*where dry = w_{opt} - 2%, optimum = w_{opt}, and wet = w_{opt} + 2%

4.2.3.1 Small-Scale One-Dimensional Swell-Compression

Small-scale laboratory swell-compression tests (SSC) were performed on specimens 6.03E-5 m^2 in initial total volume and 19 mm in height. Two lifts were used in specimen preparation, with a lift thickness of 9.5 mm. Lift material was scarified in between compacted layers to promote bonding. Post-compaction specimen geometry was measured before specimens were introduced to the consolidation apparatus with dry filter paper and dry porous stones surrounding each specimen. According to ASTM D4546, porous stones and filter papers should be applied dry in order to limit expansive behavior prior to inundation.

Loading increments were carried out according to ASTM D4546. Displacement was monitored throughout the test using a single LVDT (linear variable differential transformer) displacement transducer, and subsequent loads were not applied until secondary swell, compression, or recompression was observed (Budhu 2010). Displacement gauges were set to take incremental readings with increasing durations between readings as each incremental load progressed. A uniform seating vertical stress of 6.1 kPa was applied 24 hours prior to inundation. Specimens were inundated under

the seating vertical stress and allowed to swell completely before additional loading increments were applied. Applied vertical stresses were doubled during each subsequent incremental load until a maximum vertical stress of 1561.6 kPa was obtained. Specimens were unloaded in 3 decrements, back to the seating vertical stress, in order to fully quantify the recompression index. In general displacements for all loading increments and unloading decrements were measured for a duration of 24 hours, with the exception of the inundation stage. During inundation, specimens were allowed to swell until maximum displacement was reached, typically occurring in less than 48 hours. Measurements of C_R, w, and RC were determined by drying specimens after testing, separating the 6.7-mm granulated rubber by wet sieving, and drying the sieved rubber. A picture of the consolidation apparatus used for small-scale laboratory swell-compression tests is provided in Figure 4.7.

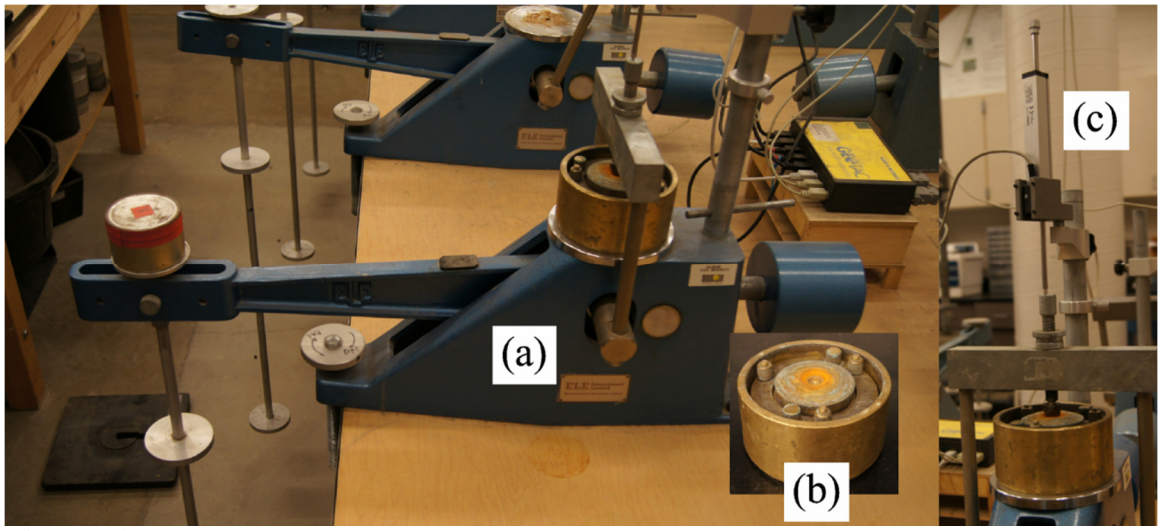

Figure 4.7 Small-scale laboratory swell-compression apparatus including: (a) entire consolidation apparatus; (b) fixed specimen ring including porous stones, top platen, well, and associated hardware; and (c) LVDT displacement transducer used to measure axial strains during testing

4.2.3.2 Large-Scale One-Dimensional Swell-Compression

Large-scale laboratory swell-compression (LSC) tests were performed on specimens 1.74E-2 m^3 in initial total volume and 152 mm in height. Specimens were compacted in three lifts with a lift thickness of 51 mm. Lift material was scarified to allow appropriate bonding between lifts and dry filter paper and dry porous material was applied to the top and bottom of each specimen to allow for an even application of de-aired, de-ionized water across both horizontal, top and bottom surfaces. Specimen geometry was measured upon the completion of compaction and before the application of vertical stresses. The apparatus used for large-scale laboratory swell-compression testing can be seen in Figure 4.8.

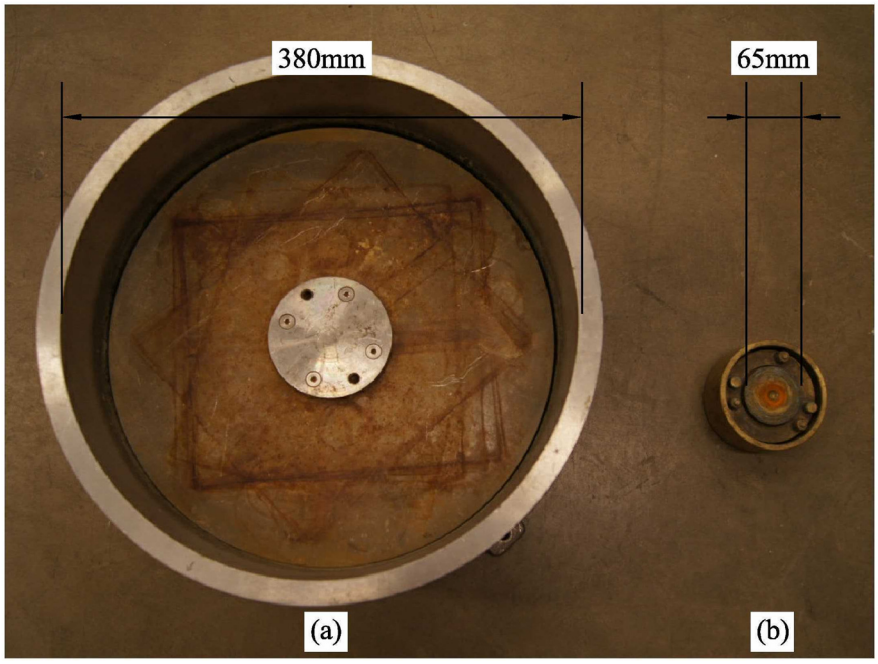

Figure 4.8 Size comparison of: (a) large-scale one-dimensional swell-compression apparatus; and (b) small-scale one-dimensional swell-compression apparatus

Similar to small-scale laboratory swell-compression testing, loading increments were carried out according to ASTM D4546. Displacement was monitored throughout the test using three LVDT displacement transducers, and subsequent vertical stresses increments/decrements were not applied until secondary swell or compression was obtained. A uniform seating vertical stress of 6.1 kPa was applied prior to inundation. After seating de-aired, de-ionized water was introduced and specimens were allowed to expand vertically to a maximum value. Incremental loadings were applied after swelling at varying increments until the specimen was once again compressed to the volume prior to inundation, enabling swell pressure calculations (Nelson and Miller, 1992). Large applied vertical stresses in excess of the swell pressure were not feasible due to the large cross section specimen area and the direct application of the load to the top of each specimen through dead weights. Unloading was performed until the seating pressure was obtained. Measurements of C_R, w, and RC were again determined by drying the specimen after testing, separating the 6.7-mm granulated rubber or 19.0-mm tire chips by wet sieving, and drying the sieved rubber. A summary of all LVDT displacement transducers used in swell-compression testing is provided in Table 4.7.

Table 4.7 Summary of the characteristics for all displacement transducers used in swell-compression analyses including the capacity, excitation voltage, calibration factor, resolution, and accuracy

Transducer ID	LPT 7	LPT 8	LPT 9	LPT 10	LPT 11	LPT 20
Capacity (mm)	76.2	76.2	76.2	76.2	76.2	76.2
Excitation Voltage, V_e	9.9754	9.9754	9.9754	9.9754	9.9754	9.9754
Calibration Factor ($mm/V_s/V_e$)	76.8633	76.8283	75.5754	77.0082	76.7800	76.7526
Resolution (mm)	0.001	0.001	0.001	0.001	0.001	0.001
Accuracy (%)	0.0296%	0.0312%	0.0235%	0.0273%	0.0773%	0.0635%

4.2.3.3 Field-Scale Swell Monitoring

In addition to laboratory swell-compression testing, ESR field plots were utilized to evaluate swell characteristics of more real-scale plots in the field. Field plots used Pierre shale residual expansive soil from the same location and identical scrap tire rubber in comparison to large and small-scale compression tests performed in the laboratory. Appropriate amounts of expansive soil, water and rubber were thoroughly mixed to produce compacted mixtures at optimum *w* and 20% *RC*.

All three materials were initially mixed in a large 0.1 m^3 (3.5 ft^3) concrete mixer to assure a homogeneous mixture. Several mixer volumes were required in order to achieve desired amounts of materials for each plot. Once thoroughly homogenized mixtures were allowed to cure for 24 hours determined to be an adequate amount of time for water to evenly distribute throughout the clay component of the mixture. Target field plot dimensions were 0.19 m^3 in initial total volume and 102 mm (4 in) in height. Prior to compaction, mixture lift thicknesses were measured at heights of approximately 200 mm (8 in) to 250 mm (10 in), representing un-compacted or loose lift thicknesses (similar to Figure 2.13). Material weights were determined using target geometries and compaction specifications discussed in Section 4.1.3.

Compaction was accomplished with a 73.4 kN C-433 vibratory roller manufactured by Caterpillar. The large cross sectional area of the field plots and the need to use common field compaction equipment employed in the industry prompted the use of a large roller with vibratory capabilities. During compaction, mixtures were confined to the target

cross sectional area of 1.85 m^2 (20 ft^2) with locally-available non-expansive soil in order for the maximum compaction energy to pass from the roller to the ESR mixture. In order to compact mixtures to the target thickness of 152 mm, 6 to 16 passes without vibration and 6 to 20 passes with vibration were required. As discussed in Section 2.8.3, a single roller pass is defined as a single pass for a single direction (not back and forth) of the roller compactor over the entire plot area at a rate slow enough to simulate a static, monotonic compaction effect.

Sand cone density testing was performed on each field plot according to ASTM D1556. Sand cone material was dried in a laboratory convection oven to determine the compaction water content, after which material was washed over a 2.0 mm sieve (#10 standard sieve) to retain scrap tire rubber and determine the rubber content of each mixture. Field plot compaction information and state parameters are presented in Chapter 5.

After compaction, the locally-available non-expansive soil used for confinement was removed and concrete was poured laterally around each field plot. Plots were underlain by a thin (10 mil) plastic sheet, underlain by a smooth concrete slab. Therefore, base confinement material was also provided by a rigid concrete base. A uniform surcharge of 6 kPa was applied to each plot by adding 230 mm (9 in) of gravel inside a plywood box to the top of each plot. Seating was monitored for 14 to 16 hours or until compression was no longer evident before plots were inundated with water. Water was applied constantly to the top of each plot during the inundation stage. Swell was monitored for

approximately 2 weeks or until the maximum swell was realized. Figure 4.9 displays the compacted field plots prior to inundation and the monitoring of swell in this study.

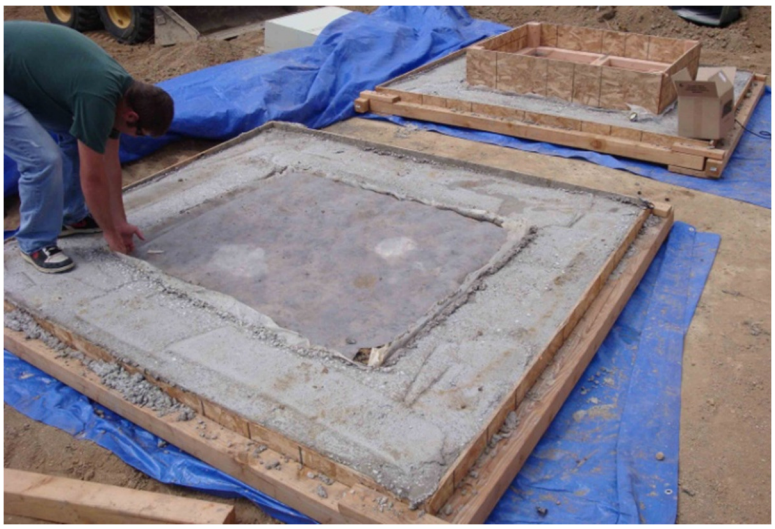

Figure 4.9 Expansive soil-rubber field plots post compaction, prior to the application of vertical seating stress and subsequent inundation

Displacement gauges were attached to the surcharge box on all four corners of each field plots. Displacement gauges were not calibrated and information relating to each identical gauge is presented in Table 4.8. Gauge selection was based on the smallest resolution with a minimum 25.4 mm range. Readings were taken with an increasing duration between readings for both the seating vertical stress and when plots were inundated with water. Swell results for field plots are displayed in Chapter 5.

Table 4.8 Information relating to displacement gauges including resolution, range, and manufacturer

Field Plot Displacement Gauges	
Manufacturer	MHC Industrial Supply
Resolution (mm)	0.025
Range (mm)	25.4

4.2.4 One-Dimensional Consolidation

In additional to monitoring displacements to determine differential vertical strains, consolidation theory can be applied to determine the time rate of consolidation during each loading increment. Using consolidation theory the coefficient of consolidation and the hydraulic conductivity can be estimated according to equations presented in Chapter 3. Permeability testing would provide a more reliable estimate for k, but was outside of the scope of the present research. For SSC testing, c_v and k were calculated for loading increments on the NCL. In most SSC testing cases, the NCL was reached at an effective vertical stress of 97.6 kPa, therefore the coefficient of consolidation and the hydraulic conductivity were calculated at effective vertical stress values of 97.6, 195.2, 390.4, 780.8 and 1561.6 kPa. For LSC testing, c_v and k were calculated for all loading increments, due to the limited range of effective vertical stresses applied to each specimen. The effective vertical stress range used to calculate c_v and k for LSC testing ranged from 12.0 to 36.0 kPa. Tabulations of c_v and k for both SSC and LSC testing can be seen in Table 5.5.

4.2.5 Large-Scale Axisymmetric Compression Testing

4.2.5.1 Specimen Preparation

Specimens prepared for axisymmetric compression testing were mixed with appropriate amounts of STR, de-aired, de-ionized water and Pierre shale residual expansive soil. All mixtures were prepared to w equal to optimum and C_R equal to 95% based on Standard Proctor compaction (Section 4.1.5) and a target RC of 20%. Three specimens were

prepared for 19.0-mm tire chips and 6.7-mm granulated rubber to quantify and determine the effect of rubber particle size on ESR behavior. Mean effective stress values of 50, 100 and 200 kPa were employed for each rubber type. Specimens were mixed thoroughly in six separate layers and material for each layer was allowed to cure for 24 hours to ensure homogeneous water content in each layer prior to compaction. *RC* and C_R variations were limited by utilizing six layers for each specimen as opposed to using fewer layers during compaction. By isolating C_R, *RC* and *w* in each layer variations in state parameters over the entire specimen volume were effectively reduced. A specimen homogeneity analysis was conducted and will be discussed in Section 5.1.

Specimens were compacted in a split mold specifically manufactured for large-scale triaxial (LSTX) testing, shown in Figure 4.10 (a). The split mold was originally designed for the preparation of 150-mm-diameter large-scale triaxial specimens. Additional reinforcement was required to compact fine grained ESR mixtures with large applied vertical loads necessary for adequate compaction (Figure 4.10). Layer thicknesses of 50 mm were utilized during static compaction of each layer. Specimen target heights were set to 300 mm due to the height limitation of the load frame (Figure 4.11) and specimen diameters were limited to 150 mm by the split mold. A 100-kN load frame was used to compact specimens (Figure 4.10 (b)). Vertical stresses required to compact each specimen layer a target 50 mm heights ranged from 50.4 to 100.7 kPa. Layers were scarified between lifts to facilitate bonding. Figure 4.10 displays the mold and load frame used for compacting ESR specimens.

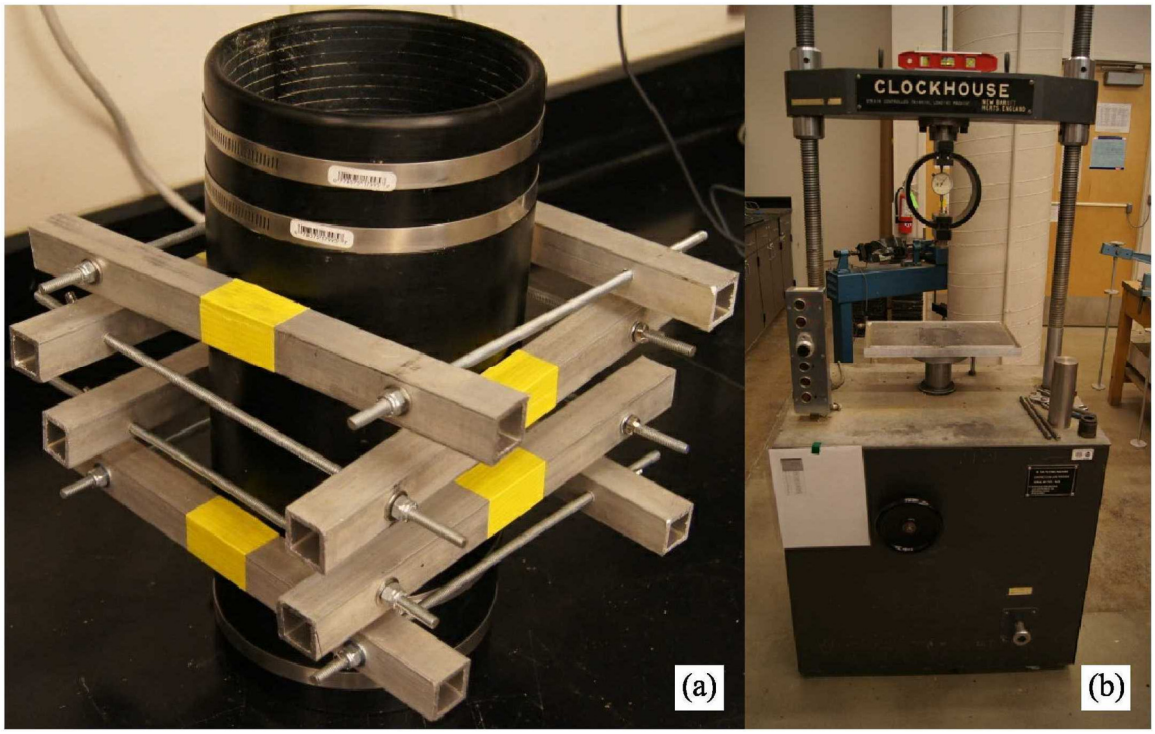

Figure 4.10 (a) Large scale triaxial mold and (b) load frame used in the compaction of expansive soil-rubber mixture specimens tested in undrained axisymmetric compression

LSTX testing was conducted in accordance with the Head (1998). Specimens were surrounded laterally by two 0.75-mm thick rubber membranes. Membrane calibration data is presented in Appendix A, and will be discussed in Section 4.2.4.7. Dry filter paper and porous stones were applied to the top and bottom of each specimen prior to filling the triaxial cell with de-aired water. Cell pressure and pore water pressures were monitored by pressure transduces manufactured by ELE International and GeoTac, respectively. A full calibration of pressure transducers, traxial cell and membranes is presented in Appendix A.2. Specimen area and membrane corrections accounted for during undrained loading will be discussed at the end of Chapter 4.

4.2.5.2 Flushing

After specimens were compacted according to the procedure outlined in Section 4.2.5.1 flushing was conducted with de-aired, de-ionized water under an effective radial stress of 20 kPa. Water was allowed to percolate through specimens from base to top under a hydraulic gradient *(i)* of 4.8 to 5.1. Due to the relatively large specimen volume and low hydraulic conductivity of ESR specimens, flushing termination criterion included reaching maximum expansion due to swell and the absence of air bubbles in the drainage lines. Using these two criteria, 0.3 to 1.5 pore volumes were flushed through the specimen in durations ranging from 24 to 36 hours. Less pore volumes were flushed though 19.0-mm ESR specimens due to a higher dry density obtained upon compaction, as well as less distributed rubber particles throughout the specimen; both factors leading to a lower hydraulic conductivity of the relatively more compacted soil matrix. Specimen expansion (swell) during flushing and back pressure saturation was monitored using the cell volume burets (see Figure 4.11).

4.2.5.3 Back Pressure Saturation

After flushing, specimens were back pressure saturated according to the procedure outlined in Head (1998). Back pressure increments of 50 kPa were applied while maintaining a differential effective stress between cell pressure and pore pressure of 20 kPa. Pressures were increased until a specified level of saturation was obtained. Assessment of the level of specimen saturation is reported as *B* values (Skempton 1954), which were required to reach or exceed 0.98. Achieving this level of saturation required radial stresses of 350 to 450 kPa depending on (a) the compacted mixture type (6.7-mm

vs 19.0-mm ESR), (b) duration of flushing, (c) effectiveness of flushing (expansion potential realized), and (d) the level of saturation at the end of flushing. *B* values were typically relatively high immediately after flushing (0.82 to 0.85) due to an effective flushing protocol (Section 4.2.5.1). During back pressure saturation, additional de-aired, de-ionized water was forced into the remaining unsaturated pore space, increasing specimen expansion. Therefore, cell volume burets were also monitored during back pressure saturation and differential volumes were added to expansion experienced during flushing (after taking an appropriate cell calibration into account) to calculate the total percent swell of each ESR specimen. Triaxial cell calibration curves can also be seen in Appendix A.

4.2.5.4 Isotropic Compression

Isotropic compression was carried out after *B* values of 0.98 were obtained. Pore water pressure values were allowed to dissipate until target p' values of 50, 100 and 200 kPa were obtained. Mean effective stress values were increased from 20 to 50, 50 to 100, and 100 to 200 kPa depending on the target p'. Volumetric strains were recorded using volume change burettes to determine the change in density (in this study reported as relative compaction) during each staged increase of p'. Isotropic compression results are presented in Figure 5.7 and are reported in Table 5.7.

4.2.5.5 Isotropic Consolidation

Consolidation theory was applied to determine time rate of consolidation parameters c_v and k. During isotropic consolidation pore pressures were measured with time to

determine consolidation characteristics of LSTX ESR specimens. Specimens were consolidated in steps from mean effective stress values of 20 to 50, 50 to 100, and from 100 to 200 kPa. Pore pressure change (Δu) was measured until the internal specimens stress state equilibrated or Δu = 0 kPa. Pore water pressures were measured and recorded during back pressure saturation, isotropic compression, and undrained axisymmetric compression using in-line pressure transducers manufactured by ELE Int. and GeoTAC Inc. A summary of each pressure transducer used throughout LSTX testing is included in Table 4.9.

Table 4.9 Pertinent information relating to the pressure transducers manufactured by ELE Int. and GeoTAC Inc. and used throughout LSTX testing including the excitation voltage (V_e), calibration factor ($mm/V_s/V_e$), resolution (kPa), and accuracy (%)

Manufacturer	**ELE Int.**	**Geotac Inc.**
Excitation Voltage, V_e	9.9593	9.9593
Calibration Factor ($mm/V_s/V_e$)	7013.084011	13981.89879
Resolution (kPa)	0.499	0.628
Accuracy (%)	0.044%	0.056%

4.2.5.6 Undrained Axisymmetric Compression

In order to assess the intrinsic critical state parameters M_{cs}, ϕ_{cs}, Γ_{cs}, λ_{cs} and κ_{cs} associated with 6.7- and 19.0-mm ESR mixtures, specimens were tested in undrained monotonic axisymmetric compression to levels of axial strain of approximately 30% after isotropic compression. As discussed previously, specimens were reconstituted to similar levels of C_R and RC, and isotropically consolidated to a wide range of p' values in order to more rigorously characterize the mechanical response of ESR mixtures.

ESR mixtures were axisymmetrically compressed under a constant axial strain. The strain rate was estimated based on the time required for pore water pressure changes to completely dissipate during isotropic consolidation (Head 1998). Strain rates estimated from isotropic consolidation data ranged from 25 to 50 % per day (1.74E-2 to 3.4774E-2% per minute) depending on the target p' and ESR mixture type. A consistent strain rate of 20% per day (1.39E-2% per minute) was applied for all ESR mixtures tested. During testing, axial strains were measured using a LVDT displacement transducer and deviatoric loads were measured using a force transducer. A summary of both transducers is presented in Table 4.10. A depiction of the large-scale triaxial apparatus (LSTX) used to is displayed in Figure 4.11.

Table 4.10 Pertinent information relating to the LVDT displacement transducer and force transducer used throughout LSTX testing including the excitation voltage (V_e), calibration factor ($mm/V_s/V_e$), resolution (kPa), and accuracy (%) (after Fox 2011)

	Displacement Transducer	**Force Transducer**
Excitation Voltage	10.00	3.00
Calibration Factor ($mm/V_s/V_e$)	65.4379	-26.5657
Resolution (mm)	0.07	0.29
Accuracy (%)	0.27	0.59

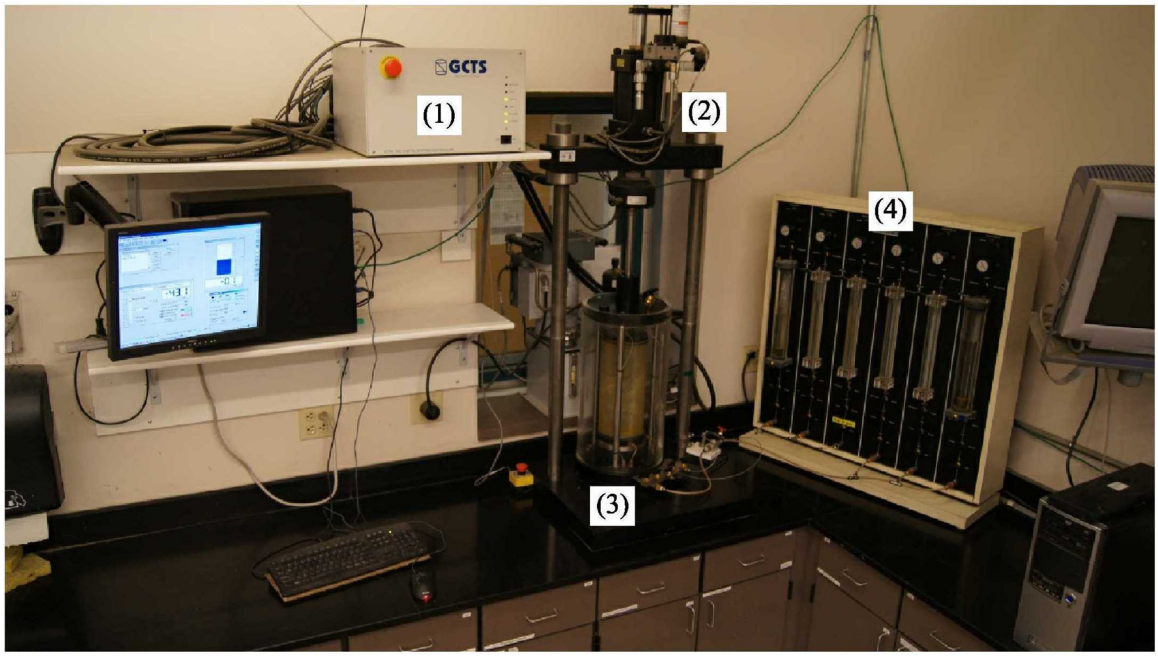

Figure 4.11 LSTX apparatus and major components including: (1) data acquisition and load frame control system, (2) 100-kN load frame, (3) triaxial cell housing specimens 150 mm in diameter and 300 mm in height, and (4) pressure panel board used to control cell and pore water pressures and measure resulting volume changes during testing

4.2.5.7 Area Correction for Axisymmetric Compression Results

Corrections for the changes in specimen cross sectional area during undrained axisymmetric compression were calculated according to Lochelle et al. (1988). Geo-materials compressed axisymmetrically exhibit failure in bulging, along a well-defined shear plane, or in some combination of bulging and shear plane. When specimens exhibit bulging failure with no apparent shear plane the corrected cross sectional area (A_c) at any ε_a during axisymmetric compression is given by:

$$A_c = A_0 \left(\frac{1-\varepsilon_p}{1-\varepsilon_a} \right) \qquad (4.4)$$

where A_0 denotes the initial specimen area (m^2); ε_p denotes the volumetric strain during axisymmetric compression (%); and ε_a denotes the axial strain during axisymmetric

compression (%). All LSTX conducted in this study were undrained, therefore equation 4.4 simplifies to the following form:

$$A_c = A_0\left(\frac{1}{1-\varepsilon_a}\right) \tag{4.5}$$

When specimens exhibit a shear plane failure during axisymmetric compression the corrected A_c at a specific axial strain, ε_a, during axisymmetric compression is given by:

$$A_c = A_f + \left(A_e - A_f\right)\left(\frac{\varepsilon_a - \varepsilon_f}{\varepsilon_e - \varepsilon_f}\right) \tag{4.6}$$

where A_f denotes the cross sectional area at peak strength (m^2); A_e denotes the cross sectional area at the end of the test (m^2); ε_f denotes the axial strain at peak strength (%); and ε_c denotes axial strain at the end of the test (%). All specimens exhibited a bulging type failure in this study, therefore equation 4.5 was applied when correcting the cross sectional area during axisymmetric compression.

4.2.5.8 Membrane Correction for Axisymmetric Compression Results

Membrane corrections for triaxial specimens during undrained axisymmetric compression were calculated according to Lochelle et al. (1988). Membrane corrections can range from insignificant to extreme when accounted for during axisymmetric compression depending on (a) the type of membranes employed, (b) the type of geo-material tested, (c) the primary mode of failure (bulging or shear plane), and (d) the maximum ε_a at the end of testing (Lochelle 1988). The primarily fine grained ESR mixtures tested and the thin (0.75 mm) membranes employed lead to relatively small

membrane corrections during axisymmetric compression. Membranes apply lateral confining pressures to specimens, which can be significant at relatively low confining pressures. Therefore, to correct for the initial confining pressure, p_{0m}, the following equation was employed:

$$p_{0m} = 2E_i \frac{d_0 - d_{im}}{d_0 \cdot d_{im}} \qquad (4.7)$$

where E_i is the initial tangent modulus of the membrane (kN/m); d_{im} is the initial diameter of the membrane (m); and d_0 is the diameter of the specimen at the end of isotopic compression (m). Values of p_{0m} calculated in this study ranged from 0 to 0.25 kPa depending on the mixture type (6.7 or 19.0-mm ESR), initial C_R, and p' obtained after isotropic compression. Soft soils tested at low confining pressures are impacted most by p_{0m} which becomes significant in excess of 1 kPa (LaRochelle et al. 1988).

Confining membranes contribute additional hoop stresses which increase the radial effective stress experienced by each specimen. As mentioned previously, all specimens yielded in bulging, therefore the increased hoop stresses induced by the confining membranes, $\Delta\sigma_r$, were corrected using the following equation:

$$\Delta\sigma_r = p_{om} + \frac{E\sqrt{\varepsilon_a}}{d_0} \qquad \text{Equation 43}$$

where E denotes the elastic modulus of the membrane (kN/m).

E used in membrane corrections during axisymmetric compression was determined according to Head (1998). The results of the membrane *E* determination are summarized in Table 4.11. A complete calibration of the membranes used in testing is presented in Appendix A.2.5. Two identical membranes were used to confine each specimen during LSTX testing. Due to the primarily fine grained ESR mixtures tested, membranes employed were thin and corrections were relatively small.

Table 4.11 Membrane data used to correct axisymmetric compression testing including the thickness and elastic modulus (*E*)

Membrane Data	
Thickness (mm)	0.75
E (kPa)	944.9

CHAPTER 5: PRESENTATION OF RESULTS

5.1 LSTX Specimen Uniformity

Uniformity was studied for specimens tested in axisymmetric compression. Specimens tested in axisymmetric compression were more likely to experience heterogeneities in C_R, w and RC in comparison to specimens tested in one-dimensional swell-compression due to a greater number of lifts and removal of compaction split-mold upon compaction completion. Both rubber particle sizes utilized throughout this research, 6.7-mm and 19.0-mm STR, were studied for heterogeneities in ESR specimens used in axisymmetric compression. Six layers were utilized for compaction. Specimen layers were separated with a thin sheet of wax paper, enabling RC and w to be accurately characterized for each layer. Both specimens were compacted to target C_R, w and RC equal to 95, 20 and 20%, respectively.

Images of the specimens in various stages of the uniformity study are presented in Figure 5.1. Figure 5.2 displays the variations of C_R, w and RC versus vertical depth within the specimen for both specimens tested. Average, measured C_R, w and RC shown are referred to the midpoint of each layer. Horizontal axis ranges were set to ±5% around the target value for (a) C_R, (b) w, and (c) RC. Table 5.1 displays value of C_R, w and RC determined for each of the six layers during the uniformity study in addition to the average and coefficient of variation for the three parameters. A complete discussion of measured specimen uniformity and basic statistical data as it relates to potential discrepancies in measured results will be provided in Chapter 6.

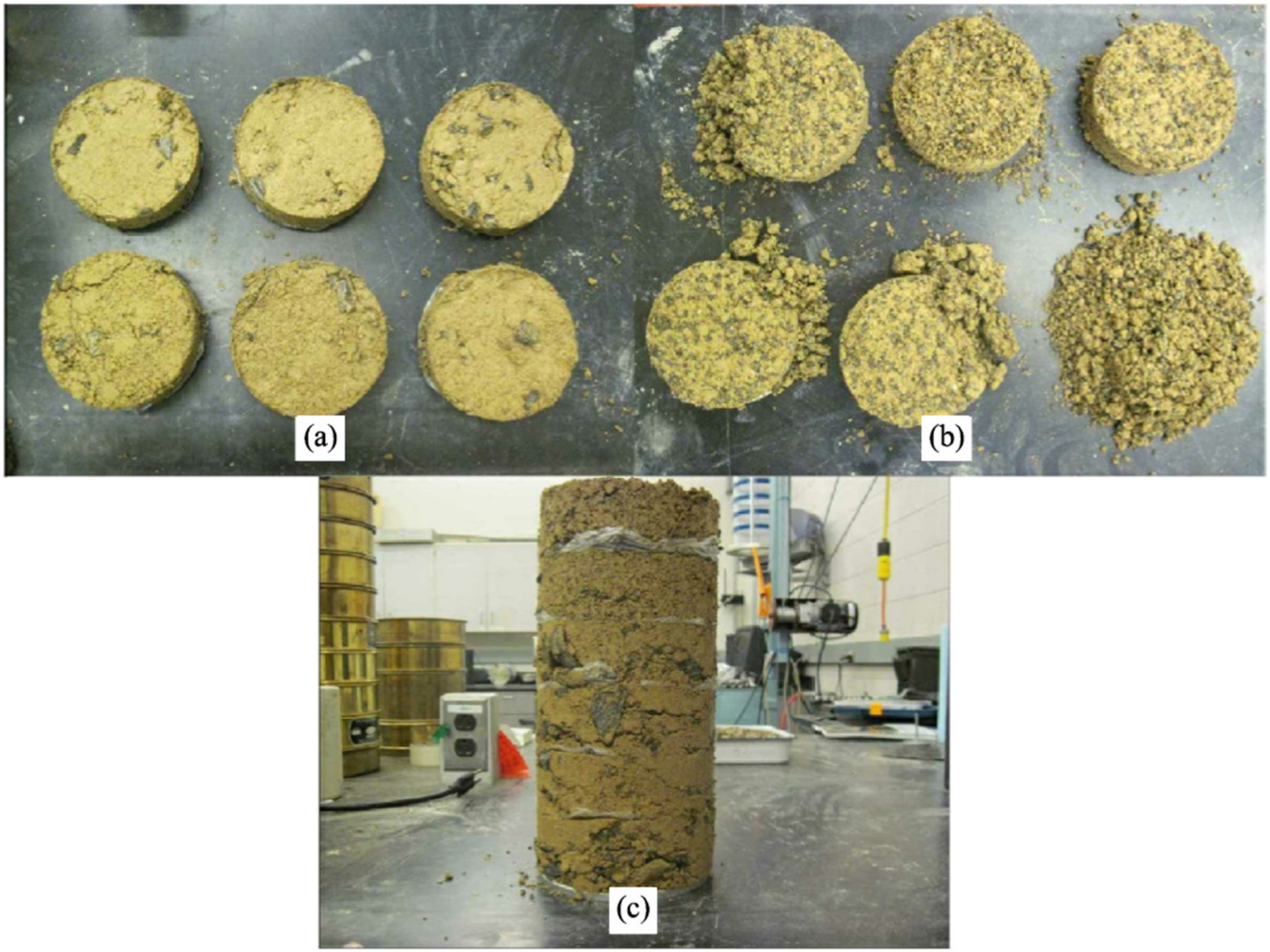

Figure 5.1 Compacted triaxial specimens employed in axisymmetric compression testing used in uniformity study: (a) subdivided 19.0-mm ESR mixture layers, (b) subdivided 6.7-mm ESR mixture layers, and (c) compacted 19.0-mm ESR mixture with layers divided by wax paper

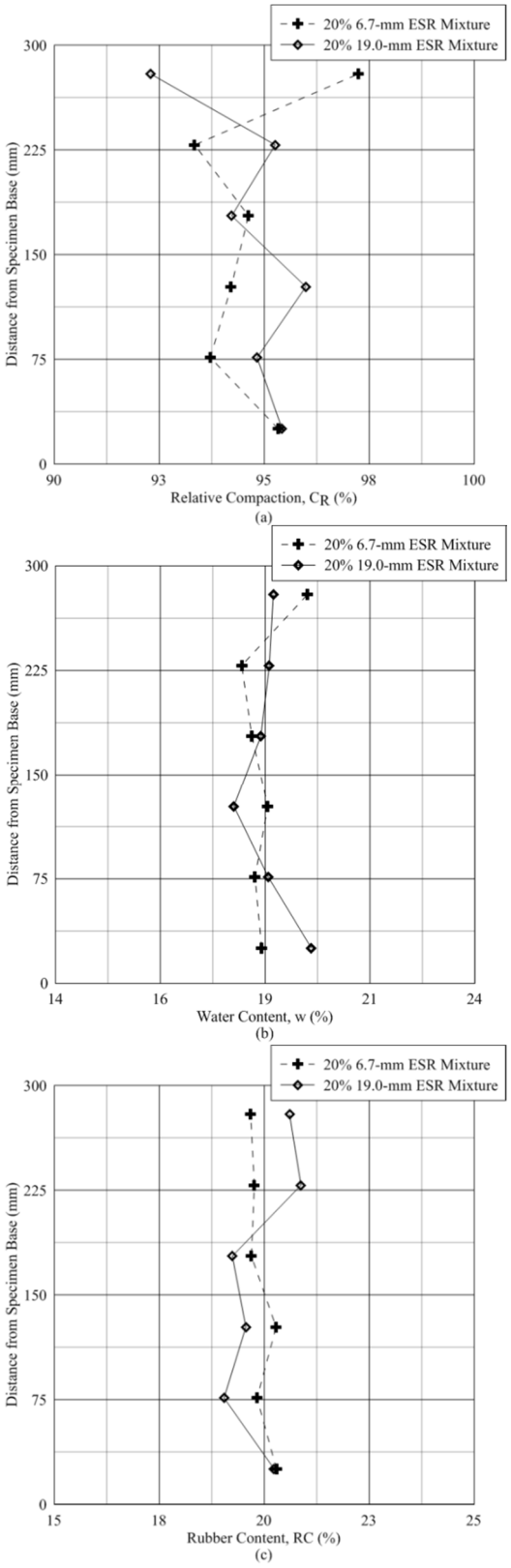

Figure 5.2 Distance from the specimen base within each specimen for 6.7- and 19.0-mm ESR specimens versus (a) C_R, (b) w, and (c) RC

Table 5.1 Uniformity study results for 6.7- and 19.0-mm expansive soil-rubber specimens tested in axisymmetric compression

Height from base (mm)	6.7mm Granulated Rubber			19mm Tire Chips		
	C_R (%)	w (%)	RC (%)	C_R (%)	w (%)	RC (%)
25	95.3	18.4	20.3	95.4	19.6	20.2
76	93.7	18.3	19.8	94.8	18.6	19.0
127	94.2	18.6	20.3	96.0	17.8	19.6
178	94.6	18.2	19.7	94.2	18.4	19.2
229	93.3	17.9	19.8	95.3	18.6	20.9
279	97.2	19.5	19.7	92.5	18.7	20.6
Average	94.7	18.5	19.9	94.7	18.6	19.9
Coefficient of Variation	1.5%	3.0%	1.4%	1.3%	3.2%	3.8%

5.2 One-Dimensional Swell-Compression

Results from one-dimensional swell-compression laboratory testing carried out on small and large scale specimens (SSC and LSC, respectively), and field scale swell monitoring (FSSM) will be discussed separately. Comparisons alluding to the potential scalability effects that both overall specimen size and maximum rubber particle size have on swell-compression parameters will be discussed in Chapter 6.

5.2.1 Small-Scale One-Dimensional Swell-Compression (SSC) Results

Provided in Table 5.2 are the pertinent state parameters and a summary of results related to small-scale one-dimensional swell-compression (SSC) testing. The initial state parameters were required to be within ±1.5% of the target C_R, ±0.5% of the target w, and ±1.0% of the target RC. If actual values of C_R, w and RC fell significantly outside of respective acceptable ranges, specimens were retested. Narrow acceptable ranges were adopted for C_R, w and RC due the proposed testing program and the small variations in C_R, w and RC of 5, 2 and 10%, respectively. One of the primary goals of SSC testing was

to systematically determine the effect C_R, w and RC have on swell and compression responses when tested in SSC, further necessitating the need for small tolerances in the initial state parameters of interest.

Initial state parameters are indicated in the left portion of Table 5.2. Displayed in the state parameter columns for C_R, w and RC is the target, actual (measured), and differential (Δ) values for each initial state parameter of interest. The four right-most columns in Table 5.2 display testing parameters determined from swell-compression tests (Figure 5.3, 5.4 and 5.5). Assessment of swell potential is given by the swell percent ($S_{\%}$) and swell pressure σ'_{zs} columns. Compressibility values are presented in terms of the compression (C_c) and recompression indices (C_r), as discussed in Chapter 3.

Table 5.2 Summary of initial state parameters and results of small-scale one-dimensional swell-compression tests

Initial State Parameters									Swell Parameters		Compressibility Parmaeters	
C_R (%)			w (%)			RC (%)			$S_{\%}$ (%)	σ'_{zs} (kPa)	C_c	C_r
Target	Actual	ΔC_R	Target	Actual	Δw	Target	Actual	ΔRC				
90.0	89.6	-0.4	17.8	18.0	0.1	N/A			6.6	138	0.236	0.060
90.0	89.8	-0.2	19.8	19.7	-0.2				5.0	126	0.245	0.068
90.0	89.8	-0.2	21.8	21.3	-0.5				4.1	114	0.234	0.066
90.0	90.3	0.3	17.5	18.6	1.1	10.0	9.9	-0.1	5.6	58	0.242	0.084
90.0	90.2	0.2	19.5	20.0	0.6	10.0	10.6	0.5	3.4	13	0.255	0.090
90.0	90.4	0.4	21.5	22.1	0.6	10.0	10.9	0.9	1.9	27	0.248	0.093
90.0	89.7	-0.3	16.6	17.0	0.4	20.0	19.9	-0.2	4.7	32	0.261	0.129
90.0	89.9	-0.1	18.6	18.4	-0.2	20.0	19.9	-0.1	2.5	22	0.256	0.109
90.0	89.2	-0.8	20.6	20.6	0.0	20.0	20.8	0.8	1.1	17	0.247	0.102
95.0	94.5	-0.5	17.8	17.7	-0.2	N/A			8.2	243	0.223	0.074
95.0	94.8	-0.2	19.8	19.9	0.0				7.3	167	0.230	0.071
95.0	94.4	-0.6	21.8	21.6	-0.2				5.7	123	0.225	0.072
95.0	94.2	-0.8	17.5	17.8	0.3	10.0	9.6	-0.4	6.2	89	0.237	0.087
95.0	93.8	-1.2	19.5	19.9	0.4	10.0	9.9	-0.1	5.6	58	0.235	0.094
95.0	94.2	-0.8	21.5	21.9	0.4	10.0	9.6	-0.4	4.2	53	0.236	0.094
95.0	94.6	-0.4	16.6	15.8	-0.8	20.0	20.6	0.6	5.2	53	0.225	0.107
95.0	94.7	-0.3	18.6	18.5	-0.2	20.0	19.9	-0.1	3.6	34	0.208	0.113
95.0	95.0	0.0	20.6	20.8	0.1	20.0	20.0	0.0	2.2	29	0.239	0.107
100.0	100.2	0.2	17.8	18.2	0.4	N/A			9.2	252	0.217	0.081
100.0	100.5	0.5	19.8	19.7	-0.2				8.0	279	0.206	0.078
100.0	101.5	1.5	21.8	22.7	0.9				6.6	166	0.212	0.075
100.0	99.7	-0.3	17.5	17.9	0.5	10.0	10.2	0.2	6.9	117	0.221	0.095
100.0	99.4	-0.6	19.5	19.9	0.5	10.0	10.3	0.3	4.3	80	0.217	0.089
100.0	99.3	-0.7	21.5	21.9	0.4	10.0	10.4	0.4	5.6	91	0.221	0.095
100.0	99.6	-0.4	16.6	16.7	0.0	20.0	20.3	0.3	5.5	63	0.231	0.111
100.0	99.9	-0.1	18.6	18.5	-0.1	20.0	20.2	0.2	4.4	42	0.229	0.118
100.0	99.8	-0.2	20.6	20.5	-0.1	20.0	20.2	0.2	3.7	33	0.226	0.110

Figures 5.3, 5.4 and 5.5 display swell and stress-deformation response for all small-scale mixtures tested under zero-lateral strain boundary condition. The initial state parameters prior to the application of the seating pressure for each test are displayed in the legend. The vertical response under an applied vertical stress, σ'_z, of 6.1 kPa indicates the swell percent, $S_{\%}$, realized upon inundation. Additional vertical stresses were applied until a σ'_z of 1561.6 kPa was obtained. Swell pressures, σ'_{zs}, were calculated by interpolating the σ'_z necessary to compress specimens back to their respective volumes prior to inundation (see Chapter 3). Identical axes limits for all subfigures of Figure 5.3 were employed to allow a direct comparison between SSC results. A maximum effective vertical stress of 1561.6 kPa allowed assessment of the compression index, C_c. C_c values were calculated from the slope of the semi-logarithmic-linear portion of the normal compression line (NCL). C_r values were determined from the semi-logarithmic-linear portion of the unloading curve. Additional information regarding how $S_{\%}$, σ'_{zs}, C_c and C_r values were calculated is presented in Chapter 3.

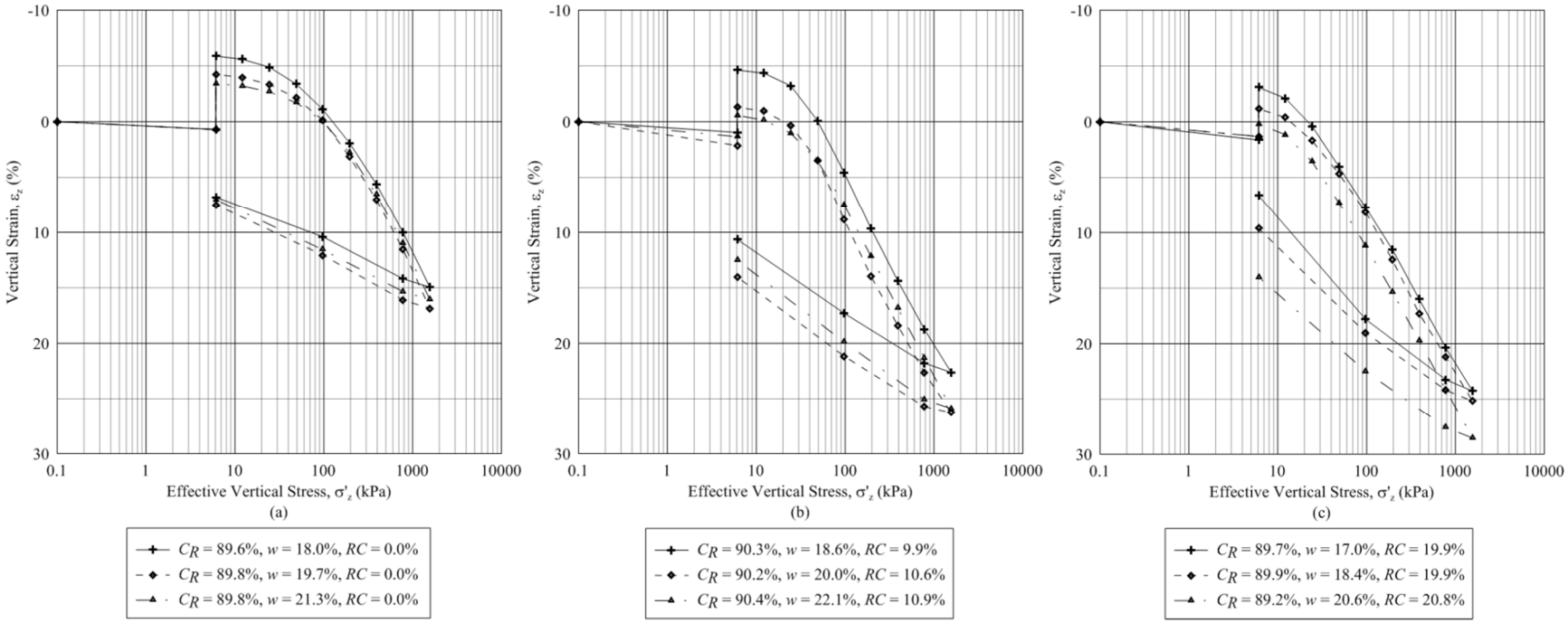

Figure 5.3 Small-scale laboratory swell-compression curves for specimens with target initial relative compaction of 90% and rubber content values of: (a) 0%; (b) 10%; and (c) 20%. Initial state parameters are indicated in the legend for each specimen

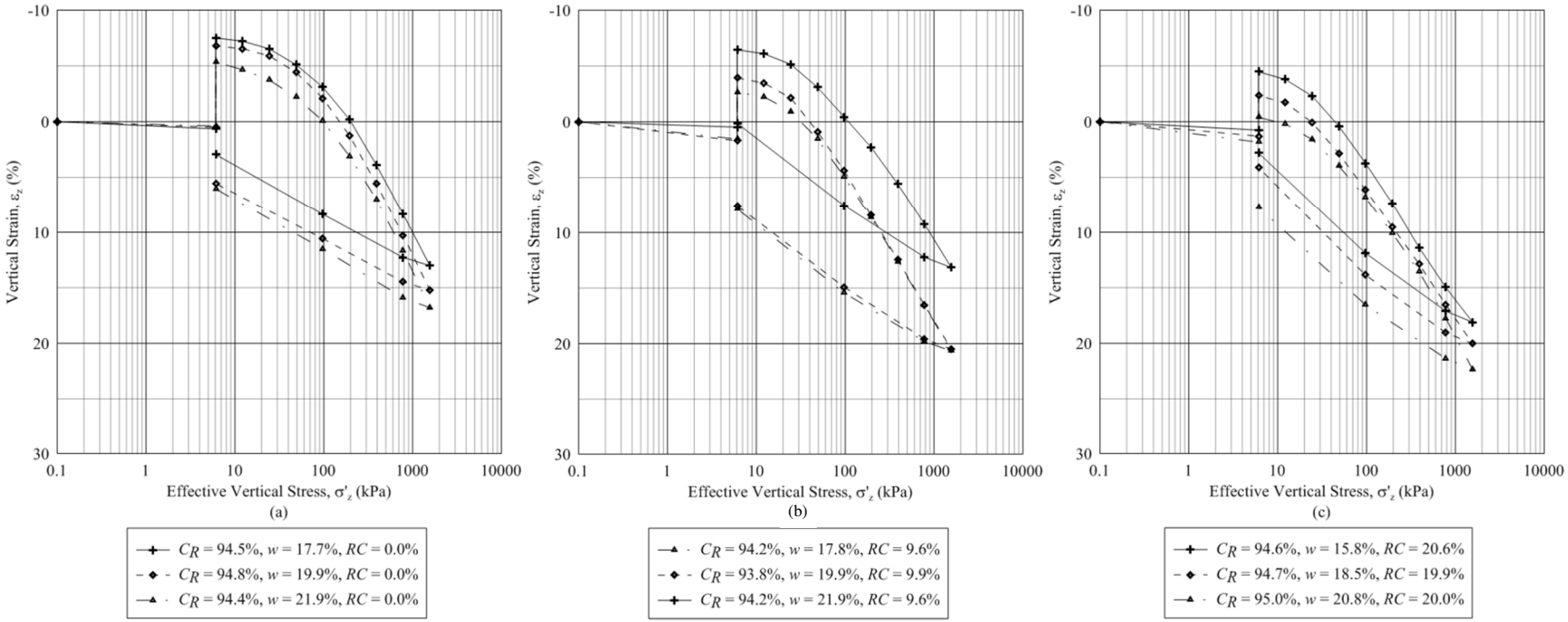

Figure 5.4 Small-scale laboratory swell-compression curves for specimens with target initial relative compaction of 95% and target rubber content values of: (a) 0%; (b) 10%; and (c) 20%. Initial state parameters are indicated in the legend for each specimen

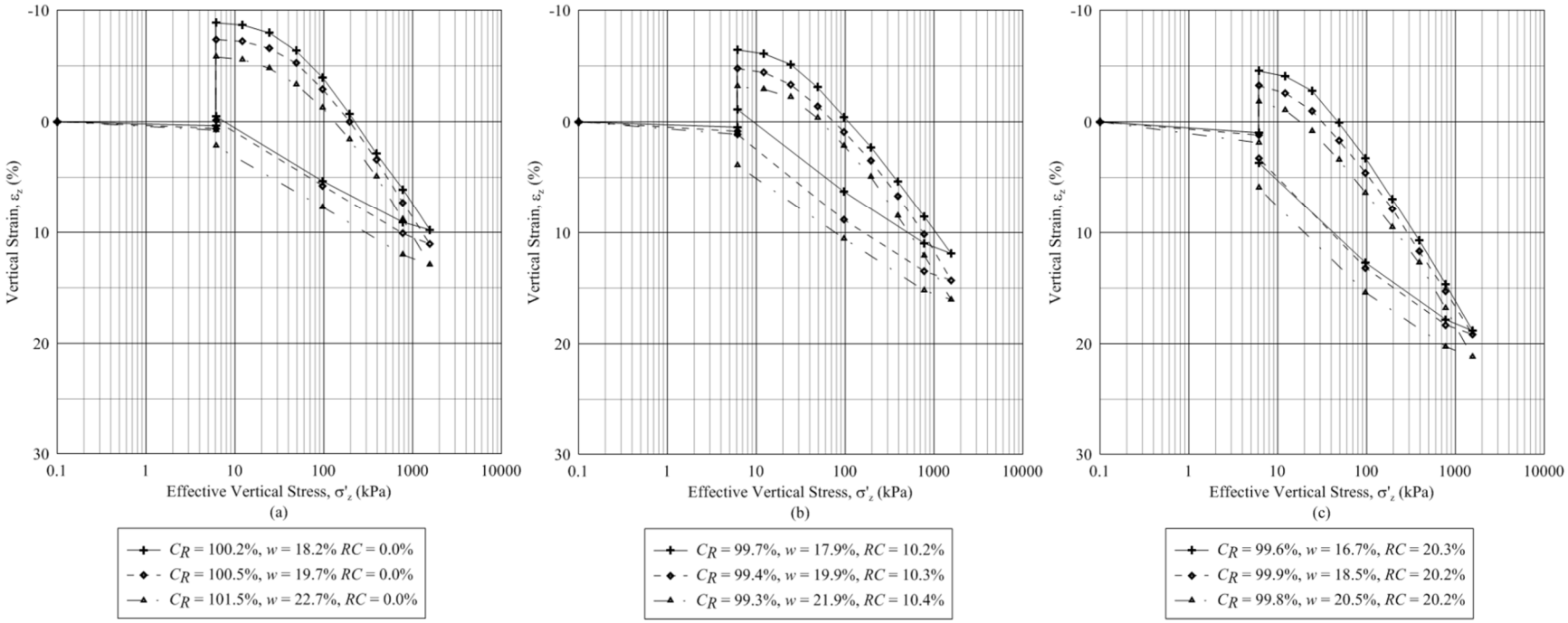

Figure 5.5 Small-scale laboratory swell-compression curves for specimens with target initial relative compaction of 100% and rubber content values of: (a) 0%; (b) 10%; and (c) 20%. Initial state parameters are indicated in the legend for each specimen

5.2.2 Large-Scale One-Dimensional Swell-Compression (LSC) Results

Table 5.3 displays pertinent values relating to large-scale one-dimensional swell-compression testing (LSC). Acceptable state parameter ranges for LSC tests for C_R, w and RC were ±1.0%, ±0.5%, and ±1.0%, respectively. Acceptable ranges were again based on the premise that initial state parameters for each test must be close enough to target parameters to accurately define how the nominal rubber particle size (d_R) and w affect swell-compression parameters. If state parameters were outside acceptable ranges, tests were discarded and retested. The actual, target and differential (Δ) values for C_R, RC and w are included in the left columns of Table 5.3.

Swell and compression parameters pertinent to LSC testing are shown in the four right-most columns of Table 5.3. Calculations of $S_{\%}$ and σ'_{zs} were performed identically to SSC, as explained in Sections 3.2.2 and 5.2.1. Compressibility parameters, C_c and C_r were also defined identically to SSC, as explained in Sections 3.2.2 and 5.2.1. As discussed earlier, dead weight loading was somewhat limited by the large cross sectional area of the LSC specimens. Applied vertical stress was limited to dead weight available and necessary to compress specimens back to their respective volumes prior to inundation. Therefore, it is important to note that the slope of the NCL (C_c) was based on the largest applied vertical stresses for each test.

Table 5.3 Summary of initial state parameters and results of large-scale swell-compression testing

d_R (mm)	Initial State Parameters									Swell Parameters		Compression Parameters	
	C_R (%)			w (%)			RC (%)			$S_{\%}$ (%)	σ'_{zs} (kPa)	C_c*	C_r
	Target	Actual	ΔC_R	Target	Actual	Δw	Target	Actual	ΔRC				
6.7	95.0	95.7	0.7	16.6	16.5	-0.1	20.0	20.3	0.3	4.2	31	0.186	0.032
6.7	95.0	95.1	0.1	18.6	19.1	0.5	20.0	19.9	-0.1	3.0	23	0.179	0.038
6.7	95.0	94.6	-0.4	20.6	20.8	0.2	20.0	19.9	-0.1	1.2	14	0.156	0.031
19.0	95.0	94.9	-0.1	16.5	15.7	-0.8	20.0	20.4	0.4	4.7	34	0.171	0.032
19.0	95.0	95.9	0.9	18.5	18.8	0.3	20.0	19.3	-0.7	3.5	27	0.146	0.037
19.0	95.0	95.5	0.5	20.5	21.0	0.5	20.0	20.2	0.2	2.5	22	0.119	0.034

*C_c values are based on the the largest vertical stress increment applied, and may not be fully representative of NCL slope

Figure 5.6 displays swell and stress-deformation responses for LSC ESR mixtures under the zero-lateral strain boundary condition. The initial state parameters prior to seating for each test are displayed in the legend. Identical axes limits for all subfigures of Figure 5.6 were used to allow a direct comparison between LSC results. A complete analysis discussing the variations in swell and compression parameters for SSC and LSC testing will be covered in Chapter 6. The comparison of initial state parameters, swell characteristics, normal compression indices, and recompression indices for various specimen sizes will also be discussed in Chapter 6.

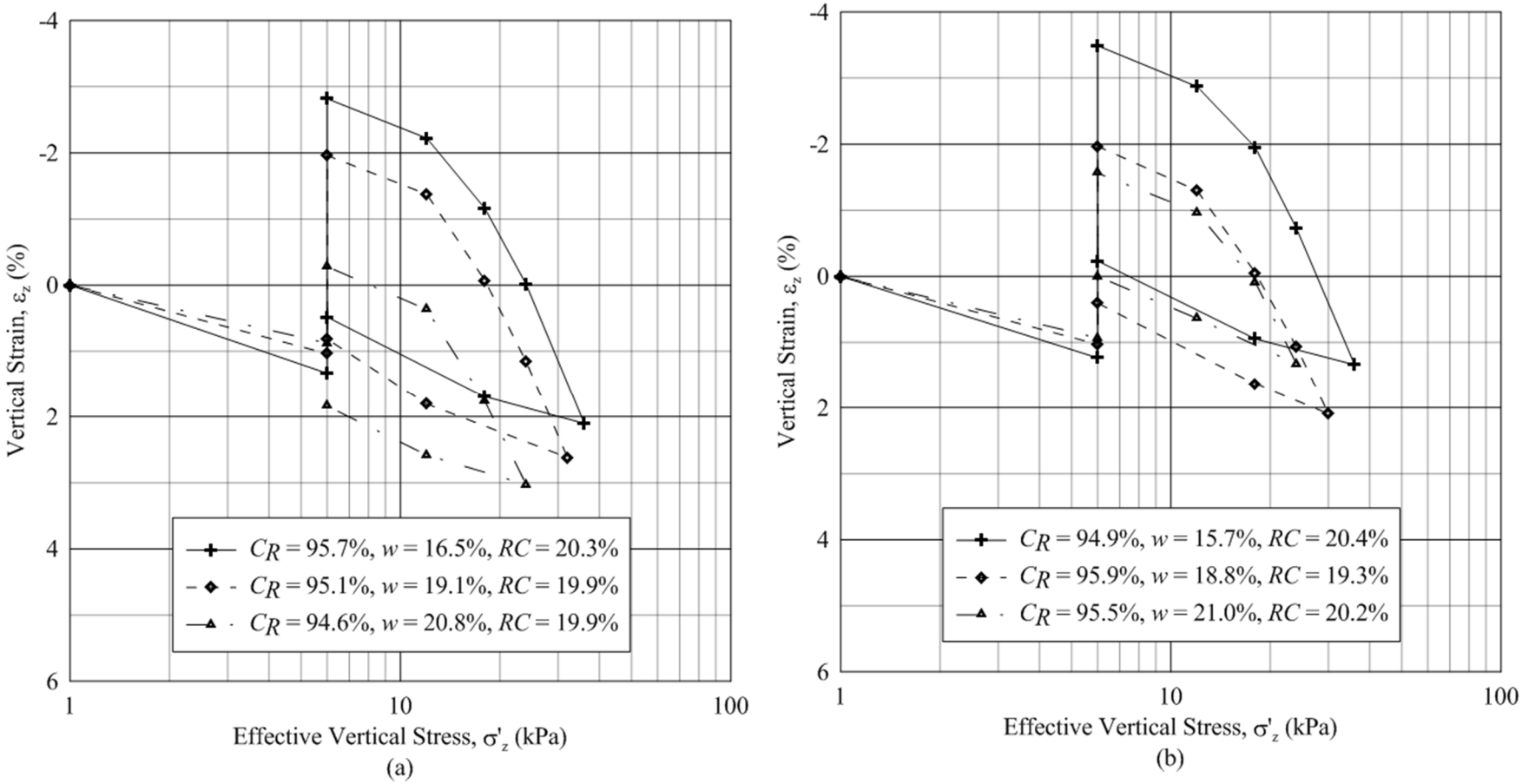

Figure 5.6 Large-scale laboratory swell-compression curves for specimens with (a) 6.7-mm granulated rubber and (b) 19.0-mm tire chips. Initial state parameters are indicated in the legend for each specimen

5.2.3 Field-Scale Swell-Monitoring (FSSM) Results

Field-scale swell-monitoring (FSSM) was performed on ESR specimens much larger than those typically tested in traditional geotechnical laboratories (Chapter 4). Results pertaining to FSSM are displayed in Table 5.4. As shown in Table 5.4 initial state parameters were controlled within a reasonable range at field-scale sizes. C_R, RC and w were all determined using sand cone density testing (ASTM D1556). Sand cone samples were collected in the field and brought back to the laboratory for RC and w measurements. Target C_R, RC and w are compared with their corresponding actual, measured state parameters under the columns of each parameter section displayed in Table 5.4. Larger variations in initial state parameters were accepted in FSSM in comparison to SSC and LSC testing due to (a) an extensive compaction process employing field scale compaction equipment; (b) the increased time required for field specimen preparation; (c) a broader variation in RC in comparison to both SSC and LSC testing: 0 percent and 20 percent; and (d) the increased time required to assess initial state parameters of field specimens. Highlighting results from the FSSM study is the swell response experienced in each plot after inundation. $S_{\%}$ is indicated in the right-most column of Table 5.4.

Results of FSSM can be seen in Figure 5.7. The monitoring duration for each ESR plot was 14 days and the monitoring duration for the Pierre shale soil plot was approximately 12.5 days. Swell was monitored until vertical strain deviated less than 0.10% per day. The horizontal axis of Figure 5.5 was purposefully indicated as arithmetic to focus the decrease in vertical swell response with increasing monitoring time.

Table 5.4 Summary of initial state parameters and results of field-scale swell-monitoring

d_R (mm)	Initial State Parameters									$S_{\%}$ (%)
	C_R (%)			w (%)			RC (%)			
	Target	Actual	ΔC_R	Target	Actual	Δw	Target	Actual	ΔRC	
N/A	95.0	94.0	-1.0	19.5	18.2	-1.3	N/A			7.8
6.7	95.0	90.0	-5.0	18.6	17.5	-1.2	20.0	22.4	2.4	2.4
19.0	95.0	92.1	-2.9	18.5	17.3	-1.2	20.0	19.5	-0.5	2.7

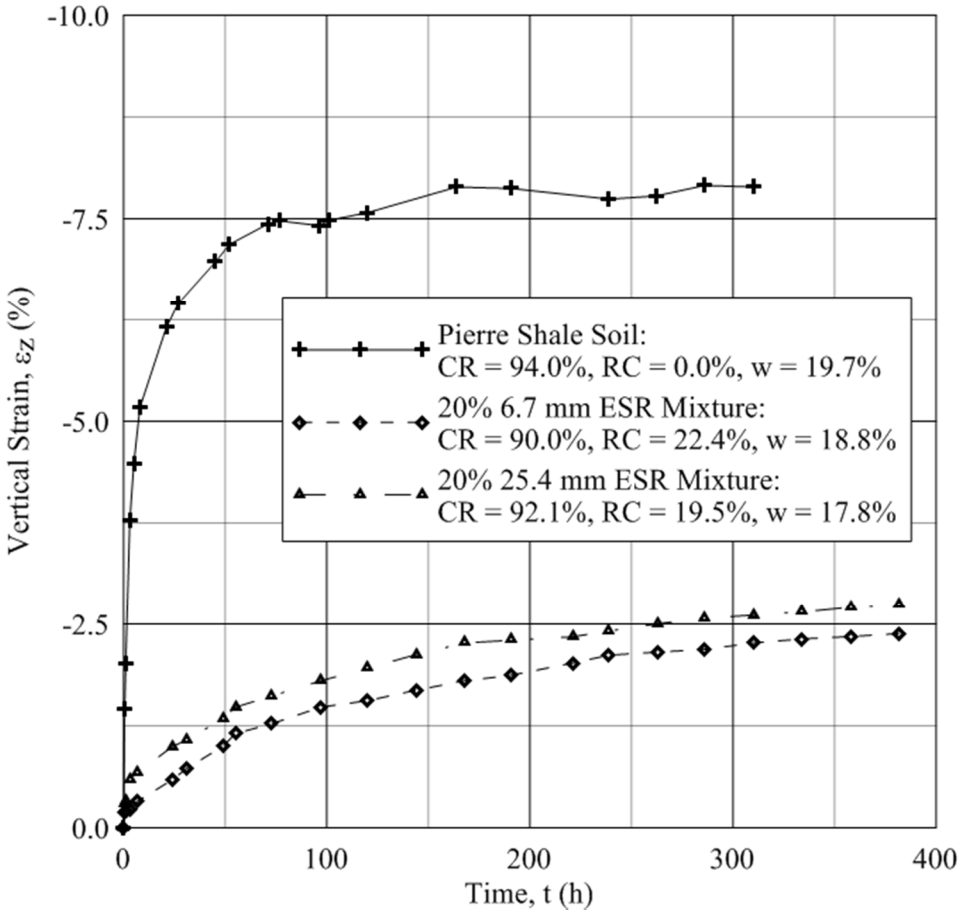

Figure 5.7 Field-scale swell monitoring results of normalized vertical strain versus time. Initial state parameters prior to seating for all plots are displayed in the legend

5.3 One-Dimensional Consolidation

Table 5.5 presentes the results from the consolidation portion of SSC and LSC, where vertical strains were monitored with time to determine the coefficient of consolidation (c_v) and the hydraulic conductivity (k). Additional information regarding the calculation of c_v and k was presented in Chapters 3 and 4. Both parameters were calculated at effective vertical stresses on the NCL, resulting in a range of values. Therefore, the average, minimum and maximum c_v and k values are presented in Table 5.5 providing a range depending on the loading increment employed to calculate each parameter.

Table 5.5 Isotropic consolidation parameters including the coefficient of consolidation (c_v), the modulus of volume compressibility (m_v) and the hydraulic conductivity (k) for small and large-scale one-dimensional swell-compression testing

Test Type	d_R (mm)	Initial State Parameters			Consolidation Parameters						
		C_R (%)	w (%)	RC (%)	m_v (1/kPa)	c_v (m^2/yr)			k (m/s)		
						Average	Minimum	Maximum	Average	Minimum	Maximum
SSC	N/A	89.6	18.0	N/A	9.54E-03	4.61	2.91	8.34	1.37E-08	8.62E-09	2.47E-08
SSC		89.8	19.7		1.00E-02	5.11	3.70	9.94	1.59E-08	1.15E-08	3.10E-08
SSC		89.8	21.3		9.70E-03	4.96	3.46	8.06	1.50E-08	1.04E-08	2.43E-08
SSC	6.7	90.3	18.6	9.9	1.68E-02	4.86	3.91	7.59	2.54E-08	2.04E-08	3.97E-08
SSC	6.7	90.2	20.0	10.6	9.00E-03	5.12	3.29	8.29	1.43E-08	9.22E-09	2.32E-08
SSC	6.7	90.4	22.1	10.9	1.48E-02	4.36	3.43	7.43	2.01E-08	1.58E-08	3.42E-08
SSC	6.7	89.7	17.0	19.9	9.32E-03	4.02	3.36	5.08	1.16E-08	9.74E-09	1.47E-08
SSC	6.7	89.9	18.4	19.9	3.13E-02	7.04	4.16	9.70	6.86E-08	4.05E-08	9.45E-08
SSC	6.7	89.2	20.6	20.8	1.51E-02	4.16	3.41	5.13	1.95E-08	1.59E-08	2.40E-08
SSC	N/A	94.5	17.7	N/A	1.20E-02	4.19	2.87	6.92	1.56E-08	1.07E-08	2.58E-08
SSC		94.8	19.9		1.30E-02	4.81	3.37	9.40	1.94E-08	1.36E-08	3.79E-08
SSC		94.4	21.6		1.00E-02	3.40	2.46	4.84	1.06E-08	7.65E-09	1.51E-08
SSC	6.7	94.2	17.8	9.6	9.12E-03	6.75	3.64	12.43	1.91E-08	1.03E-08	3.53E-08
SSC	6.7	93.8	19.9	9.9	8.81E-03	4.99	3.18	8.74	1.37E-08	8.70E-09	2.40E-08
SSC	6.7	94.2	21.9	9.6	8.80E-03	5.51	3.53	10.71	1.51E-08	9.66E-09	2.93E-08
SSC	6.7	94.6	15.8	20.6	7.86E-03	5.72	3.30	11.38	3.66E-08	2.11E-08	7.27E-08
SSC	6.7	94.7	18.5	19.9	7.70E-03	4.67	3.31	7.79	1.12E-08	7.94E-09	1.87E-08
SSC	6.7	95.0	20.8	20.0	8.98E-03	4.65	3.51	7.42	1.30E-08	9.79E-09	2.07E-08
SSC	N/A	100.2	18.2	N/A	7.65E-03	4.83	4.28	5.42	1.15E-08	1.02E-08	1.29E-08
SSC		100.5	19.7		8.11E-03	4.41	2.84	6.79	1.11E-08	7.17E-09	1.71E-08
SSC		101.5	22.7		8.30E-03	4.00	3.13	5.24	1.03E-08	8.09E-09	1.35E-08
SSC	6.7	99.7	17.9	10.2	6.46E-03	4.40	3.15	7.37	8.85E-09	6.33E-09	1.48E-08
SSC	6.7	99.4	19.9	10.3	8.11E-03	4.88	2.82	7.52	1.23E-08	7.11E-09	1.90E-08
SSC	6.7	99.3	21.9	10.4	6.52E-03	5.75	3.12	12.12	1.17E-08	6.33E-09	2.46E-08
SSC	6.7	99.6	16.7	20.3	8.71E-03	4.15	2.99	5.39	1.12E-08	8.09E-09	1.46E-08
SSC	6.7	99.9	18.5	20.2	8.29E-03	5.05	3.10	6.89	1.30E-08	7.98E-09	1.77E-08
SSC	6.7	99.8	20.5	20.2	8.57E-03	3.78	3.02	5.18	1.01E-08	8.06E-09	1.38E-08
LSC	6.7	95.7	16.5	20.3	1.76E-01	10.19	8.74	11.19	1.71E-07	1.47E-07	1.88E-07
LSC	6.7	95.1	19.1	19.9	1.82E-01	13.60	12.41	14.89	7.72E-07	7.04E-07	8.45E-07
LSC	6.7	94.6	20.8	19.9	2.10E-01	14.19	13.32	15.10	9.28E-07	8.71E-07	9.87E-07
LSC	19.0	94.9	15.7	20.4	1.72E-01	8.53	7.91	9.19	1.39E-07	1.29E-07	1.50E-07
LSC	19.0	95.9	18.8	19.3	1.70E-01	7.77	7.21	8.41	1.70E-07	1.58E-07	1.84E-07
LSC	19.0	95.5	21.0	20.2	2.06E-01	8.12	7.41	9.02	1.86E-07	1.70E-07	2.07E-07

5.4 Large-Scale Axisymmetric Compression Testing

Large-scale axisymmetric compression testing, more commonly referred to as large-scale triaxial testing (LSTX) was performed on ESR mixtures under static, monotonic, isotropically consolidated, undrained conditions. LSTX specimens were compacted to 300 mm in height in a 150-mm-diameter split mold, as discussed in Chapter 4. The use of a larger specimen size in comparison to traditional triaxial testing allowed for the inclusion of larger rubber particles. In this manuscript, shear strength parameters for both 6.7-mm and 19.0-mm ESR mixtures were evaluated using a rigorous critical state framework. The specific steps necessary to fully evaluate the critical state response of ESR mixtures and results of those steps will be discussed in subsequent sections.

5.4.1 Specimen Preparation

Specimen preparation and compaction was performed according to ASTM D4767, "Standard Test Method for Consolidated Undrained Triaxial Compression Test for Cohesive Soils." A total of 6 layers were utilized to improve specimen uniformity (Section 5.1). Similar to one-dimensional testing, initial specimen state parameters were required to fall within acceptable ranges. Initial specimen states were required to fall within ±1.5% of the target C_R, ±1.0% of the target w and ±1.5% of the target RC. Table 5.6 presents the target and actual initial state parameter measurements, in addition to the deviation between target and actual parameters (Δ). As shown in Table 5.6, initial water content (w_i), initial relative compaction (C_{Ri}) and RC measurements were acceptably close to target values. Also, initial states for 6.7-mm and 19.0-mm ESR specimens were

acceptably close to one another, allowing for direct comparisons between the nominal rubber particle size (d_R) discussed in greater detail in Chapter 6.

Table 5.6 Initial state parameters (C_R, w and RC) for axisymmetric compression testing. Initial values of RC, w and C_R are compared with target parameters, displaying discrepancies in target values and actual initial state parameter values.

Test ID	C_R (%)			w (%)			RC (%)		
	Target	Actual	ΔC_{Ri}	Target	Actual	Δw_i	Target	Actual	ΔRC
6.7-mm - 50kPa	95.0	95.4	0.4	18.6	17.8	-0.8	20.0	21.1	1.1
6.7-mm - 100kPa	95.0	96.5	1.5	18.6	18.1	-0.6	20.0	20.8	0.8
6.7-mm - 200kPa	95.0	96.6	1.6	18.6	19.1	0.4	20.0	19.1	-0.9
19.0-mm - 50kPa	95.0	95.6	0.6	18.5	18.8	0.3	20.0	18.6	-1.4
19.0-mm - 100kPa	95.0	95.4	0.3	18.5	18.4	-0.1	20.0	20.3	0.3
19.0-mm - 200kPa	95.0	94.8	-0.2	18.5	18.2	-0.3	20.0	20.9	0.9

5.4.2 Saturation

Triaxial specimens were saturated in two separate steps. First, de-aired, de-ionized water was flushed through each specimen from base to top under a hydraulic gradient of 4.8 to 5.1 until swelling ceased. Next, back pressure saturation was performed under a mean effective stress (p') of 20 kPa and incremental increases in both pore water pressure change, Δu, and cell pressure, σ_r of 50 kPa. Cell pressures required to saturate specimens to a Skempton's Pore Water Pressure Coefficient (B) of 0.98 ranged from 300 to 450 kPa, leading to back pressures ranging from 280 to 430 kPa. Actual B values ranged from 0.978 to 0.992 percent, as shown in Table 5.7. Other than an increased time required between stages of back pressure saturation, few conclusive differences in the saturation process between the six specimens tested with nominal rubber particle sizes of 6.7-mm and 19.0-mm were apparent. B values were similar for both 6.7-mm and 19.0-mm mixtures indicating a similar difficulty in saturating specimens to required levels.

5.4.3 Swell Response

Specimen swell response occurred during both the flushing and back pressure saturation stages of each LSTX test. As shown in Table 5.6 specimens were compacted to a target optimum w of 18.6 and 18.5% for 6.7-mm and 19.0-mm ESR mixtures, respectively. Expansion was monitored during flushing and back pressure saturation with cell volume burettes. Applying an appropriate cell volume correction (Appendix A) to each level of σ_r allowed for a rigorous measurement of specimen swell characteristics during flushing and back pressure saturation. Isotropic swell response during flushing and back pressure saturation ranged from 2.8 to 3.4% in the six specimens tested. Presented in Table 5.7

are the swell responses for isotropically (3D) confined specimens and a calculated equivalent one-dimensional (1D) vertical swell response of each specimen if the specimen was laterally confined; similar to one-dimensional swell-compression testing.

5.4.4 Isotropic Compression

Isotropic compression data for both 6.7-mm and 19.0-mm ESR mixtures is presented in Figure 5.8. Figure 5.8 employs a semi-logarithmic scale with v displayed on the vertical axis and p' displayed on the horizontal axis. Measured v values are plotted for each p' during isotropic compression. Therefore, for each rubber type investigated three v values are presented for p' = 20 and 50 kPa, two for p' = 100 kPa, and one for p' = 200 kPa, due to the isotropic compression sequence employed, as described in Chapter 4. Values of v plotted in Figure 5.7 are tabulated in Table 5.7 under v_{con}. Semi-logarithmic-linear slopes of the NCL and URL, λ_{cs} and κ_{cs}, respectively, and the calculation methodology will be examined in Chapter 6.

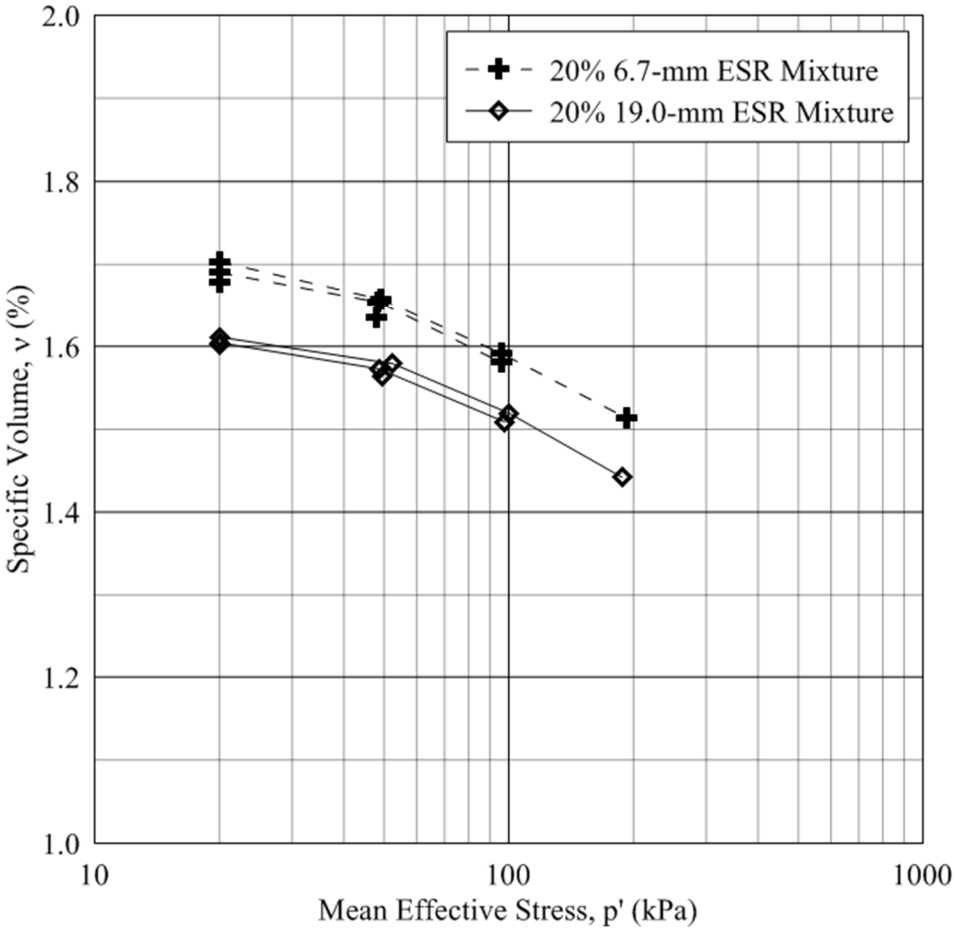

Figure 5.8 Isotropic compression data for 6.7- and 19.0-mm expansive soil-rubber specimen. Values of v and p' represent the final specimen state at each stage of isotropic compression.

Presented in Table 5.7 is v and C_R for various stages of the testing process; initially (i), after back pressure saturation (bps), and after compression (con). Due to the relatively low permeability and large sample size of ESR specimens tested in the LSTX portion of this study, the amount of time necessary to allow pore water pressure to completely dissipate and equilibrate during each stage of the compression process was excessive. Therefore, testing proceeded prior to complete dissipation of Δu, as shown in the right-most column of Table 5.7 ($\Delta p'$). Potential implications of the incomplete dissipation of Δu during isotropic compression will be addressed further in Chapter 6.

Table 5.7 Results of back pressure saturation and isotropic compression stages. Swell values are reported for both axisymmetric (3D) and one-dimensional (1D) scenarios. Values of specific volume (v) and relative compaction (C_R) are reported for the initial state (v_i and C_{Ri}), after back pressure saturation (v_{bps} and C_{Rbps}), and after compression (v_{con} and C_{Rcon}). Values of mean effective stress (p') achieved during testing are compared with target values.

Test ID	B (%)	$S_{\%}$ (%)		v			C_R (%)			p' After Consolidation		
		1D	3D	v_I	v_{BPS}	v_{Con}	C_{RI}	C_{BPS}	C_{con}	Target	Actual	$\Delta p'$
6.7mm - 50kPa	97.8	1.8	3.0	1.60	1.68	1.64	95.4	91.6	93.9	50	49.4	0.6
6.7mm - 100kPa	98.6	1.9	3.2	1.60	1.69	1.58	96.5	90.9	97.1	100	97.6	2.4
6.7mm - 200kPa	99.2	1.7	2.8	1.63	1.70	1.51	96.6	90.2	103.9	200	187.6	12.4
19mm - 50kPa	98.7	2.1	3.4	1.52	1.60	1.56	95.6	90.5	92.7	50	47.9	2.2
19mm - 100kPa	98.9	2.0	3.2	1.52	1.60	1.51	95.4	90.4	95.9	100	95.9	4.1
19mm - 200kPa	98.4	1.8	2.9	1.53	1.61	1.44	94.8	90.1	100.6	200	191.2	8.8

5.4.5 Isotropic Consolidation

Isotropic consolidation is the process of pore water leaving the soil matrix due to an change in the state of stress; in this case the increase of σ_r to higher levels of p'. For each stage of the isotropic consolidation process the pore pressure dissipated (U_z) was calculated as a function of time, as discussed in Chapter 4. The time to dissipate 50% and 100% (t_{50} and t_{100}, respectively) was used to determine the strain rate used during undrained axisymmetric compression. Using the approach outlined in Head (1998) the hydraulic conductivity (k) and the modulus of volume compressibility (m_v) were calculated (Chapter 3). Table 5.8 outlines the pertinent parameters calculated from isotropic consolidation data for the final level of p' applied to each respective specimen.

Time rate of isotropic consolidation graphs are presented in Figure 5.9, displaying the percent dissipation of Δu (U_z) versus time (t). As discussed in Section 4.2.5.4 a constant strain rate of approximately 20% ε_a per day (1.39E-2% per minute) corresponding to a displacement rate of approximately 91.4 mm per day (6.35E-2 mm per minute), depending on the final specimen height, was applied for all specimens. The maximum allowable strain rate for each specimen was determined from consolidation data (Head 1986), displayed in Figure 5.9, and a strain rate less than the maximum allowable calculated rate was applied for all specimens.

Table 5.8 Isotropic consolidation parameters including the coefficient of consolidation (c_v), the modulus of volume compressibility (m_v) and the hydraulic conductivity (k) for the final stage of isotropic consolidation experienced by each specimen

Test ID	Final Taget p' (kPa)	c_v (m^2/yr)			m_v (m^2/MN)			k (m/s)		
		20-50 kPa	50-100 kPa	100-200 kPa	20-50 kPa	50-100 kPa	100-200 kPa	20-50 kPa	50-100 kPa	100-200 kPa
6.7-mm - 50kPa	50	842			0.571			1.49E-09		
6.7-mm - 100kPa	100	1133	73		0.250	0.649		8.77E-10	1.47E-10	
6.7-mm - 200kPa	200	801	89	13	0.991	0.565	0.375	2.46E-09	1.57E-10	1.52E-11
19.0-mm - 50kPa	50	53			0.568			9.34E-11		
19.0-mm - 100kPa	100	27	33		0.229	0.598		1.95E-11	6.13E-11	
19.0-mm - 200kPa	200	63	26	–	0.435	0.503	0.365	8.53E-11	4.07E-11	–

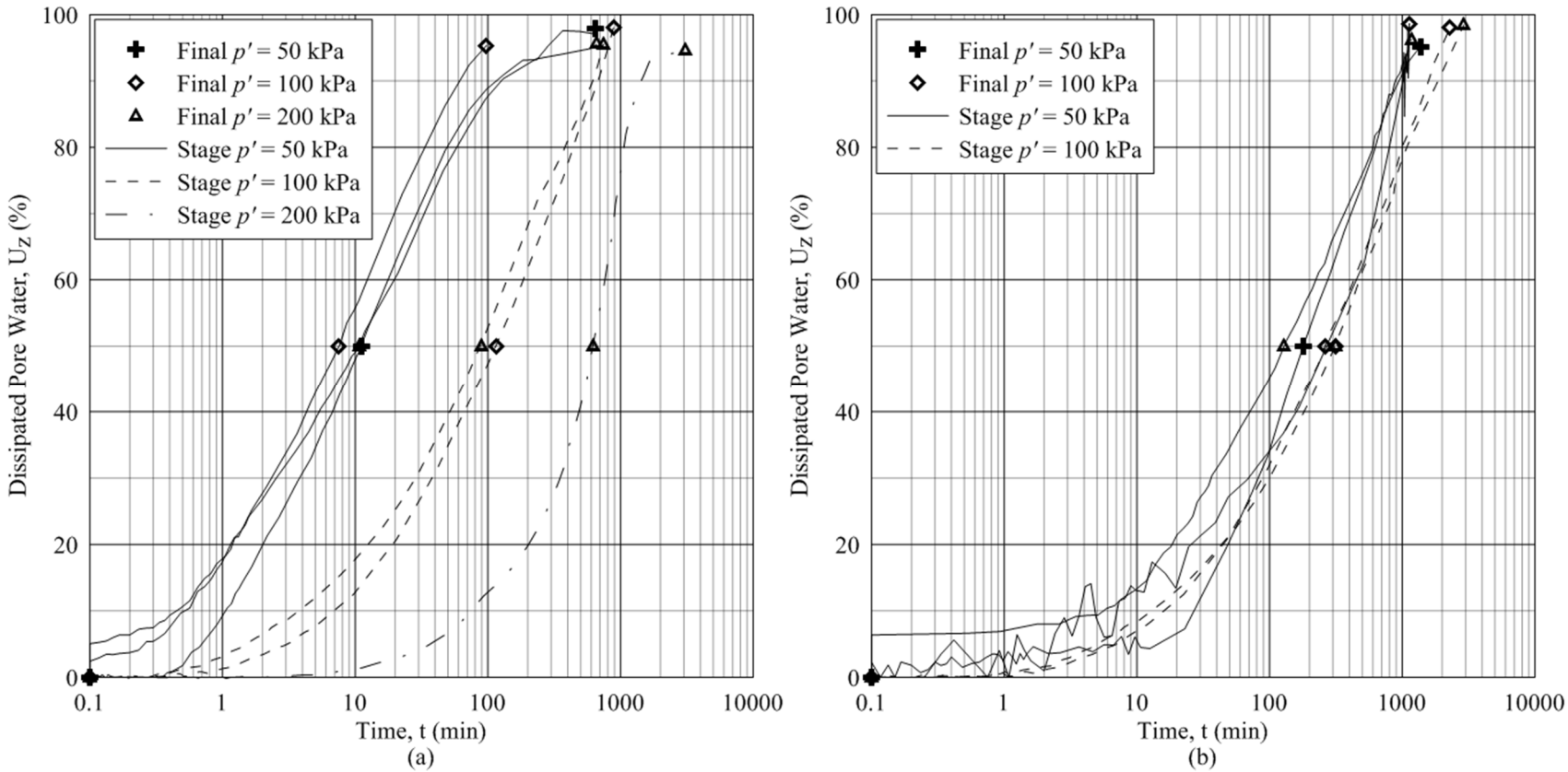

Figure 5.9 Time rate of consolidation graphs recorded during the isotropic consolidation process. Individual expansive soil-rubber specimens are indicated by the cross, diamond or triangle simple and different states of each test are indicated by different line types in the legend of each plot for (a) 6.7-mm and (b) 19.0-mm expansive soil-rubber specimen.

5.4.6 Undrained Monotonic Loading

Undrained axisymmetric compression tests were carried out on isotropically consolidated specimens with a p' range of approximately 50 to 200 kPa. Each specimen was subjected to strain controlled, undrained compressive loading until ε_a was approximately 30%, which corresponds to the limits of the apparatus. Figures 5.9 through 5.12 include the static, monotonic, isotropically consolidated, undrained response of (a) 6.7-mm and (b) 19.0-mm ESR mixtures. Figure 5.10 presents the variation in deviatoric stress (q) versus axial strain (ε_a). Figure 5.11 presents the variation in pore water pressure change (Δu) versus axial strain (ε_a). Figure 5.12 presents the variation in deviatoric stress (q) versus mean effective stress (p'). Figure 5.13 presents the variation in Skempton's Pore Water Pressure Coefficient (A) versus axial strain (ε_a). Three points are indicated on each plot: one point at the initial stress state, one point at M_p (the maximum q/p' ratio), and one point upon reaching critical state or the termination of the test.

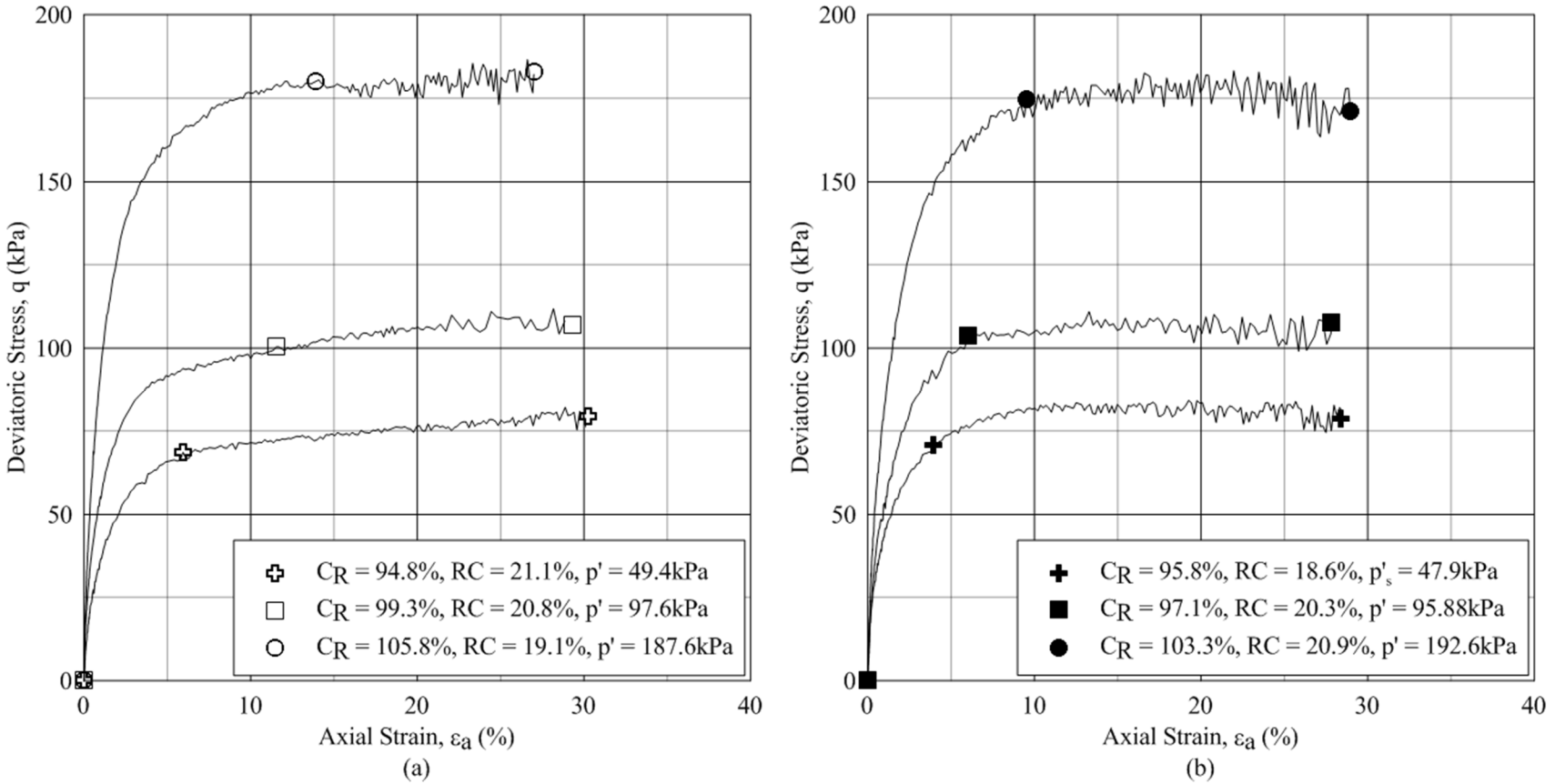

Figure 5.10 Static, monotonic, isotropically consolidated, undrained shearing data for expansive soil-rubber (ESR) mixtures. Variations in q are plotted versus ε_a for (a) 6.7-mm ESR mixtures and (b) 19.0-mm ESR mixtures. Specimen states C_R and p' represent the specimen state at the end of isotropic compression as indicated in the legend. The three specimen states indicated include: initial, the maximum q/p' ratio and the termination of the test or critical state.

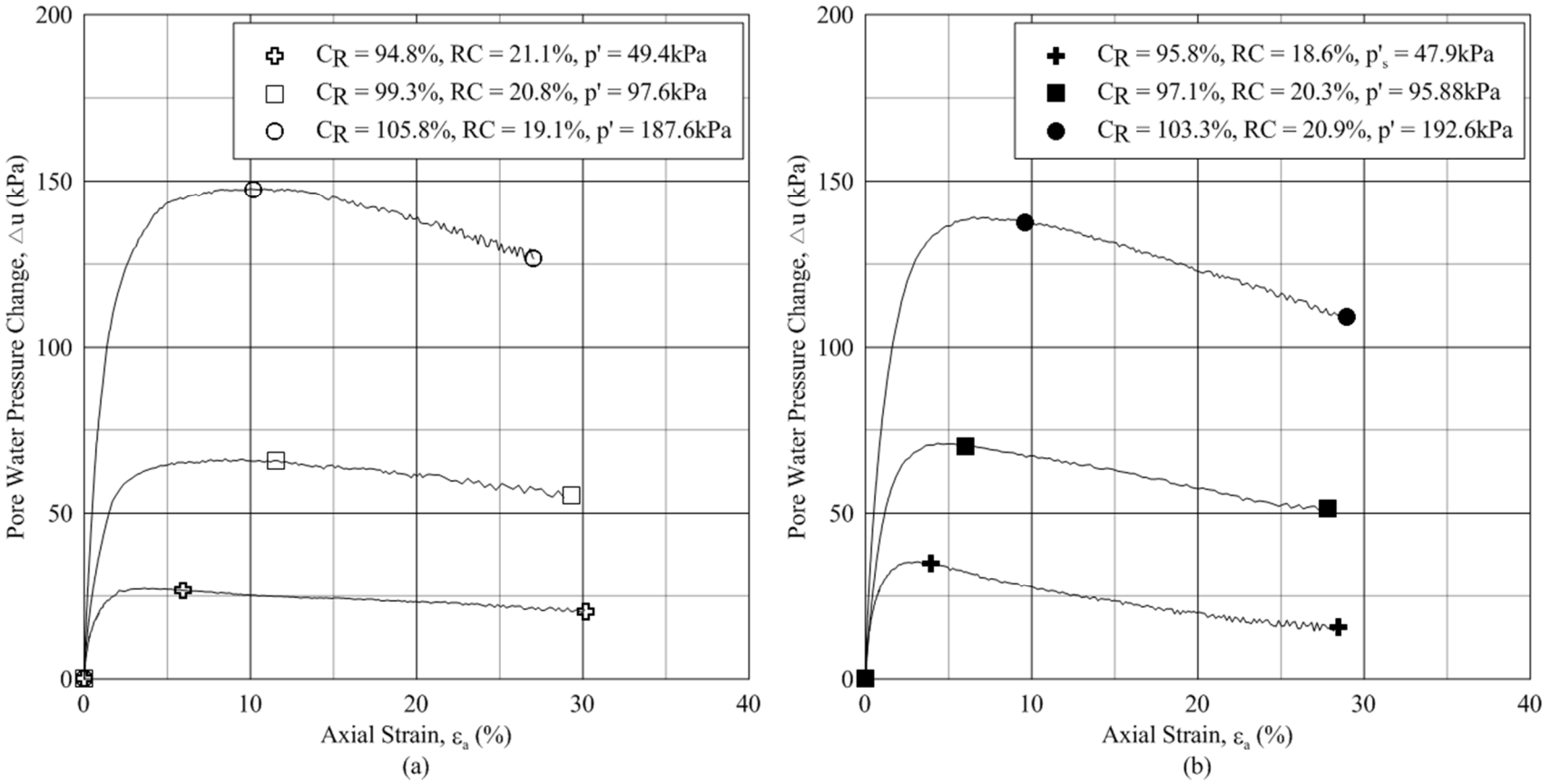

Figure 5.11 Static, monotonic, isotropically consolidated, undrained shearing data for expansive soil-rubber (ESR) mixtures. Variations in Δu are plotted versus ε_a for (a) 6.7-mm ESR mixtures and (b) 19.0-mm ESR mixtures. Specimen states C_R and p' represent the specimen state at the end of isotropic compression as indicated in the legend. The three specimen states indicated include: initial, the maximum q/p' ratio and the termination of the test or critical state.

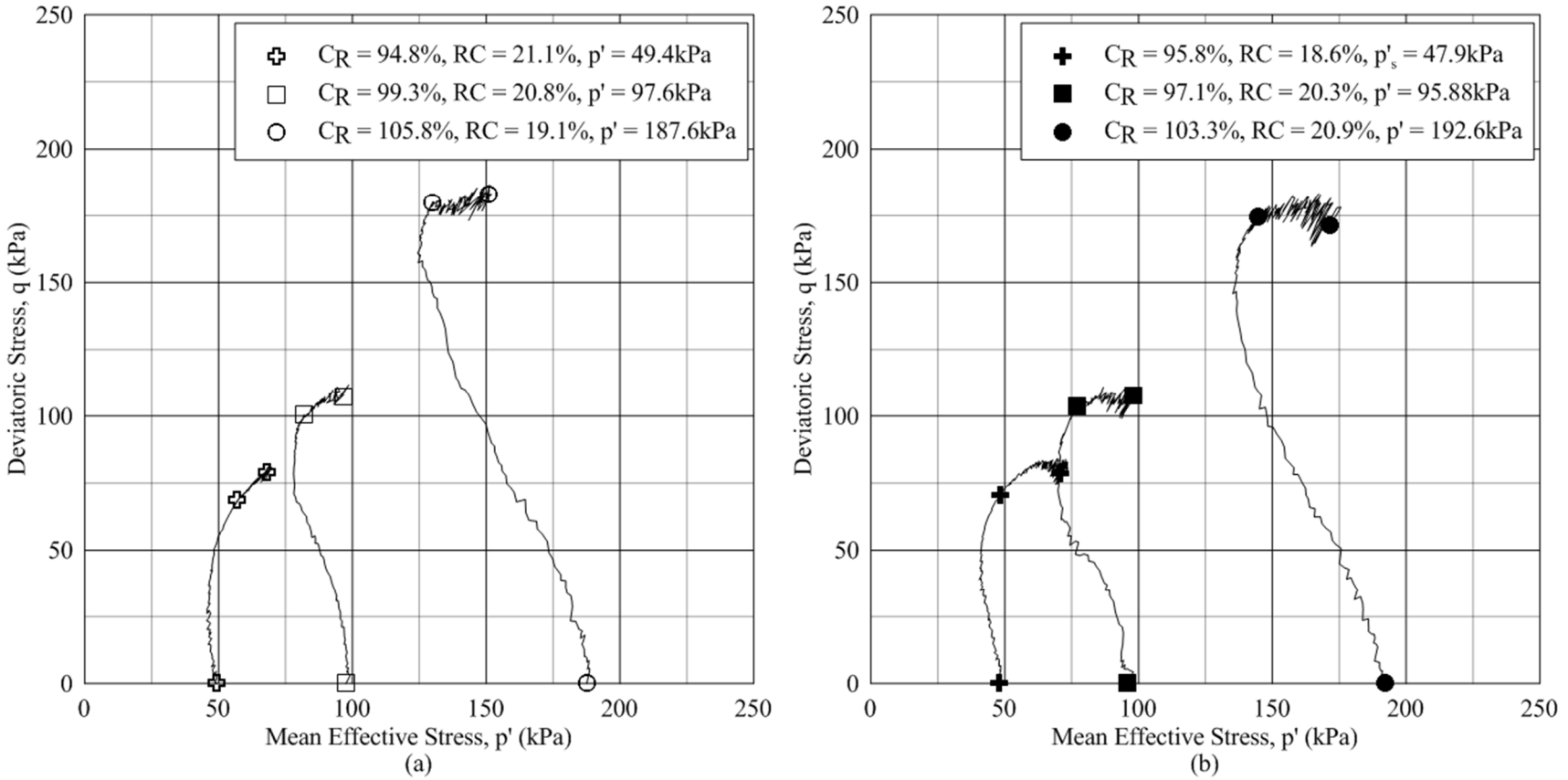

Figure 5.12 Static, monotonic, isotropically consolidated, undrained shearing data for expansive soil-rubber (ESR) mixtures. Variations in q are plotted versus p' for (a) 6.7-mm ESR mixtures and (b) 19.0-mm ESR mixtures. Specimen states C_R and p' represent the specimen state at the end of isotropic compression as indicated in the legend. The three specimen states indicated include: initial, the maximum q/p' ratio and the termination of the test or critical state.

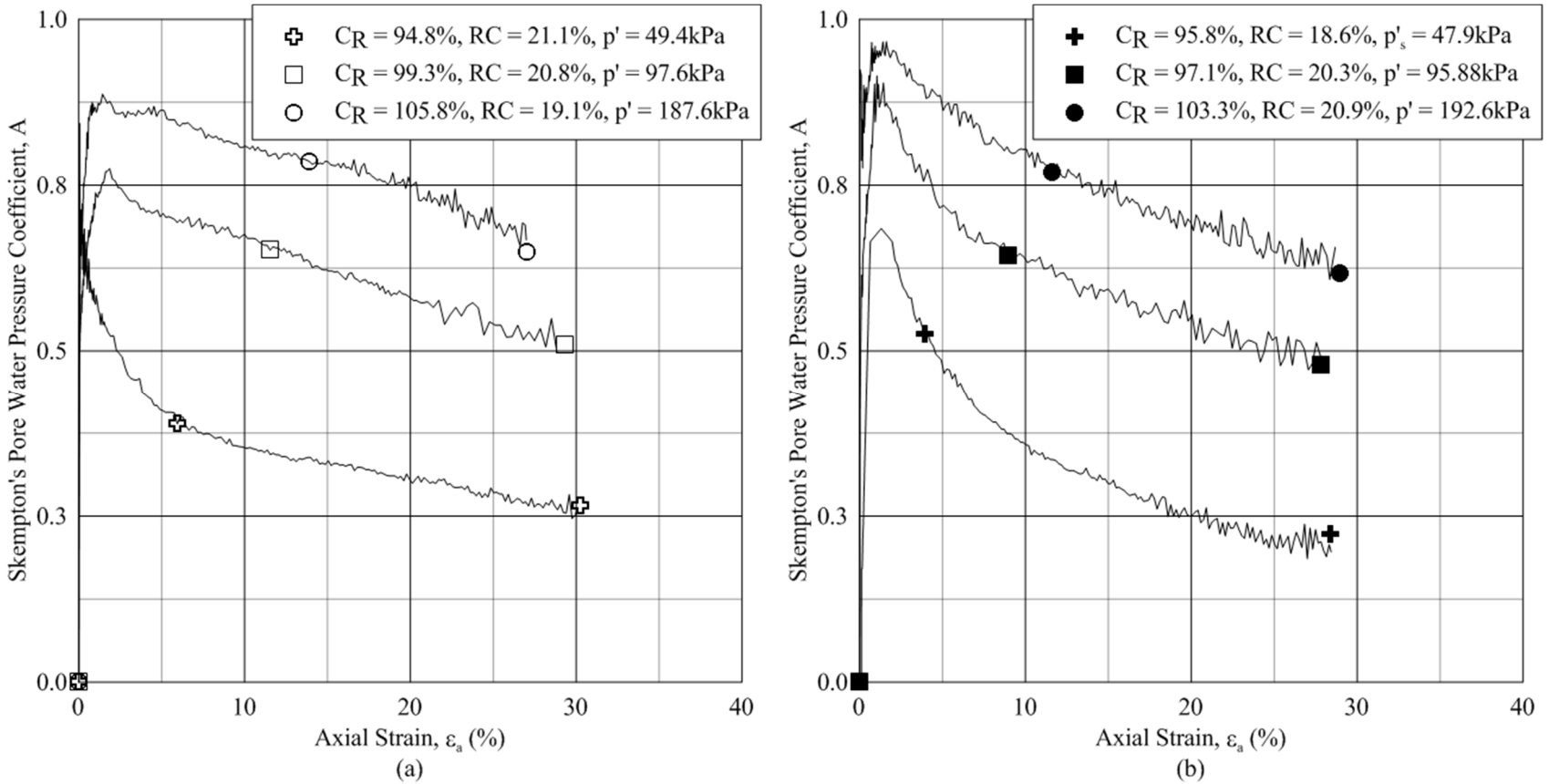

Figure 5.13 Static, monotonic, isotropically consolidated, undrained shearing data for expansive soil-rubber (ESR) mixtures. Variations in A are plotted versus ε_a for (a) 6.7-mm ESR mixtures and (b) 19.0-mm ESR mixtures. Specimen states C_R and p' represent the specimen state at the end of isotropic compression as indicated in the legend. The three specimen states indicated include: initial, the maximum q/p' ratio and the termination of the test or critical state.

Summary results from undrained axisymmetric compression testing can be viewed in Table 5.9, where peak and critical state parameters are listed. Parameters of interest including q, Δu, p', and A are included at the point of maximum q/p' (Mp *or* Δu_{max}) and at critical state (as indicated in Figures 5.9 through 5.12). Maximum ratios of q/p' correlated well with the location of Δu_{max} and generally occurs approximately 1 to 2% ε_a after Δu_{max} is obtained and specimens indicate a tendency toward dilative behavior. The subscripts p and cs represent peak and critical state, respectively. The critical state friction angle, ϕ_{cs}, was determined for each specimen utilizing equation 3.17. A more rigorous approach of determining ϕ_{cs} from the three specimens axisymmetrically compressed under undrained conditions utilizing equation 3.32 is provided in Chapter 6. A complete critical state analysis will be provided in Chapter 6, where the raw data presented in Figures 5.9 through 5.12 is manipulated into the critical state framework.

Table 5.9 Results for axisymmetric compression testing including both peak and critical state friction angles (ϕ_p and ϕ_{cs}), a summary of measured parameters at the maximum q/p' ratio (ε_{ap}, q_p, Δu_p, p'_p, A_p) and a summary of measured parameters at critical state (ε_{acs}, q_{cs}, Δu_{cs}, p'_{cs}, A_{cs})

Test ID	ϕ_p	ϕ_{cs}	ε_{ap} (%)	q_p (kPa)	Δu_p (kPa)	p'_p (kPa)	A_p	ε_{acs} (%)	q_{cs} (kPa)	Δu_{cs} (kPa)	p'_{cs} (kPa)	A_{cs}
6.7mm - 50kPa	36.7	35.3	5.9	69	27	57	0.38	30.2	79	20	68	0.27
6.7mm - 100kPa	36.2	33.8	11.5	100	65	82	0.65	29.3	107	55	97	0.51
6.7mm - 200kPa	37.7	32.3	10.2	180	127	151	0.79	27.1	183	127	151	0.65
19mm - 50kPa	44.7	32.8	3.9	71	35	71	0.53	28.4	79	16	79	0.22
19mm - 100kPa	40.0	31.8	6.0	104	70	77	0.64	27.8	108	52	77	0.48
19mm - 200kPa	37.1	31.2	9.6	175	137	144	0.77	29.0	171	109	171	0.62

CHAPTER 6: ANALYSIS OF RESULTS

6.1 Specimen Uniformity

An important aspect of testing performed throughout this research was the ability to create homogeneous compacted ESR specimens with small variations in the initial state parameters C_R, w, and RC. As discussed in Chapter 4, C_R was controlled by employing multiple lifts for each specimen imposing small fine tolerances for target lift thicknesses employed during compaction. The w and RC parameters were controlled by mixing layers with appropriate amounts of expansive soil, STR, and water thoroughly and separately and allowing specimen layers to cure for a minimum of 24 h prior to compaction in a constant-humidity room with relative humidity equal to about 75.9% (±0.1%). The results of the uniformity study were described in Chapter 5. Table 5.1 presents a basic statistical analysis of C_R, w, and RC for the six specimen layers or lifts of two ESR specimens.

As shown, the two ESR specimens tested were relatively uniform in terms C_R, w, and RC variations among the various lifts. The coefficient of variation for the three state parameters was highest for w and RC in 6.7-mm and 19.0-mm ESR specimens, respectively. The two specimens subjected to uniformity analysis were relatively close to target parameters, especially when comparisons are made to initial state parameters provided by other studies on compacted ESR specimens (Dunham-Friel 2009, Wiechert 2011) which have shown layer coefficients of variation in C_R, w and RC as high as 5.1, 4.0, and 2.5%, respectively. Given the information provided in Table 5.1 it is reasonable to assume that specimens tested are acceptably uniform.

Layer uniformity was conducted for LSTX specimens only due to the greater number of compaction lifts and a more complicated compaction procedure used for LSTX specimens where a split-mold was removed upon compaction completion. Therefore, it is reasonable to assume that specimens tested in one-dimensional compression were more uniform in comparison to specimens tested in LSTX axisymmetric compression.

6.2 One-Dimensional Swell-Compression

As discussed previously, one-dimensional swell-compression testing was conducted in the laboratory on two specimen sizes (SSC and LSC). Swell was also monitored in field plots (FSSM). The following sections discuss the effects of initial state parameters, nominal rubber particle diameter (d_R) and specimen cross sectional area on swell and compression responses of expansive soil and ESR mixtures in one-dimensional swell-compression.

6.2.1 Effect of Initial State Parameters on Swell Response

Previous research has indicated that initial state parameters C_R, w and RC affect the swell response of ESR mixtures (Seda et al. 2007, Dunham-Friel 2009, and Weichert 2011). In general, as C_R increases and w and RC decrease, the overall matrix swell potential increases. As C_R increases, the density of the soil matrix in the ESR mixture increases accordingly. As w decreases in an ESR mixture, soil suction and thus the potential for expansion increases. As RC decreases in an ESR mixture, the volume occupied by rubber is replaced by expansive soil, increasing the overall swell potential of the mixture.

The following sections will discuss general trends in swell percent ($S_{\%}$) as a function of changes in the initial state parameters C_R, w and RC as well as changes in swell pressure (σ'_{zs}) due to the same state parameters in SSC, LSC and FSSM tests.

6.2.1.1 Small-Scale One-Dimensional Swell-Compression

As presented in Chapter 5, deviations in C_R, w and RC between target and actual state parameters for small-scale one-dimensional swell-compression testing were within the corresponding designated ranges. In almost all cases, deviations in C_R, w and RC were within a range of ±1%. In the majority of cases, deviations were within a range of ±0.5% about the target value. Therefore, the effects of initial state parameters on swelling parameters, specifically $S_{\%}$ and σ'_{zs}, are discussed in this section.

In general, Pierre shale residual soil without rubber inclusion was easiest to compact and had smaller deviations in target C_R in comparison to ESR mixtures. As RC increased, so did the rebound or volume expansion after the removal of static loads used during compaction. Therefore, ESR specimens were typically compacted to a slightly denser state to account for volume increase upon removal of compaction loads. Larger variations in C_R with STR addition potentially affected results by increasing or decreasing overall swell response due to deviations from target C_R values. A slightly larger w was typically used for each specimen layer mixture prior to curing to account for moisture loss during curing and compacting. The difference between target and measured w values is likely due to a misestimate in the additional w needed to account for w losses during curing and compaction. Finally, RC values for both 10 and 20% ESR

specimens produced similar levels of accuracy when comparing deviations of target and actual values.

Figures 6.1 through 6.9 display typical trends in swell percent and swell pressure with variations of the initial state parameters C_R, w and RC. As a general trend, both $S_{\%}$ and σ'_{zs} increase as C_R increases and w and RC decrease. The maximum swell percent and swell pressure were realized in samples with highest C_R (100%), lowest RC (0%) and lowest w (2% dry of optimum) and were equal to 9.23% and 279 kPa, respectively. The minimum swell percent and swell pressure were realized in samples with lowest C_R (90%), highest RC (20%) and highest w (2% wet of optimum) and were equal to 1.10% and 17 kPa, respectively. Figures 6.1, 6.2, and 6.3 display the relative swelling characteristics for SSC testing on Pierre shale expansive soil, 10% 6.7-mm ESR mixtures, and 20% 6.7-mm ESR mixtures, respectively, for variations in C_R. Figures 6.4, 6.5, and 6.6 display the relative swelling characteristics for SSC testing on Pierre shale expansive soil, 10% 6.7-mm ESR mixtures, and 20% 6.7-mm ESR mixtures, respectively, for variations in the initial w. Figures 6.7, 6.8, and 6.9 display the relative swelling characteristics for SSC testing on Pierre shale expansive soil, 10% 6.7-mm ESR mixtures, and 20% 6.7-mm ESR mixtures for specimens compacted to 90, 95, and 100% C_R, respectively, for variations in RC.

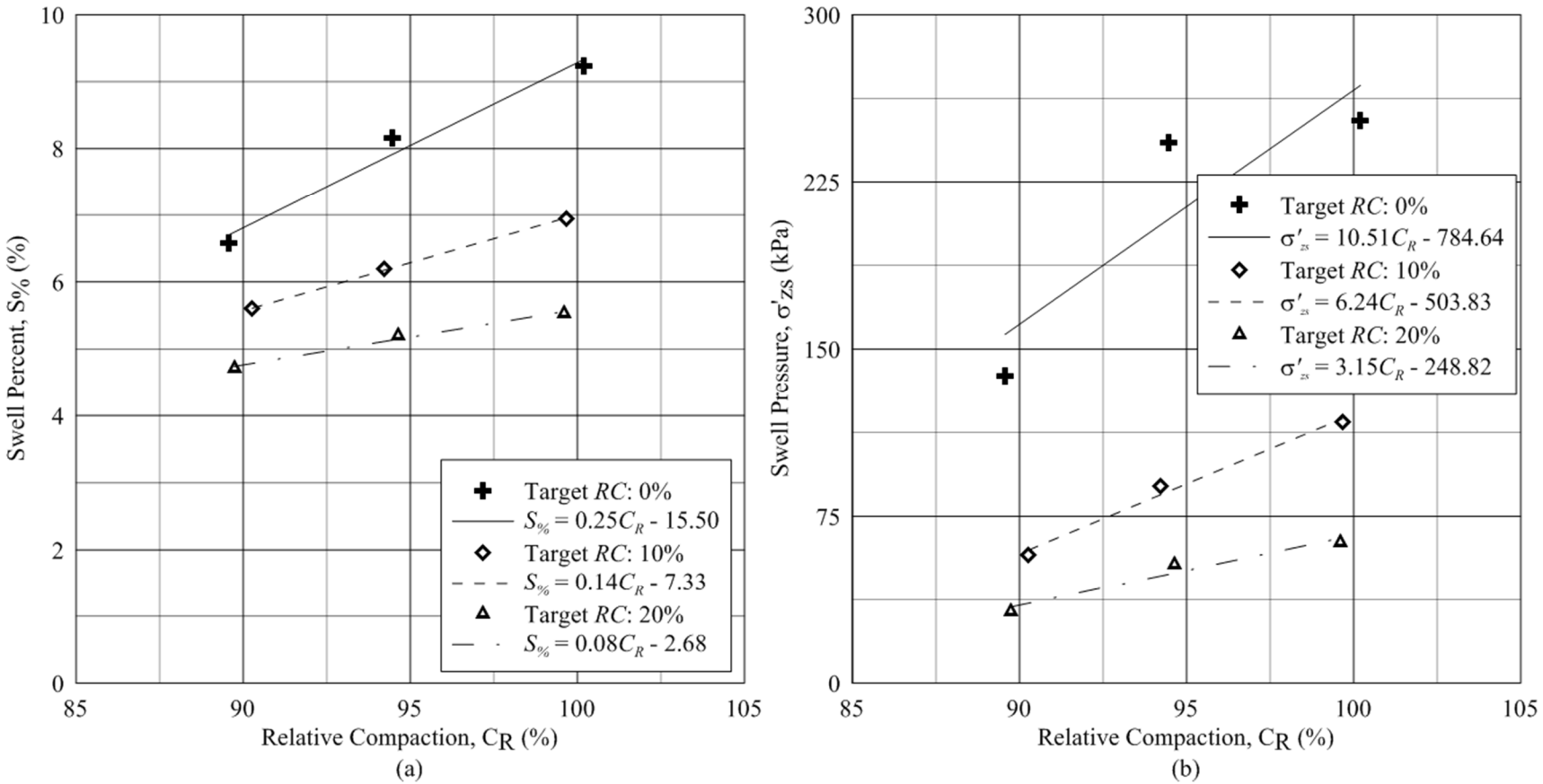

Figure 6.1 Variations in (a) $S_{\%}$ and (b) σ'_{zs} versus the initial C_R for expansive soil-rubber specimens tested at a water content of $w = w_{opt} - 2\%$ in small-scale one-dimensional swell-compression

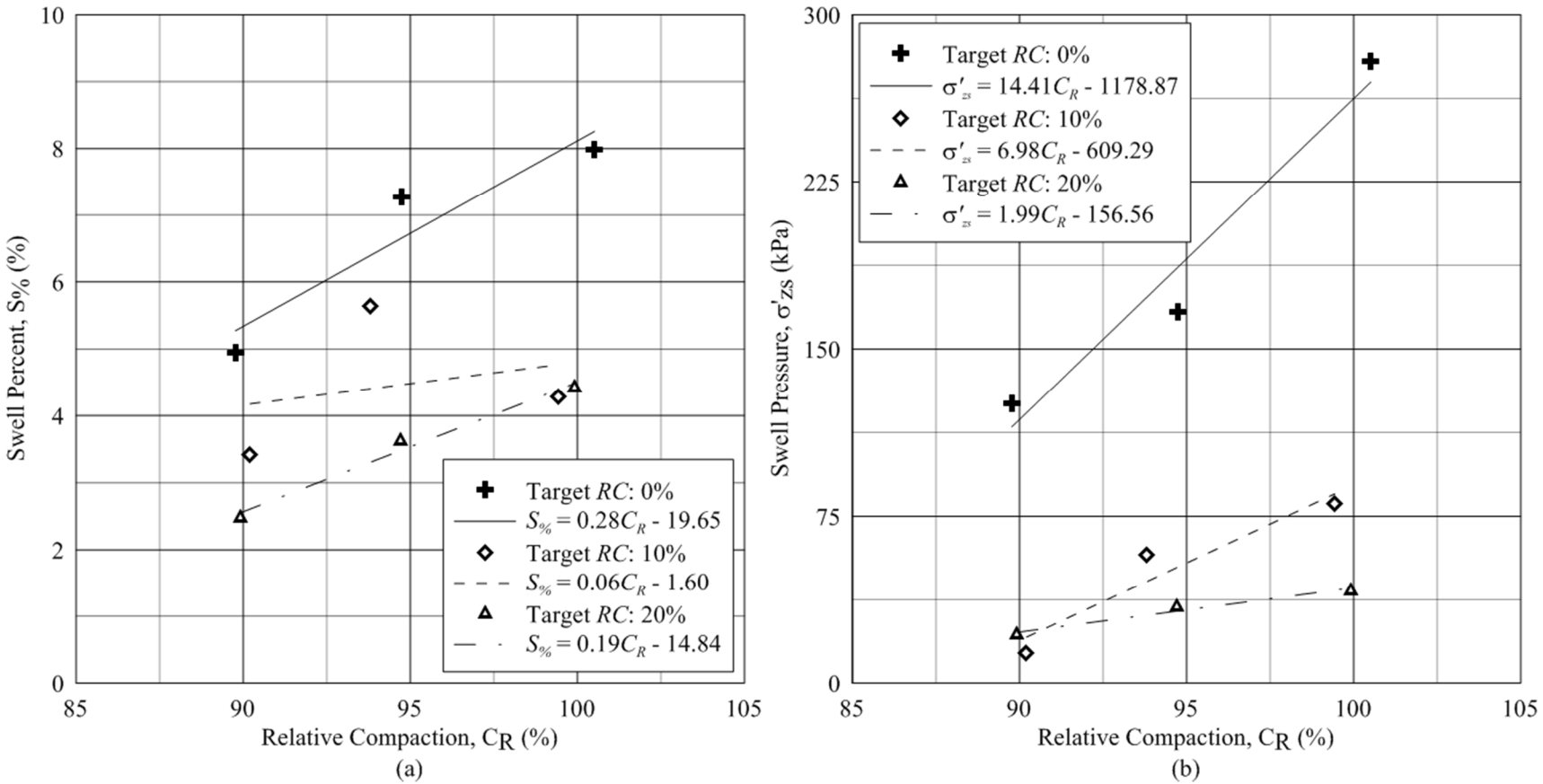

Figure 6.2 Variations in (a) $S_{\%}$ and (b) σ'_{zs} versus the initial C_R for expansive soil-rubber specimens tested at a water content of $w = w_{opt}$ in small-scale one-dimensional swell-compression

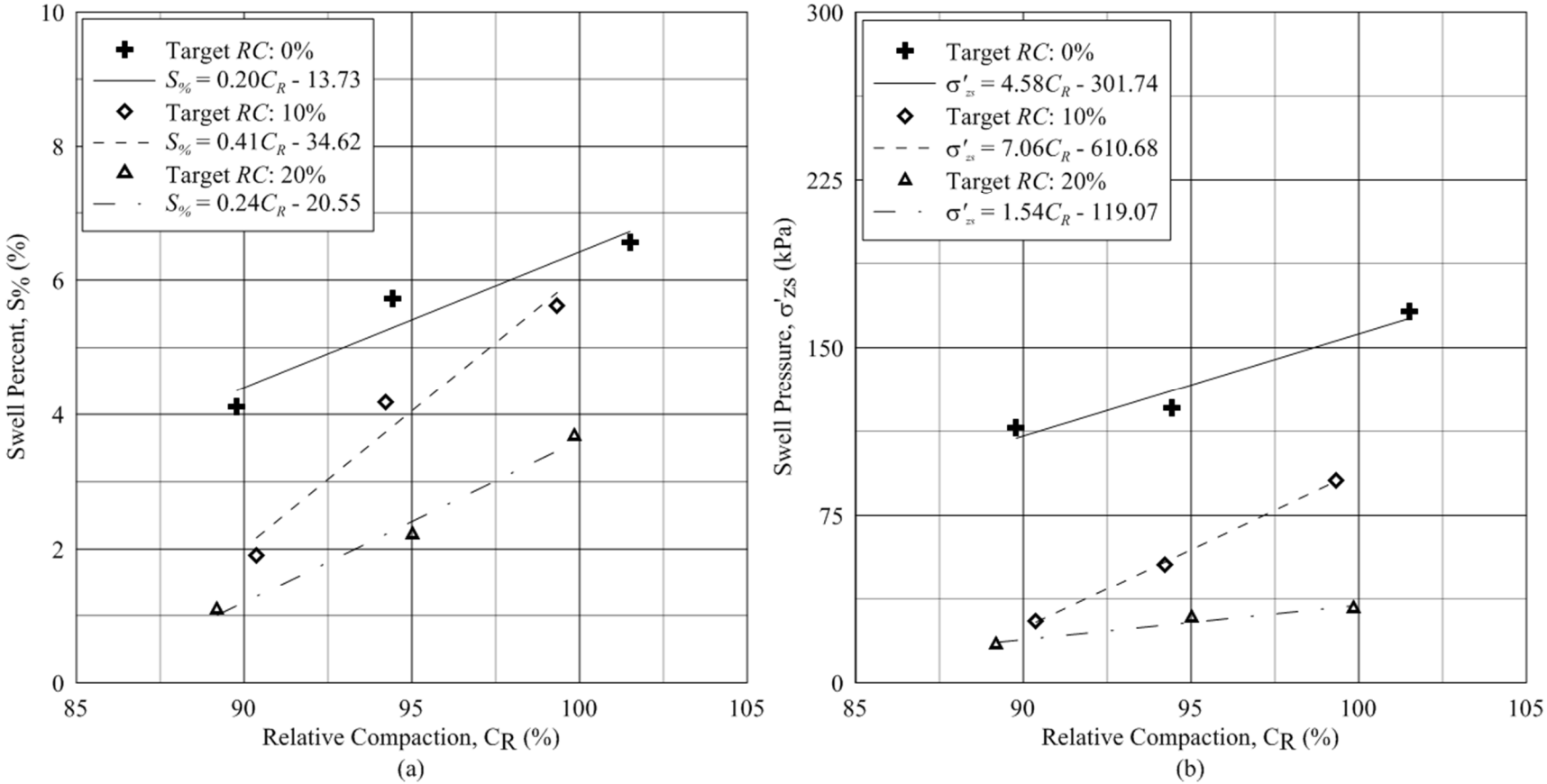

Figure 6.3 Variations in (a) $S_{\%}$ and (b) σ'_{zs} versus the initial C_R for expansive soil-rubber specimens tested at a water content of $w = w_{opt} + 2\%$ in small-scale one-dimensional swell-compression

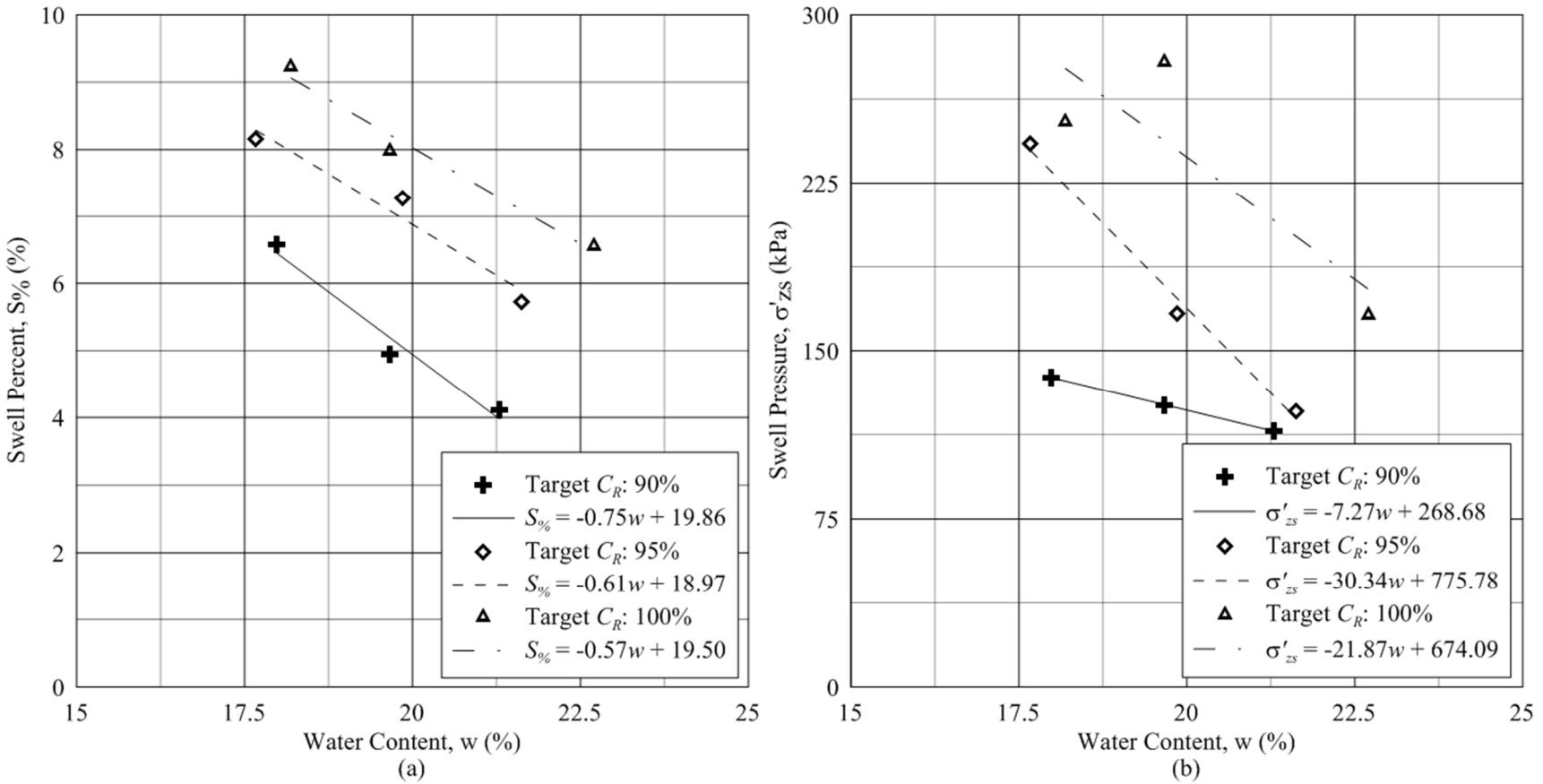

Figure 6.4 Variations in (a) $S_{\%}$ and (b) σ'_{zs} versus the initial w for Pierre shale soil specimens tested in small-scale one-dimensional swell-compression

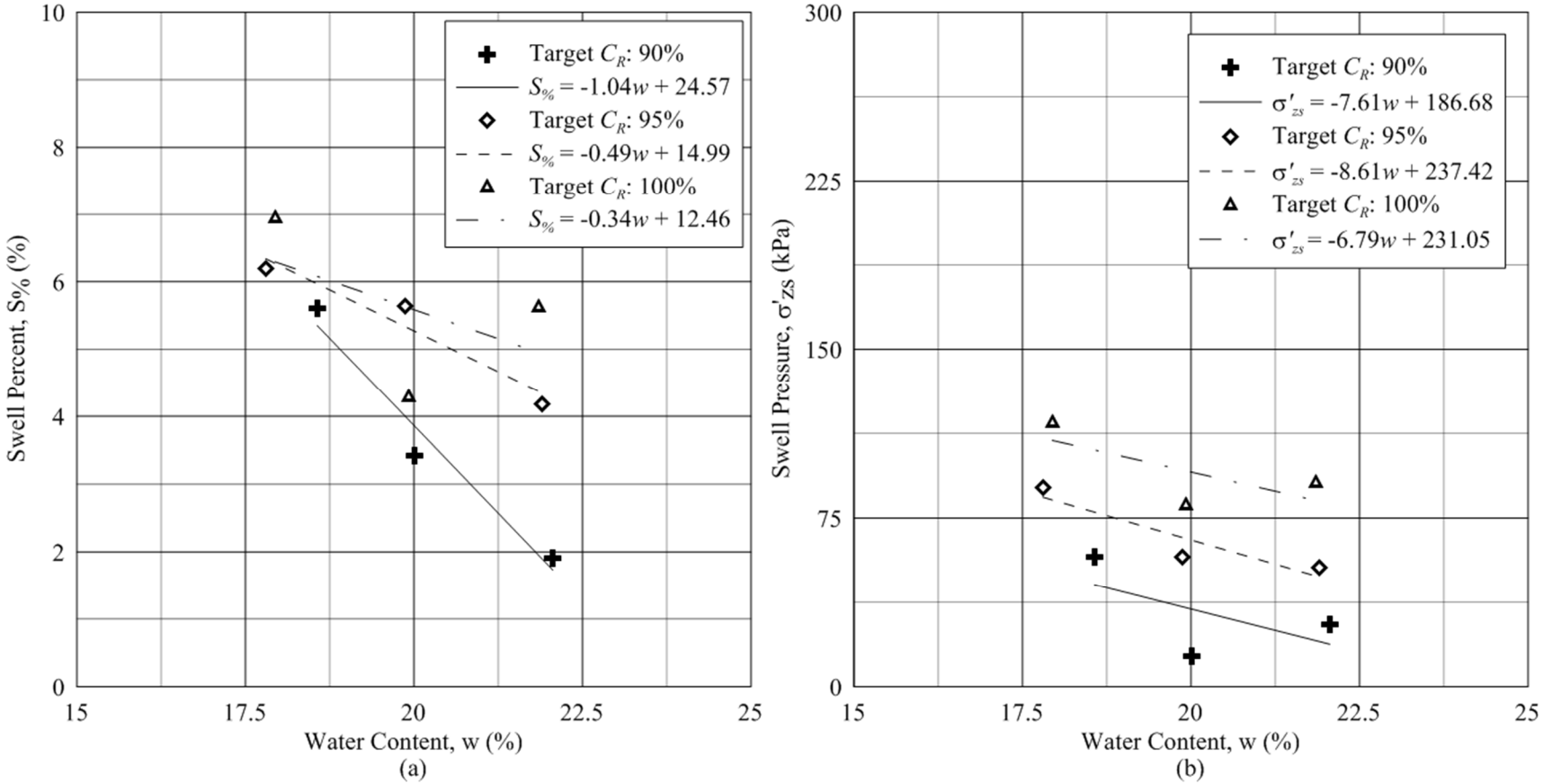

Figure 6.5 Variations in (a) $S_{\%}$ and (b) σ'_{zs} versus the initial w for 6.7-mm expansive soil-rubber specimens with a target rubber content of 10% tested in small-scale one-dimensional swell-compression

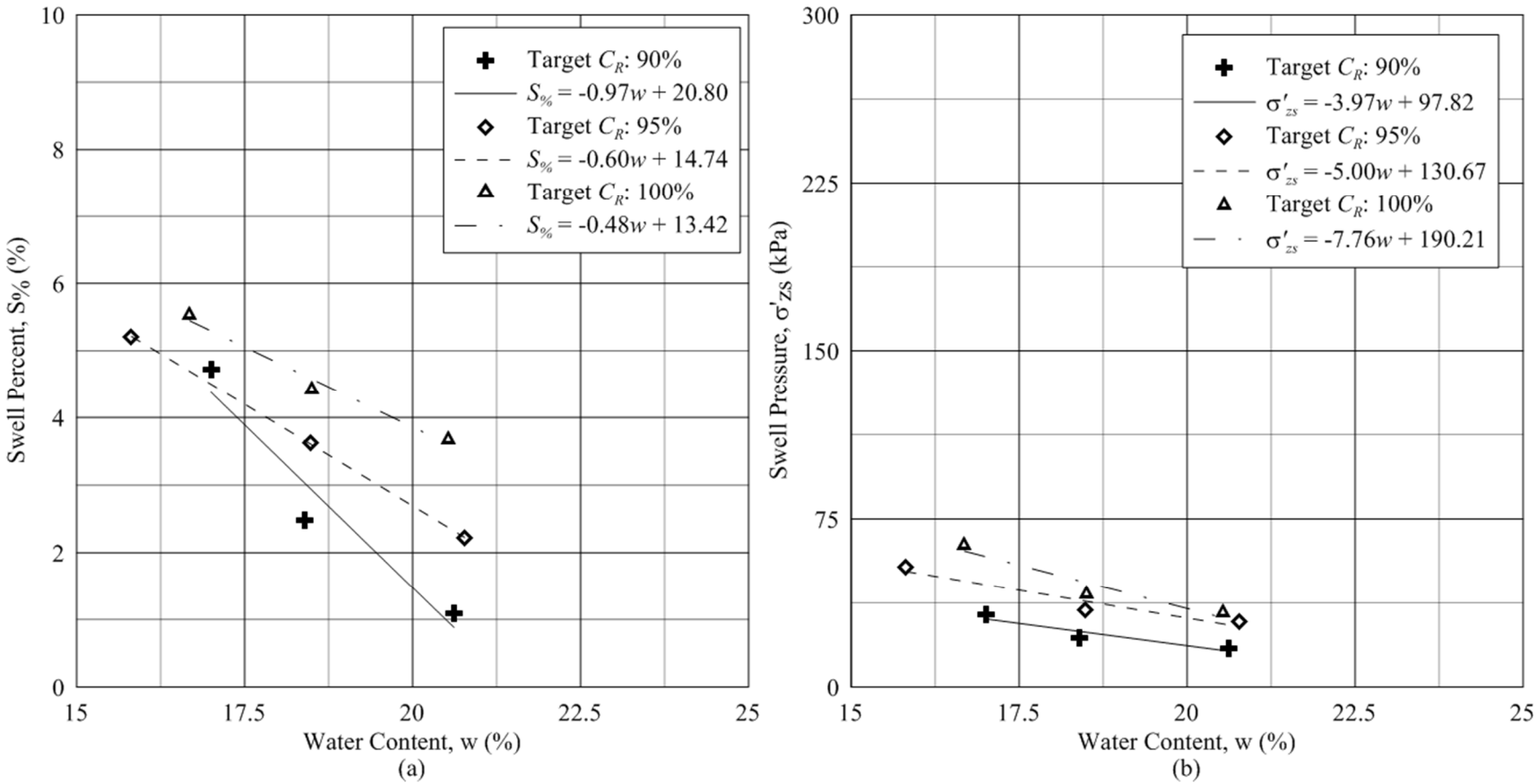

Figure 6.6 Variations in (a) $S_{\%}$ and (b) σ'_{zs} versus the initial w for 6.7-mm expansive soil-rubber specimens with a target rubber content of 20% tested in small-scale one-dimensional swell-compression

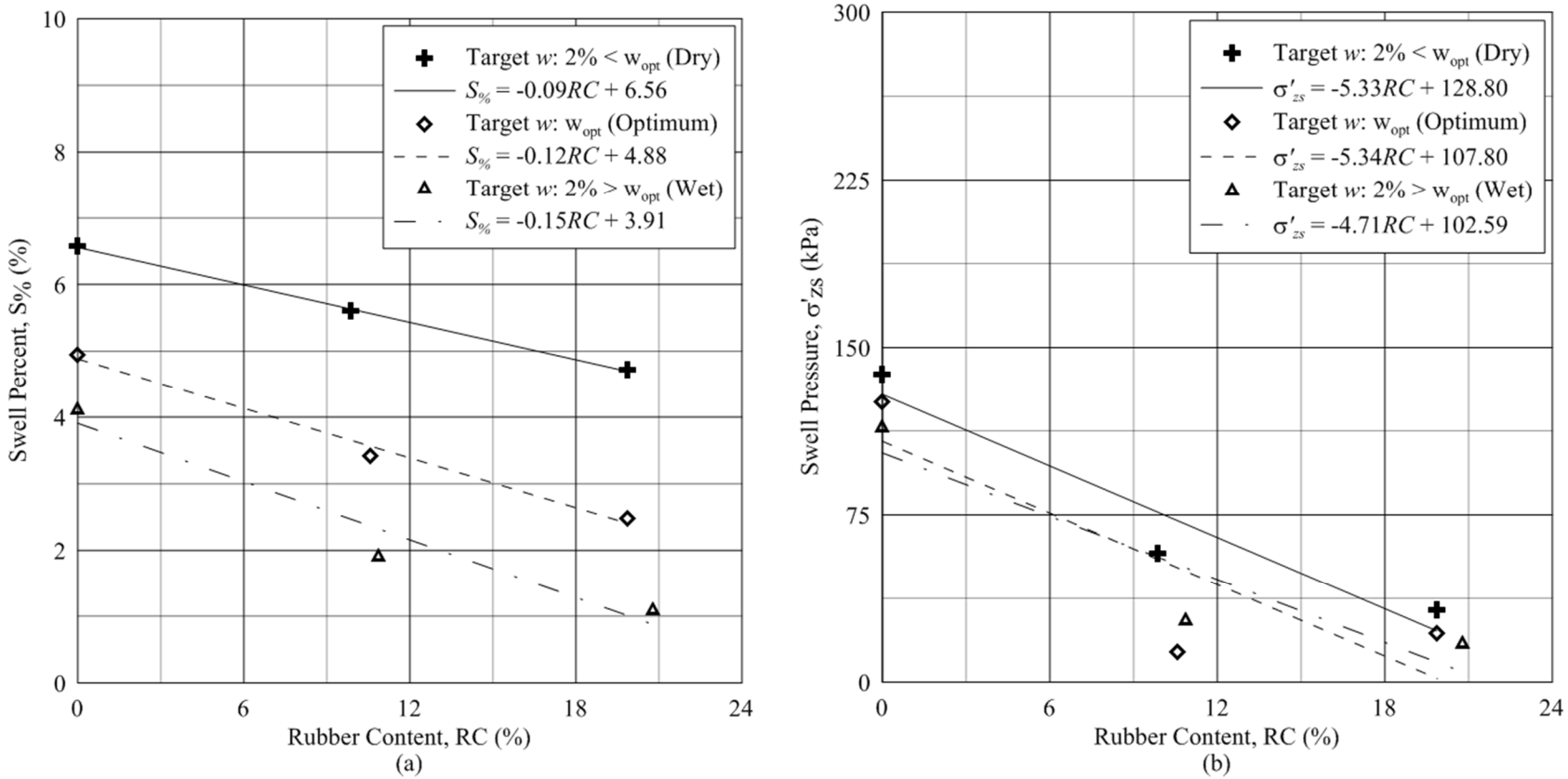

Figure 6.7 Variations in (a) $S_{\%}$ and (b) σ'_{zs} versus RC for expansive soil-rubber specimens with a target relative compaction of 90% and tested in small-scale one-dimensional swell-compression

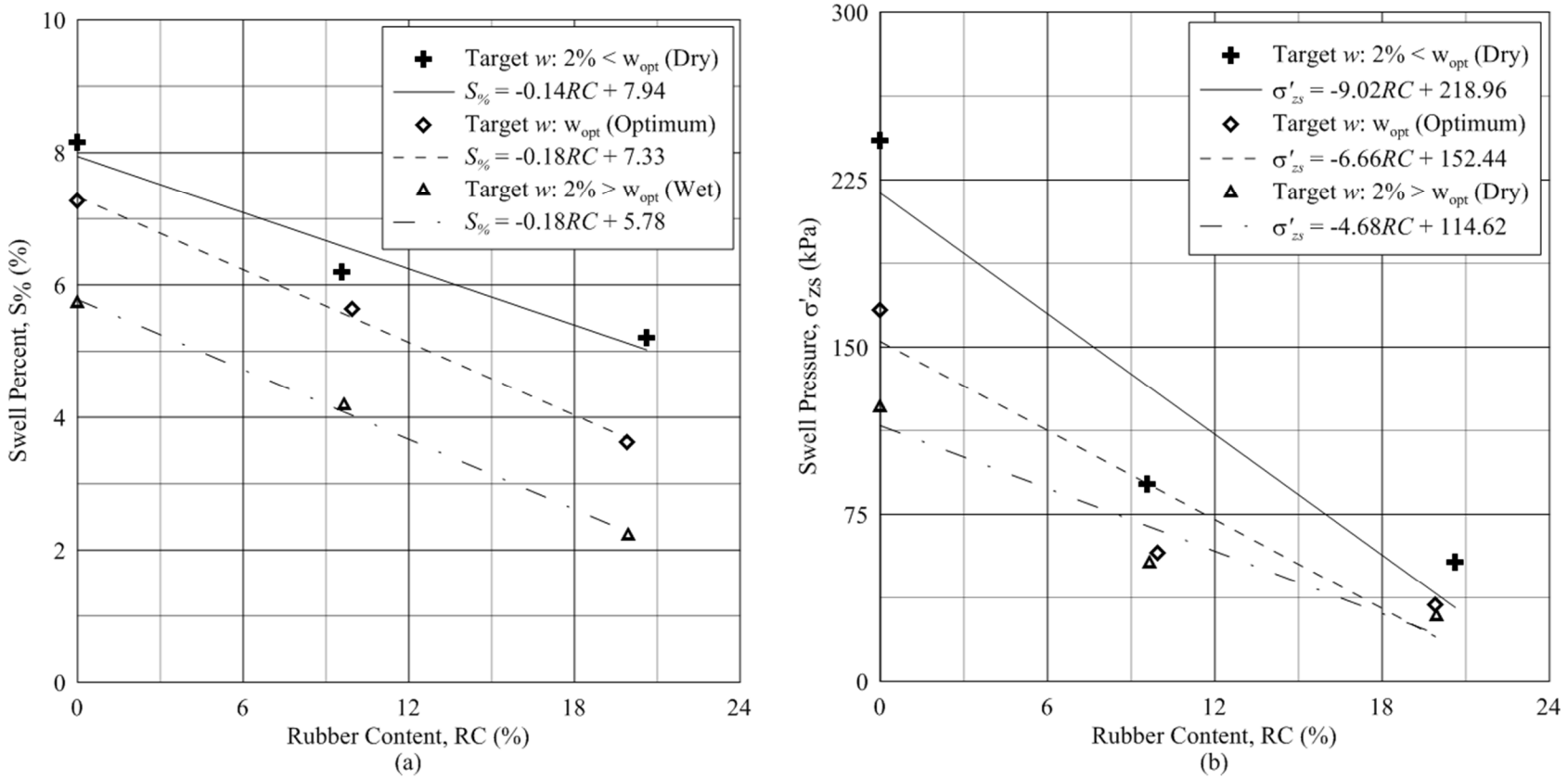

Figure 6.8 Variations in (a) $S_{\%}$ and (b) σ'_{zs} versus RC for expansive soil-rubber specimens with a target relative compaction of 95% and tested in small-scale one-dimensional swell-compression

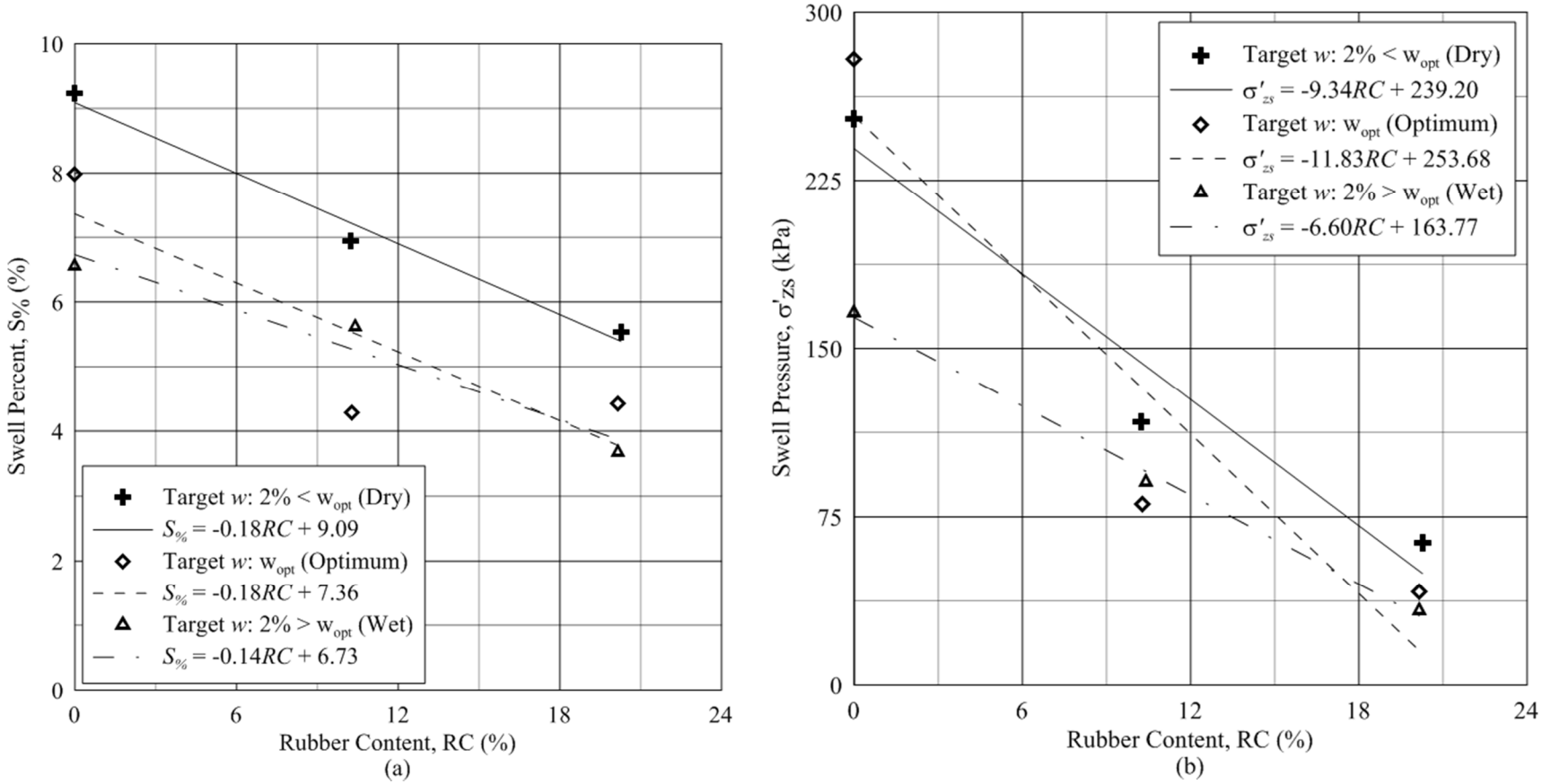

Figure 6.9 Variations in (a) $S_{\%}$ and (b) σ'_{zs} versus RC for expansive soil-rubber specimens with a target relative compaction of 100% and tested in small-scale one-dimensional swell-compression

As shown in Figures 6.1 through 6.9, variations in $S_{\%}$ and σ'_{zs} are most impacted by w, followed by C_R and RC, respectively for similar deviations in each initial state parameter investigated in this study. As discussed previously, systematic deviations investigated for C_R, w and RC were ±5, ±2 and ±10%, respectively. The relative slopes of each trend line presented in Figure 6.1 through 6.9 display the effect each state parameter investigated has on swell response. Linear trend slope averages for each state parameter indicate that $S_{\%}$ deviates by 0.21% as C_R increases, 0.59% as w decreases, and 0.15% as RC decreases by 1%. Linear trend slope averages for each state parameter indicate that $S_{\%}$ deviates by 6.27 kPa as C_R increases, 11.01 kPa as w decreases, and 7.06 kPa as RC decreases by 1%.

The reason for increased swelling with increasing C_R can be attributed to an increase in the amount of expansive material per unit volume for ESR mixtures at similar w and RC, as shown in Table 6.1. As shown the soil matrix density (γ_s) increases by about 1 kN/m$_3$ for increases in C_R from 90 to 95 and 95 to 100% for 6.7-mm and 19.0-mm ESR mixtures of similar RC. The denser soil matrix occurs due to a difference in the level of compaction energy with increasing values of C_R. The soil matrix density is defined as follows:

$$\gamma_s = \frac{W_s}{(V_t - V_r)} \tag{6.1}$$

where W_s indicates the weight of soil, V_r indicates the volume of rubber and V_t indicates the total volume.

Table 6.1 Soil matrix density values for Pierre shale expansive soil and expansive soil-rubber specimens for varying values of *RC* and C_R

Sample Type	*RC* (%)	d_R (mm)	Maximum Dry Unit Weight, γ_{dmax} (kN/m^3)	Soil Matrix Density, γ_s (kN/m^3)		
				90% C_R	95% C_R	100% C_R
Pierre Shale Soil	0	N/A	16.4	14.8	15.6	16.4
10% 6.7-mm ESR	10	6.7	15.0	13.9	14.8	15.7
20% 6.7-mm ESR	20	6.7	14.0	13.0	14.0	15.0
20% 19.0-mm ESR	20	19.0	14.8	13.2	14.1	15.1

The primary reason for the differences in the level of expansion for varying values of *RC* can be attributed to the replacement of expansive material with non-expansive material (scrap tire rubber). A secondary difference in swelling characteristics is due to the difference in the soil matrix density, as shown in Table 6.1. As presented in Section 4.1.5, as *RC* values increase, the maximum dry unit weight of ESR mixtures decreases due to a replacement of expansive material with non-expansive material and a denser soil matrix. The denser soil matrix occurs due to the increased dissipation of compaction energy with increasing and more uniform *RC*.

The differences in swelling characteristics due to variations in the initial water content prior to inundation are attributed to differences in soil suction and the relative propensity for swell. Soil matric suction has an inverse relationship with the water content, increasing with decreasing values of *w*. The total suction of a soil can be derived from two components: matric and osmotic suction (Corey 1994). The matric suction is directly related to capillary pressure forces acting as a result of tensile forces acting between the fluid and solid particle phases. Due to the inundation of specimens with de-ionized and de-aired water the osmotic component of suction can be negated (Fredlund and Raharjdo 1993). In addition to tensile forces, an additional component related to the mineralogical

component of expansive soils contributes to matric potential and propensity for expansion, as discussed in Section 2.2. Matric potential has been studied previously at CSU for a Pierre shale expansive soil with similar particle size and index properties as those presented in Sections 4.1.3 and 4.1.4. The results indicated that the matric potential deviated by more than three orders of magnitude for the range of target water contents explored in this study (Durkee 2000), highlighting the significant difference in subsequent swelling resulting from differences in the initial water content.

A complete discussion of unsaturated soil mechanics and the effect of the matric potential on ESR mixtures were outside of the scope of this study. A more complete characterization of the scrap tire rubber employed in this study including constitutive polymer types and relative matric potentials is necessary fully define the relative effects *RC* and d_R have on swelling potential. However, due to the comparative type analyses performed in this study regarding the initial state parameters a complete characterization of STR matric potential was unnecessary. The reader is directed elsewhere (Nelson and Miller 1992; Fredlund and Raharjdo 1993; Miller 1996; Durkee 2000) for a complete discussion of unsaturated expansive soils.

6.2.1.2 Large-Scale One-Dimensional Swell-Compression

Deviations in C_R, *RC* and *w* between target and actual state parameter values were within a range of ±1% in all cases. Actual C_R, *RC* and *w* values deviated from target values by more than ±0.5% in three specimens, one specimen, and 4 specimens out of the six tested specimens, respectively. Maximum deviations measured for C_R, *w* and *RC* equal to 0.9,

0.8 and 0.4%, respectively. Deviations in the initial state parameters C_R and w were similar for both STR particle sizes investigated. As discussed earlier, the only initial state parameter varied in LSC testing was w. In addition to variations in w, two nominal rubber particle sizes (d_R) were employed at 20% *RC*: 6.7 and 19.0 mm. Discussions presented in this section will therefore be limited to the single level of *RC* and C_R equal to 20 and 95%, respectively, and the three levels of w, and the two d_R investigated.

As shown in Table 5.4 and Figure 6.10, swelling magnitudes and pressures increased with decreasing w. Theoretically, specimens with a lower initial w should swell more due their relatively higher initial soil suction. General trend lines are provided in Figure 6.10 to indicate the relative significance w has on swelling response of ESR mixtures tested. Comparing the trend lines in Figure 6.10, w changes have a more significant impact on swelling parameters for 20% 6.7-mm ESR specimens in comparison to 20% 19.0-mm ESR mixtures. Both ESR specimens tested at lower w values showed more similar values of $S_{\%}$ and σ'_{zs}. From a practical standpoint, the similar swelling characteristics for both d_R would suggest that the use of tire chips is as effective as using granulated rubber for swell mitigation at lower w values around w_{opt}, where swell response is more relevant (which is desirable from an economical point of view as tire chips are less expensive to manufacture in comparison to granulated rubber as discussed in Section 2.5.3). Swell percent increases by 0.68% for 6.7-mm ESR mixtures and 0.41% for 19.0-mm ESR mixtures for each percentage decrease in w. Swell pressure increases by an average of 3.83 kPa for 6.7-mm ESR mixtures and 2.13 kPa for 19.0-mm ESR mixtures for each percentage decrease in w. Maximum swell percent and swell pressure values were 4.72%

and 31 kPa, respectively and were realized in specimens with the lowest w (2% below w_{opt}). Minimum swell percent and swell pressure values were 1.16% and 14 kPa, respectively, and were realized in specimens with the highest w (2% above w_{opt}).

The primary reason for an increase in swell and swell potential with decreases in w is due to the soil matric potential, as discussed in Section 6.2.1.1. The variation of w by ±2% around w_{opt} yields matric potentials varying by more than three orders of magnitude for similar expansive soils (Durkee 2000). Each point indicated in Figure 6.10 indicates the w prior to inundation, with the lower values of w indicating higher matric potentials.

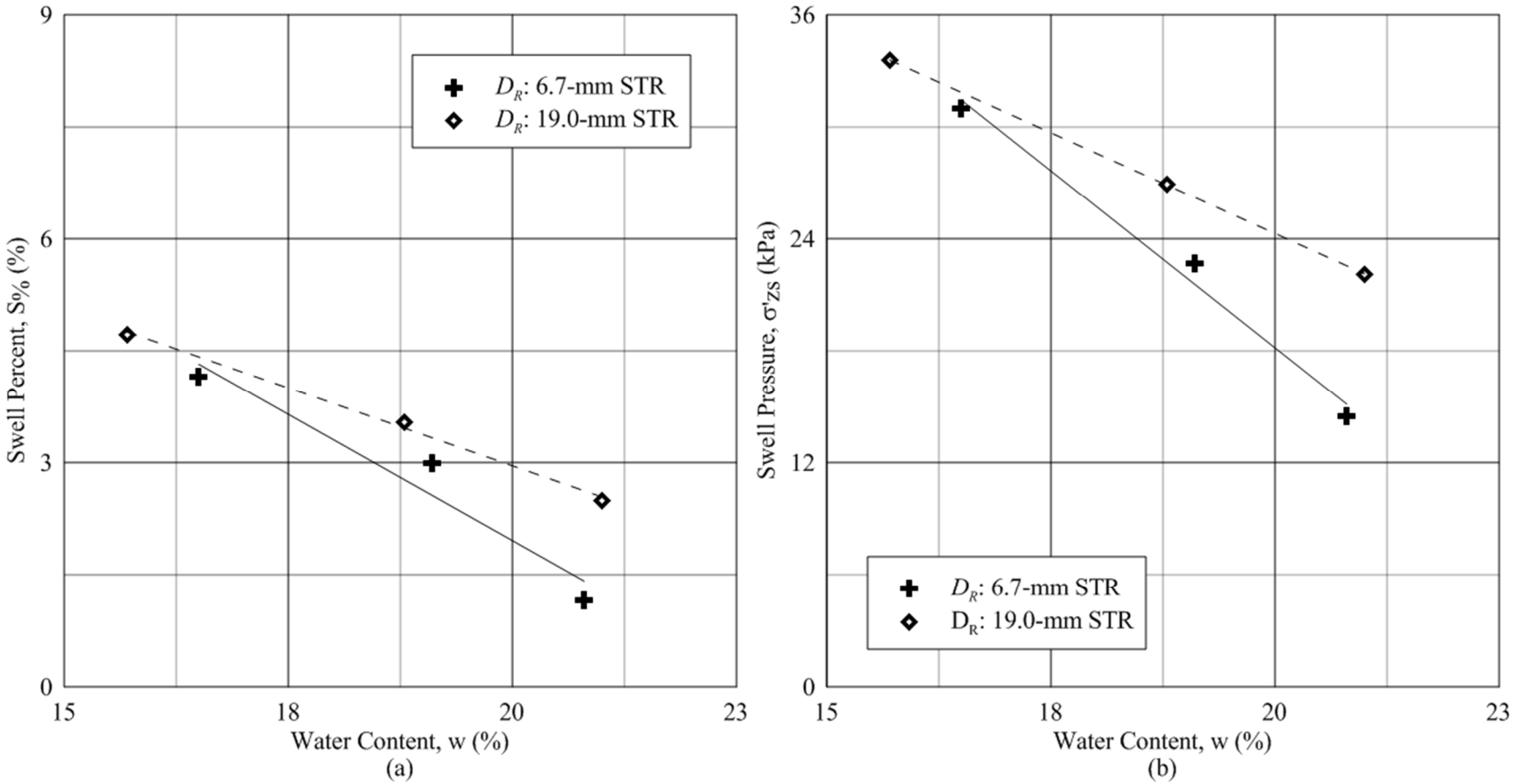

Figure 6.10 Variations in (a) $S_{\%}$ and (b) σ'_{zs} versus the initial w for 6.7- and 19.0-mm expansive soil-rubber specimens with a target rubber content of 20% tested in large-scale one-dimensional swell-compression

6.2.1.3 Field-Scale Swell-Monitoring

Deviations in initial state parameters C_R, w and RC were on average 0.8, 2.4 and 1.1% larger for FSSM in comparison to SSC testing and on average 0.8, 2.6 and 1.0% larger in comparison to LSC testing, respectively. Larger deviations for initial state parameters were accepted for FSSM due to the limited number of initial states investigated, as discussed in Chapter 5. The large deviations in w are likely due to the significant time needed to compact specimens (approximately 1.5 h), and the warm arid conditions under which lifts cured and plots were constructed. Deviations in RC are likely due to heterogeneities throughout each field plot and the potential limited representativeness of sand cone density testing to each ESR field plot in comparison to the washing method used in determining the RC of the entire specimen in SSC, LSC and LSTX specimens. The differences in initial state parameters for the field plots themselves varied substantially. For instance, C_R was highest for the Pierre shale soil field plot and 1.9 and 4% lower for the 19.0-mm and 6.7-mm ESR filed plots in comparison, respectively. Initial w differences were minimal and varied by approximately 0.1% between the three field plots. The 6.7-mm ESR field plot contained an additional 3.1% RC in comparison to the 19.0-mm field plot, likely contributing to increasing swell characteristics. Differences in the initial state parameters likely had an impact on monitored swell for each of the three field plots.

Compaction efforts required to compact the field plots varied significantly. As discussed in Section 4.2.3.3, compaction was performed with a C-433 Caterpillar vibratory single-drum roller providing static compaction energy of 73.4 kN. The total number of roller

passes required to compact the Pierre soil field plot to a C_R value of 94.0% was 16. The total number of roller passes required to compact 6.7- and 19.0-mm ESR filed plots to C_R values of 90.0 and 92.1% was 32 and 33, respectively. The decrease in relative compaction with increasing number of roller passes for ESR filed plots studied was likely due to utilizing an existing concrete pad to compact plots upon and to confine specimen bases during inundation, as discussed in Chapter 4. It was visually observed that utilizing the concrete pad as a rigid subgrade, especially during vibratory compaction, increased dissipation of compaction energy in comparison to a soil subgrade studied prior.

As presented in Table 5.5, $S_{\%}$ deviated by more than 5% for the three field plot types investigated. The maximum swell realized for ESR plots was 31 to 35% of the Pierre shale soil plot for d_R values of 6.7 and 19.0-mm, respectively. The swell percent for both 6.7- and 19.0-mm ESR mixtures was very similar, deviating by 0.3%. As discussed earlier, post-swell compression was not studied in FSSM due to the significant dead load that would be required for the proper determination of σ'_{zs} and compression indices.

The Pierre shale soil plot encountered a greater swell rate post-inundation in comparison to both ESR mixtures. As shown in Figure 5.5 the majority of swelling was realized within the first few hours of testing for the Pierre shale soil plot, while the majority of swell took longer to realize in the ESR plots. Within the first day of testing, 80, 25 and 36% of the total swell was realized in the Pierre shale, 20% 6.7-mm and 20% 19.0-mm ESR field plots, respectively. The shorter timeframe required for maximum swell in the Pierre shale soil field plot is likely due to: (1) an increasing amount of expansive material

in a representative field plot volume causing increased matric suction; (2) plot constraint variations in the interfaces between concrete and soil (Figure 4.6); or (3) differences in the initial state parameters C_R, w and RC.

6.2.2 Compressibility of ESR mixtures in One-Dimensional Compression

Compressibility is an important aspect contributing to the overall mechanical response of specimens tested in one-dimensional compression. Initial state parameter impacts on compressibility are the primary focus of the following discussions. As the initial state parameters C_R and RC increase in ESR mixtures overall matrix compressibility should decrease. As C_R increases more material pore volume is decreased, yielding less potential for compressibility. Individual particles of rubber are less compressible than an equal volume of soil and water, yielding less compressibility (Lee et al. 2010). Trends in E and M with variations in initial state parameters C_R, w and RC and variations in d_R for SSC and LSC testing are discussed in the following sections.

6.2.2.1 Small-Scale One-Dimensional Compression

Compression indices C_c and C_r were presented previously in Table 5.3. The largest variation for C_c was 0.027 and for C_r was 0.040 for similar values of C_R and RC. Both of these relatively large variations occurred in samples with a target C_R of 90% and a target RC of 20%. Assuming that the initial w has little effect on compression indices and that normal compression was obtained during testing, the large variations in C_c and C_r provide evidence of a lower degree in testing accuracy for decreasing C_R and increasing RC. C_c values increased with increasing RC, and were similar for all three levels of w

investigated for each mixture type. Values of C_r increased with increasing *RC*. In general curves followed expected behavior with similar compression and recompression indices for specimens with similar C_R and *RC* values.

Table 6.20 includes volumetric compressibility values m_v and m_{vr} and Table 6.2 includes the constrained and elastic modulus values *M* and *E*, respectively. *M* and m_v provide a direct indication of the stress-strain response during normal compression. *E* and m_{vr} provide a direct indication of the stress-strain response during unloading and recompression. As shown in Table 6.3 *M* and *E* are relatively consistent with variations in initial state parameters C_R and *w*. The largest variation in compressibility due to variations in initial state parameters occurs for elastic modulus results for variations in *RC*.

Table 6.2 Compressibility parameters including the moduli of volume compressibility and recompressibility (m_v and m_{vr}) for 6.7-mm expansive soil-rubber specimens tested in small-scale one-dimensional swell-compression at specified levels of applied vertical effective stress

Initial State Parameters			Compressibility Parameters										
			m_v (1/kPa)								m_{vr} (1/kPa)		
C_R (%)	w (%)	RC (%)	6-12 (kPa)	12-24 (kPa)	24-49 (kPa)	49-98 (kPa)	98-195 (kPa)	195-390 (kPa)	390-781 (kPa)	781-1562(kPa)	1562-781 (kPa)	781-98 (kPa)	98-6 (kPa)
89.6	18.0	N/A	4.77E-02	5.75E-02	6.15E-02	4.70E-02	3.09E-02	1.89E-02	1.13E-02	6.33E-03	9.77E-04	5.54E-03	3.96E-02
89.8	19.7		4.45E-02	5.08E-02	5.00E-02	4.09E-02	3.36E-02	1.97E-02	1.17E-02	6.77E-03	9.49E-04	5.93E-03	4.99E-02
89.8	21.3		3.55E-02	4.27E-02	3.99E-02	3.39E-02	2.92E-02	1.93E-02	1.13E-02	6.52E-03	8.98E-04	5.53E-03	4.99E-02
90.3	18.6	9.9	4.77E-02	9.23E-02	1.28E-01	9.54E-02	5.22E-02	2.41E-02	1.12E-02	4.97E-03	1.07E-03	6.57E-03	7.28E-02
90.2	20.0	10.6	5.51E-02	1.07E-01	1.27E-01	1.10E-01	5.25E-02	2.27E-02	1.09E-02	4.62E-03	6.95E-04	6.67E-03	7.80E-02
90.4	22.1	10.9	6.97E-02	9.63E-02	1.01E-01	8.17E-02	4.79E-02	2.38E-02	1.16E-02	5.84E-03	1.01E-03	7.63E-03	8.06E-02
89.7	17.0	19.9	1.61E-01	2.05E-01	1.48E-01	7.62E-02	3.90E-02	2.28E-02	1.13E-02	4.98E-03	1.31E-03	7.96E-03	1.22E-01
89.9	18.4	19.9	1.27E-01	1.72E-01	1.20E-01	7.10E-02	4.47E-02	2.46E-02	1.01E-02	5.10E-03	1.27E-03	7.58E-03	1.03E-01
89.2	20.6	20.8	1.55E-01	1.98E-01	1.52E-01	8.02E-02	4.25E-02	2.26E-02	1.13E-02	5.64E-03	1.24E-03	7.47E-03	9.27E-02
94.5	17.7	N/A	4.77E-02	5.65E-02	5.81E-02	4.13E-02	2.98E-02	2.08E-02	1.14E-02	5.98E-03	9.50E-04	5.71E-03	5.92E-02
94.8	19.9		3.50E-02	5.45E-02	6.04E-02	4.72E-02	3.46E-02	2.21E-02	1.20E-02	6.35E-03	9.58E-04	5.69E-03	5.48E-02
94.4	21.6		1.10E-01	7.66E-02	6.32E-02	4.35E-02	3.25E-02	1.99E-02	1.20E-02	6.54E-03	1.17E-03	6.42E-03	5.97E-02
94.2	17.8	9.6	4.10E-02	5.87E-02	8.39E-02	7.13E-02	3.78E-02	2.26E-02	1.08E-02	4.91E-03	1.01E-03	6.62E-03	7.23E-02
93.8	19.9	9.9	7.60E-02	1.10E-01	1.23E-01	7.18E-02	4.16E-02	2.06E-02	1.04E-02	5.07E-03	1.16E-03	6.82E-03	8.03E-02
94.2	21.9	9.6	1.07E-01	1.01E-01	7.00E-02	3.76E-02	2.06E-02	1.01E-02	5.23E-03	1.07E-03	6.41E-03	8.27E-02	1.29E+00
94.6	15.8	20.6	1.13E-01	1.21E-01	1.11E-01	6.85E-02	3.72E-02	2.05E-02	9.21E-03	4.01E-03	1.28E-03	7.64E-03	9.92E-02
94.7	18.5	19.9	1.01E-01	1.46E-01	1.14E-01	6.72E-02	3.45E-02	1.72E-02	9.37E-03	4.49E-03	1.26E-03	7.60E-03	1.07E-01
95.0	20.8	20.0	9.70E-02	1.15E-01	9.70E-02	5.90E-02	3.32E-02	1.78E-02	1.07E-02	5.89E-03	1.26E-03	7.06E-03	9.62E-02
100.2	18.2	N/A	3.25E-02	5.76E-02	6.60E-02	4.95E-02	3.34E-02	1.82E-02	8.24E-03	4.71E-03	8.68E-04	5.47E-03	6.36E-02
100.5	19.7		2.78E-02	5.11E-02	5.47E-02	4.82E-02	2.94E-02	1.77E-02	9.92E-03	4.80E-03	1.21E-03	6.38E-03	6.39E-02
101.5	22.7		3.74E-02	6.49E-02	5.90E-02	4.36E-02	2.87E-02	1.71E-02	9.98E-03	5.25E-03	1.15E-03	6.35E-03	6.05E-02
99.7	17.9	10.2	6.02E-02	7.74E-02	8.41E-02	5.46E-02	2.77E-02	1.69E-02	9.33E-03	5.03E-03	1.18E-03	6.85E-03	8.09E-02
99.4	19.9	10.3	4.13E-02	5.96E-02	7.62E-02	5.09E-02	2.87E-02	1.82E-02	9.20E-03	5.05E-03	1.04E-03	6.84E-03	7.27E-02
99.3	21.9	10.4	5.82E-02	9.02E-02	7.83E-02	4.75E-02	2.66E-02	1.61E-02	9.02E-03	5.27E-03	1.02E-03	6.78E-03	8.47E-02
99.6	16.7	20.3	7.75E-02	1.08E-01	1.17E-01	6.47E-02	3.78E-02	1.91E-02	1.02E-02	5.34E-03	1.29E-03	7.49E-03	9.90E-02
99.9	18.5	20.2	1.07E-01	1.31E-01	1.09E-01	5.91E-02	3.37E-02	1.97E-02	9.22E-03	4.96E-03	1.10E-03	7.51E-03	1.09E-01
99.8	20.5	20.2	1.27E-01	1.55E-01	1.05E-01	6.07E-02	3.20E-02	1.67E-02	1.05E-02	5.58E-03	1.21E-03	7.12E-03	1.03E-01

Table 6.3 Compressibility parameters including the constrained and elastic moduli (*M* and *E*) for 6.7-mm expansive soil-rubber specimens tested in small-scale one-dimensional swell-compression at specified levels of applied vertical effective stress

Initial State Parameters			Compressibility Parameters										
			M (kPa)								*E* (kPa)		
C_R (%)	*w* (%)	*RC* (%)	6-12 (kPa)	12-24 (kPa)	24-49 (kPa)	49-98 (kPa)	98-195 (kPa)	195-390 (kPa)	390-781 (kPa)	781-1562(kPa)	1562-781 (kPa)	781-98 (kPa)	98-6 (kPa)
89.6	18.0	N/A	20.9	17.4	16.2	21.3	32.4	53.0	88.6	158.1	1023.8	180.4	25.3
89.8	19.7		22.5	19.7	20.0	24.5	29.7	50.7	85.7	147.6	1054.2	168.7	20.0
89.8	21.3		28.2	23.4	25.1	29.5	34.3	51.8	88.8	153.4	1114.1	180.7	20.0
90.3	18.6	9.9	21.0	10.8	7.8	10.5	19.2	41.5	89.2	201.4	936.3	152.2	13.7
90.2	20.0	10.6	18.1	9.4	7.9	9.1	19.1	44.1	91.6	216.3	1438.9	149.9	12.8
90.4	22.1	10.9	14.4	10.4	9.9	12.2	20.9	42.0	86.5	171.1	989.8	131.0	12.4
89.7	17.0	19.9	6.2	4.9	6.8	13.1	25.7	43.9	88.8	200.7	762.9	125.7	8.2
89.9	18.4	19.9	7.8	5.8	8.3	14.1	22.4	40.6	99.4	196.2	786.7	132.0	9.7
89.2	20.6	20.8	6.5	5.1	6.6	12.5	23.5	44.3	88.6	177.2	807.2	133.8	10.8
94.5	17.7	N/A	21.0	17.7	17.2	24.2	33.6	48.0	87.7	167.2	1053.0	175.2	16.9
94.8	19.9		28.5	18.4	16.6	21.2	28.9	45.2	83.6	157.4	1044.1	175.7	18.2
94.4	21.6		9.1	13.0	15.8	23.0	30.8	50.3	83.0	152.8	858.3	155.7	16.8
94.2	17.8	9.6	24.4	17.0	11.9	14.0	26.5	44.3	92.3	203.8	985.8	151.1	13.8
93.8	19.9	9.9	13.2	9.1	8.1	13.9	24.0	48.5	96.2	197.1	861.6	146.7	12.5
94.2	21.9	9.6	9.3	9.9	14.3	26.6	48.7	99.3	191.2	931.9	155.9	12.1	0.8
94.6	15.8	20.6	8.9	8.2	9.0	14.6	26.9	48.7	108.6	249.4	783.9	130.8	10.1
94.7	18.5	19.9	9.9	6.9	8.8	14.9	28.9	58.1	106.7	222.6	794.8	131.6	9.4
95.0	20.8	20.0	10.3	8.7	10.3	17.0	30.1	56.3	93.0	169.7	792.2	141.7	10.4
100.2	18.2	N/A	30.8	17.3	15.2	20.2	30.0	54.9	121.4	212.1	1152.4	182.7	15.7
100.5	19.7		36.0	19.6	18.3	20.7	34.0	56.4	100.8	208.3	823.1	156.6	15.6
101.5	22.7		26.8	15.4	17.0	22.9	34.8	58.3	100.2	190.4	867.9	157.6	16.5
99.7	17.9	10.2	16.6	12.9	11.9	18.3	36.1	59.1	107.2	198.8	844.2	146.0	12.4
99.4	19.9	10.3	24.2	16.8	13.1	19.6	34.9	55.0	108.7	198.1	957.6	146.2	13.8
99.3	21.9	10.4	17.2	11.1	12.8	21.1	37.5	62.0	110.8	189.9	978.3	147.4	11.8
99.6	16.7	20.3	12.9	9.3	8.5	15.5	26.4	52.3	97.7	187.4	773.9	133.5	10.1
99.9	18.5	20.2	9.3	7.6	9.2	16.9	29.7	50.7	108.4	201.6	909.0	133.1	9.2
99.8	20.5	20.2	7.8	6.5	9.6	16.5	31.3	59.9	95.2	179.2	828.3	140.4	9.7

Figures 6.11 through 6.13 display M values for each effective vertical stress increment on the compression portion of small-scale laboratory one-dimensional swell-compression curve (see Figure 3.4). The slope of the stress-deformation curve at each load increment produces M (Lee et al. 2010). Figures 6.11, 6.12 and 6.13 are separated to include three plots per graph, distinguishing the difference in M for various RC. In general the constrained modulus decreases slightly over the lower range of applied stresses displayed; 24.4 to 48.8 kPa. Log-log linear increases in the constrained modulus are seen at effective stress values greater than 195.2 kPa in virtually all cases. The increase in constrained modulus with increasing RC is apparent for all cases of C_R and w. The discrepancy in M is more pronounced for lower values of C_R, as shown in Figures 5.11 through 5.13. M values increased by an average of 73.6, 44.2 and 46.5 kPa for C_R values of 90, 95 and 100%, respectively, over the range of vertical stresses and RC considered. M values increased by an average of 50.5, 4.3 and 53.4 kPa for RC values of 0, 10 and 20%, respectively over the range of vertical stresses and C_R considered. Of the three variable state parameters, variations in RC have the most significant impact on values of M in followed by C_R and w, respectively.

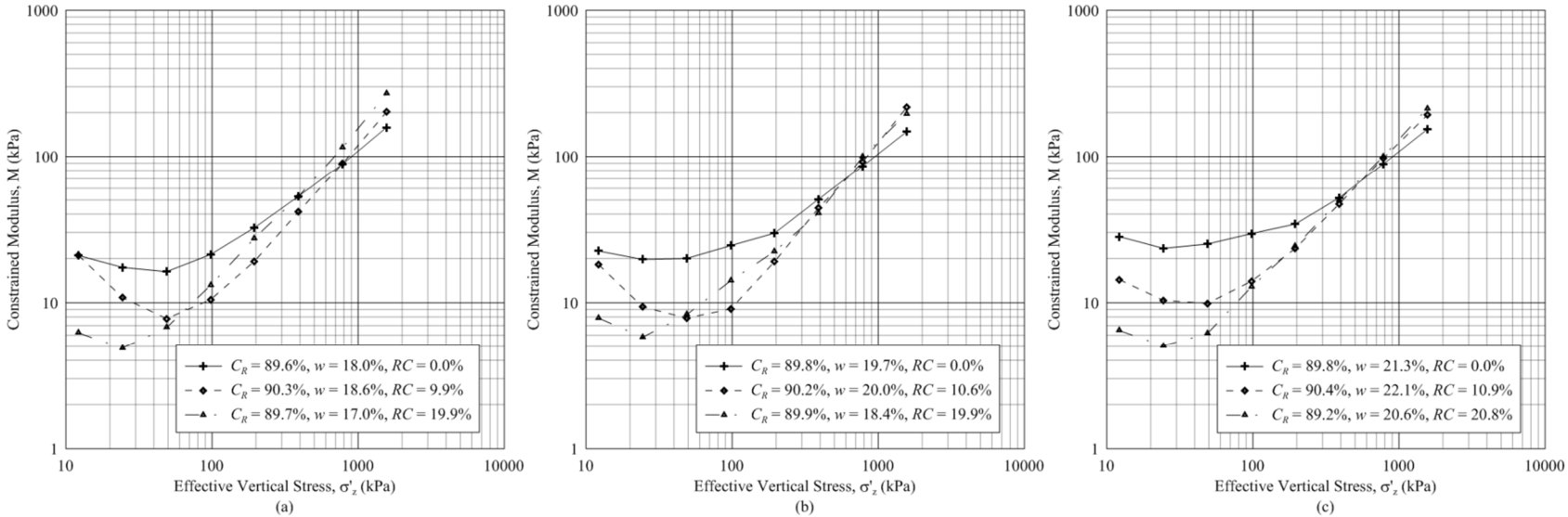

Figure 6.11 Variations in M versus σ'_z for expansive soil-rubber specimens tested in small-scale swell-compression with a target C_R of 90% and initial water content values equal to (a) w_{opt} – 2%; (b) w_{opt}; and (c) w_{opt} + 2%

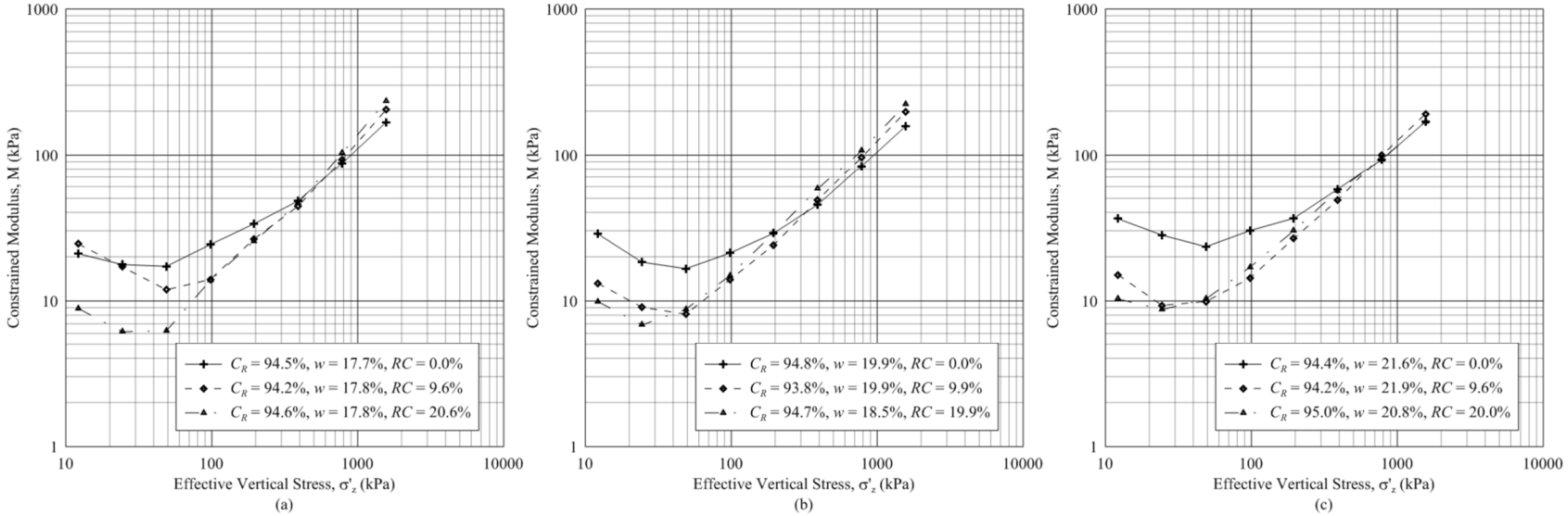

Figure 6.12 Variations in M versus σ'_z for expansive soil-rubber specimens tested in small-scale swell-compression with a target C_R of 95% and initial water content values equal to (a) w_{opt} – 2%; (b) w_{opt}; and (c) w_{opt} + 2%

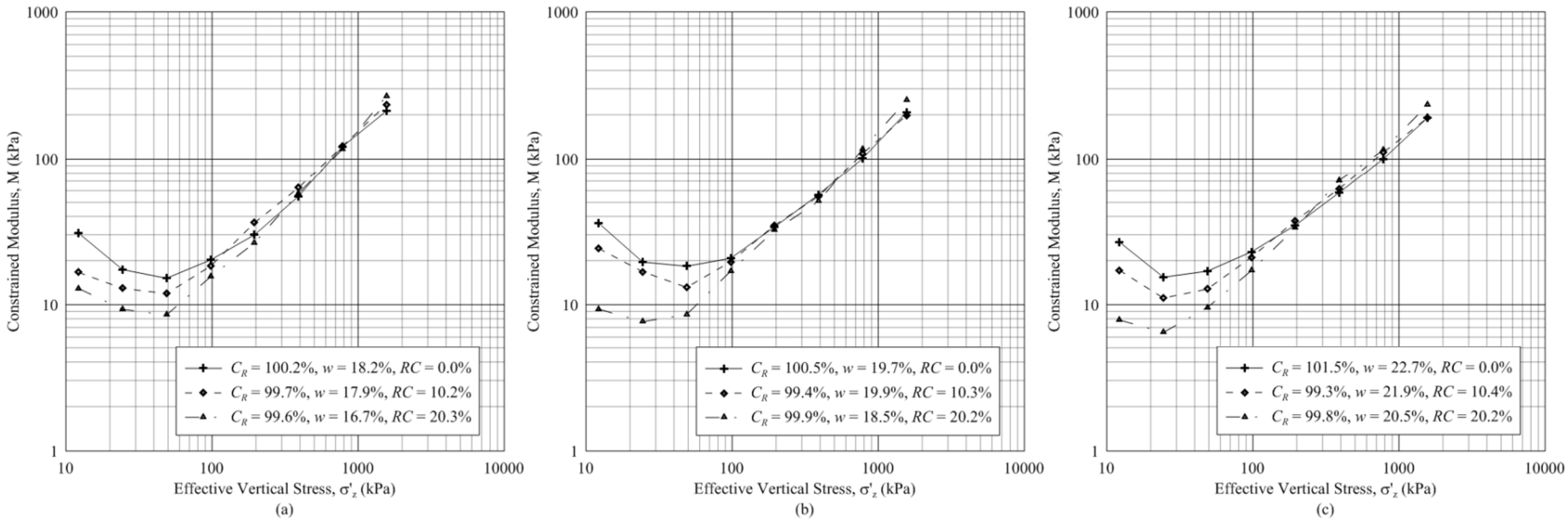

Figure 6.13 Variations in M versus σ'_z for expansive soil-rubber specimens tested in small-scale swell-compression with a target C_R of 100% and initial water content values equal to (a) w_{opt} – 2%; (b) w_{opt}; and (c) w_{opt} + 2%

Figures 6.14 through 6.16 present general trends in M with variations in RC for specimens tested in SSC. As shown, variations in C_R have the most significant impact on M, followed by RC and w, respectively. Linear trend equations for changes in M induced by variations in RC are presented in the legend of each subplot of Figures 6.14 through 6.16. Figure 6.14 presents variations in M versus C_R. Figure 6.15 presents variations in M versus w. Figure 6.16 presents variations in M versus RC. The average difference of M over the range of C_R investigated for similar levels of RC and w is 21.89%. The average difference of M over the range of RC investigated for similar levels of C_R and w is 18.45%. The average difference of M over the range of w investigated for similar levels of C_R and RC is 8.49%.

Figures 6.17 through 6.19 displays general trends in E with variations in RC for specimens tested in SSC. E values were calculated over the range of strains for the entire unloading effective vertical stress portion of the swell-compression curve (see Figure 3.4). As shown in Figures 6.17 through 6.19, RC has the largest impact of E, followed by C_R and w, respectively. Figure 6.17 presents variations in E versus C_R. Figure 6.18 presents variations in E versus w. Figure 6.19 presents variations in E versus RC. The average difference of E over the range of C_R investigated for similar levels of RC and w was 14.16 kPa. The average difference of E over the range of w investigated for similar levels of C_R and RC was 8.57 kPa.

The constrained and elastic moduli presented in Table 6.1 and Figures 6.14 through 6.19 provide a good indication of the overall stiffness over a wide range of strain values. The

large discrepancy in *M* and *E* for variations in *RC* is especially pertinent to ESR research. Past research on ESR mixtures has noted the significant stiffness degradation, especially at small strains (Dunham-Friel 2009 and Weichert 2011). The constrained and elastic moduli were calculated over identical applied vertical effective stress ranges for all points indicated in Figures 6.14 through 6.19. Although smaller strains are immediately less stiff (Dunham-Friel 2009 and Weichert 2011), Figures 6.14 through 6.19 suggest that as increases in stiffness occur with increasing *RC* at large strains. Although outside the strain range of typical geotechnical applications, ESR mixtures provide advantageous stiffness parameters at large strains.

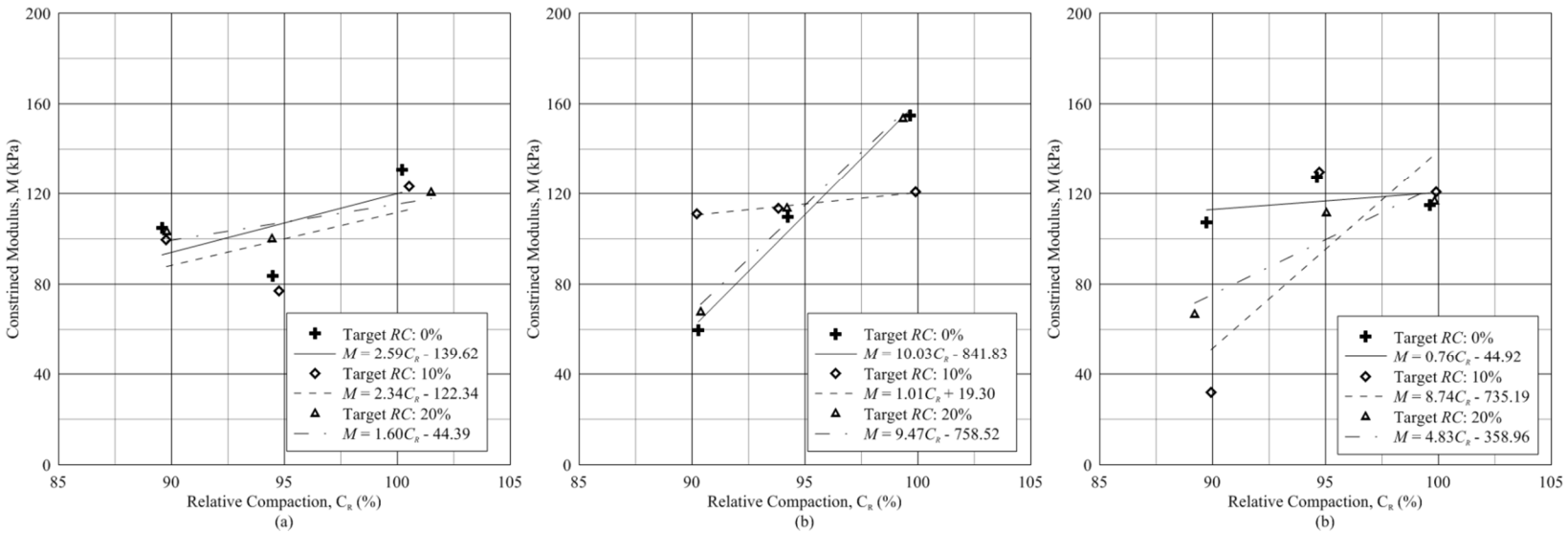

Figure 6.14 Variations in M versus C_R for Pierre shale soil and 6.7-mm expansive soil-rubber specimens with rubber contents of 10 and 20% tested in small-scale swell-compression with initial water content values equal to (a) w_{opt} – 2%; (b) w_{opt}; and (c) w_{opt} + 2%

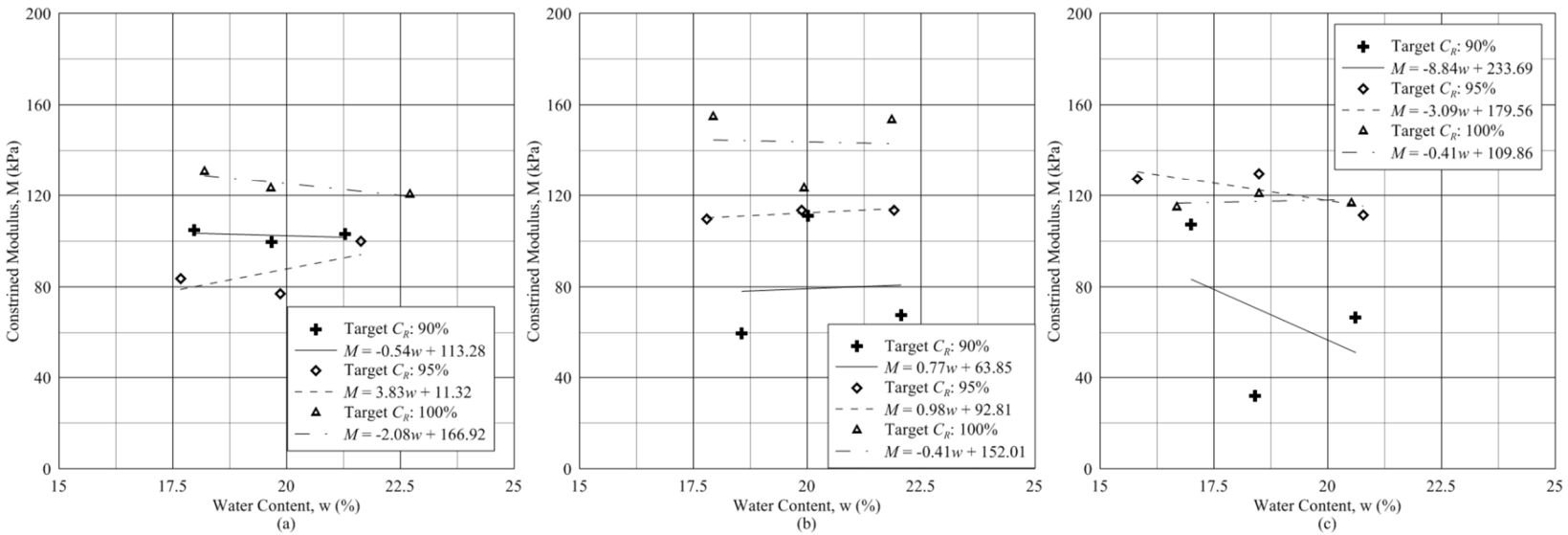

Figure 6.15 Variations in M versus the initial specimen w for Pierre shale soil and 6.7-mm expansive soil-rubber specimens with rubber contents of 10 and 20% tested in small-scale swell-compression with rubber content values of (a) 0%; (b) 10%; and (c) 20%

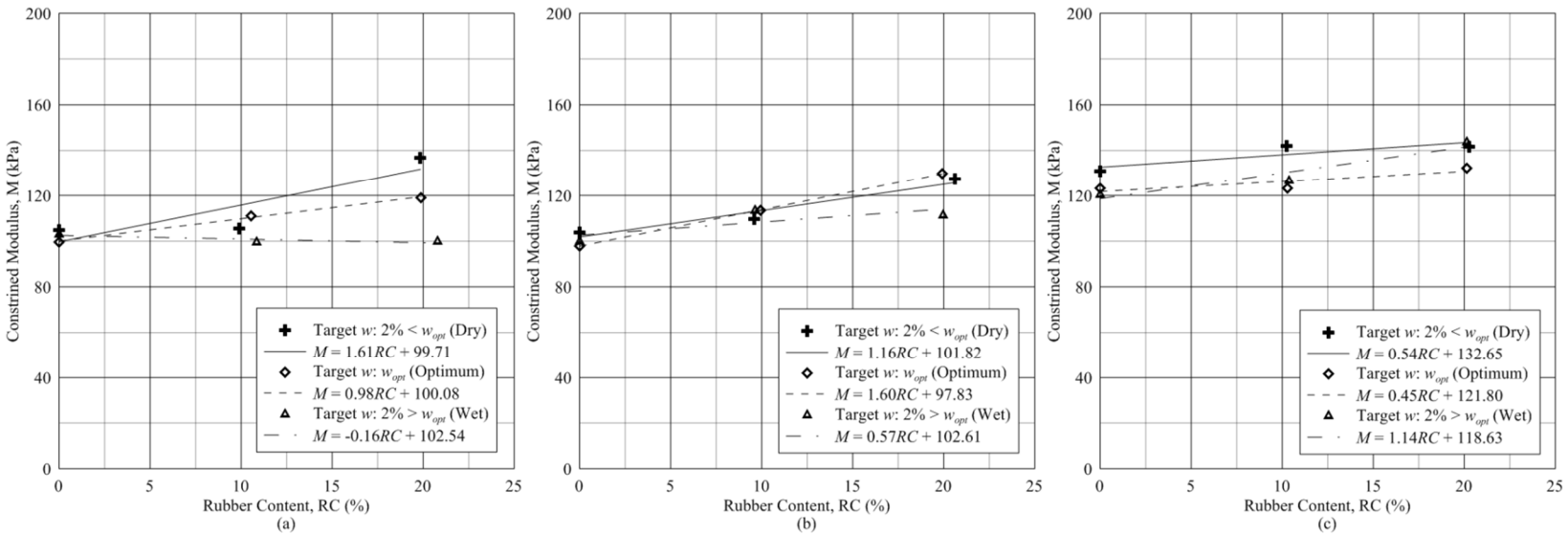

Figure 6.16 Variations in *M* versus *RC* for Pierre shale soil and 6.7-mm expansive soil-rubber specimens with rubber contents of 10 and 20% tested in small-scale swell-compression with initial relative compaction values of (a) 90%; (b) 95%; and (c) 100%

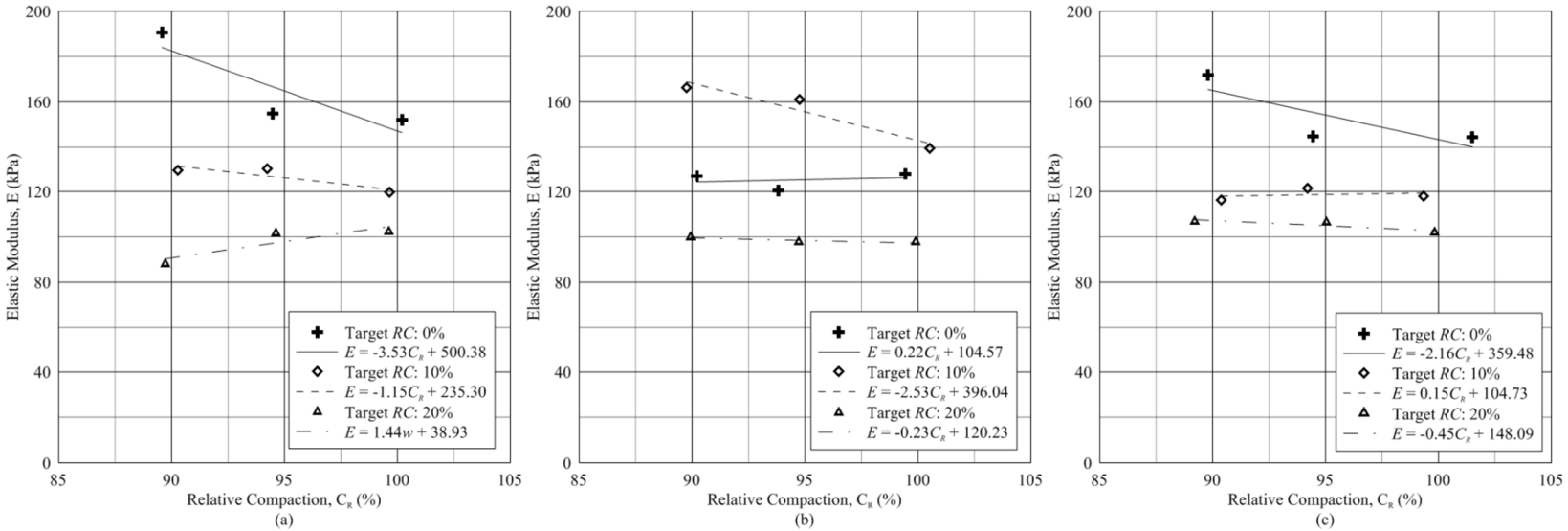

Figure 6.17 Variations in E versus C_R for Pierre shale soil and 6.7-mm expansive soil-rubber specimens with rubber contents of 10 and 20% tested in small-scale swell-compression with initial water content values equal to (a) w_{opt} – 2%; (b) w_{opt}; and (c) w_{opt} + 2%

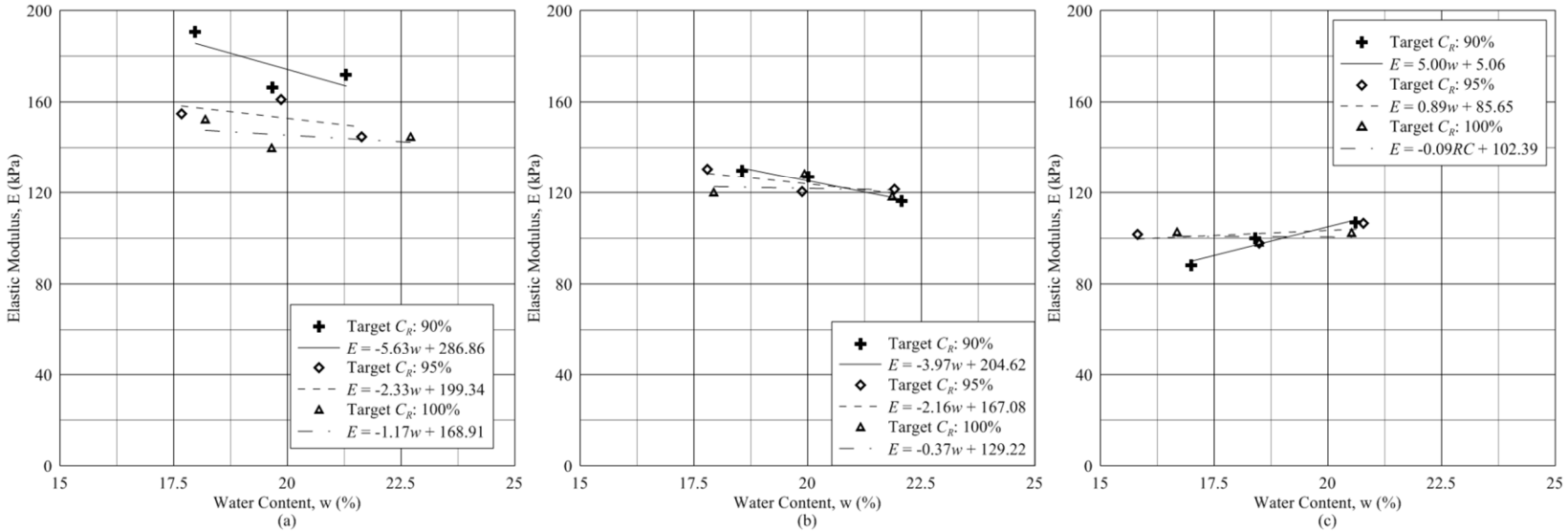

Figure 6.18 Variations in E versus the initial specimen w for Pierre shale soil and 6.7-mm expansive soil-rubber specimens with rubber contents of 10 and 20% tested in small-scale swell-compression with rubber contents of (a) 0%; (b) 10%; and (c) 20%

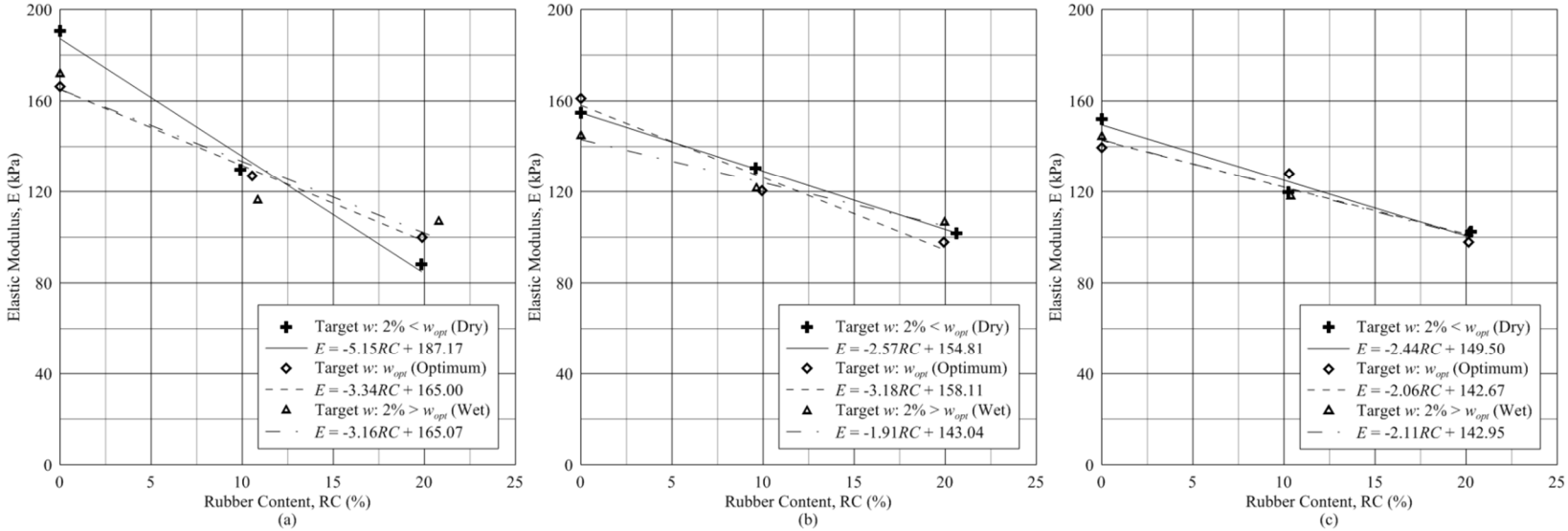

Figure 6.19 Variations in *E* versus *RC* for Pierre shale soil and 6.7-mm expansive soil-rubber specimens with rubber contents of 10 and 20% tested in small-scale swell-compression with initial relative compactions of (a) 90%, (b) 95% and (c) 100%

6.2.2.2 Large-Scale One-Dimensional Compression

As shown in Table 5.4, C_c values varied in magnitude from 0.119 to 0.186, but in general ESR mixtures with larger nominal rubber particle sizes were less compressible. C_r values were more consistent than C_c values ranging from 0.038 to 0.031. Additional compressibility parameters are provided in Tables 6.4 and 6.5. As shown volumetric compressibility values m_v and m_{vr} vary insignificantly for changes in d_R and w in comparison to ESR mixtures tested in SSC. Also, differences in M and E for changes in d_R and initial w are minimal in comparison to ESR mixtures tested in SSC.

Table 6.4 Compressibility parameters including the moduli of volume compressibility and recompressibility (m_v and m_{vr}) for 6.7- and 19.0-mm expansive soil-rubber specimens with a target rubber content of 20% tested in large-scale one-dimensional swell-compression at specified levels of applied vertical effective stress

d_R (mm)	Initial State Parameters			Compressibility Parameters					
	C_R (%)	w (%)	RC (%)	m_v (1/kPa)				m_{vr} (1/kPa)	
6.7	95.7	16.5	20.3	6-12 (kPa)	12-18 (kPa)	18-24 (kPa)	24-36 (kPa)	36-18 (kPa)	18-6 (kPa)
				9.94E-02	1.77E-01	1.92E-01	1.76E-01	2.27E-02	1.01E-01
6.7	95.1	19.1	19.9	6-12 (kPa)	12-18 (kPa)	18-24 (kPa)	24-32 (kPa)	32-12 (kPa)	12-6 (kPa)
				9.76E-02	2.17E-01	2.05E-01	1.82E-01	4.06E-02	1.65E-01
6.7	94.6	20.8	19.9	6-12 (kPa)	12-18 (kPa)	18-24 (kPa)	-	24-12 (kPa)	12-6 (kPa)
				1.08E-01	2.33E-01	2.10E-01	-	3.72E-02	1.24E-01
19.0	94.9	15.7	20.4	6-12 (kPa)	12-18 (kPa)	18-24 (kPa)	24-36 (kPa)	36-18 (kPa)	18-6 (kPa)
				1.03E-01	1.53E-01	2.05E-01	1.72E-01	2.18E-02	9.82E-02
19.0	95.9	18.8	19.3	6-12 (kPa)	12-18 (kPa)	18-24 (kPa)	24-30 (kPa)	30-18 (kPa)	18-6 (kPa)
				1.12E-01	2.07E-01	1.87E-01	1.70E-01	3.80E-02	1.02E-01
19.0	95.5	21.0	20.2	6-12 (kPa)	12-18 (kPa)	18-24 (kPa)	-	24-12 (kPa)	12-6 (kPa)
				9.89E-02	1.76E-01	2.06E-01	-	5.74E-02	1.06E-01

Table 6.5 Compressibility parameters including the constrained and elastic moduli (M and E) for 6.7- and 19.0-mm expansive soil-rubber specimens with a target rubber content of 20% tested in large-scale one-dimensional swell-compression at specified levels of applied vertical effective stress

d_R (mm)	Initial State Parameters			Compressibility Parameters					
	C_R (%)	w (%)	RC (%)	M (kPa)				E (kPa)	
6.7	95.7	16.5	20.3	6-12 (kPa)	12-18 (kPa)	18-24 (kPa)	24-36 (kPa)	36-18 (kPa)	18-6 (kPa)
				10.1	5.6	5.2	5.7	44.0	9.9
6.7	95.1	19.1	19.9	6-12 (kPa)	12-18 (kPa)	18-24 (kPa)	24-32 (kPa)	32-12 (kPa)	12-6 (kPa)
				10.2	4.6	4.9	5.5	24.7	6.0
6.7	94.6	20.8	19.9	6-12 (kPa)	12-18 (kPa)	18-24 (kPa)	-	24-12 (kPa)	12-6 (kPa)
				9.3	4.3	4.8	-	26.9	8.1
19.0	94.9	15.7	20.4	6-12 (kPa)	12-18 (kPa)	18-24 (kPa)	24-36 (kPa)	36-18 (kPa)	18-6 (kPa)
				9.7	6.5	4.9	5.8	45.8	10.2
19.0	95.9	18.8	19.3	6-12 (kPa)	12-18 (kPa)	18-24 (kPa)	24-30 (kPa)	30-18 (kPa)	18-6 (kPa)
				8.9	4.8	5.3	5.9	26.3	9.8
19.0	95.5	21.0	20.2	6-12 (kPa)	12-18 (kPa)	18-24 (kPa)	-	24-12 (kPa)	12-6 (kPa)
				10.1	5.7	4.8	-	17.4	9.4

Presented in Figure 6.20 are trends describing the relationships of M and E versus w for LSC testing. Both compressibility parameters were determined for similar levels of applied effective vertical stress. As shown, M is relatively consistent for variations in the initial w, with a maximum difference of 1.06 kPa over all specimens tested. It is expected that w should have little effect on normal compression parameters calculated post inundation. Also, E decreases with slightly with increasing w. The most likely explanation for the decreasing E is the decreasing $S_{\%}$ and σ'_{zs}, leading to a decreased σ'_z and E due to the nature of swell-compression curves prior to reaching normal compression. Strain upon unloading was not as pronounced and more horizontal for σ'_z values likely below normal compression. If the normal compression line (Figure 3.4) were obtained the overall effect of initial w on E values be minimal (similar to SSC). Also presented are the minimal differences in E when comparing 20% 6.7 and 19.0-mm ESR mixtures in LSC. Due to employing a single C_R value for LSC testing, conclusions regarding the effect of C_R on E are not discussed.

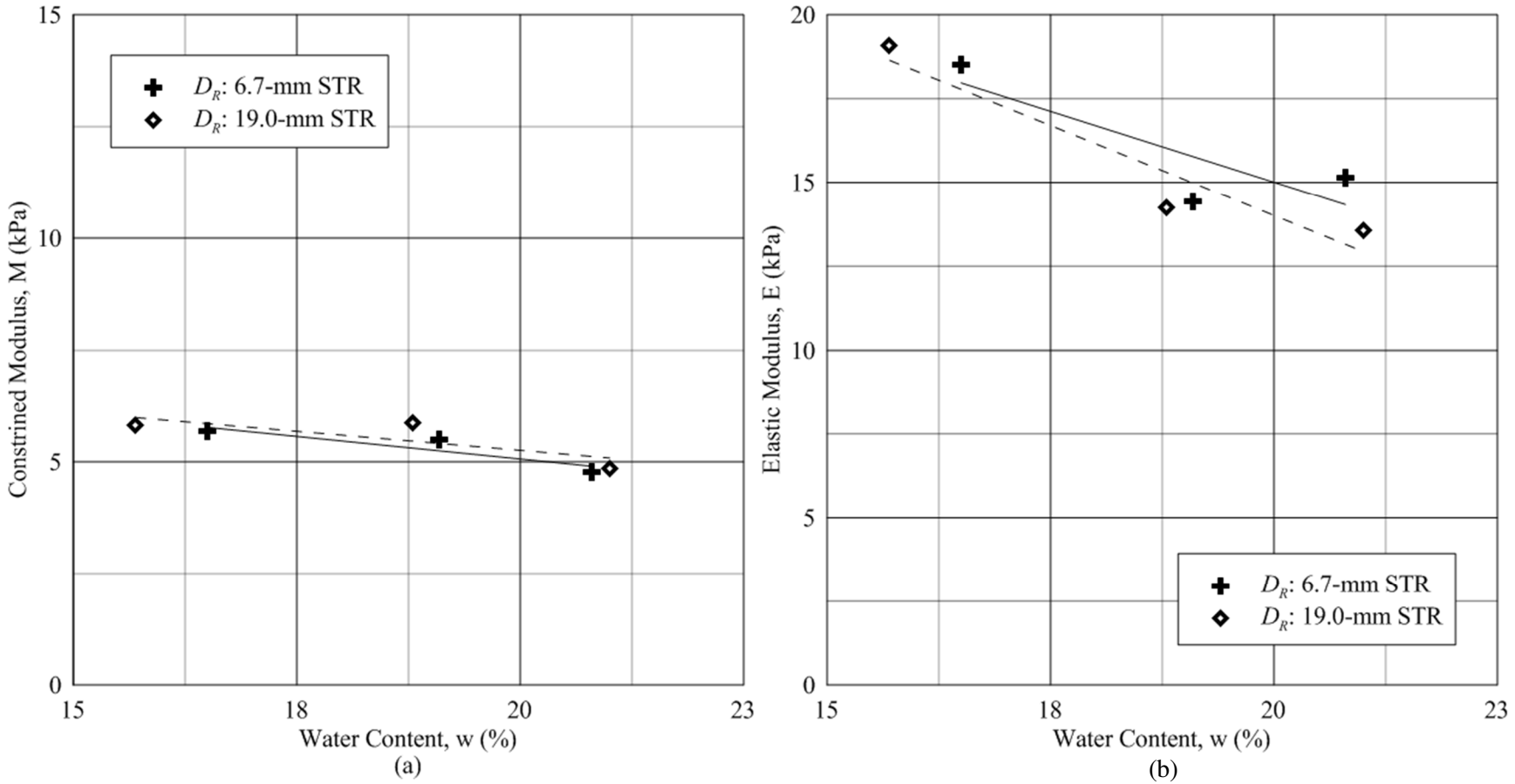

Figure 6.20 Variations in (a) *M* and (b) *E* versus the initial water content prior to inundation for 6.7- and 19.0-mm expansive soil-rubber specimens with a target rubber content of 20% tested in one-dimensional swell-consolidation

6.2.3 Effect of Rubber Particle Size

Deviations in target and actual *RC* values in LSC testing were smaller for 6.7-mm STR in comparison to 19.0-mm STR ESR mixtures. Reasons for larger discrepancies in *RC* for 19.0-mm mixtures might be due to an increased mass of rubber per particle due to larger particle sizes, relatively higher density of individual particle, the inclusion of impurities such as steel reinforcement, and larger compaction load requirements. Also, the particle size and arrangement during compaction yield a slightly higher compacted soil density for 19.0-mm ESR specimens in comparison to 6.7-mm ESR specimens, as shown in Table 6.1. The possible implications of a larger *RC* deviation include increased deviations in the initial state parameters C_R and w leading to increased differences in swell and compressibility.

Swelling parameters increased with increasing d_R as shown in Figure 6.21. The primary reason for the increase in swelling response for 19.0-mm ESR mixtures is likely due to the differences in w_{opt} for the two d_R sizes investigated. A secondary reason could be the relative deformability of 6.7- and 19.0-mm STR particles yielding differences in specimen fabric and particle orientations pre and post inundation. Both specimen types exhibited similar soil matrix densities (varying by only 0.1 kN/m^3 at a C_R of 95%), therefore the expansive soil's contribution to swelling characteristics in both mixtures was likely similar, as shown in Table 6.1.

Compressibility parameters M and E are displayed versus the two d_R employed in LSC testing in Figure 6.22. As shown the relative effect d_R has on both compressibility

parameters is minimal. Tends are inconclusive as to whether d_R would have had an effect on compressibility if the NCL was obtained during vertical stress application. Minimal differences in compressibility are likely due to difference total solid material (soil and rubber), as opposed to the differences in STR type.

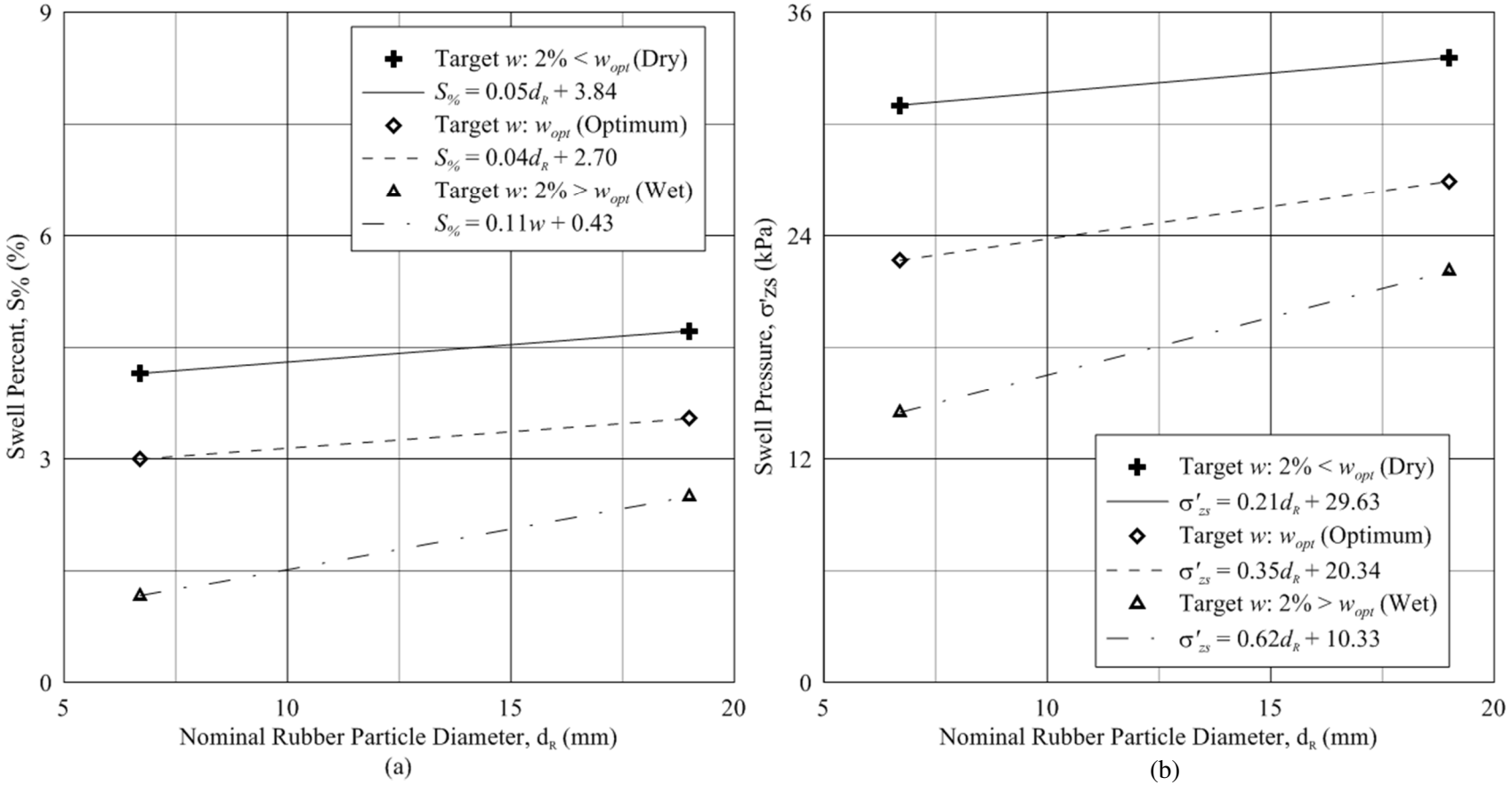

Figure 6.21 Trends in (a) $S_{\%}$ and (b) σ'_{zs} versus d_R for 6.7- and 19.0-mm expansive soil-rubber specimens with a target rubber content of 20% tested in one-dimensional swell-consolidation

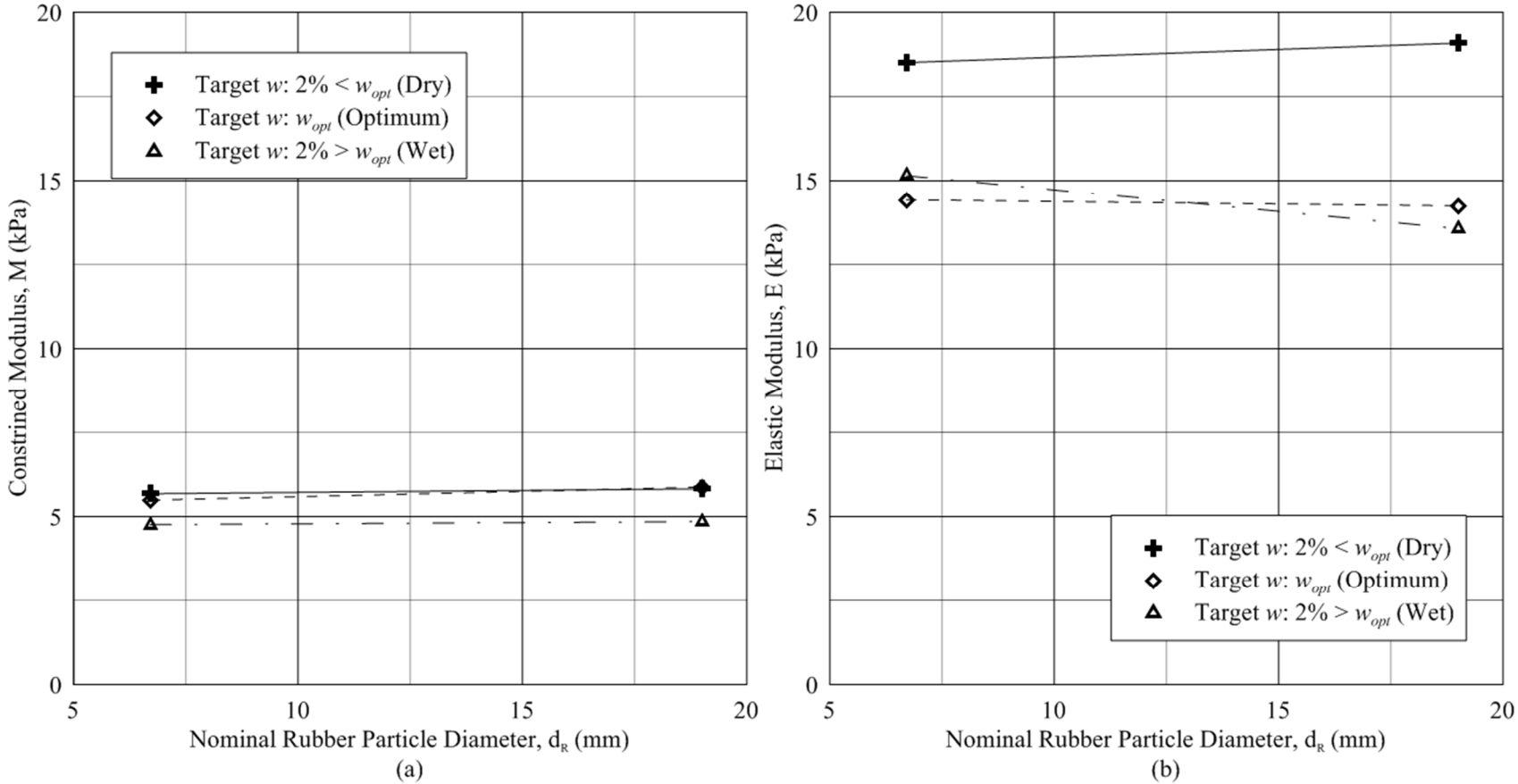

Figure 6.22 Trends in (a) M and (b) E versus d_R for 6.7- and 19.0-mm expansive soil-rubber specimens with a target rubber content of 20% tested in one-dimensional swell-consolidation

6.2.4 Effect of Specimen Size

One-dimensional response was studied on three different specimen volumes (V_{ESR}) or at three different scales (SSC, LSC, and FSSM), as discussed in Chapter 4. The A_C of the three scales studied ranges approximately three orders of magnitude. 6.7-mm granulated rubber was employed in all three scales; therefore Figure 6.23 displays $S_{\%}$ and σ'_{zs} versus V_{ESR} for 20% 6.7-mm ESR mixtures only. Tested specimens with identical target state parameters C_R, w and RC are compared in Figure 6.23.

As presented in Figure 6.23 both $S_{\%}$ and σ'_{zs} decrease slightly with increasing V_{ESR} over the more than three order of magnitude difference in specimen sizes tested. Specific log-linear trend equations are provided in the legend to indicate the effect of V_{ESR} on $S_{\%}$ and σ'_{zs}. The slopes of the trends indicate the significance V_{ESR} has on swell. The range in $S_{\%}$ is similar for both SSC and LSC testing over the w range employed. However, a much larger range of σ'_{zs} exists for SSC testing in comparison to LSC testing, with σ'_{zs} values much more similar for LSC testing. Theoretically, swell should be relatively similar if both the initial state parameters were identical and the characteristics of each apparatus were similar. Differences in swell were likely due to (a) differences in C_R post compaction; (b) differences in lateral confining material (brass, aluminum and plastic for SSC, LSC and FSSM, respectively) and subsequent interfacial friction differences between ESR specimens and lateral confinement; (c) differences in the height to V_{ESR} ratio (6.0, 13.2 and 0.1 m^{-1} for SSC, LSC and FSSM, respectively); (d) potential saturation differences at the end of inundation; and (e) other specimen impurities including adequate contact between the specimen and confining material.

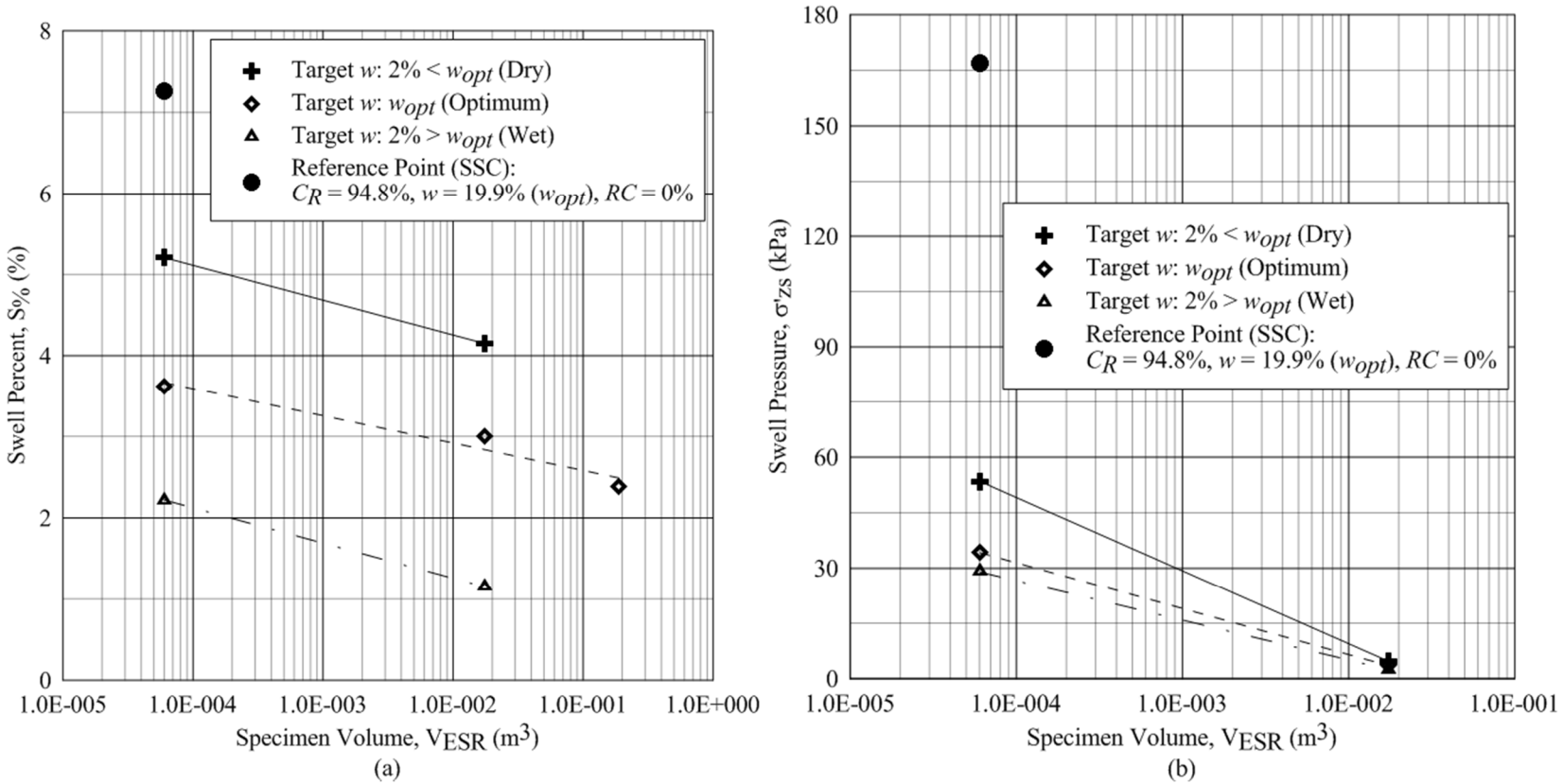

Figure 6.23 Variations in (a) $S_{\%}$ and (b) σ'_{zs} versus V_{ESR} for small, large and field-scale 6.7-mm expansive soil-rubber specimens with a target rubber content of 20% tested in one-dimensional swell-consolidation and monitored for swell

A summary of compressibility values m_v, m_{vr}, M and E for SSC and LSC is presented in Table 6.6. All mixtures displayed were compacted to C_R and RC values equal to 95 and 20%, respectively. As shown, compressibility was similar for 20% 6.7-mm ESR SSC and LSC specimens tested under one-dimensional laterally confined conditions. The maximum deviation in compressibility was displayed for m_{vr} and E. A larger application of σ'_z during LSC testing would yield better comparison to SSC compressibility values.

Table 6.6 Compressibility parameters for small-scale and large-scale 6.7-mm expansive-soil-rubber specimens with a target rubber content (RC) of 20% tested in one-dimensional swell-compression. Parameters include the moduli of volume compressibility and recompressibility (m_v, m_{vr}) and the constrained and elastic moduli (M and E) for similar levels of applied vertical effective stress.

Summary Table of Large-Scale Swell-Consolidation Compressibility Results							
Specimen Size	Initial State Parameters			Compressibility Parameters			
	C_R (%)	w (%)	RC (%)	m_v (1/kPa)			m_{vr} (1/kPa)
				6-12 (kPa)	12-24 (kPa)	24 - ~36 (kPa)	~36-6 (kPa)
SSC	94.6	15.8	20.6	1.13E-01	1.21E-01	1.11E-01	9.92E-02
	94.7	18.5	19.9	1.01E-01	1.46E-01	1.14E-01	1.07E-01
	95.0	20.8	20.0	9.70E-02	1.15E-01	9.70E-02	9.62E-02
LSC	95.7	20.3	16.0	9.94E-02	1.77E-01	1.76E-01	6.19E-02
	95.1	19.9	18.6	9.76E-02	2.17E-01	1.82E-01	1.03E-01
	94.6	19.9	20.3	1.08E-01	2.33E-01	-	8.04E-02
				M (kPa)			E (kPa)
SSC	94.6	15.8	20.6	8.9	8.2	9.0	10.1
	94.7	18.5	19.9	9.9	6.9	8.8	9.4
	95.0	20.8	20.0	10.3	8.7	10.3	10.4
LSC	95.7	20.3	16.0	10.1	5.4	5.7	26.9
	95.1	19.9	18.6	10.2	4.7	5.5	15.4
	94.6	19.9	20.3	9.3	4.5	-	17.5

Figure 6.24 presented compressibility (M and E) variations with differences in V_{ESR} for SSC and LSC testing. A significant decrease is displayed for compressibility for SSC and LSC testing. A reference point is provided in Figures 6.23 and 6.24 to display parameter results for a reference point on Pierre shale soil alone tested in SSC and compacted to a C_R of 95% and w_{opt}.

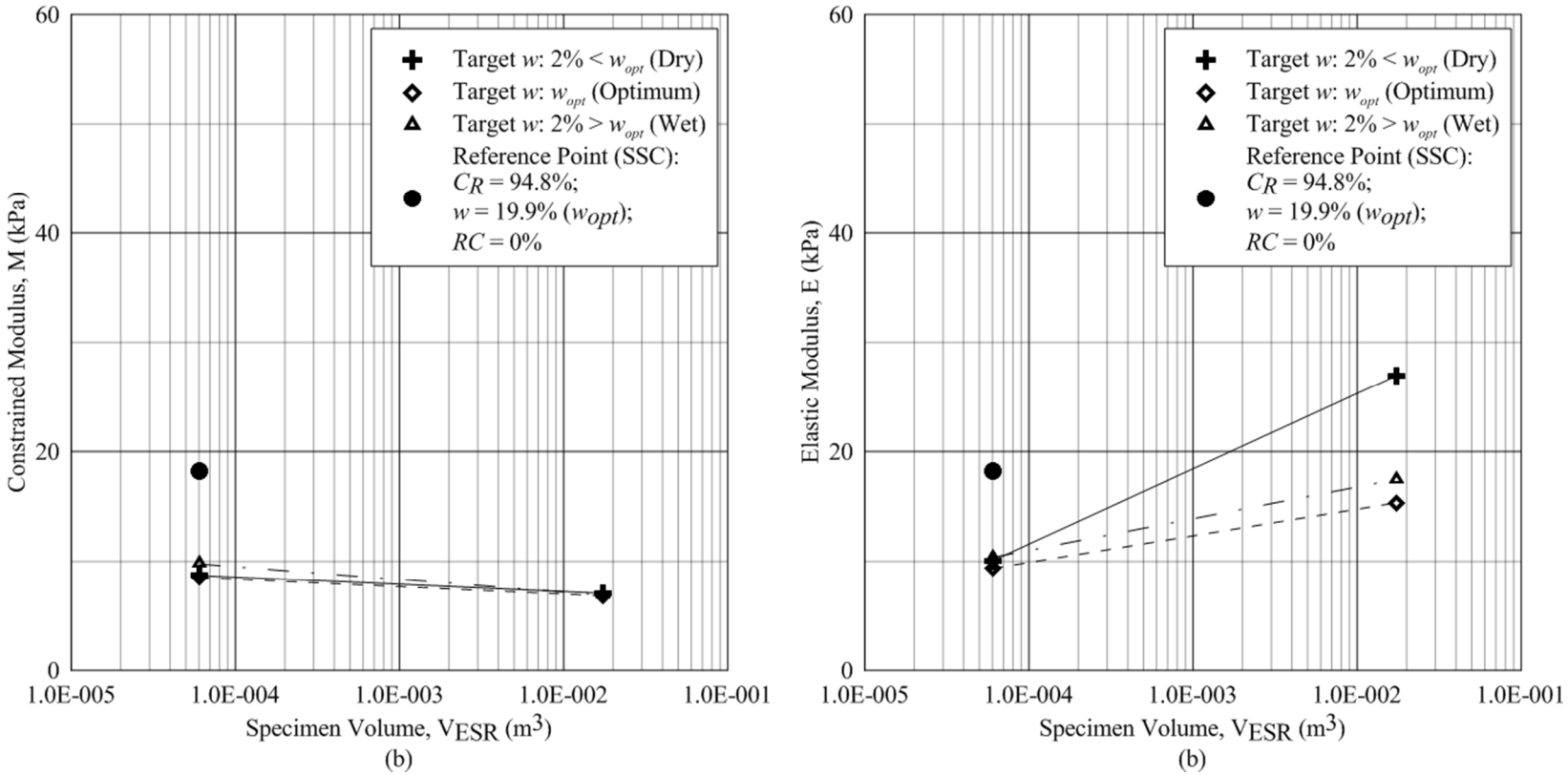

Figure 6.24 Variations in (a) *M* and (b) *E* versus V_{ESR} for small and large-scale 6.7-mm expansive soil-rubber specimens with a target rubber content of 20% tested in one-dimensional swell-consolidation

One potential explanation for the discrepancy in swelling characteristics is differences in the initial state parameters C_R, RC and w. The differences in initial state parameters were within 0.4% when comparing SSC and LSC testing. Initial state parameters for FSSM were much lower in C_R and w, by 5 and 1%, respectively, and much higher in RC by 2.4%, when comparing target to actual values. Discrepancies in initial state parameters likely contributed significantly to the lower swelling characteristics in FSSM in comparison to SSC and LSC testing.

Differences in $S_{\%}$ and σ'_{zs} for SSC and LSC testing are likely due to a differing height to A_C ratio and differences in the apparatuses employed in testing. The ratio of specimen height to A_C normal to the effective vertical stress varies significantly for SSC, LSC, and FSSM with values of 4.2E-1, 3.4E-2, and 1.4E-3 in^{-1}, respectively. Apparatuses employed in testing also used differing interfacial materials; brass, aluminum, and plastic (see Figures 4.7 through 4.9), which likely contributed to differences in sidewall friction and therefore differences in $S_{\%}$ and σ'_{zs}. In addition to different interfacial materials the ratio of contact area versus specimen volume decreases dramatically as A_C increases. Finally, differences in specimen saturation were likely at the end of inundation given the differencing inundation techniques and the larger difference in V_{ESR}.

Minor differences in compressibility parameters (M and E) are likely that the differences are due to the inability to obtain the NCL during compression, and limited applied vertical stress ranges similar and comparable for SSC and LSC. Trends are inconclusive as to whether obtaining the NCL during LSC testing would have yielded M and E values

closer to those obtained during SSC testing. Due to the similar differences in initial soil matrix density post compaction, it is likely that the larger specimen area utilized in LSC testing would have produced M and E values more similar to those obtained during SSC testing.

6.3 One-Dimensional Consolidation

Figures 6.25 through 6.27 display variations in the coefficient of consolidation (c_v) with variations in C_R, w and RC, respectively, for SSC testing. Figure 6.28 presents the variations in the coefficient of consolidation with variations in w for LSC testing. Figure 6.29 displays variations in c_v with variations in the initial specimen volume for SSC and LSC testing. As indicated in Figures 6.25 through 6.27, c_v trends with varying initial states of C_R, w and RC were inconclusive and c_v values ranged from 7.0 to 3.4 m^2/yr for all SSC specimens. Figure 6.28 displays variations in c_v for LSC specimens, in general displaying trends of decreasing c_v with increasing d_R. Figure 6.29 displays differences in estimated c_v versus V_{ESR}. As presented in Figure 6.29, calculated c_v values tend to increase with increasing V_{ESR}. The increase in c_v for increasing specimen volume is directly linked to differences in the height to diameter ratio for the two specimen sizes. In using the coefficient of consolidation to estimate the hydraulic conductivity values presented in Table 5.5, k values are within the typically accepted bounds for remolded specimens tested in one-dimensional consolidation (Navy 1954).

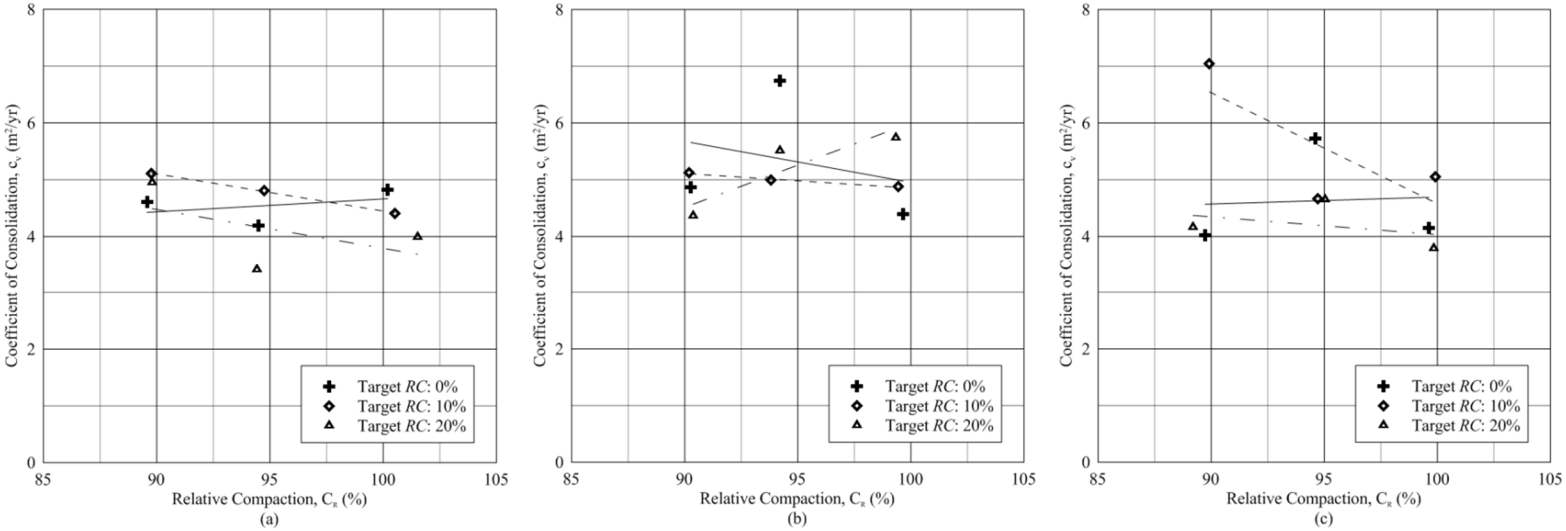

Figure 6.25 Variations in c_v versus C_R for initial water content (w) values equal to (a) the optimum water content (w_{opt}) – 2%; (b) w_{opt}; and (c) w_{opt} + 2% for small-scale specimens tested in one-dimensional swell-compression

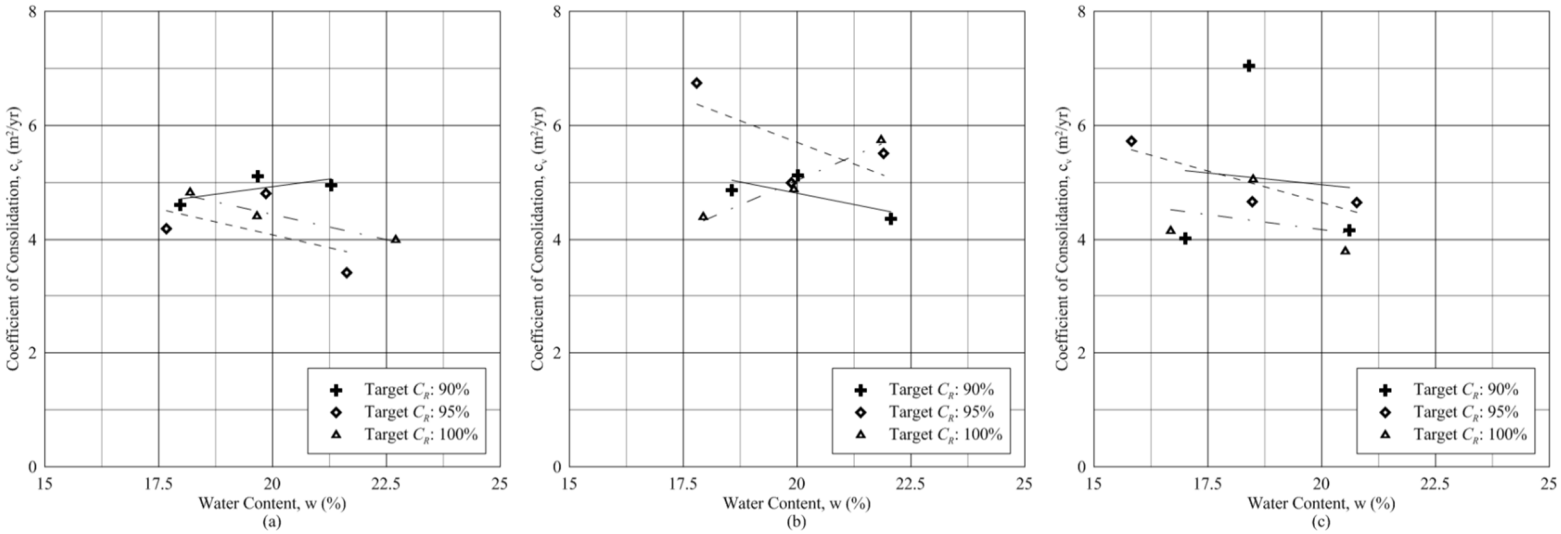

Figure 6.26 Variations in c_v versus w for rubber content (RC) values of (a) 0%; (b) 10%; and (c) 20% for small-scale specimens tested in one-dimensional swell-compression

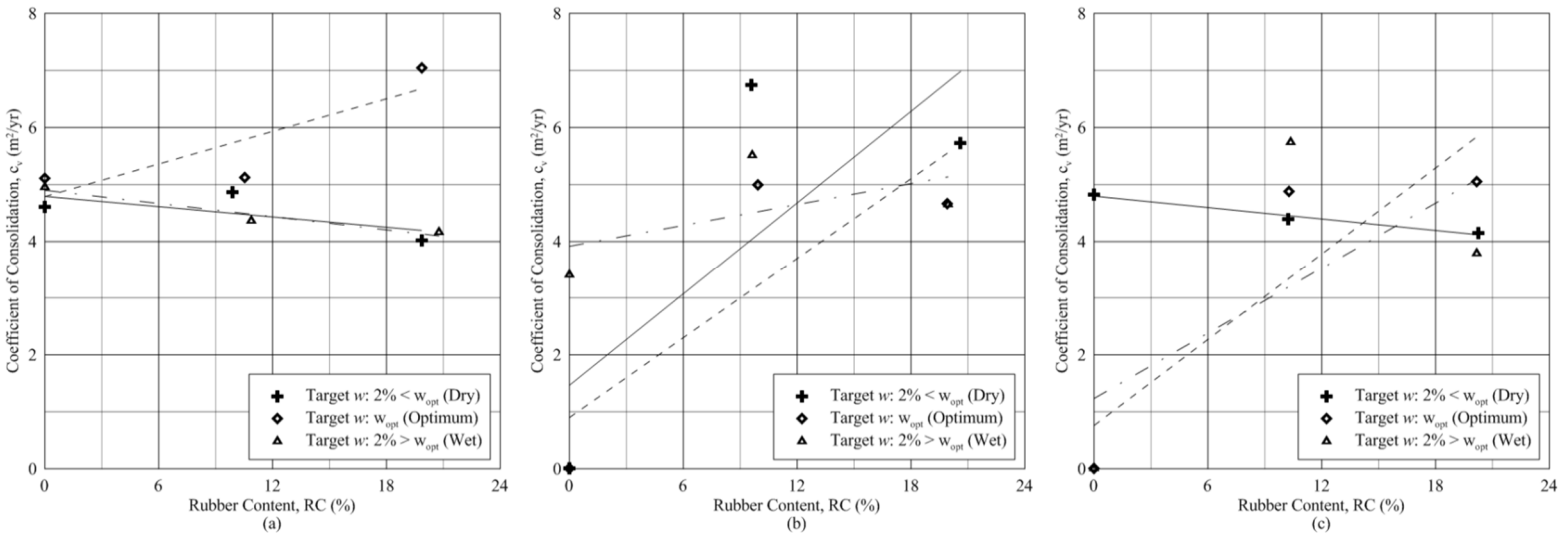

Figure 6.27 Variations in c_v versus RC for initial relative compaction (C_R) values of (a) 90%; (b) 95%; and (c) 100% for small-scale specimens tested in one-dimensional swell-compression

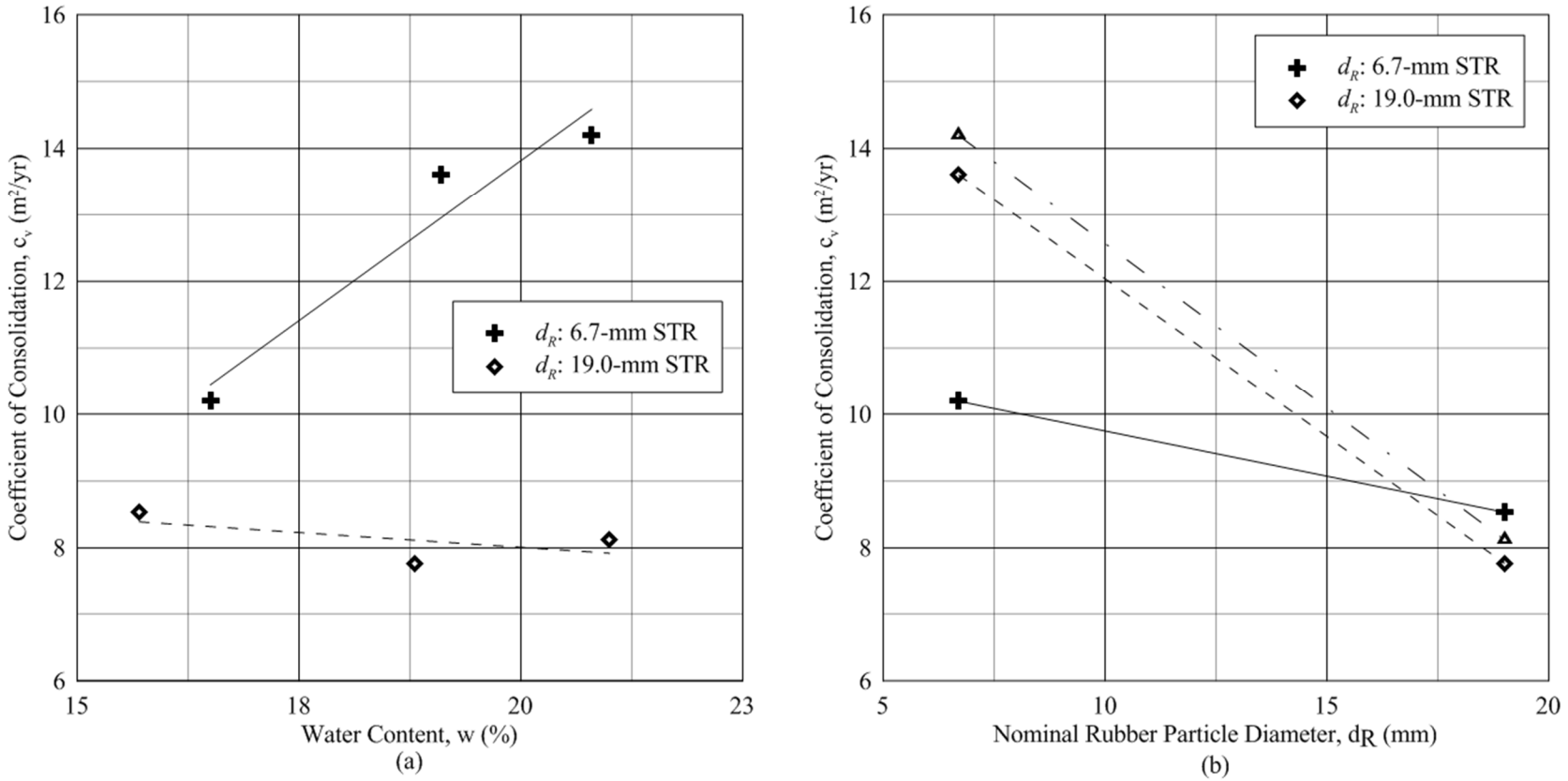

Figure 6.28 Variations in the c_v versus (a) initial water content prior to inundation; and (b) nominal rubber particle diameter for large-scale 6.7- and 19.0-mm specimens with a target rubber content of 20% tested in one-dimensional swell-compression

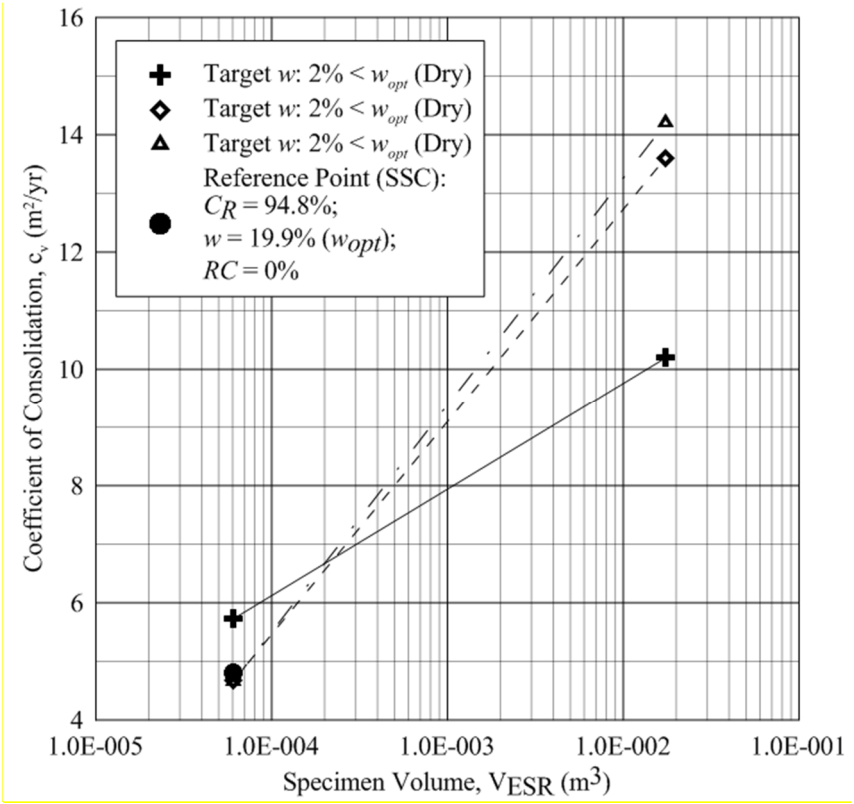

Figure 6.29 Variations in the c_v versus V_{ESR} for small and large-scale 6.7-mm expansive soil-rubber specimens with a target rubber content of 20% tested in one-dimensional swell-consolidation

6.3 Large Scale Axisymmetric Compression Testing

LSTX axisymmetric compression testing was performed on both 20% 6.7-mm and 19.0-mm ESR mixtures. The following sections present explanations of back-pressure saturation, isotropic compression, isotropic compression, and axisymmetric compression, in addition to a discussion of the effect d_R and specimen size has on axisymmetric compressive results and critical state parameters.

6.3.1 Flushing and Back-Pressure Saturation

Specimen expansion occurred primarily during flushing, where the majority of total specimen swell was recognized. Swell response was greater for 19.0-mm ESR mixtures in comparison to 6.7-mm ESR mixtures. At each specimen's respective measured relative compaction, initial saturation values ranged from 72.1 to 80.0%, leaving a significant amount of pore space occupied with air and increasing matric potential (Section 6.2.1.1). As p' values required for a minimum B value of 0.98 increased, so did swell percent during the back pressure saturation stage. In general 19.0-mm ESR mixtures displayed more swell during back pressure saturation in comparison to 6.7-mm ESR mixtures. Cell calibration factors used to differentiate between specimen and apparatus expansion are presented in Appendix A. The percentage of total swell realized during flushing in comparison to back pressure saturation ranged from 80.2% to 96.6% for all specimens saturated.

6.3.2 Isotropic Compression

Isotropic compression data for 6.7-mm and 19.0-mm LSTX ESR mixtures is presented in Figure 5.7 and Table 5.7. In this LSTX study, the mechanical response of two ESR mixture types were evaluated in axisymmetric compression at p' values of 50, 100, and 200 kPa for a single initial target C_R of 95%. The limited range of specific levels of p' were not sufficient to define an exact normal compression line and unloading reloading line. In addition to the limited range of p', incremental volumetric readings with time were not recorded during the isotropic compression process. Specimens were observed to follow a general URL trend at lower p' values (20 and 50 kPa) and follow a general NCL trend at higher p' values (100 and 200 kPa) with differentiable slopes. Therefore, URLs were approximated assuming intersections at p' values of 20 and 50 kPa and NCLs were approximated assuming intersections at p' values of 100 to 200 kPa. An important distinction can be made in the accuracy of the NCL and URL based on the relative number of points defining each log-linear trend. Due to the isotropic compression process (as discussed in Section 4.2.5.4) a total of 6 points define each URL and 3 points define each NCL. Figure 6.30 presents the NCL and URL lines for both 20% 6.7 and 19.0-mm ESR mixtures.

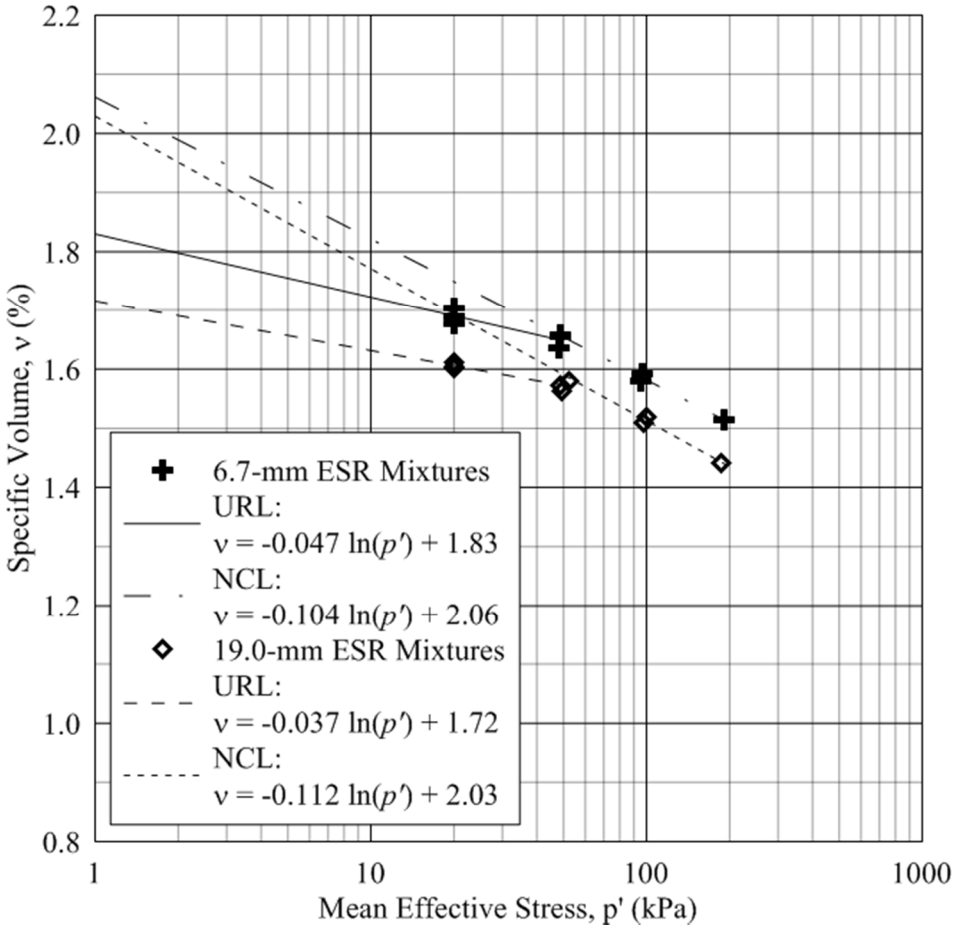

Figure 6.30 Normal compression and unloading reloading lines for large-scale 6.7- and 19.0-mm expansive soil-rubber specimens

NCL and URL definitions are presented in Table 6.7 according to Equations 28 and 29, respectively. As presented, slopes of the NCL and URL, λ_{cs} and κ_{cs} were similar for both 6.7 and 19.0-mm ESR mixture types. As expected v increased and C_R decreased during flushing and back pressure saturation (due to specimen expansion), and v decreased and C_R increased during the isotropic compression process. Compressibility of 19.0-mm ESR mixtures is slightly less in comparison to 6.7-mm ESR mixtures. Similar decreases in specimen v are shown for increases in p' of 50, and 100 kPa. Also presented in Figure 6.30 and Table 6.4 is the difference in specific volume at equal p' values. The differences

in compressibility and specific volume at specific p' values are likely due to the inherent difference in the γ_{dmax} each mixture based on standard Proctor compaction characteristics (Section 4.1.5).

Table 6.7 Normal compression and unloading-reloading line summaries determined from isotropic compression for 6.7- and 19.0-mm expansive soil-rubber specimens

Test ID	λ_{cs}	v_{λ}	κ_{cs}	v_{κ}
6.7-mm - 50kPa	0.10	2.06	0.05	1.83
6.7-mm - 100kPa				
6.7-mm - 200kPa				
19.0-mm - 50kPa	0.11	2.03	0.04	1.72
19.0-mm - 100kPa				
19.0-mm - 200kPa				

6.3.3 Isotropic Consolidation

Isotropic consolidation data including c_v, m_v and k was presented in Table 5.8. As shown, c_v and k both decrease with increasing p'. Reasons for the decrease in pore pressure dissipation with increasing p' include a higher C_R yielding less void space for pore water migration and an incremental increase in p' during the consolidation process leading to additional Δu. Few conclusive differences in m_v were determined with increases in p'.

Table 6.8 compares consolation parameters c_v, m_v and k for LSTX and SSTX testing performed on 20% 6.7-mm ESR specimens. All specimens presented were compacted to an initial target C_R, w and RC of 95%, optimum and 20%, respectively. As shown, c_v and k both decrease with increasing p' for LSTX and SSTX testing. In general, both c_v and m_v values for LSTX testing are approximately double c_v and m_v values for SSTX testing. k

values were approximately one order of magnitude for all three tests compared, and fell within a typical range of shale, unweathered marine clay, and glacial till (Freeze and Cherry 1979). Previous research on ESR mixtures (Dunham-Friel 2009 and Weichert 2011) has not indicated a significant increase in k measured during isotropic consolidation with increasing RC.

Table 6.8 Comparison of the coefficient of consolidation (c_v), the modulus of volume compressibility (m_v) and the hydraulic conductivity (k) for isotropically compressed large and small-scale triaxial specimens

Test ID	c_v (m^2/yr)	m_v (m^2/MN)	k (m/s)
LSTX 6.7-mm - 50kPa	842	0.57	1.49E-09
LSTX 6.7-mm - 100kPa	73	0.65	1.47E-10
LSTX 6.7-mm - 200kPa	13	0.37	1.52E-11
SSTX 6.7-mm - 50kPa	491	0.80	9.99E-08
SSTX 6.7-mm - 100kPa	31	1.30	9.77E-09
SSTX 6.7-mm - 200kPa	0.94	0.79	1.73E-10

6.3.4 Undrained Axisymmetric Response

An explanation of the undrained axisymmetric response for ESR specimens subjected to a static, monotonic axial load is included in the following sections. Results are presented in a rigorous CS framework, providing a unique insight for each mixture type tested. Also, d_R is compared for two mixtures closely resembling CS, and results of this study are compared to previous research on ESR mixtures tested in a smaller scale triaxial apparatus (SSTX).

6.3.4.1 Critical State

Critical state values of p', q, and v are defined at the point of maximum ε_a for all tests. Critical state lines (CSL) in $\ln(p') - v$ and $p' - q$ space can be estimated from Figures 6.31 and 6.32, respectively. Γ_{cs}, values are within the range of values published for highly plastic clays (Atkinson 2007). Slopes of the CSL in $\ln(p') - v$ space seem to increase with increasing nominal rubber particle diameter. The slope of the CSL in $p' - q$ space indicates the critical state parameter M_{cs}. M_{cs} values are greater for 6.7-mm ESR mixtures than 19.0-mm ESR mixtures. CSL results for both ESR mixtures are similar to those presented in literature for similar cohesive soil rubber mixtures (Dunham-Friel 2011).

Figure 6.31 (a) presents the differences in the NCL obtained during isotropic compression and the CSL obtained a critical state. As described in Schofield and Wroth (1969), the NCL and URL should be parallel in $\ln(p') - v$ space. The discrepancy in slopes could be accounted for by assuming that the NCL was not obtained over a lower range of p' and specimens were still over consolidated due to the large static efforts required for compaction (discussed in Chapter 4). Another potential factor contributing to the discrepancies is the difference in target and actual p' values obtained post isotropic compression (Table 5.7). Figure 6.31 (b) presents the stress paths during undrained axisymmetric compression in the compression ($\ln(p') - v$) plane.

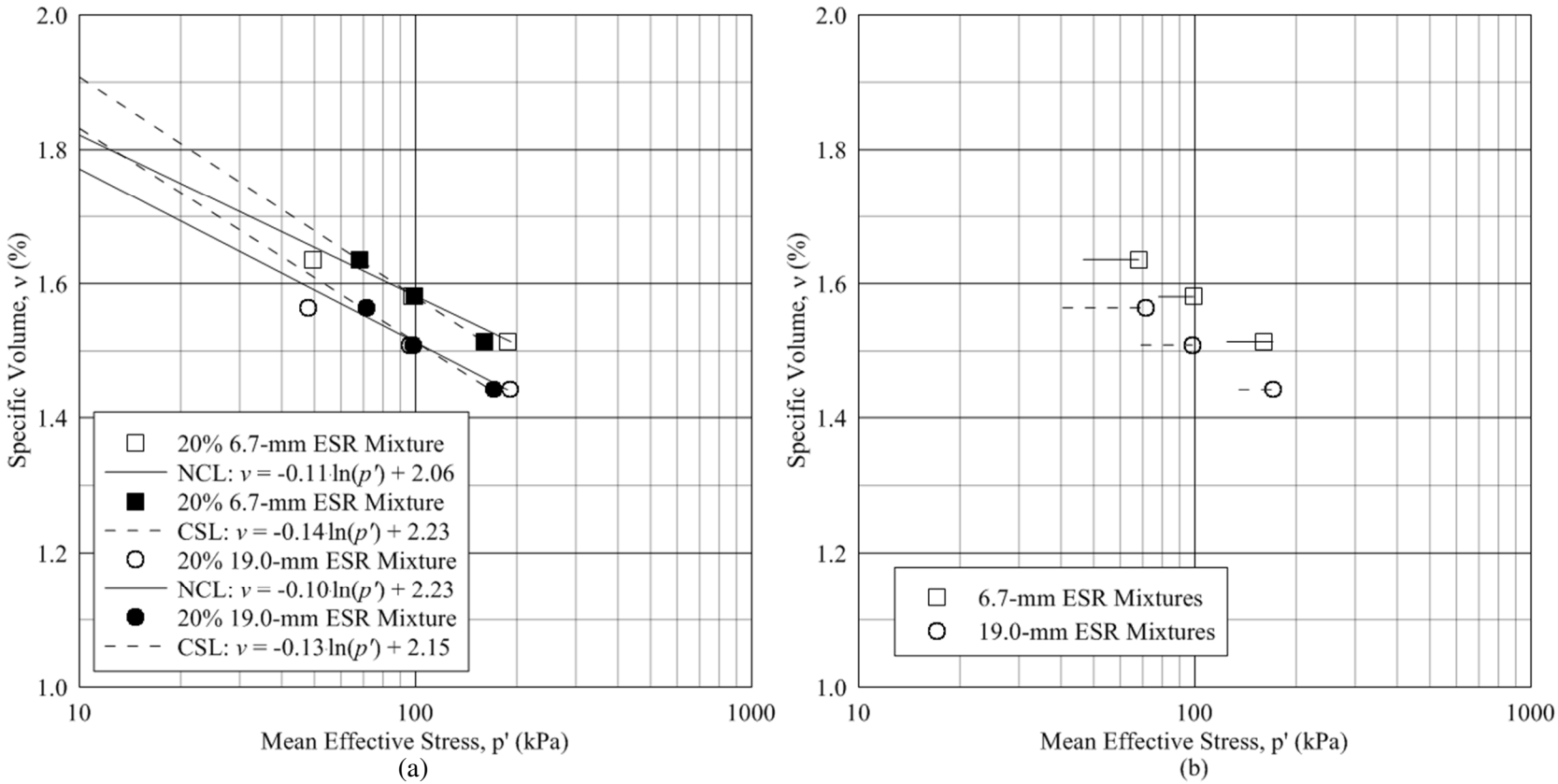

Figure 6.31 Undrained axisymmetric compression results for 6.7- and 19.0-mm expansive soil-rubber specimens: (a) a comparison of the normal compression and critical state lines in the compression ($\ln(p') - v$) plane used to determine critical state parameters (Γ_{cs} and λ_{cs}); and (b) variations in the mean effective stress in the compression plane

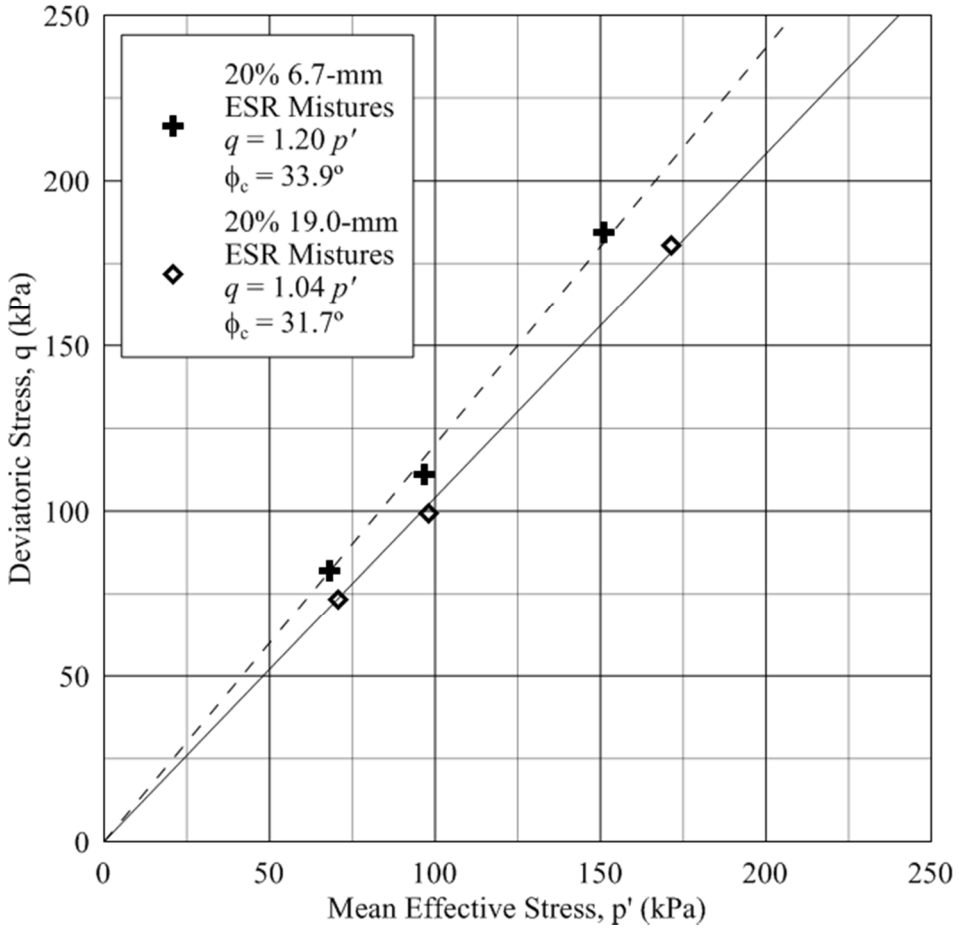

Figure 6.32 CSL in p' – q space for both 6.7 and 19.0-mm ESR specimens used to determine the critical state parameter M_{cs}

Critical state parameters (M_{cs}, Γ_{cs}, κ_{cs} and λ_{cs}) are summarized in Table 6.9. Both ϕ_p and ϕ_{cs}, as well as M_{cs} were greater for 6.7-mm ESR mixtures in comparison to 19.0-mm ESR mixtures. Critical state friction angles were calculated at the maximum value of ε_a for all specimens. The critical state friction angle was approximately 4° larger for 6.7-mm ESR specimens in comparison to 19.0-mm ESR specimens. The peak friction angle was determined at the point of maximum q/p', which occurred after phase transformation or Δu_{max} for all specimens. The peak friction angle displayed a decreasing tendency with increasing p' post isotropic compression for 19.0-mm ESR specimens. In addition, A_f and

M_{cs} values were also greater for the smaller 6.7-mm nominal rubber particle diameter. A_f values ranged from 0.21 to 0.69 for all tests. Clay soils with A_f values between 1.0 and 0.7 have over consolidation ratio's (OCR's) of approximately 1, clay soils with A_f values between 0.5 and 0.7 have OCR's between 1 and 2, and clay soils with A_f values between 0.2 and 0.5 have OCR's between 2 and 3 (Mayne and Stewart 1988). According to Mayne and Stewart (1988) specimens axisymmetrically compressed under a target p' of 50, 100, and 200 kPa exhibit OCR values between 2 and 3, between 1 and 3, and approximately 1, respectively. Finally, critical state lines in the compression plane were similar for both mixtures tested with Γ_{cs} values varying by 0.06 and λ_{cs} values varying by 0.01; as shown in Table 6.9. Reasons for the discrepancies in shear strength between 6.7- and 19.0-mm ESR mixtures will be discussed in Section 6.3.4.

Table 6.9 Comparison of and peak and critical state friction angles (ϕ_p and ϕ_{cs}), Skempton's pore water pressure coefficient at failure (A_f) and critical state parameters (M_{cs}, λ_{cs} and Γ_{cs}) for 6.7- and 19.0-mm expansive soil-rubber mixtures axisymmetrically compressed under undrained conditions

Test ID	ϕ_p	M_{cs}	ϕ_{cs}	A_f	λ_{cs}	Γ_{cs}
6.7mm - 50kPa	36.7	1.20	30.0	0.27	0.14	2.23
6.7mm - 100kPa	36.2			0.51		
6.7mm - 200kPa	37.7			0.69		
19mm - 50kPa	37.7	1.04	26.3	0.21	0.13	2.15
19mm - 100kPa	36.5			0.48		
19mm - 200kPa	35.3			0.65		

As discussed in Chapter 3, a theoretical CS condition during axisymmetric compression is obtained when additional shearing results in constant deviator stress, constant confining stress, and constant pore pressure change or equilibrium in the stress state

(Schofield and Wroth 1968), or $\delta q/\delta\varepsilon_a = \delta p'/\delta\varepsilon_a = \delta\Delta u/\delta\varepsilon_a = 0$. Figures 5.10 through 5.13 display the undrained monotonic response of ESR mixtures during LSTX axisymmetric compression testing. As presented in Figure 5.10, 6.7-mm ESR mixtures exhibit continued increase in q and 19.0-mm ESR mixtures exhibit relatively constant q at ε_a of approximately 30%. As presented in Figure 5.11, both 6.7-mm and 19.0-mm ESR mixtures exhibited a more constant Δu at ε_{acs} as p' after isotropic compression decreases. Also, as presented in Figure 5.12, stress paths generally display an increasing cohesiveness with the CSL in the effective stress plane for lower values of p' after isotropic compression. Therefore, the specimens most closely resembling critical state at maximum ε_a are those with the lowest v and p' after isotropic compression, and in general the 19.0-mm ESR specimen with the lowest v and p' after isotropic compression is more representative of CS in comparison to the 6.7-mm ESR specimen with the lowest v and p' after isotropic compression due to a more constant q with increasing ε_a.

6.3.4.2 Effect of Rubber Particle Size

As shown in Figure 6.33, q_{cs} and Δu_{cs} deviate by 1, 3 and 21 kPa and 5, 1 and 13 kPa, respectively, for 6.7-mm and 19.0-mm ESR mixtures at identical target p' values. Δu transitions to greater values for the 6.7-mm ESR specimens in comparison to the 19.0-mm specimens at ε_{ap} to ε_{acs} values. The evolution of q with ε_a is different for the two nominal rubber particle sizes studied. In 6.7-mm ESR specimens, q continues to increase for the duration of the test, although the rate of increase decreases for increasing values of ε_a. In 19.0-mm ESR specimens q reaches a peak value, or asymptote, at 10 to 15% ε_a (decreasing with decreasing post-isotropic compression p') and stays relatively constant throughout the remainder of each axisymmetric compression. Both 6.7- and 19.0-mm

ESR mixtures indicate a tendency toward volume change dilative response in undrained conditions resulting in a decrease in Δu post Δu_{max}. In general increases in Δu were more rapid and ε_a values at which a maximum Δu was obtained were less for 19.0-mm ESR mixtures in comparison to 6.7-mm ESR mixtures for a given post-isotropic compression p'. Failure mechanisms were determined as bulging for all specimens tested in undrained axisymmetric compression (Figures D.8 (h) and (i)). Area corrections based on bulging failures were presented in Chapter 4.

Effective stress paths (Figure 6.33 (c)) showed similar trends toward critical state for both mixtures values of post-isotropic compression p'. Both mixtures are initially rigid and variations in q do not induce large alterations in p'. Further increases in q over ε_a ranges of strains from small (described in Section 3.3.4) to Δu_{max} result in a strain hardening behavior. Undrained instability states (Murthy et al. 2007) did not develop during axisymmetric compression of the six specimens, rather phase transformations (tendency toward a dilative volume response in undrained conditions) were observed. Phase transformations were observed at the onset of Δu_{max}. The strain at which phase transformation was observed increases with post-isotropic compression p' for both 6.7-mm and 19.0-mm ESR specimens. Finally, A_f values were greater for 19.0-mm ESR mixtures in comparison to 6.7-mm ESR mixtures for a given post isotropic compression p'. As discussed earlier larger A_f values indicate lower OCR values (Mayne and Stewart 1988). Therefore, it is likely that 19.0-mm ESR specimens had higher OCR values in comparison to 6.7-mm ESR specimens, primarily due to an increase in solid material for a representative unit volume and a slightly denser soil matrix fabric obtained during

compaction and carried through subsequent steps of LSTX testing, as discussed in Section 6.2.1.

A comparison of the effect d_R has on CS parameters was conducted based upon the six specimens axisymmetrically compressed, and is discussed in Section 6.3.3. As discussed previously, the point at which 6.7- and 19.0-mm ESR specimens were deemed closest to critical state ($\delta q/\delta\varepsilon_a = \delta p'/\delta\varepsilon_a = \delta\Delta u/\delta\varepsilon_a = 0$) occurred at ε_{acs} (Table 5.9). Figure 6.24 presents the general trends in q and u_e versus ε_a and the stress paths q versus p' for 6.7 and 19.0-mm ESR mixtures.

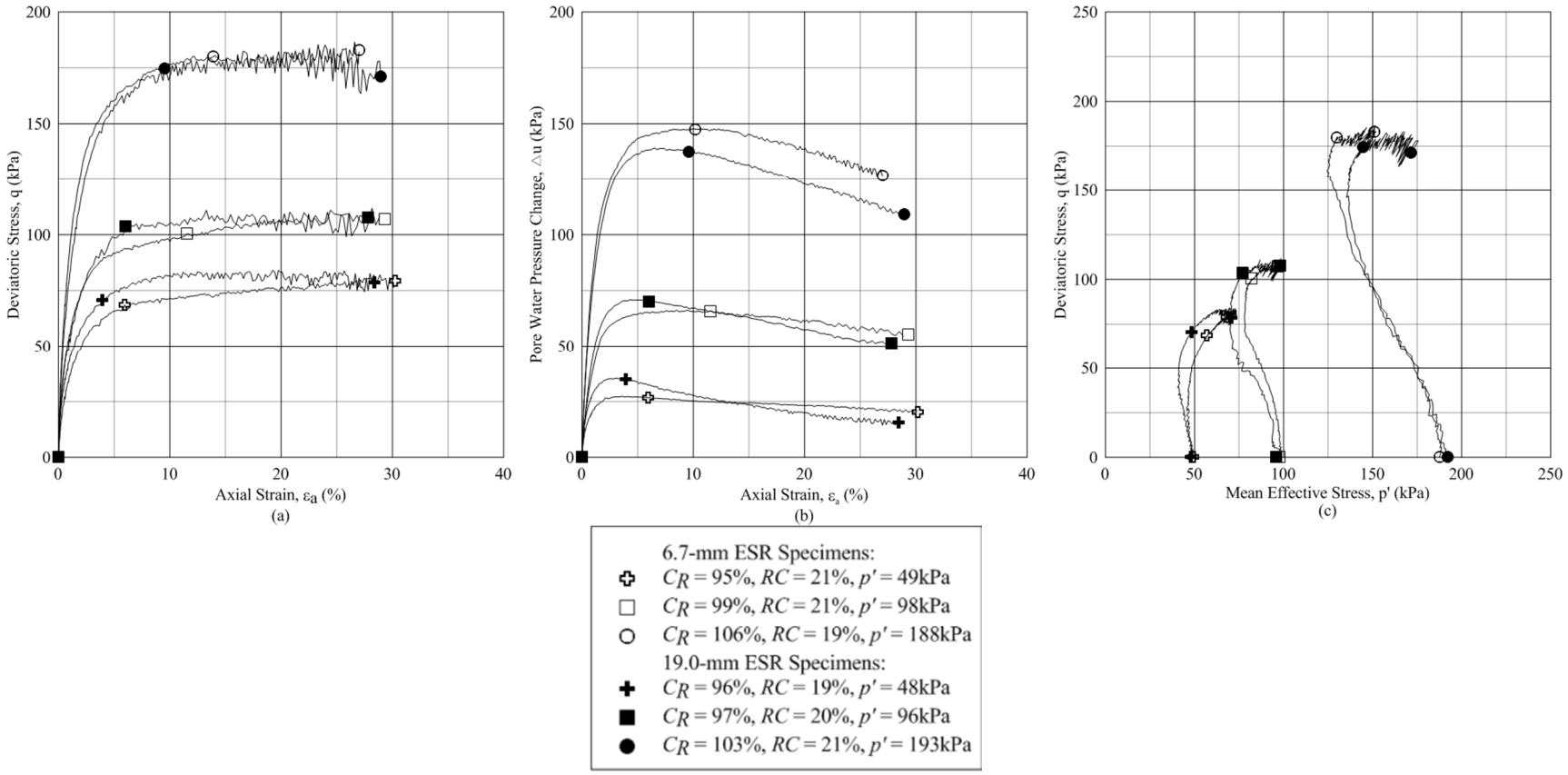

Figure 6.33 Static and monotonic axisymmetric compression response under isotropically compressed undrained conditions for 6.7- and 19.0-mm expansive soil-rubber mixtures: (a) q versus ε_a; (b) Δu versus ε_a; and (c) q versus p'. The three specimen states indicated include: initial, the maximum q/p' ratio and the termination of the test or critical state.

As presented in Figure 6.14, 19.0-mm ESR mixtures was able to mobilize a larger q at ε_a < 25% although 6.7-mm ESR mixtures demonstrate a continued increase in q, or strain hardening, over the entire range of ε_a investigated. 19.0-mm ESR mixtures indicated a larger and more rapid decline in Δu for levels of ε_a exceeding Δu_{max} in comparison to 6.7-mm ESR mixtures. For example, the maximum $\delta\Delta u/\delta\varepsilon_a$ during axisymmetric compression for 6.7-mm and 19.0-mm ESR specimens isotropically compressed to a p' = 50 kPa was 0.33 and 3.65 kPa/%, respectively. Also, Δu_{max} - Δu_{cs} is approximately 3 times larger (6.5 versus 20.2) for the 19.0-mm ESR mixture in comparison to the 6.7-mm ESR mixture, both isotropically compressed to a p' = 50 kPa.

6.3.4.3 Effect of Specimen Size

Data collected during LSTX testing on 6.7-mm ESR specimens was compared to previous research by Dunham-Friel (2009) during SSTX testing on 6.7-mm ESR mixtures. Similar to research presented in this study, Dunham-Friel (2009) analyzed initial state parameter (C_R, w and RC) effects on the mechanical response of ESR mixtures in monotonic, undrained, axisymmetric compression. The CS framework was employed to analyze mechanical response, and p' post isotropic compression ranged from 50 to 200 kPa. The mechanical behavior of 6.7-mm specimens tested in LSTX axisymmetric compression were compared to the three specimens tested in SSTX axisymmetric compression most closely resembling equal levels of p', RC, and C_R (or v) post isotropic compression. Figure 6.34 compares the deviatoric stress and pore water pressure change response with increasing axial strains in addition to the stress path for mixtures tested in both LSTX and SSTX axisymmetric compression. Figure 6.35

compares the CSL in (a) $\ln(p') - v$ space and (b) $p' - q$ for LSTX and SSTX specimens sheared in undrained axisymmetric compression. Critical state parameters indicated in each legend of Figure 6.35 are reflected in Table 6.7.

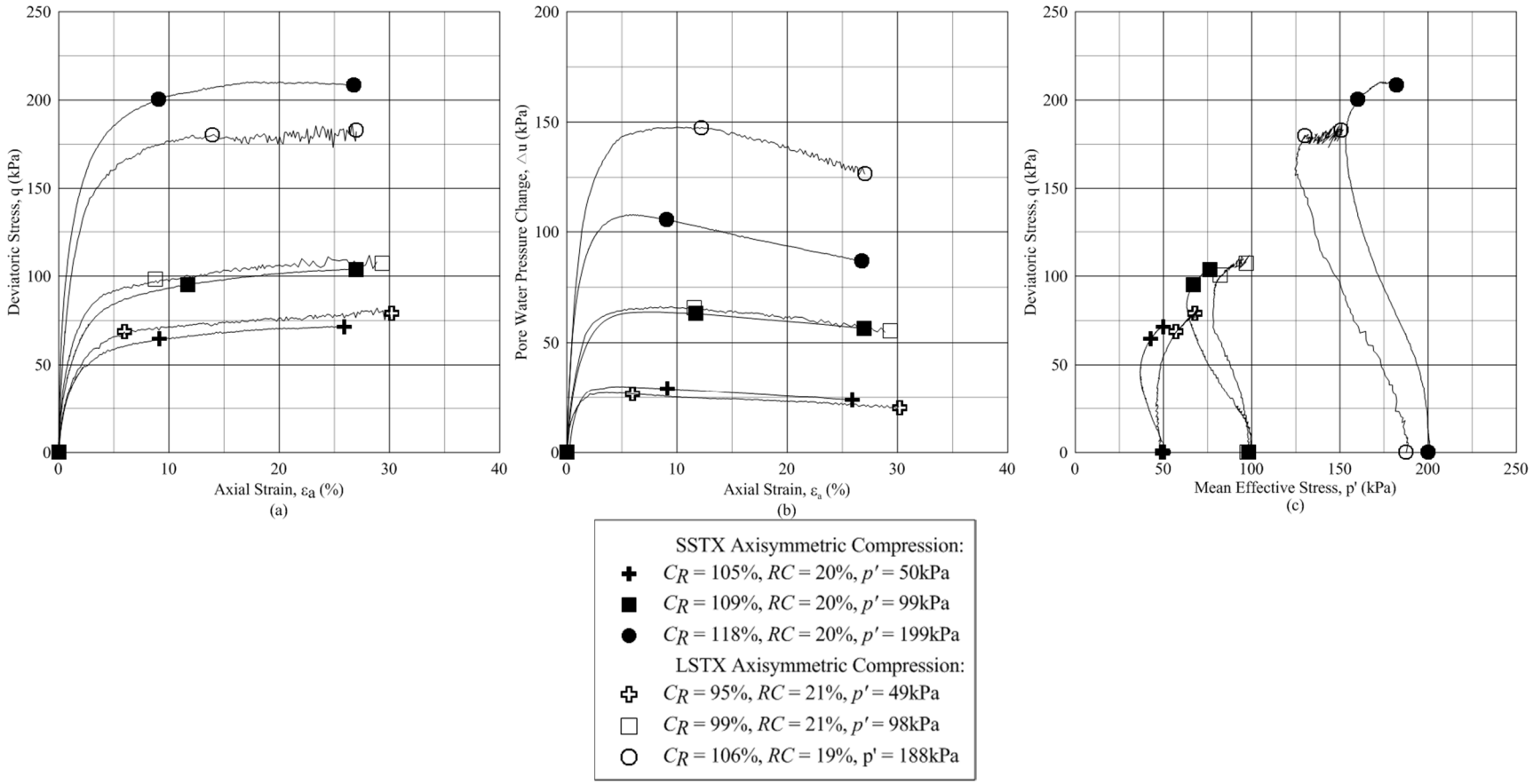

Figure 6.34 Static and monotonic axisymmetric compression response under isotropically compressed undrained conditions for small and large-scale 6.7-mm expansive soil-rubber mixtures: (a) q versus ε_a; (b) Δu versus ε_a; and (c) q versus p'. The three specimen states indicated include: initial, the maximum q/p' ratio and the termination of the test or critical state.

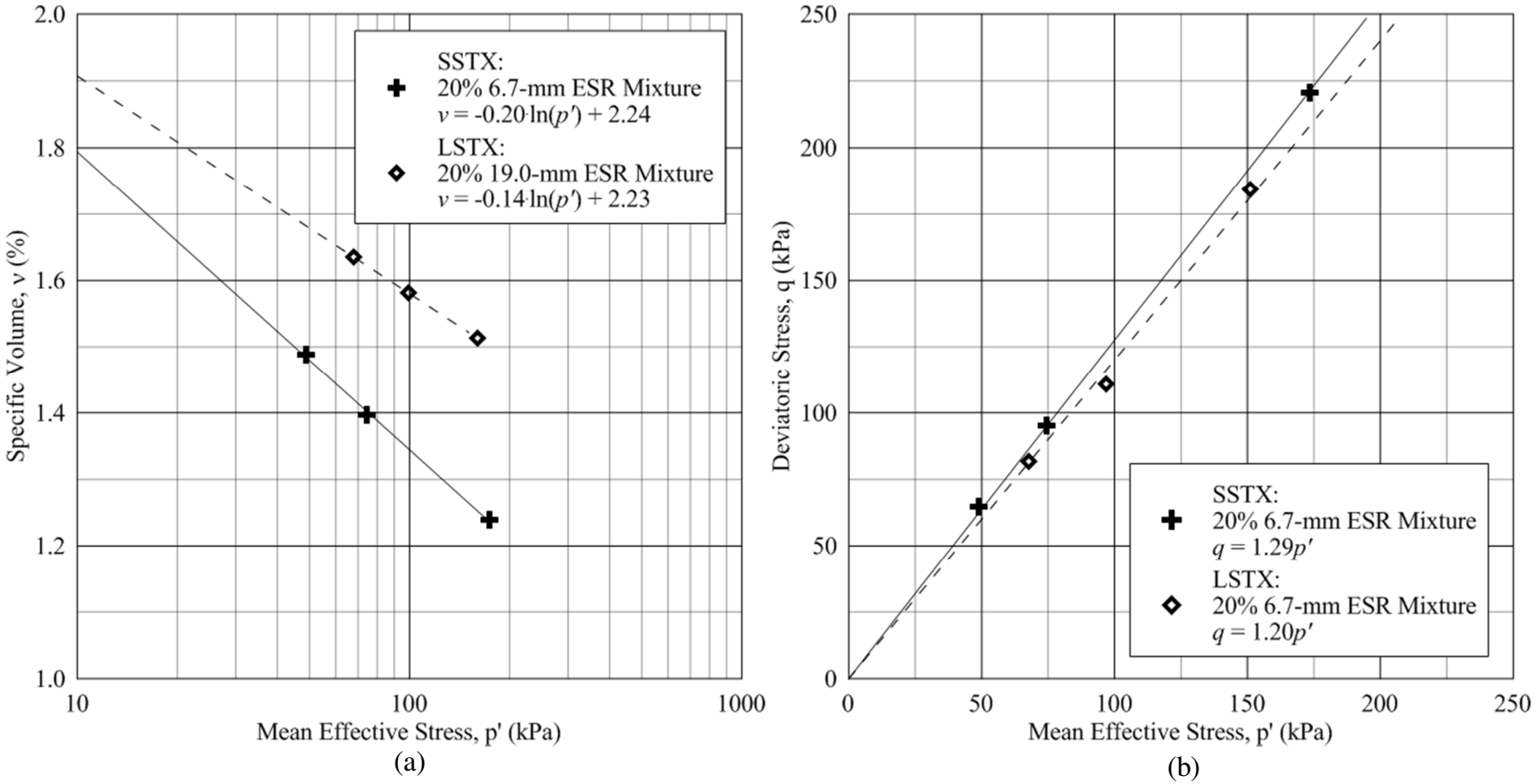

Figure 6.35 ESR mixtures tested in LSTX and SSTX axisymmetric compression: (a) CSL in ln(p') – v space used to determine the critical state parameters Γ_{cs} and λ_{cs}; (b) CSL in p' – q space used to determine the critical state parameter M_{cs}

Peak and critical state friction angles, A_f and CS parameters for the two LSTX and SSTX compared are summarized in Table 6.10. Larger decreases in ϕ_p were observed with increasing p' post for SSTX testing in comparison to LSTX testing. As shown, A_f is higher for SSTX specimens than for LSTX specimens, but the same general trend of increasing A_f with increasing p' is displayed for both specimen sizes. Finally, the CS parameters for the CSL in the compression plane ($\ln(p') - v$ space), λ_{cs} and Γ_{cs}, are appreciably close for both LSTX and SSTX testing. Deviations of Γ_{cs} are likely due to a different C_R post isotropic compression and differences in γ_{dmax} and w_{opt} based on standard Proctor compaction testing. Both density factors likely contributed to differences in the soil matrix density and subsequent specimen behavior during undrained axisymmetric compression. The CS parameter M_{cs} varies by 0.09 and when comparing SSTX to LSTX testing. The differences in M_{cs} are also likely due differences in the soil matrix density and differences in ε_{acs} for LSTX specimens in comparison to SSTX specimens.

Table 6.10 Comparison of and peak and critical state friction angles (ϕ_p and ϕ_{cs}), Skempton's pore water pressure coefficient at failure (A_f) and critical state parameters (M_{cs}, λ_{cs} and Γ_{cs}) for large and small-scale expansive soil-rubber mixtures axisymmetrically compressed under undrained conditions

Test ID	ϕ_p	M_{cs}	ϕ_c	A_f	λ_{cs}	Γ_{cs}
LSTX 6.7-mm - 50kPa	37.4	1.20	30.0	0.27	0.14	2.23
LSTX 6.7-mm - 100kPa	38.0			0.51		
LSTX 6.7-mm - 200kPa	37.6			0.69		
SSTX 6.7-mm - 50kPa	38.4	1.29	30.1	0.63	0.20	2.24
SSTX 6.7-mm - 100kPa	36.8			0.72		
SSTX 6.7-mm - 200kPa	32.0			0.78		

As presented in Table 6.10, critical state parameters are similar for both LSTX and SSTX testing. Also, as presented in Section 6.3.4, critical state parameters were similar for both 6.7- and 19.0-mm ESR mixtures. A comparative analysis from all TX conducted in the presented study in addition to those produced in previous studies (Dunham-Friel 2009) indicate the ability to reasonably predict the undrained axisymmetric compression response for larger tire chip ESR specimens using conventional specimen and triaxial sizes with ESR specimens employing granulated rubber at similar state parameters of C_R or v, RC and p'.

6.4 Swell and Compression Response Comparison for SC and TX Testing

Comparisons between one-dimensional swell-compression testing and axisymmetric compression testing indicate that in general swell response was less for LSTX and greater for both SSC and LSC testing. The equivalent vertical $S_{\%}$ for mixtures with similar initial state parameters is summarized in Table 6.11. Differences in $S_{\%}$ are likely due to the larger inundation pressure subjected to LSTX specimens. In order to validate the use of various apparatuses (SSC, LSC, LSTX, and FSSM) to measure the swell response of ESR mixtures, similar effective stress conditions during inundation are necessary.

Table 6.11 Swell percent for 6.7- and 19.0-mm expansive soil-rubber mixtures tested in various scales and apparatuses with similar initial state parameters (C_R, w and RC)

Test Type	d_R (mm)	Initial State Parameters			Inundation Pressure (kPa)	$S_{\%}$ (%)
		C_R (%)	w (%)	RC (%)		
SSUSC	6.7	94.7	18.5	19.9	6.1	3.6
LSUSC	6.7	95.1	18.6	19.9	6.1	3.0
FSSM	6.7	90.0	17.5	22.4	6.1	1.7
LSTX	6.7	95.4	17.8	19.1	20.0	1.8
LSUSC	19.0	95.9	19.0	19.3	6.1	3.5
FSSM	19.0	92.1	17.3	19.5	6.1	2.7
LSTX	19.0	95.4	18.4	20.3	20.0	2.0

Comparisons between one-dimensional swell-compression testing and axisymmetric compression testing can be accomplished through the plastic volume strain ratio (Λ), or the difference in the slope of the NCL and URL divided by the slope of the NCL. Table 6.12 presents Λ for various ESR specimens tested in different apparatuses with similar initial states prior to the application of effective stress or isotropic compression (LSTX). The definition of slopes of the NCL and URL for SSC testing is more pronounced in comparison to other methods due to the large number of effective stresses defining each curve. A Λ value of 0.5 indicates a URL slope that is one-half of the respective NCL slope. Λ values presented in Table 6.12 for SSC are generally less than rubber alone, greater than rubber sand mixtures with *RC* values less than 50% (Lee et al. 2010) and generally less than remolded clayey soils presented in this study. For example, Λ for a SSC specimen with initial states C_R, w and *RC* equal to 94.8, 19.9 and 0%, respectively, is 0.69 (from Table 5.2) which is significantly greater than 0.43 (Table 6.9) displaying the more elastic behavior for ESR specimens in comparison to expansive soil without the addition of rubber. In general, more elastic behavior is represented for specimens tested in LSC, likely due to an inadequate applied effective stress necessary to accurately define the slope of the NCL. LSTX specimens indicated similar plastic volume ratios for 6.7- and 19.0-mm specimens. An increased number of specimens one-dimensionally and isotropically compressed at similar state parameters (C_R or v, *RC* and p' or σ'_z) are needed to fully assess the differences in the method of compression and specimen size on the slopes of the NCL and URL and Λ.

Table 6.12 Plastic volume strain ratio for 6.7- and 19.0-mm expansive soil-rubber mixtures tested in various scales and apparatuses with similar initial state parameters (C_R, w and RC)

Test Type	d_R (mm)	Initial State Parameters			Λ (%)
		C_{RI} (%)	w_I (%)	RC (%)	
SSC	6.7	94.7	18.5	19.9	0.43
LSC	6.7	95.1	18.6	19.9	0.79
LSTX	6.7	95.4	17.8	19.1	0.59
LSC	19.0	95.9	19.0	19.3	0.75
LSTX	19.0	95.4	18.4	20.3	0.60

CHAPTER 7: CONCLUSIONS

7.1 Summary

A rigorous and systematic study was conducted to characterize the mechanical response of expansive soil-rubber (ESR) mixtures tested in one-dimensional swell-compression (small and large scales), field-scale swell-monitoring and undrained axisymmetric compression. The expansive soil was sampled from a Pierre shale deposit in Fort Collins, CO. The STR utilized had nominal maximum particle sizes equal to 6.7 and 19.0 mm. ESR mixtures were compacted to various specimen sizes to target C_R, w and RC values based on standard Proctor compaction testing parameters (ASTM D698). One-dimensional testing was utilized to characterize the swell and compression response of ESR mixtures tested under laterally confined boundary conditions. Axisymmetric compression characterized the intrinsic critical state parameters M_{cs}, ϕ_c, Γ_{cs}, λ_{cs} and κ_{cs} under static, monotonic, undrained triaxial compression. The main conclusions resulting from this study are summarized in the following sections.

7.1.1 Specimen Preparation and Uniformity

A specimen preparation method with the ability to produce uniform specimens was implemented in this study. Specimen compaction methods were based on ASTM D4546 and ASTM D4767 for remolded specimens tested in one-dimensional compression and axisymmetric compression, respectively. ASTM D4767 provided uniform specimens producing absolute deviations in C_R, w and RC between layers within 2.5, 1 and 1% of target values, respectively, for LSTX ESR specimens (Table 5.1). SSC indicated that, as

RC increased, specimens became more difficult to compact to a target C_R value. LSC indicated *RC* values varied more for 19.0-mm ESR specimens in comparison to 6.7-mm ESR specimens. Larger variations in the initial state parameters were observed for field-scale swell-monitoring in comparison to laboratory testing. Using conventional techniques for specimen preparation and reconstitution resulted in relatively uniform ESR specimens and produced actual state parameters within acceptable limits to target values.

7.1.2 One-Dimensional Swell-Compression

7.1.2.1 Effect of Initial State Parameters

For the range and deviation of each parameter investigated, swelling parameters ($S_{\%}$ and σ'_{zs}) are most impacted by *w*, C_R and *RC*, in sequential order. The increase in swell due to variations in *w*, C_R and *RC* are caused by differences in the matric potential, level of compaction, and soil matrix density and replacement of expansive material, respectively. *RC* variations had the most significant impact on *M* and m_v followed by C_R and *w*. Both *M* and *E* increased with increasing C_R and decreased with increasing *RC* and were most impacted by *RC*, followed by C_R and *w*. Both *E* and m_{vr} decreased with increasing C_R and with decreasing *RC* and were most impacted by *RC*, followed by C_R and *w*. *M*, m_v, *E* and m_{vr} were less impacted by *w* in comparison to C_R and *RC*. Variations in compressibility are primarily due to differences in the soil matrix density, compressibility differences of the rubber particles in comparison to the soil matrix and the initial level of compaction. When implementing ESR mixtures, it will be paramount to adequately control the initial *w* to control swelling parameters and adequately control C_R and *RC* to limit variations in compressibility.

Both $S_{\%}$ and σ'_{zs} increased with increasing d_R and decreasing initial w. The slight increase in swell due to d_R can be attributed to differences the optimum water content for both mixtures and potential differences in the relative deformability of both d_R sizes. Swell response was more impacted by the initial water content in comparison to the nominal maximum rubber particle diameter due to large variations in the matric potential and similar soil matrix densities. In general, M and E decreased with increasing initial w, and both M and E values showed little variation for both 6.7-mm and 19.0-mm ESR mixtures.

Observed $S_{\%}$ was largest for the Pierre shale soil field plot followed by the 19.0-mm and 6.7-mm ESR field plots, respectively. The significant decrease in $S_{\%}$ for ESR mixtures can be attributed to the replacement of expansive material with non-expansive (STR) material. During swell-monitoring, swell occurred more rapidly in the Pierre shale soil in comparison to the ESR mixture plots due to higher compaction resulting in a denser soil matrix and a larger amount of expansive soil per unit volume resulting in a higher matric potential. An increased number of roller passes (32 to 33) were required to compact ESR mixtures to a lesser C_R in comparison to the Pierre shale soil plot (16). The increase in roller passes is likely due to an increased dissipation of compaction energy as a result of employing a concrete pad as a rigid subgrade to compact and confine each plot base.

7.1.2.2 Effects of Particle and Specimen Sizes

Swelling parameters $S_{\%}$ and σ'_{zs} were similar and increased by about 1% and 6 kPa, respectively, with increasing d_R in LSC due to a decrease in the optimum water content of

both 20% STR ESR specimen types. As specimen sizes increased from SSC to LSC to FSSM both $S_{\%}$ and σ'_{zs} may have decreased due to differing height to diameter ratios, interfacial materials and levels of saturation post inundation. Increased specimen sizes had a negligible effect on compressibility (M, m_v, E and m_{vr}) parameters for SSC and LSC testing over a comparable range of applied vertical stresses. The relatively small differences in swelling and compressibility for variations in d_R and specimen size yield a promising potential to reasonably simulate the one-dimensional mechanical response of larger (LSC and FSSM) tire chip ESR mixtures using conventional laboratory techniques with smaller specimens sizes (SSC) with the inclusion of granulated rubber at approximately equal rubber contents.

7.1.4 Isotropic Compression and Undrained Axisymmetric Compression

7.1.4.1 Isotropic Compression

Isotropic-compression critical state parameters κ_{cs} and λ_{cs} were determined: κ_{cs} was 0.05 and 0.04 and λ_{cs} was 0.10 and 0.11 for 6.7-mm and 19.0-mm ESR specimens, respectively. Therefore, the NCL and URL are very similar for 6.7- and 19.0-mm ESR specimens at similar RC, promoting the reasonable prediction of isotropic compression response of tire chip specimens using more conventional laboratory particle sizes (granulated rubber).

7.1.4.2 Undrained Axisymmetric Compression

The CS parameters Γ_{cs} and λ_{cs} were 2.23 and 0.14 for 6.7-mm ESR specimens and 2.15 and 0.13 for 19.0-mm ESR specimens, respectively. M_{cs} was 1.20 and 1.04 for 6.7-mm

and 19.0-mm ESR specimens, respectively. The critical state friction angle was found to be 4° greater for 6.7-mm ESR specimens in comparison to 19.0-mm specimens. The slopes of the CSL in the compression plane and effective stress plane were within 0.1 and 0.16, respectively, for the 6.7- and 19.0-mm ESR specimens at approximately equal *RC* values. Therefore, a reasonable approximation with conservative shear strength (friction angle) results of the undrained axisymmetric compression response of tire chip specimens using more conventional laboratory particle sizes with granulated rubber is possible.

7.1.4.3 Effect of Specimen Size in Undrained Axisymmetric Compression

CS parameters λ_{cs} and Γ_{cs} were 0.13 and 2.23 for LSTX and 0.10 and 1.83 for SSTX testing. M_{cs} was observed to be 1.20 for LSTX testing and 1.29 for SSTX testing. Critical state friction angles were 2° less for LSTX in comparison to SSTX (Dunham-Friel 2009) ESR specimens compacted to similar initial state parameters (C_R, w and RC) and isotropically compressed to similar levels of p'. The slopes of the CSL in the compression plane and effective stress plane were within 0.03 and 0.09, respectively, for the LSTX and SSTX 6.7-mm ESR specimens at approximately equal values of *RC*. Therefore, a reasonable approximation with conservative shear strength (friction angle) results of the undrained axisymmetric compression response of LSTX specimens using more conventional laboratory specimen sizes (SSTX) is possible. Using granulated rubber specimens in SSTX will likely yield a similar behavior and conservative shear strength parameters in comparison to larger specimen sizes (LSTX) utilizing tire chips at approximately equal *RC* values.

7.2 Suggestions for Future Work

Several areas for future development and study involving the mechanical behavior of expansive soil-rubber mixtures:

1. Additional one-dimensional and axisymmetric compressive studies addressing the mechanical response of ESR mixtures utilizing larger variations in d_R (ie the d_R when mechanical behavior deviates significantly from this research and the research by Dunham-Friel (2009));
2. Comparative studies relating the mechanical behavior of ESR mixtures presented in this study with other, more rigid waste products of similar particle size in one-dimensional compression and axisymmetric compression;
3. Unsaturated and cyclic (dynamic) strength to further define the mechanical response of ESR mixtures under varying loading conditions;
4. Additional field scale studies on the swell and compressive response of ESR mixtures employing a wider range of initial state parameters (C_R, w and RC) under typical loads encountered in various civil engineering applications (backfill, traffic and structural loads);
5. Modeling and implementation of ESR mixtures into various civil engineering applications to determine limitations and potential uses of ESR technology in practice.

LIST OF REFERENCES

Abshire M., (2002). "Differential Moisture Migration and Heave Beneath Slabs Over Dripping Expansive Shale." MS thesis, Colorado State University, Fort Collins, CO.

Al-Rawas A.A., Al-Sarmi H., Hago A.W. (2005). "Effect of Lime, Cement, and Sarooj (artificial Pozzolan) on the Swelling Potential of an Expansive Soil from Oman." *Elsevier* vol. 40, 681-687.

Araei A. A., Soroush A., Rayhani M. (2010). "Large_scale Triaxial Testing and Numberical Modeling of Rounded and Angular Rockfill Materials." *Transaction A: Civil Engineering*, vol. 17, no. 3, 169-183.

A-Rawas A. A., Taha R., Nelson, J. D., Al-Shab T. B., Al-Siyabi H., (2002). "A Comparative Evaluation of Various Additives Use in the Stabilizations of Expansive Soils." *Geotechnical Testing Journal* 25(2) 199-209.

Abdi M. R., Parsapajouh A., Arjomand M A. (2008). "Effects of Random Fiber Inclusion on Consolidation, Hydraulic Conductivity, Swelling, Shrinkage Limit and Desiccation Cracking of Clays." *International Journal of Civil Engineering*, vol. 6, no. 4, 284-292.

Al-Tabbaa A., Aravinthan T., (1998). "Natural Clay-Shredded tire Mixtures as Landfill Barrier Materials." *Waste Management* 18, 9-16.

American Society for Testing and Materials, (1998). ASTM D 6270-98. Standard practice for use of scrap tires in civil engineering application.

Amari T., Themelis N. J., Wernick I. K., (1999). "Resource Recovery from Used Rubber Tires." Resources Pollicy 25, 179-188.

ASTM C618. "Standard Specification for Coal Fly Ash and Raw or Calcined Natural Pozzolan for Use in Concrete." *ASTM International*.

ASTM C6270. "Standard Practice for Use of Scrap Tires in Civil Engineering Applications." *ASTM International*.

Atkinson, J. H. (2000). "Non-linear Soil Stiffness in Routine Design." *Géotechnique 50*, 487-508.

Baddock W. A., Calvert, R. H., O'Connor J. T., Swann G. A. (1989). "Geologic Map of the Horestooth Reservoir Quadrangle, Larimer County, Colorado." G.Q. 1625, United States Geological Survey.

Basma A. A., Al-Rawas A. A., Al Saadi S. N., Al-Zadjali R. F., (1998). "Stabilization of Expansive Clays in Oman." *Environmental and Engineering Geoscience* 4(4), 503-510.

Bell F. G., (1996). "Lime Stabilization of Clay Minerals and Soils." *Engineering Geology* 42, 223-237.

Beer F. P., Johnston R. E., DeWolf J. T., Mazurek D. F. (2009). "Mechanics of Materials." McGraw-Hill Book Company: New York.

Benson, C., (1995). "Using shredded scrap tires in civil and environmental construction." University of Wisconsin, Report No. 95-2, *Use of Scrap Tires in Civil and Environmental Construction*.

Benvenga M. M. (2005). "Pier-Soil Adhesion Factor for Drilled Shart Piers in Expansive Soils." MS thesis, Colorado State University, Fort Collins, CO.

Bernal, A., Lovell, C.W., Salgado, R., (1996). "Laboratory study on the use of tire shreds and rubber–sand in backfills and reinforced soil applications." Report FHWA/IN/ JHRP-96/12, Indiana Department of Transportation.

Bergado D. T., Youwa S., Rittirong A. (2005). "Strength and Deformaiton Characteristics of Flay and Cubical Rubber Tyre Chip-Sand Mixtures." *Geotechnique,* vol. 55, no. 8, 603-606.

Bishop A.W., Henkel D J. (1957). "The Measurement of Soil Properties in the Triaxial Test." London: William Arnold.

Bohn, H.L., McNeal, B., L., and O'Conner, G. A. (1985). "Soil Chemistry." John Wiley, New York.

Bozbey I., Garaisayev S., (2010). "Effects of Soil Pulverization Quality on Lime Staibilization of and Expansive Clay." *Environmental Earth Science* 60, 113-1151.

Bressette, T. (1984). "Used Tire Material as an Alternative Permeable Aggregate," *Report No. FHWA/CA/TL-84/07*, Office of Transportation Laboratory, California Department of Transportation, Sacramento, CA.

Budhu M. (2011). "Soil Mechanics and Foundations." John Wiley & Sons: New York.

Carraro, J.A.H., Wiechert, E., Dunham-Friel, J. (2011). "Beneficial Use of Off-Specification Fly Ash to Improve the Small-Strain Stiffness of Expansive Soil-Rubber Mixtures." Proceedings of The World of Coal Ash 2011. http://www.worldofcoalash.org/index.html

CDPHE (2009). "Annual Report to the Transporation Legislation Review Committee on the Status of Waste Tire Recycling in Colorado for the Calendar Year 2009." Section 25-17-202.7, C.R.S.

Cetin H., Fener M., Gunaydin O. (2006). "Geotechnical Properties of Tire-Cohesive Clayey Soil Mixtures as a Fill Material." *Engineering Geology*, 88, 110-120.

Chen F.H., (1988). "Foundations on Expansive Soils." *American Elsevier Science Publ.*, New York.

Cokca E., (2001). "Use of Class C Fly Ashes for the Stabilization of an Expansive Soil." *Journal of Geotechnical and Geoenvironmental Engineering* 127:7, 568-573.

Corey A. T. (1994). "Mechanics of Immiscible Fluids in Porous Media." *Water Resources Publications*, LLC.

Croft J. B. (1967). "The Influence of Soil Mineralogical Composition on Cement Stabilization." *Géotechnique* vol. 19, 119-135.

Dickson, E. L., Rasiah, V. and Groenevelt, P. H. (1991). Comparison of four prewetting techniques in wet aggregate stability determination. *Canadian Journal of Soil Sciences* 7l:67-72.

Dickson, T. H., Dwyer, D.F., Humphrey, D.N., (2001). "Prototypes tire-shred embankment construction." Transportation Research Record 1755, TRB, National Research Council, Washington, DC, pp. 160–167.

Donaghe R. T. and Torrey III V. H. (1994). "A Compaction Test Method for Soil-Rock Mixtures in which Equipment Size Effects are Minimized." *Geotechnical Testing Journal*, vol. 17, no. 3, 363-370.

Dunham-Friel J., (2009). "Shear Strength and Stiffness of Expansive Soil and Rubber (ESR) Mixtures in Undrained Axisymmetric Compression." MS thesis, Colorado State University, Fort Collins, CO.

Dunham-Friel, J. and Carraro, J.A.H. (2011). "Shear Strength and Stiffness of Expansive Soil and Rubber (ESR) Mixtures in Undrained Axisymmetric Compression." Proceedings of ASCE GeoFrontiers 2011, http://dx.doi.org/10.1061/41165(397)114

Durkee D. B (2000). "Active Zone Depth and Edge Moisture Variations Distance in Expansive Soils." MS thesis, Colorado State University, Fort Collins, CO.

Edil T. B. (2004). "A Review of Mechnical and Chemical Properties of Shredded Tires and Soil Mixtures." *Recycled Materials in Geotechnics* 1-21.

Edincliler, A., (2007). "Using waste tire–soil mixtures for embankment construction In: International Workshop on Scrap Tire Derived Geomaterials ''Opportunities and Challenges"." *Kanto Branch of Japanese Geotechnical Society*, pp. 319–328.

Edincliler A., Baykal G., Saygili A., (2010).” Influence of Different Processing Techniques on the Mechanical Properties of Used Tires in Embankment Construction.” *Waste Management* 30, 1073-1080.\

FEMA (1998). “Special Report: Scrap and Shredded Tire Fires.” *U.S. Fire Administration – Technical Report Series*, USFA-TA-093.

FHWA (2008). “User Guidelines for Waste and Byproduct Materials in Pavement Construction.” FHWA-RD-97-148.

Fityus S. G., Smith D. W., Allman M. A. (2004). “Expansive Soil Test Site Near Newcastle.” *Journal of Geotechnical and Geoenvironmental Engineering* July 2004, vol. 130, no. 7, 686-695.

Fumagalli, E., “Tests on Cohesionless Materials for Rockfill Dams.” *Journal of Soil Mechanics and Foundation Engineering, ASCE*, vol. 95, 207-233.

Fredlund D. G. and Rahardjo H. (1993). “Soil Mechanics in Unsaturated Soils.” John-Wiley and Sons.

Frost. R. J. (1973) “Some Testing Experiences and Characteristics of Boulder-Gravel Fills in Earth Dams.” *ASTM, STP 523*, 207-233.

Fox (2011). “Critical State, Dilantancy and Particle Breakage of Mine Waste Rock.” MS thesis, Colorado State University, Fort Collins, CO.

Ghazavi, M. (2004). “Shear strength characteristics of sand–mixed granular rubber.” *Geotechnical and Geological Engineering* 22, 401–416.

Goode, J.C. (1982). “Heave prediction and moisture migration beneath slabs on expansive soils.” M.S. thesis, Colorado State University, Fort Collins, CO.

Graham, J., Saadat, F., Gray, M.N., Dixon, D.A., and Zhang, Q.-Y. (1989) “Strength and volume change behaviour of a sand.bentonite mixture.” *Canadian Geotechnical Journal*, vol. **26,** 292-305.

Grefe R. (1989). “Review of waste characterization of shredded tires.” Interdepartmental Memorandum, Wisconsin Department of Natural Resources, Madison, Wisconsin.

Gue S.S. and Liew S.S. (2001) “Fill Compaction and Its Consequences of Non-Compliance.” *Conference Technology CONTEC, Kota Kinabalu*, Sabah, 11-13.

Hamberg D. J. (1985). “A Simplified Method for Predicting Heave in Expansive Soils.” MS thesis, Colorado State University, Fort Collins, CO.

Harvey O. R., Harris J. P., Herbert B. E., Stiffler E. A., Haney S. P., (2010). "Natural Organic Matter and the Formation of Calcium-Silicate-Hydrates in Lime-Stabilized Smectites: A Thermal Analysis Study." *Thermochimica Acta* 505, 106-113.

Holtz W. G. and Willard M. (1956). "Triaxial Shear Characteristics of Clayey Gravel Soils." *Journal of Soil Mechanics and Foundation Engineering*, ASCE, vol. 85, 143-149.

Howell J. L., Shachelford, C. D., Amer, N. H., and Stern, R.T. (1997). "Compaction of Sand-Processed Clay Soil Mixtures." *Geotechnical Testing Journal*, vol. 20, 443-458.

Humphrey, D.N. (2005). "Effectiveness of Design Guidelines for Use of tire Derived Aggregate as Lightweight Embankment Fill." *Recycled Materials in Geotechnics*.127:61-74.

Hunt R. E. (2005). "Geotechnical Engineering Investigation Handbook." United States: CRC Press.

Jang J. W., Taek-Soo Y., Jae-Hyum O., Iwao I., (1998). "Discarded Tire Recycling Practices in the United States, Japan and Korea." *Resources, Conservation and Recycling* 22, 1-14.

Johnson, L.D. (1979). Overview for design of foundations on expansive soils. U.S. Army Eng. Waterways Exp. Sta., Vicksburg, MS, Mics. Paper GL-79-21.

Juma M., Markoš K. J., Bafrnec J. M., (2006). "Experimental Study of Pyrolysis and Combustion of Scrap Tire." *Polymers for Advanced Technologies* 18, 144-148. John Wiley and Sons.

Kasangaki G. J., Towhata I., (2009). "Wet Compcation and Lime Stabilization to Mitigate Volume Change Potential of Swelling Clayey Soils." *Soils and Foundations* 49:5, 813-821.

Kim H. K., Santamarina J C. (2008). "Sand-Rubber Mixtures (Large Rubber Chips)." *Canadian Geotechnical Journal*, 45: 1457-1466.

Knechtel, M. M., and S. H. Patterson. (1962). Bentonite deposits of the Northern Black Hills District-Wyoming, Montana, and South Dakota. Geol. Survey Bull. 1082-H. U.S. Gov. Printing Office, Washington, D.C.

Kumar A., Walia B. S., Bajaj A. (2007). "Influence of Fly Ash, Lime, and Polyester Fibers on Compaction and Strength Properties of Expansive Soil." *Journal of Materials in Civil Engineering*, vol. 19, no. 3, 242-248.

Lee C., Truong Q. H., Lee W., Lee J. S. (2010). "Characteristics of Rubber-Sand Particle Mixtures According to Size Ratio." *Journal of Materials in Civil Engineering*, vol. 22, no. 4, 323-331.

Lee J. S., Dodds J., Santamarina C. (2007). "Behavior of Rigid-Soft Particle Mixtures." *Journal of Materials in Civil Engineering*, vol 19, no 2, 179-184.

Lin C., Huang C., Shern C. (2008). "Recycling Wast Tire Powder for the Recovery of Oil Spills." *Resources, Conservation and Recycling* 52, 1162-1166.

Lowe, J. "Shear Strength of Coarse Embankment Dam Materials." *Proc., 8th Int. Congress on Large Dams*, vol. 3, 745-761.

Manion, W. P., and Humphrey, D. N. (1992) "Use of Tire Chips as Lightweight and Conventional Embarkment Fill, Phase I—Laboratory," *Technical Paper 91-1*, Technical Services Division, Maine Department of Transportation, Augusta, ME.

Mayne, P. W., Stweart, H. E. (1988). "Pore Pressure Behavior of K_0-Consolidated Calys." *Journal of Geotechnical Engineering*, vol. 114, no. 11, 1340-1346.

Miller D. J. (1996). "Osmotic Suction as a Valid Stress State Variable in Unsaturated Soils." PhD thesis, Colorado State University, Fort Collins, CO.

Miller E. A. and Sowers G. F. (1957). "Strength Charateristics of Soil-Aggregate Mixtures." *Highway Research Bulletin*, vol. 183, 16-23.

Miller W. L., Chadik P. A. (1993). "A study of waste tire leachability in potential disposal and usage environments." Amended Final Report to Florida Department of Environmental Regulation No. SW67.

Mitchell, J.K., and Raad, L., (1973). "Control of volume changes in expansive earth materials." Proc. *Workshop Expansive Clays and Shales in Highway Design and Construction*, 2, 200-219.

Mitchell J. K. (1976). "Fundamentals of Soil Behavior." John Wiley and Sons: New York.

Murthy T. G., Loukidis D., Carraro J. A. H., Prezzi M., Salgado R. (2007). "Undrained Monotonic Response of Clean and Silty Sands." *Géotechnique*, vol. 57, no. 3, 273-288.

Navy (1986). "Soil Mechanics Design Manual." *Naval Facilities Engineering Command.*

Nalbantoğlu Z., (2004). "Effectiveness of Class C Fly Ash as an Expansive Soil stabilizer." *Construction and Building Materials* 18, 377-381.

Nelson, J.D., and Edgar, T.V. (1978). Moisture migration beneath impermeable membranes Proc. 15th Anny. Symp. Eng. Geol. Soil Eng., Idaho Dept. of Highways, Boise, Idaho, April.

Nelson, J. D. and Miller, D. J. (1992). "Expansive Soils: Problems and practice in foundation and pavement engineering," John Wiley and Sons: New York.

Nicolas M.P.B. and Bamburak J.D. (2009). "Geochemistry and mineralogy of Cretaceous shale, Manitoba (parts of NTS 62C, F, G, H, J, K, N): preliminary results." Report of Activities 2009, Manitoba Innovation, Energy and Mines, *Manitoba Geological Survey*, 165-174.

Oquendo W. F., Munoz J. D., Lizcano A. (2010). "Influence of Rotations on the Critical Sate of Soil Mechanics." Computer Physics Communications, 182, 1860-1865.

Őzkul Z., Baykal G. (2007). "Shear Behavior of Compacted Rubber Fiber-Clay Composite in Drained and Undrained Loading." *Journal of Geotechnical and Geoenvironmental Engineering*, vol. 133, no. 7, 767-781.

Park, J.K., Edil, T.B., Kim, J.Y., Huh, M., Lee, S.H., and Lee, J.J. (2003). "Suitability of Shredded Tires as a Substitue for a Landifll Leachate Collection Medium." *Waste Management and Research*, (21)3, 278-289.

Parry R. H. G. (1958). "On the Yeilding of Soils". *Géotechnique* vol. 8, no. 4, 183-186.

Patil U., Valdes J. R., Evans M. T., (2011). "Swell Mitigation with Granulated Tire Rubber." *Journal of Materials in Civil Engineering*, May 2011, 721-727.

Patrick S. M., Wartman J., Grubb D. G., Humphrey D. N., Natale M. F. (2007). "Variability and Scale-Dependency of Tire-Derived Aggregate." *Journal of Materials in Civil Engineering*, March 2007, vol. 19, No.3, 233-241.

Patwardhan A. S., Rao J. S., Gaidhane R.B., (1970). "Interlocking Particle Effects and Shearing Resistance of Boulders and Large Size Particles in a Matrix of Fines on the Basis of Large Scale Direct Shear Tests." *In Proceedings of the 2nd Southeast Asian Conference on Soil Mechanics, Singapore, Southeast Asian Geotechnical Society*, Pathumthani, Thailand, 256-273.

Perko, H. A. (2009). "Helical Piles, A Practical Guide to Design and Installation." Hoboken, New Jersey: John Wiley & Sons Inc.

Pierce, C.E., Blackwell, M.C., (2003). "Potential of Scrap Tire Rubber as Lightweight Aggregate in Flowable Fill." *Waste Management* 23, 197–208.

Porter, A. A. (1977). "The Mechanics of Swelling in Expansive Clays." M.S. thesis, Colorado State University, Fort Collins, CO.

Powrie, W. (2004). "Soil Mechanics Concepts and Applications." New Yourk, NY: Taylor and Francis.

Punthutaecha K., Puppala A. J., Vanapalli S. K., Inyang H. (2006). "Volume Change Behaviors of Expansive Soils Stabilized with Recycled Ashes and Fibers." *Journal of Materials in Civil Engineering*, vol. 18, no. 2, 295-306.

Puppala A. J., Pillapa G. S., Hoyos L. R., Vasudev D., Devulapalli D. (2007). "Comprehensive Field Studies to Address the Performance of Stabilized Expansive Clays." *Transportation Research Record: Journal of the Transportation Research Board*, No. 1989, Vol. 2, 3-12.

Qubain B. S., Seksinsky E. J., Li J., (2000). "Incorporating Subgrade Lime Stabilization into Pavement Design." *Transportation Research Record 1721* 00-0608, 3-8.

Ramamurthy T., Gupta K. K. (1986). "Response Paper on how one Ought to Determine Soil Parameters to be Used in Design of Earth and Rockfill Dams." *Proc. Indian Geotechnical Conf.*, New Delhi, India, vol. 2, 15-19.

Recycling Research Institute (2004). "Scrap Tire and Rubber Users Directory 2004." Thirteenth Edition, *Recycling Research Institute*, Suffield, CT, p 66.

Rochelle P. L., Leroueil S., Trak B., Blais-Leroux L., Tavenas F. (1988). "Observational Approach to Membrane and Area Corrections in Triaxial Tests." Advanced Triaxial Testing of Soil and Rock, *ASTM* STP 977, 715-731.

Rodgers C. D. F., Glendinning S., (2000). "Lime Requirement for Staibilization." *Transportation Research Record 1721* 00-0604, 9-18.

Roscoe K. H., Schofield A. N., and Wroth C. P. (1958). "On the Yielding of Soils." *Géotechnique* vol. 8, no. 1, 22-52.

Rowe P. W. (1959). "Measurement of the Coefficient of Consolidation of Lacustrine Clay." *Proceedings of the Royal Society of London, Series A. Mathematical and Physical Sciences*, 107-116.

Salgado R. (2008). "The Engineering of Foundations." McGraw-Hill: New York.

Salgado, R., Yoon, S., (2003). "Construction of tire shreds test embankment." FHWA/IN/ JTRP-2002/35.

Schlegel M.G., and Stangl K. O. (1987). "Use of Weathered Rock for Engineering Fill in Permafrost Regions of Alaska." *EBA Engineering Inc.*, 379-388.

Schofield A. N., and Wroth C. P. (1968). "Critical State Soil Mechanics." McGraw-Hill Book Company: New York.

Seda, J.H.; Lee, J. C.; Carraro, J.A.H. (2007) "Beneficial Use of Waste Tire Rubber for Swelling Potential Mitigation in Expansive Soils." Proceedings of ASCE Geo-Denver 2007, http://dx.doi.org/10.1061/40916(235)5

Shafiee A. and Jafair M. K. (2004). "Monechanical Behavior of Compacted Composite Clays." *Canadian Geotechnical Journal*, vol. 41, 1152-1167.

Shirley D. J., & Hampton, D. L. (1977). "Shear-wave Measurements in Laboratory Sediments." Austin: The University of Texas at Austin.

Skempton A. W. (1953). "The colloidal Activity of Clays." Proc. 3rd Int. Conf. Soil Mech. Found. Eng., Switzerland. Vol 1:57-61.

Strenk P. M., Wartman J., Grubb D. G., Humphery D. N., Natale M. F. (2007). "Variability and Scale-Dependency of Tire-Derived Aggregate." *Journal of Materials in Civil Engineering*, vol. 19, no. 3, 233-241.

Sunthonpagasit N., Duffey M. R., (2004). "Scrap Tires to Crumb Rubber: Feasibility Analysis for Processing Facilities." *Resources, Conservation and Recycling* 40, 281-299.

Tan T. S., Goh T. C., Karunaratne G. P., Lee S. L. (1994). "Shear Strength of Very Soft Clay-Sand Mixtures." *Geotechnical Testing Journal*, vol. 17, no. 1, 27-34.

Tang A. M., Cui Y. J., Trinh V. N., Szerman Y., Marchadier G. (2009). "Analysis of the Railway Heave Induced by Soil Swelling at a Site in Southern France." *Engineering Geology* vol. 106, 68-77.

Tatlisoz N., Edil T. B., Benson C. H., Park J. K., Kim J. Y., (1996). "Review of environmental suitability of scrap tires." Environmental Geotechnics Report No. 96-7, Department of Civil and Environmental Engineering, University of Wisconsin-Madison.

Tweedie, J.J., Humphrey, D.N., and Sandford, T.C. (1998a). "Full Scale Field Trials of Tire Chips as Lightweight Retaining Wall Backfill, At-Rest Conditions." *Transportation Research Record No*. 1619, Transportation Research Board, 64-71.

USEPA (2005). "Using Coal Ash in Highway Construcion: A Guide to Benefits and Impacts." *EPA*.

USEPA (1999). "Westley Tire Fire." Westley, Stanislaun County, Califonia. U.S. EPA Region IX, San Francisco.

Viswanadham B. V. S., Phanikumar B R., Mukherjee R. V. (2009). "Effect of Polypropylene Tape Fibre Reinforcement on Swelling Behavior of and Expansive Soil." *Geosynthetics International*, vol. 16, no. 5, 393-401.

Warith M. A., Rao S. M. (2005). "Predicting the Compressibility Behavior of Tire Shred Samples for Landfill Applications." *Waste Management*, vol. 26, 268-276.

Wolfe, S.L., Humphrey, D.N., and Wetzel, E.A. (2004). "Development of Tire Shred Underlayment to Reduce Groundborn Vibrations from LTR Track." *Geo-trans* 2001, ASCE (in-press).

Wu, W.Y., Benda, C.C., Cauley, R.F., *(1997). "Triaxial determination of shear strength of tire chips." *Journal of Geotechnical and Geoenvironmental Engineering* 123 (5), 479–482.

Vallejo L. E. and Lobo-Guerrero S. (2005). "The Elastic Moduli of Clays with Dispersed Oversized Particles." *Engineering Geology*, vol. 78, 163-171.

Vallejo L. E., and Mawby R. (1999). "Porosity Influence on the Shear Strength of Granular Material-Clay Mixtures." *Engineering Geology*, vol. 58, 125-136.

Youwai, S., Bergado, D.T., (2004). Numerical analysis of reinforced wall using rubber tire chips–sand mixtures as backfill material. *Computers and Geotechnics* 31, 103–114.

Yoshida R. T., Fredlund D. G., Hamilton J. J. (1983). "The Prediction of Total Heave of a Slab-on-Grade Floor on Regina Clay." *Canadian Geotechnical Journal*, 20, 69-81.

Zeller J. W., Wullimann R. "The Shear Strength of Shell Materials for the Ge-Schenenalp Dam, Switzerland." *Proc., 4th Inst., J. SMFE, London*, vol. 2, 399-404.

Zha F., Liu S., Cui K., (2008). "Behavior of Expansive Soils Stabilized with Fly Ash." *Natural Hazards* 47, 509-523.

Zornberg, J.G., Alexandre, R.C., Viratjandr, C., (2004). "Behavior of tire shred–sand mixtures." *Canadian Geotechnical Journal* 41 (2), 227–241.

APPENDIX A – CALIBRATION RESULTS

A.1 Compression Calibration Results

A.1.1 Displacement Transducer Calibration

Axial displacements presented throughout the one-dimensional compression portion of this study were measured using LVDTs (linear variable differential transformers). Figure A.1 displays relationships between the sensor voltage normalized by the excitation voltage (V_s/V_e) and displacement (mm) for all displacement transducers used in one-dimensional compression studied. Table A.1 displaces information pertinent to each transducer including V_e, the calibration factor, resolution, and accuracy. Transducer LPT 7 was used exclusively with Consolidation Apparatus 1; transducer LPT 8 was used exclusively with Consolidation Apparatus 2; transducer LPT 9 was used exclusively with Consolidation Apparatus 3; transducer LPT 20 was used with both Consolidation Apparatus 4 and with the large-scale consolidation apparatus; and transducers LPT 10 and LPT 11 were used exclusively with the large-scale consolidation apparatus.

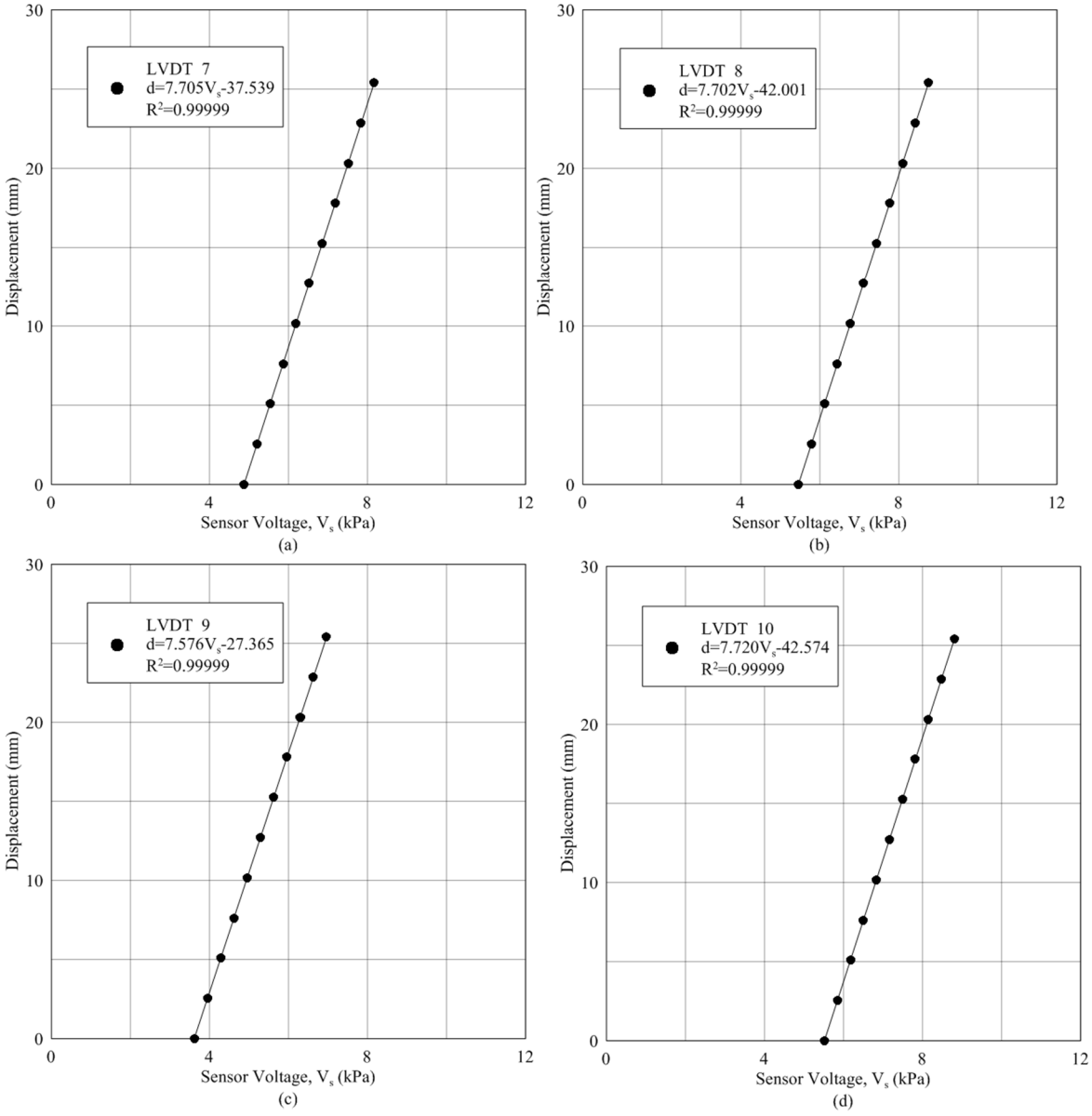
LVDT 7
d=7.705V$_s$-37.539
R^2=0.99999
Displacement (mm)
Sensor Voltage, V$_s$ (kPa)
(a)
LVDT 8
d=7.702V$_s$-42.001
R^2=0.99999
Displacement (mm)
Sensor Voltage, V$_s$ (kPa)
(b)
LVDT 9
d=7.576V$_s$-27.365
R^2=0.99999
Displacement (mm)
Sensor Voltage, V$_s$ (kPa)
(c)
LVDT 10
d=7.720V$_s$-42.574
R^2=0.99999
Displacement (mm)
Sensor Voltage, V$_s$ (kPa)
(d)

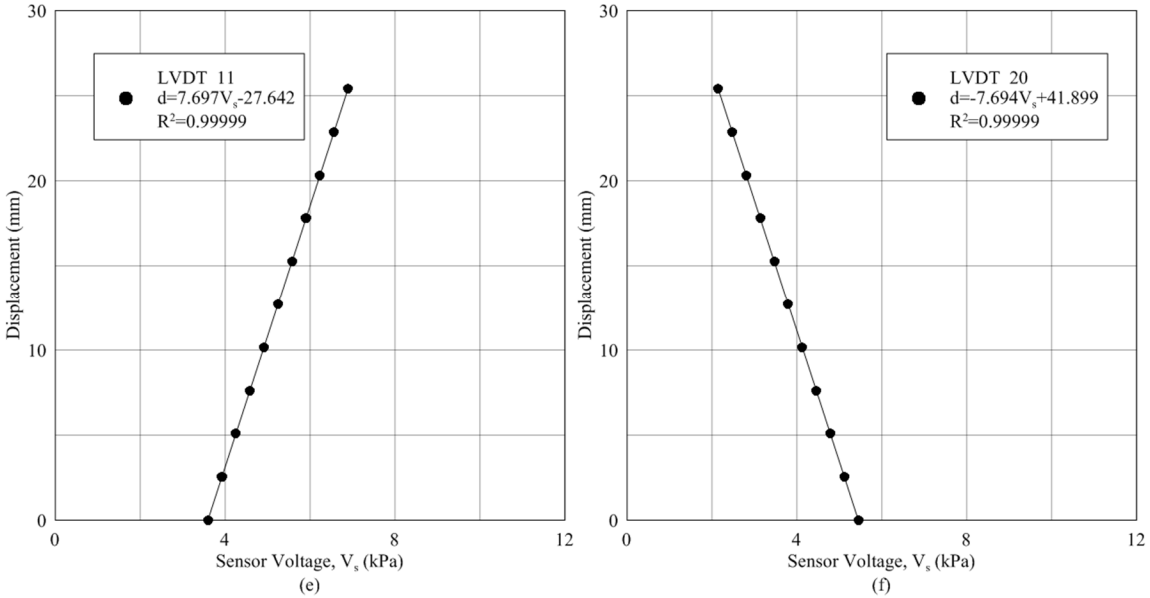

Figure A.1 Sensor voltage normalized by the excitation voltage (V_s/V_e) versus displacement (mm) for displacement transducers used throughout one-dimensional consolidation analyses: (a) LPT 7, (b) LPT 8, (c) LPT 9, (d) LPT 10, (e) LPT 11, and (f) LPT 20.

Table A.1 Calibration information pertinent to each axial displacement transducer used throughout the one-dimensional consolidation analyses

Transducer ID	LPT 7	LPT 8	LPT 9	LPT 10	LPT 11	LPT 20
Excitation Voltage, V_e	9.9754	9.9754	9.9754	9.9754	9.9754	9.9754
Calibration Factor ($mm/V_s/V_e$)	76.8633	76.8283	75.5754	77.0082	76.7800	76.7526
Resolution (mm)	0.001	0.001	0.001	0.001	0.001	0.001
Accuracy (%)	0.0296%	0.0312%	0.0235%	0.0273%	0.0773%	0.0635%

A.1.2 Consolidation Apparatus Calibration

A total of four consolidation apparatuses, manufactured by ELE, were used throughout the small-scale laboratory swell-compression portion of the research. One large-scale consolidation apparatus, manufactured by CSU, was employed during the large-scale laboratory swell-compression portion of the research. Each apparatus was calibrated according to ASTM D2435. According to ASTM D2435, axial deformations shall be corrected for apparatus compressibility whenever the equipment deformations exceed

0.1% of the initial specimen height of when using filter paper screens. During small-scale calibration a metal plug, approximately the same height as tested specimens, was inserted in place of an actual specimen. During large-scale calibration a plug was not used, and the apparatus was void of any specimen-type objects. The exact loading and unloading schedule described in Section 4.2.3 was employed when calibrating each apparatus. A sufficient amount of time was allowed to elapse for each apparatus to equilibrate between loadings. The results of the calibration study are displayed in Table A.2. Calibrations for each loading increment were applied to test results prior to reporting.

Table A.2 Apparatus calibration results for both small-scale and large-scale one-dimensional compression testing. Incremental measured displacements (mm) are shown for respective loadings (kPa)

Small Scale Apparatus Calibrations					Large Scale Apparatus Calibration	
Load (kPa)	**Apparatus 1**	**Apparatus 2**	**Apparatus 3**	**Apparatus 4**		
	Displacement (mm)	Displacement (in)	Displacement (in)	Displacement (in)	Load (kPa)	Displacement (mm)
0.1	0.00E+00	0.00E+00	0.00E+00	0.00E+00	0.1	0.00E+00
6.1	-9.61E-04	-3.28E-04	-1.40E-04	-1.76E-04	6	-2.90E-03
6.1	-8.61E-04	-2.83E-04	-1.89E-04	-1.96E-04	6	-3.02E-03
12.2	-1.70E-03	-9.82E-04	-1.13E-03	-1.01E-03	12	-5.65E-03
24.4	-2.60E-03	-3.26E-03	-2.99E-03	-1.30E-03	18	-7.90E-03
48.8	-4.24E-03	-2.80E-03	-4.77E-03	-2.16E-03	24	-1.01E-02
97.6	-4.89E-03	-4.34E-03	-4.19E-03	-3.13E-03	32	-1.42E-02
195.2	-4.51E-03	-6.44E-03	-5.27E-03	-4.76E-03	36	-1.74E-02
390.4	-6.21E-03	-3.95E-03	-6.11E-03	-5.92E-03	18	7.12E-03
780.8	-6.29E-03	-5.67E-03	-6.59E-03	-7.63E-03	12	1.54E-02
1561.6	-9.04E-03	-7.03E-03	-6.60E-03	-7.04E-03	6	1.27E-02
780.8	4.24E-03	3.53E-03	3.96E-03	4.88E-03		
390.4	1.11E-02	9.04E-03	1.21E-02	1.10E-02		
6.1	9.37E-03	6.52E-03	1.08E-02	6.09E-03		

A.2 LSTX Calibration Results

A.2.1 Displacement Transducer Calibration

Axial displacements presented throughout the LSTX portion of this study were measured using and LVDT (linear variable differential transformer). Figure A.2 displays the relationship between the sensor voltage normalized by the excitation voltage (V_s/V_e) and displacement (mm) for the displacement transducer used in LSTX testing. Table A.3 displaces information pertinent to the displacement transducer including V_e, the calibration factor, resolution, and accuracy. Calibration data was collected from the previous researcher employing the LSTX (Fox 2011). Calibrations were performed for analyses conducted immediately preceding the research in this manuscript; therefore additional calibrations were not viewed as necessary.

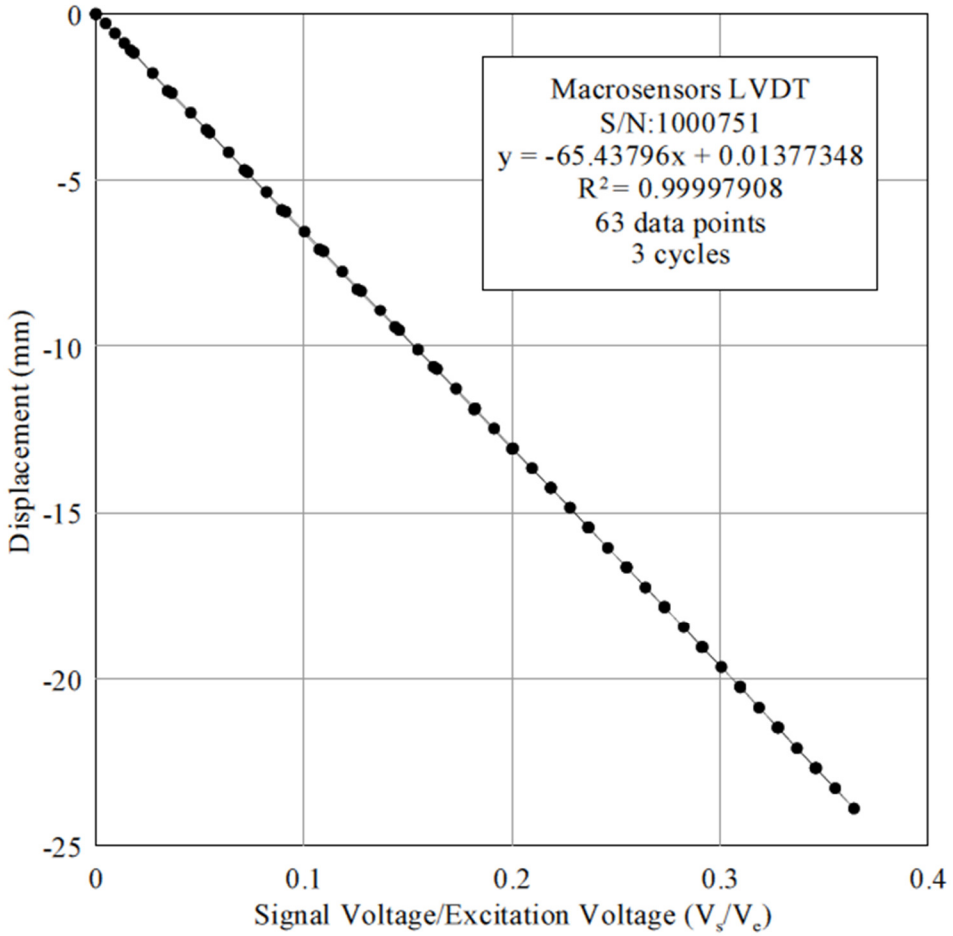

Figure A.2 Sensor voltage normalized by the excitation voltage (V_s/V_e) versus displacement (mm) for the displacement transducer used throughout LSTX analyses (after Fox 2011)

Table A.3 Calibration information pertinent to the axial displacement transducer used throughout the LSTX analyses (after Fox 2011)

Displacement Transducer Calibration	
Excitation Voltage, V_e	10
Calibration Factor (mm/V_s/V_e)	65.4379
Resolution (mm)	0.07
Accuracy (%)	0.27

A.2.2 Force Transducer Calibration

During monotonic loading, a force transducer was utilized to measure deviatoric loads applied to LSTX specimens. Figure A.3 displays the relationship between the sensor voltage normalized by the excitation voltage (V_s/V_e) and load (kN) applied to a 50-kN proving ring (Section A.3.2). Table A.4 displaces information pertinent to the force transducer including V_e, the calibration factor, resolution, and accuracy, determined by the manufacturer of the transducer (Tovey Inc., Phoenix, AZ). As explained by Fox 2011, force transducer calibration data provided by the manufacturer had a much greater level of accuracy in comparison to accuracy provided by the proving ring check. Manufacture data was used throughout all analyses conducted in this thesis.

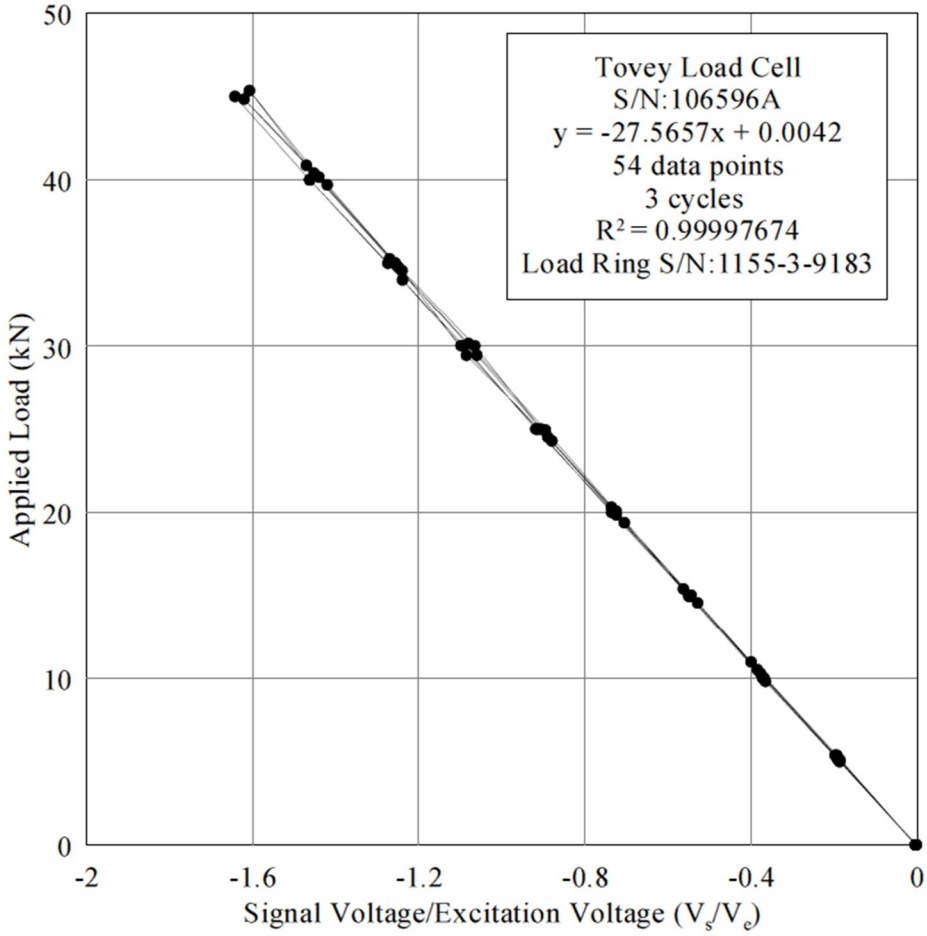

Figure A.3 Sensor voltage normalized by the excitation voltage (V_s/V_e) versus applied load (kN) for the force transducer used throughout LSTX testing (after Fox 2011)

Table A.4 Calibration information pertinent to the force transducer used throughout LSTX testing (after Fox 2011)

Force Transducer Calibration	
Excitation Voltage, V_e	3.00
Calibration Factor (mm/V_s/V_e)	-26.566
Resolution (kN)	0.29
Accuracy (%)	0.59

A.2.3 Pressure Transducer Calibration

Two different pressure transducers were used to measure pore water and cell water pressures for all LSTX tests presented in this manuscript. A pressure transducer manufactured by ELE International was used to measure the cell water pressure, or confining stress (σ_r), and a pressure transducer manufactured by GeoTAC Inc. was used to measure pore water pressure changes (Δu) in pressure lines leading into and out of each specimen during testing. Figures A.4 and A.5 displays the relationship between the sensor voltage (V_s) and the applied pressure (kPa) for the ELE and GeoTAC pressure transducers, respectively. Table A.5 displaces information pertinent to the force transducer including V_e, the calibration factor, resolution, and accuracy for both pressure transducers. Section A.3.3 presents additional information pertaining to how calibrations for the pressure transducers were determined.

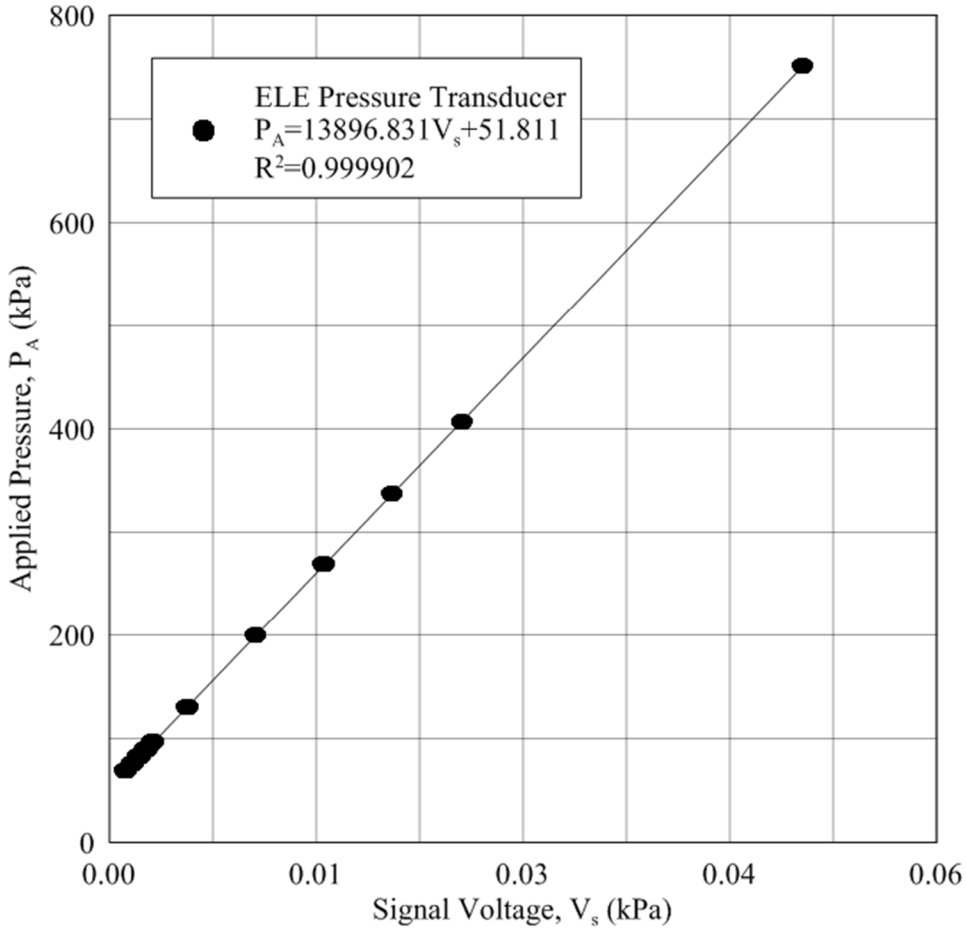

Figure A.4 Sensor voltage (V_s) versus applied pressure (kPa) for the ELE pressure transducer used to measure confining stresses throughout LSTX testing

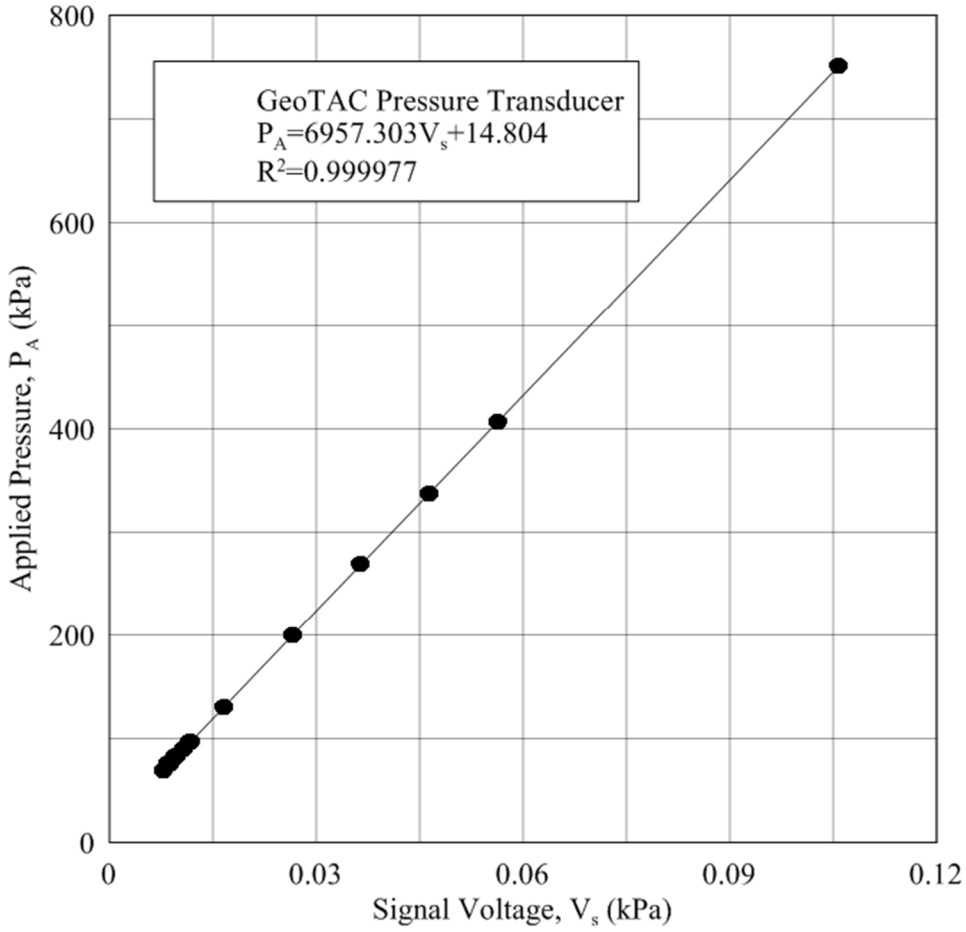

Figure A.5 Sensor voltage (V_s) versus applied pressure (kPa) for the GeoTAC pressure transducer used to measure pore water pressures throughout LSTX testing

Table A.5 Calibration information pertinent to the pressure transducers used throughout LSTX testing

Manufacturer	**ELE Int.**	**Geotac Inc.**
Excitation Voltage, V_e	9.9593	9.9593
Calibration Factor (mm/V_s/V_e)	7013.084011	13981.89879
Resolution (kPa)	0.499	0.628
Accuracy (%)	0.044%	0.056%

A.2.4 Cell Volume Calibration

A cell volume calibration was performed on the LSTX cell in order to determine a) the amount of cell expansion due to the application of varying pressures and b) the amount of creep expansion due to cell expansion over time with the application of a single pressure. Both expansion due to applied pressures and creep calibrations were performed according to *Manual of Soil Laboratory Testing* (Head 1998). For applied pressure expansion, pressure applications of 20, 100, 200, 300, 400, 500, 600, and 700 kPa were selected. 700 kPa is near the recommended operating limits of the cell (Research Engineering LLC, Grass Valley, CA). Pressures were applied in sequential order every 5 minutes, and the change in volume was measured by cell volume burettes. The results of the pressure application calibration can be seen in Figure A.6 and Table A.6. Figure A.6 displays the relative volume change (cm^3) versus the pressure application. Table A.6 displays the numerical values represented in Figure A.6. A total of six pressure loading calibrations were performed. Creep calibration was performed at the two extremes used during LSTX testing; 20 and 700 kPa. Creep calibration results can be seen in Figure A.7 and Table A.7. Figure A.7 displays the relative volume change (cm^3) versus time (minutes) from the initial reading. Table A.7 displays the numerical values represented in Figure A.7. An average applied pressure and creep calibration was applied to LSTX swelling results presented in Chapters 5 and 6.

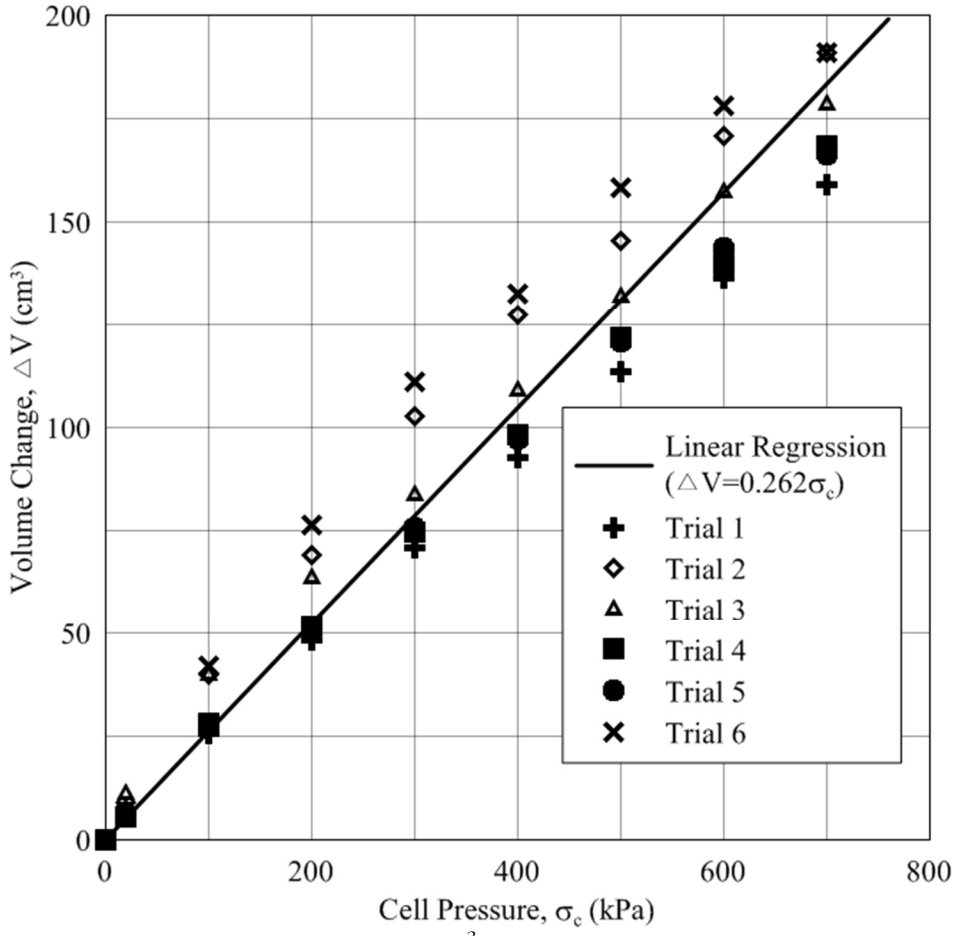

Figure A.6 Relative volume change (cm^3) versus applied pressure for the pressure application calibration on the LSTX cell.

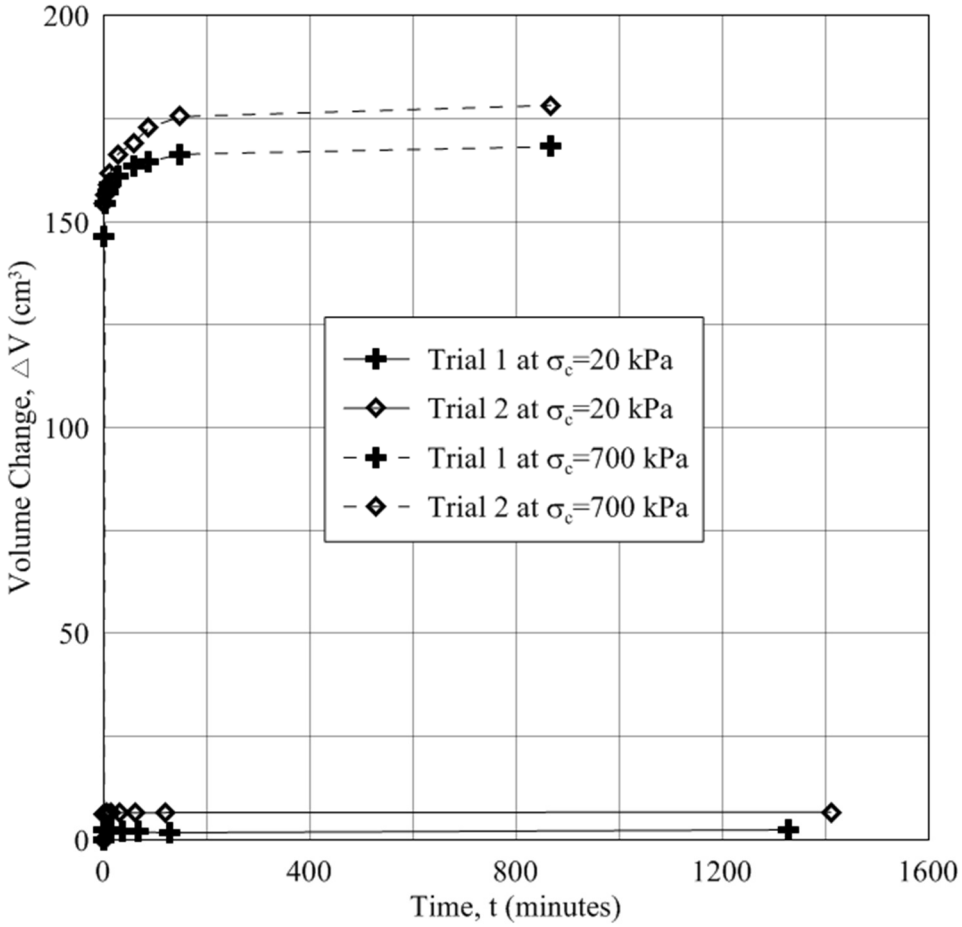

Figure A.7 Relative volume change (cm^3) versus time (minutes) for the creep calibration on the LSTX cell.

Table A.6 Relative volume change (cm^3) versus applied pressure for the pressure application calibration on the LSTX cell

Expansion of Cell Due to Pressure Increase							
Pressure Application (kPa)	**Volume Change, ΔV (cm^3)**						
	Trial 1	**Trial 2**	**Trial 3**	**Trial 4**	**Trial 5**	**Trial 6**	**Average**
0	0.00	0.00	0.00	0.00	0.00	0.00	0.00
20	7.27	7.27	10.91	5.45	6.36	5.45	7.12
100	41.82	40.00	40.00	28.18	27.27	25.45	33.79
200	76.36	69.09	63.64	51.82	50.91	48.18	60.00
300	110.91	102.73	83.64	74.55	75.45	70.91	86.36
400	132.73	127.27	109.09	98.18	97.27	92.73	109.55
500	158.18	145.45	131.82	121.82	120.91	113.64	131.97
600	178.18	170.91	157.27	140.00	143.64	136.36	154.39
700	190.91	190.91	178.55	168.18	166.36	159.09	175.67

Table A.7 Relative volume change (cm^3) versus time (minutes) for the creep calibration on the LSTX cell

Continued Expansion of Cell (Creep) with Time Under Pressure							
Trail 1 - 20 kPa		**Trail 2 - 20 kPa**		**Trail 1 - 700 kPa**		**Trail 2 - 700 kPa**	
Time (min)	**ΔV (cm^3)**	**Time (min)**	**ΔV (cm^3)**	**Time (min)**	**ΔV (cm^3)**	**Time (min)**	**ΔV (cm^3)**
0.01	0.00	0.01	0.00	0.01	0.00	0.01	0.00
0.05	2.30	0.05	6.05	1	146.36	1	154.55
2	2.35	1	6.30	2	154.55	2	156.36
5	2.35	2	6.35	7	157.27	7	159.09
7	2.35	5	6.40	12	159.09	12	161.82
15	2.25	15	6.45	27	160.91	27	166.36
37	2.15	30	6.50	57	163.64	57	169.09
67	1.85	60	6.50	87	164.55	87	172.73
127	1.70	120	6.55	147	166.36	147	175.45
1327	2.40	1410	6.70	867	168.18	867	178.18

A.2.5 Membrane Calibration

The elastic modulus of LSTX membranes was determined according to the procedure outlined in *Manual of Soil Laboratory Testing* (Head 1998). Membrane calibration results can be viewed in Tables A.8 and A.9. Table A.8 presents the geometrical configuration of membranes used in LSTX testing. Table A.9 present the raw calibration data for membranes. Membrane calibration was performed in an orientation in the direction of membrane elongation. Membrane stains encountered during calibration are similar to those experienced during axisymmetric compression. During LSTX testing, two membranes similar to those calibrated below were used to confine the ESR specimens.

Table A.8 Geometrical representation of membranes used in LSTX testing.

Membrane Dimensions	
Thickness (mm)	0.75
Width (mm)	22.08
Area (mm^2)	0.030
Membrane Diameter (mm)	152.87

Table A.9 Raw calibration data of membranes used in LSTX testing.

Trial	Mass Applied (g)	Length (mm)	E (kPa)	ε (%)
Trial 1	0.00	53.34	-	0.00%
	70.26	55.3	975.65	3.67%
	140.56	57.3	966.07	7.42%
	210.86	59.6	916.77	11.74%
	281.16	62.3	854.06	16.80%
Trial 2	0.00	52.34	-	0.00%
	70.28	53.6	961.60	2.41%
	140.58	54.9	946.71	4.89%
	210.88	56.3	918.07	7.57%
	281.23	58.1	841.73	11.00%
Trial 3	0.00	52.47	-	0.00%
	70.28	53.7	987.51	2.34%
	140.56	55	960.18	4.82%
	210.89	56.4	927.42	7.49%
	281.19	57.9	894.98	10.35%
Trial 4	0.00	53.34	-	0.00%
	70.28	54.5	1064.46	2.17%
	140.55	55.8	1003.81	4.61%
	210.88	57.2	959.85	7.24%
	281.23	58.6	939.36	9.86%

A.2.6 Volume Change Burette Calibration

Volume changes encountered during cell volume calibration, flushing, back-pressure saturation, and isotropic compression were measured using volume change burettes. Volume change burettes were calibrated under applied pressures of 0, 300, and 600 kPa (Fox 2011). Testing by Fox 2011 concludes that volume changes in volume change burettes due to pressure applications are less than 0.01% of a typical LSTX specimen volume. Creep volume change is also minimal in volume change burettes even at high pressure; less than 0.01% of a typical LSTX specimen volume (Fox 2011). Due to the

relative insignificance of volume change in the volume change burettes, calibration factors were not calculated or accounted for.

A.3 Standard Measuring Devices Used for Calibration Studies

Calibration devices employed to calibrate transducers were carefully selected with a high level of precision and accuracy. Three separate devices were utilized in calibrating displacement, force, and pressure transducers. Specific information pertaining to the three devices will be presented in Sections A.3.1 – A.3.2.

A.3.1 Standard Measuring Device for Displacement Transducer Calibrations

All displacement transducers were calibrated using a micrometer manufactured by Mitutoyo Corporation, USA. The accuracy and resolution of the micrometer, as reported by the manufacturer, is 0.004% and 0.001mm, respectively. The accuracy and resolution of the micrometer is much higher than the accuracy and resolution of displacement transducers utilized in this study.

A.3.2 Standard Measuring Device for Force Transducer Calibration

As reported by Fox 2011, a 50-kN proving ring manufactured by ELE International was used to provide a check for manufacturer calibration data provided with the force transducer utilized in this study. However, the proving ring reported accuracy and resolution was reported as 0.5-kN and 1.0%, respectively. Due to the inability to provide an accurate calibration using the aforementioned proving ring, a separate calibration of the force transducer was conducted by the manufacturer (Tovey Inc.). The accuracy of

the instruments employed by Tovey Inc. were much greater in comparison to the proving ring, therefore calibration by Tovey Inc. was utilized throughout the research.

A.3.3 Standard Measuring Device for Pressure Transducer Calibration

Pressure transducers were calibrated using a dead weight tester manufactured by SI Pressure Instruments, UK. The capacity and accuracy of the dead weight tester utilized for calibration was reported by the manufacturer as 3500 kPa and 0.025%, respectively. The accuracy of the dead weight tester is significantly higher than the accuracy of the pressure transducers utilized in this study.

APPENDIX B – ADDITIONAL ONE-DIMENSIONAL RESULTS

Figures B.1 through B.3 present several examples of vertical strain versus time plots for SSC testing performed on Pierre shale soil and ESR mixture specimens. Differences in vertical strain with time are presented for one specimen without the addition of rubber, one specimen with the inclusion of 10% *RC* and one specimen with the inclusion of 20% *RC*. The seating load, inundation, load 1 through 8 and unloading 1 through 3 (as presented in Chapter 4) are presented for all three specimens. All three specimens shown were compacted to C_R equal to 95% and w_{opt}. Although C_R and w initial states vary slightly, the discrepancy between the three figures is due primarily to the different amounts of rubber added to the soil matrix. Other specimens compacted to lower and higher levels of C_R and w presented similar trends, and are not included in Appendix B.

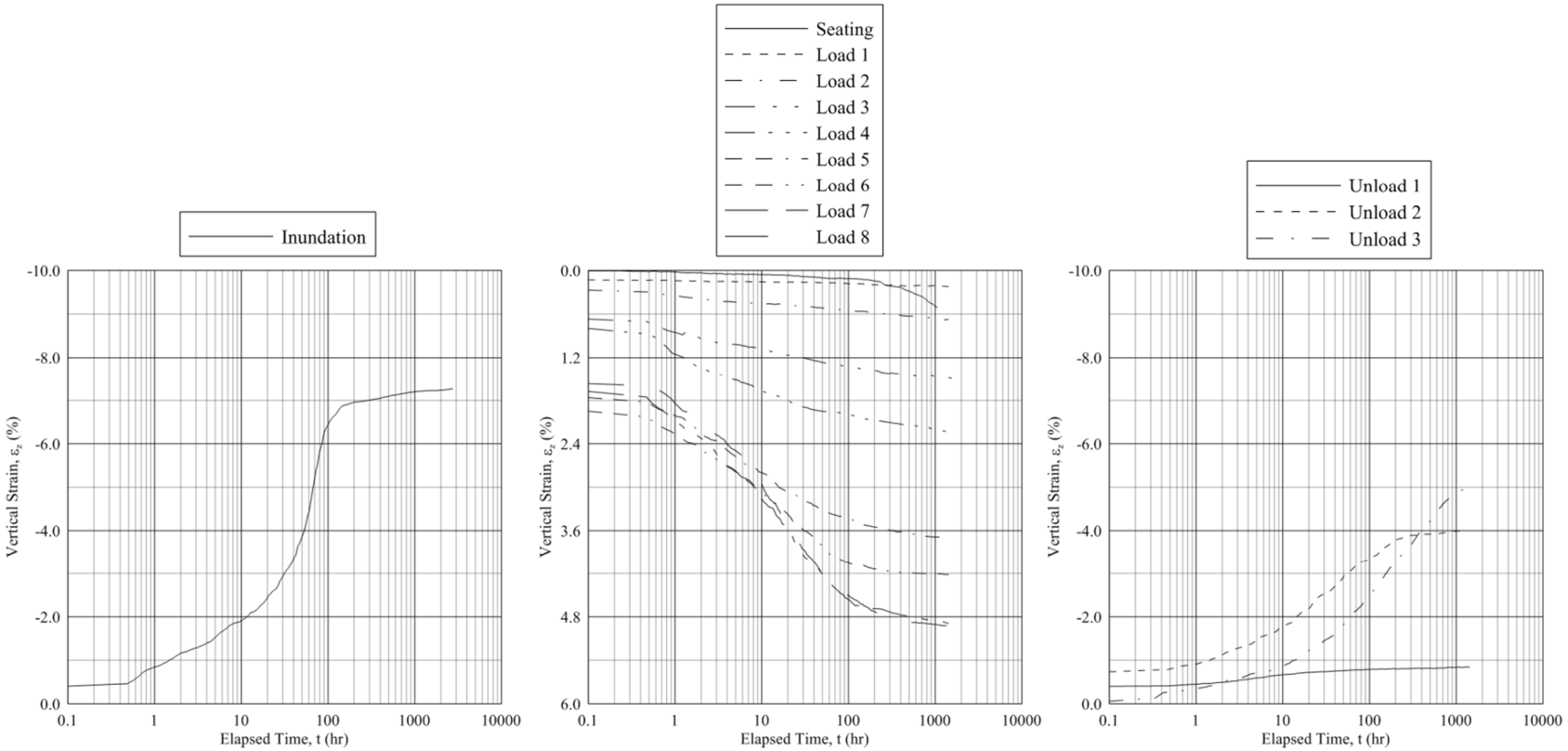

Figure B.1 Example of the difference in vertical strain with time for varying loading increments for the SSC specimen compacted with initial states C_R, w, and RC equal to 90%, w_{opt}, and 0%, respectively. From left to right loading increments are as follows: inundation, seating and load 1 through 8, and unloading 1 through 3.

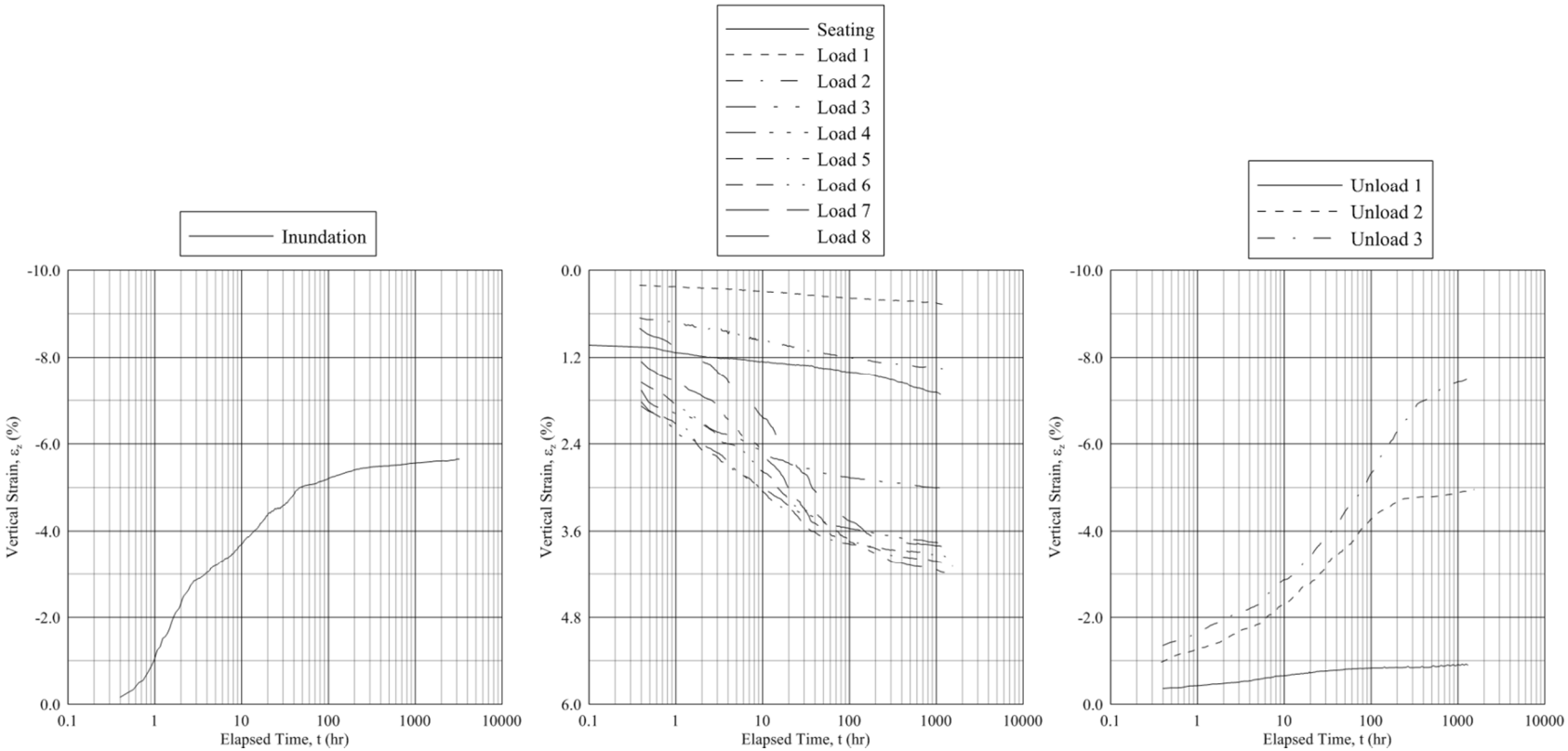

Figure B.2 Example of the difference in vertical strain with time for varying loading increments for the SSC specimen compacted with initial states C_R, w, and RC equal to 90%, w_{opt}, and 10%, respectively. From left to right loading increments are as follows: inundation, seating and load 1 through 8, and unloading 1 through 3.

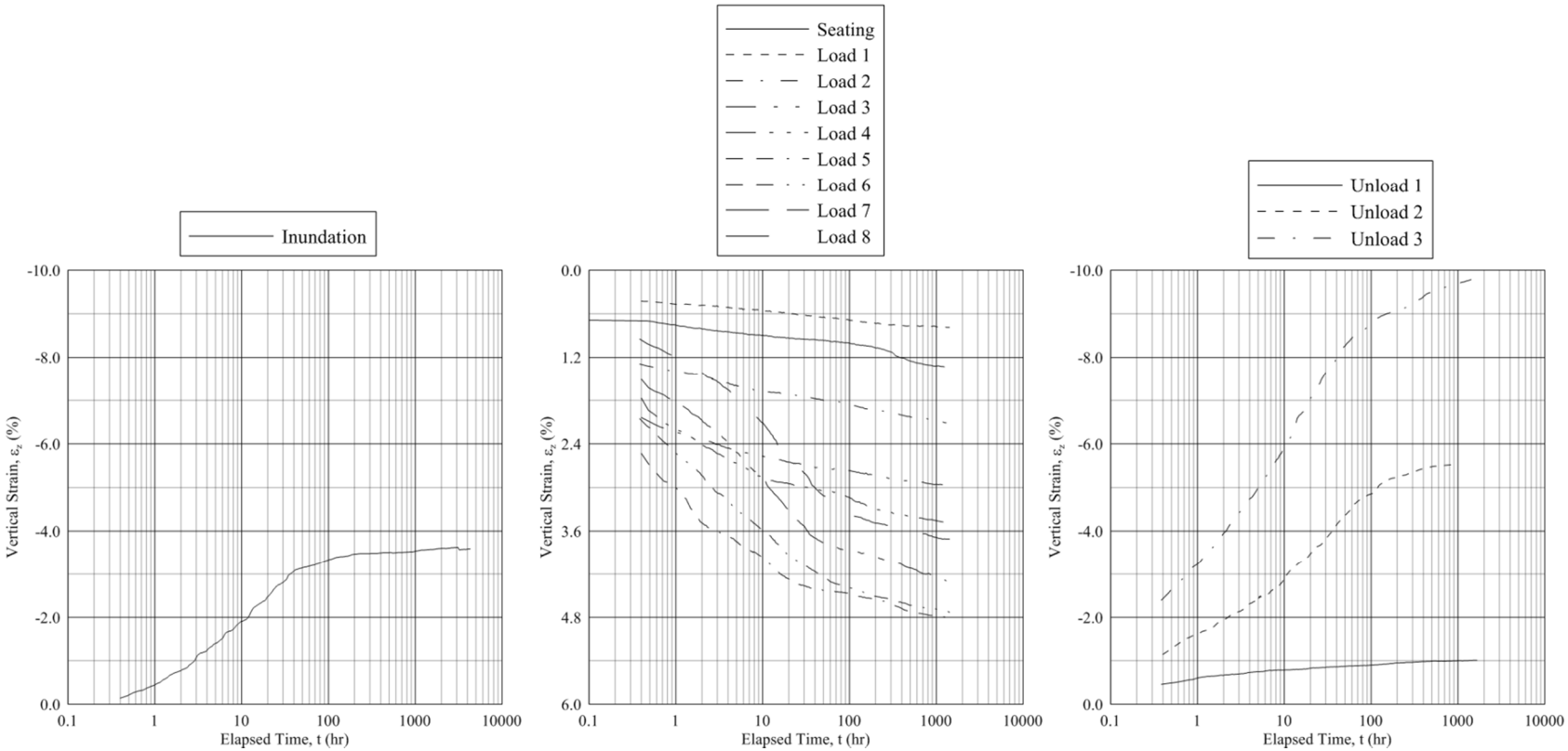

Figure B.3 Example of the difference in vertical strain with time for varying loading increments for the SSC specimen compacted with initial states C_R, w, and RC equal to 90%, w_{opt}, and 20%, respectively. From left to right loading increments are as follows: inundation, seating and load 1 through 8, and unloading 1 through 3.

APPENDIX C – MINERALOGICAL COMPOSITION

As mentioned in Chapter 4, Section 4.1.3 the mineralogical composition of soil collected from the Pierre Shale residual soil deposit was determined using X-ray diffraction analysis. A singular specimen of approximately 3 g was collected and shipped to H&M Analytical Services, Inc. for XRD analysis. Figures C.1 – C.3 identify the peak intensity of Pierre shale expansive soil over a specified two-theta range when tested in a Panalytical X'Pert Pro diffractometer. Also shown in Figures C.1 – C.3 are the peak identifications when comparing collected data to the Powder Diffraction File (PDF) published by the International Centre for Diffraction Data with over 700,000 entries. Vertical lines indicate the magnitude and two-theta location of data extracted from the PDF. Figures C.2 and C.3 provide condensed intensity and two-theta axis ranges for enhanced viewing.

Specimen size is always important to consider when performing geotechnical analyses. Research has shown that a limited amount of expansive mineral in a representative soil matrix can yield significant expansion, denoted by the high activity, A (Skempton 1953) and CEC (Mitchell) of the montmorillonite mineral. A comparison of A and CEC values for montmorillonite are compared in Tables C.1. As explained in Chapter 4, the Pierre shale expansive soil deposited has shown a relatively large montmorillonite component. The specimen analyzed in the XRD analysis was relatively small. 3 g of Pierre shale expansive soil was shipped to H&M Analytical Services, Inc. and approximately 10% of the total amount (or 0.3 g) was used in the XRD analysis. Therefore, it is likely that the

isolated specimen used for XRD analysis was not representative of the mineralogical composition of Pierre shale soil used in this study.

Table C.1 Activity and CEC values for various clay minerals (after Skempton 1953, and Mitchell 1976)

Mineral	Activity, *A*	CEC (meq/100g)
Kaolinite	0.33 -0.46	3-15
Illite	0.9	10-40
Montmorillonite (Ca)	1.5	80-150
Montmorillonite (Na)	7.2	

Testing procedures are hypothesized to have had a significant role in the results collected in this analysis. Different analysis procedures are available for XRD depending on the sample material tested. For expansive soils it is generally recommended to saturate the specimen prior to the application of Cu radiation. Expansion can cause a significant shift in the peak location, and therefore expansive minerals are more likely to be identified. The specimen shipped to H&M Analytical Services for XRD analysis was tested under dry conditions, potentially limiting expansive minerals from the results. The limited understanding of XRD by the author prior to testing lead to the conclusion that the expansive nature of the shipped specimen should not be discussed with to H&M Analytical Services, Inc. in order to limit any subjectivity in the results.

The Pierre shale residual expansive soil employed in this study is clearly expansive, as shown in the analyses, and due to the comparative (as opposed to absolute) treatment of results the precise quantities of expansive material should not be considered significant.

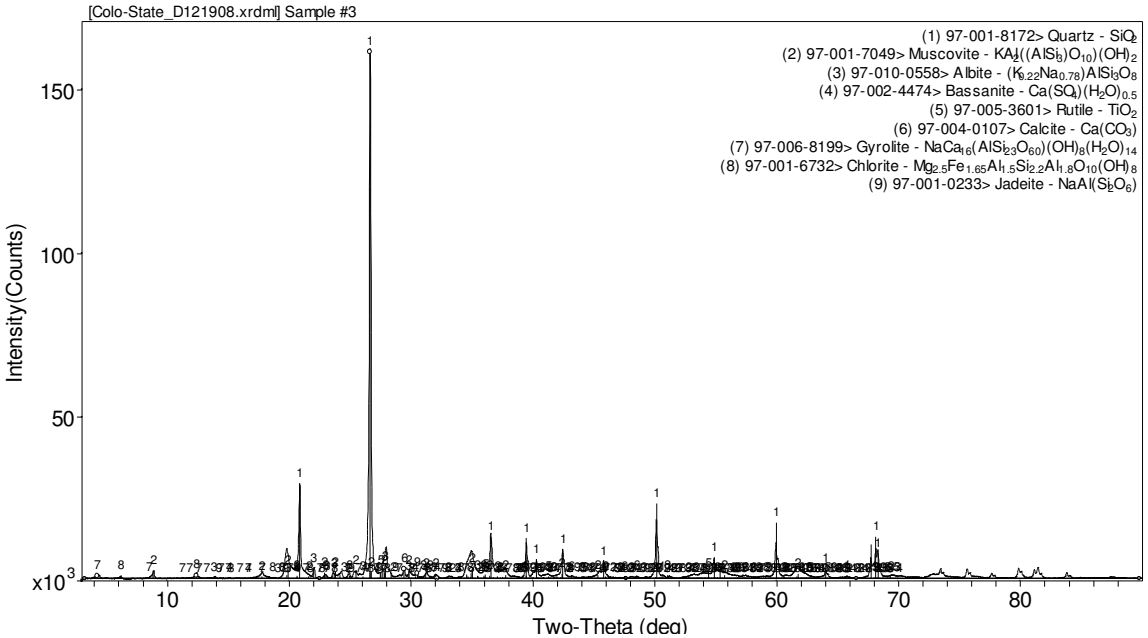

Figure C.1 Phase identification for a 3-g Pierre shale expansive soil specimen over a 0 to 80 two-theta range and a 0 to $150*10^3$ intensity range.

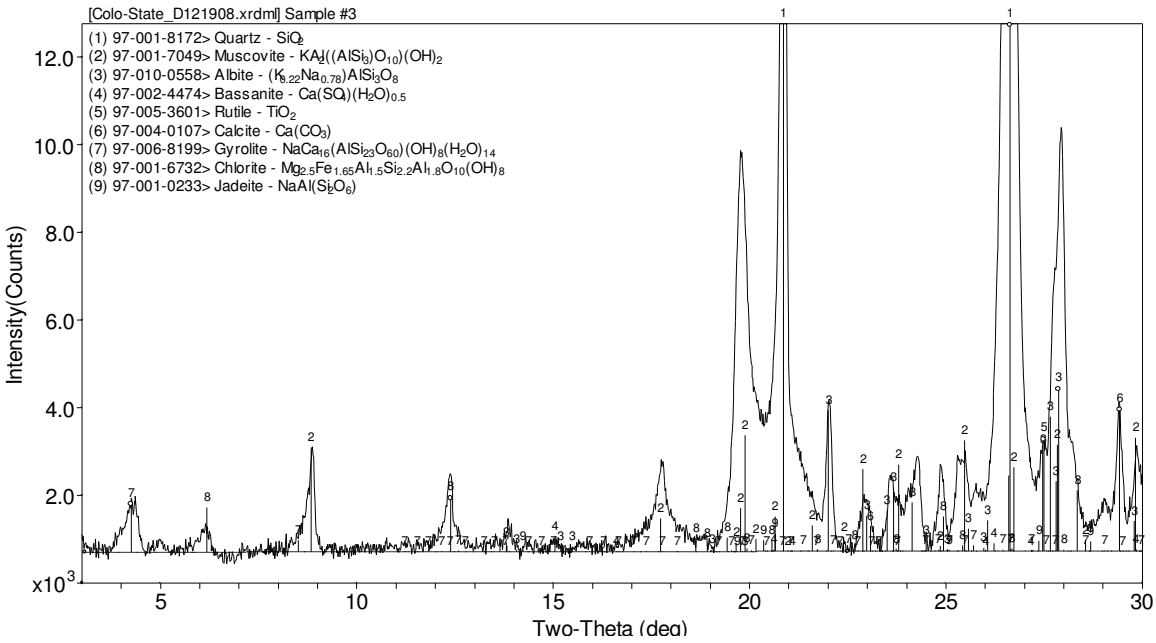

Figure C.2 Phase identification for a 3-g Pierre shale expansive soil specimen over a 0 to 30 two-theta range and a 0 to $12*10^3$ intensity range.

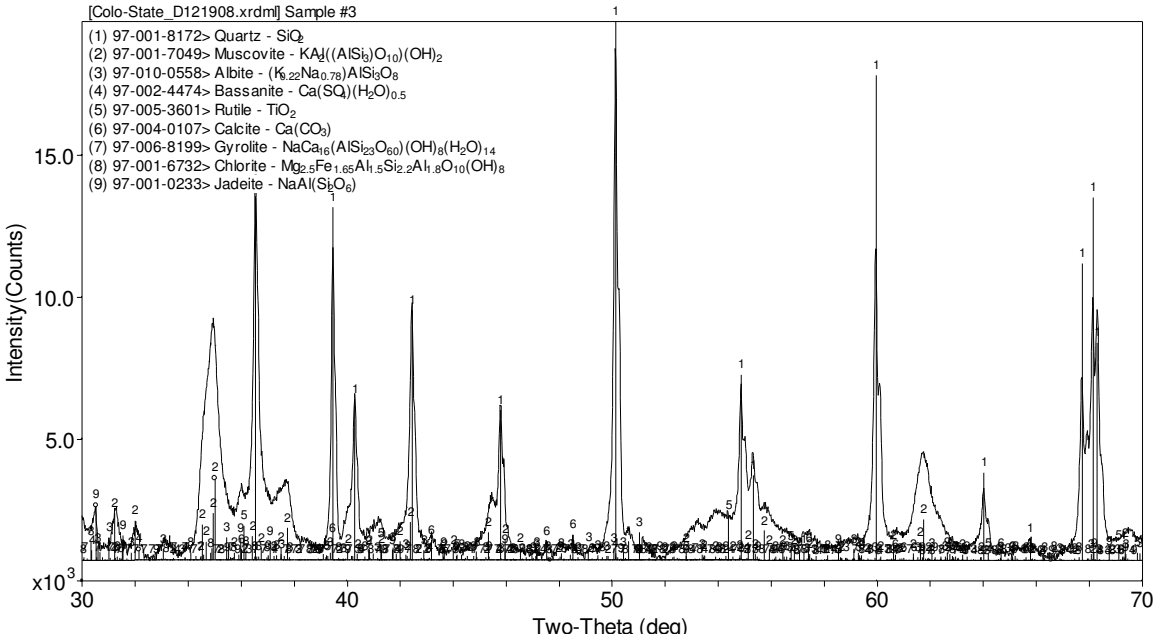

Figure C.3 Phase identification for a 3-g Pierre shale expansive soil specimen over a 30 to 70 two-theta range and a 0 to $20*10^3$ intensity range.

Figure D.1 Photograph of the ESTS looking northeast (after Benvenga 2005)

Figure D.2 Photograph of the ESTS looking East southeast (after Benvenga 2005)

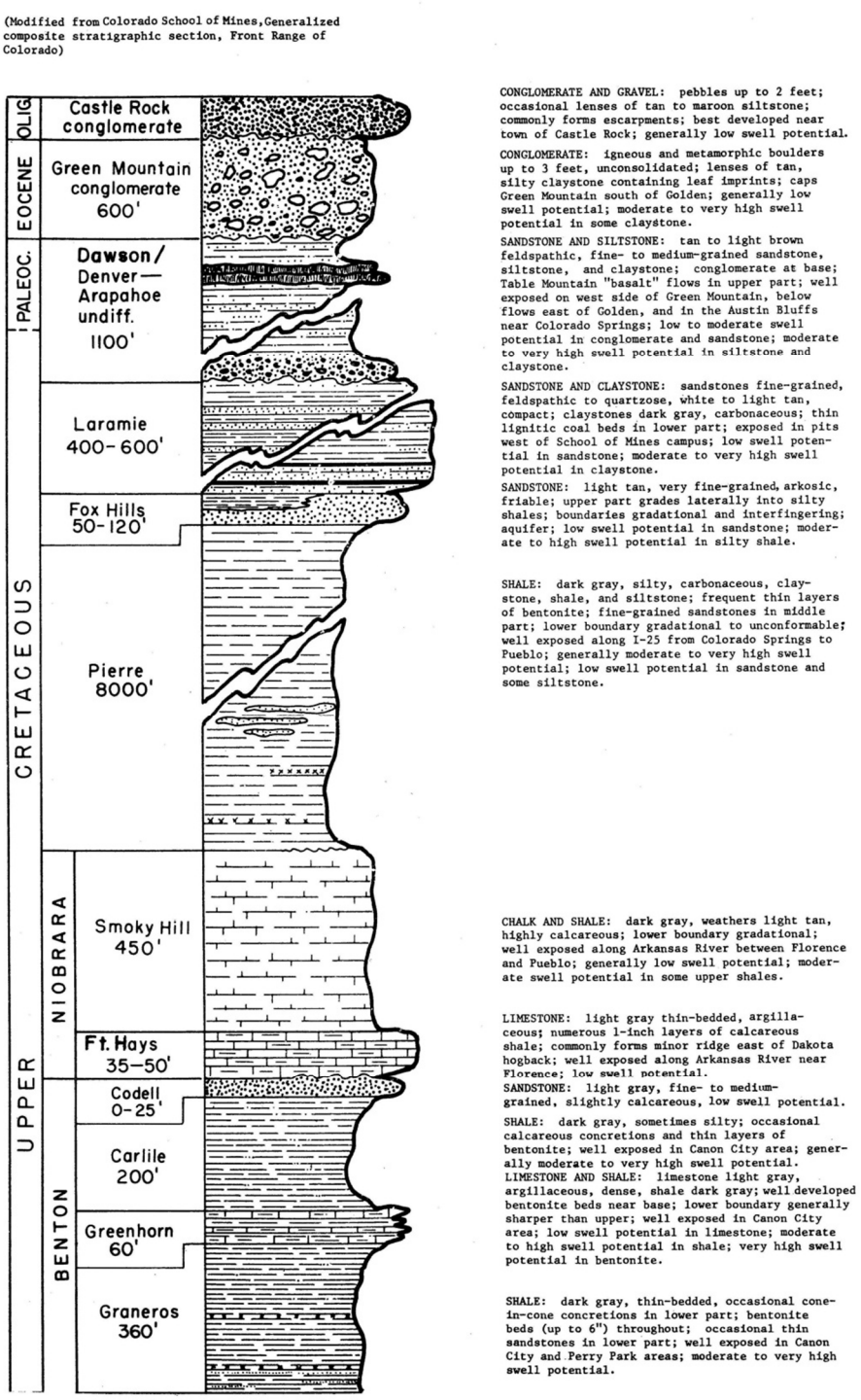

Figure D.3 Diagram presenting the time and rock stratigraphic sequences of the geologic units beneath the ERC expansive soil testing site (Hart 1974)

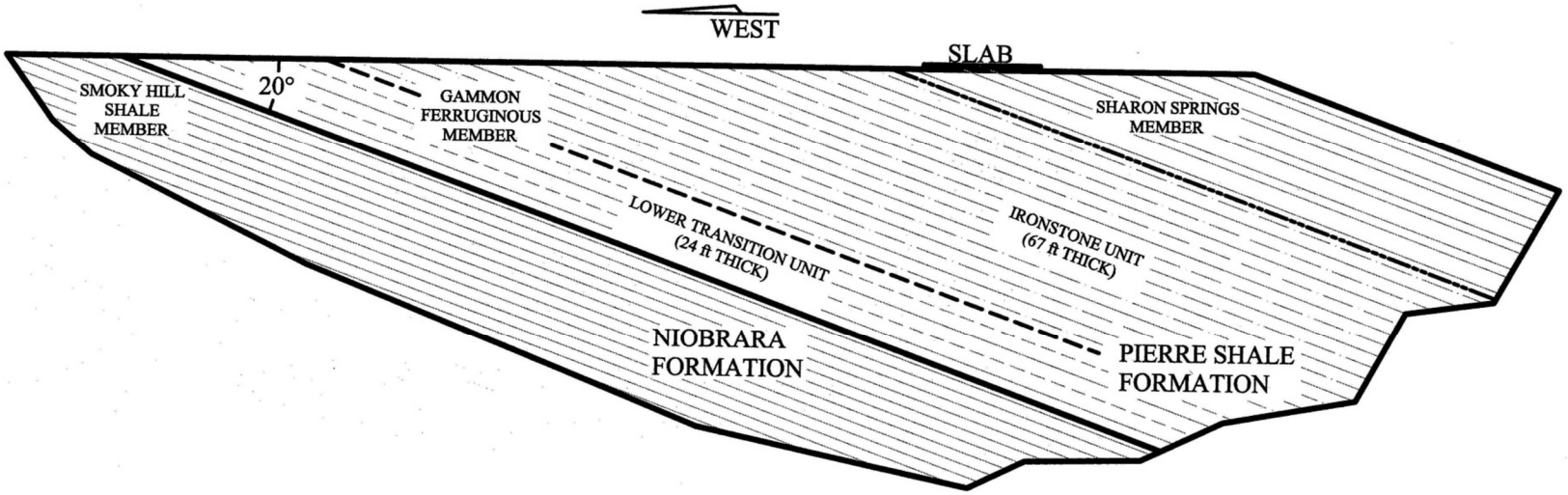

Figure D.4 Cross-section of the subsurface lithology below the ERC expansive soil testing site (after Abshire 2002)

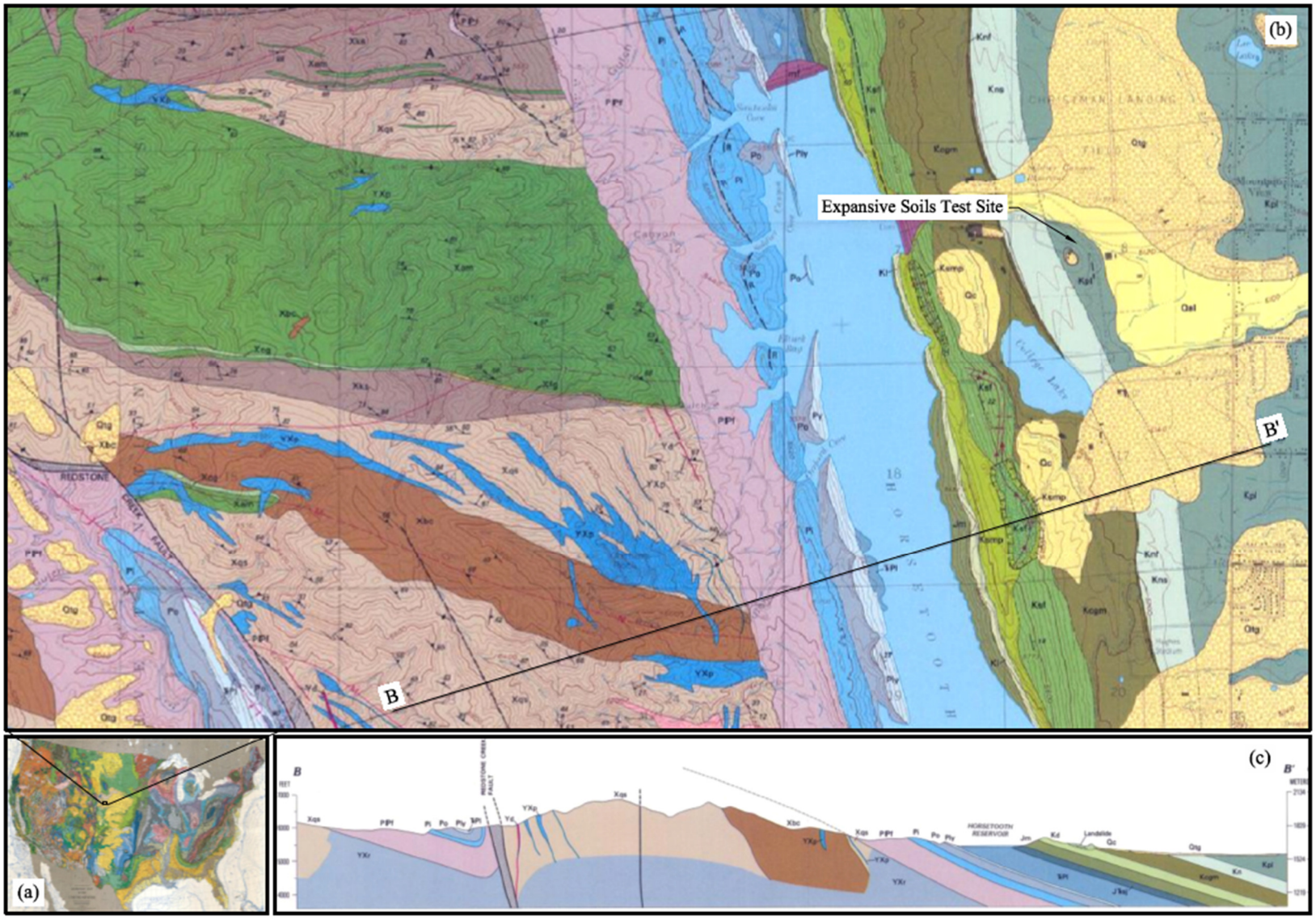

Figure D.5 Geologic Map of the Expansive Soil Test Site near the ERC (a) a geologic map of the US, (b) the geology in the immediate vicinity of the testing site and (c) a typical cross section taken through B-B' of (a) (after Baddock et al. 1989)

Figure D.6 Map key for Figure E.5 showing the major geologic formations near the ERC after Baddock et al. 1989)

Figure D.7 Large weight application for LSUSC displaying the limitations in applied vertical stress due to large normal cross sectional area and direct dead weight application

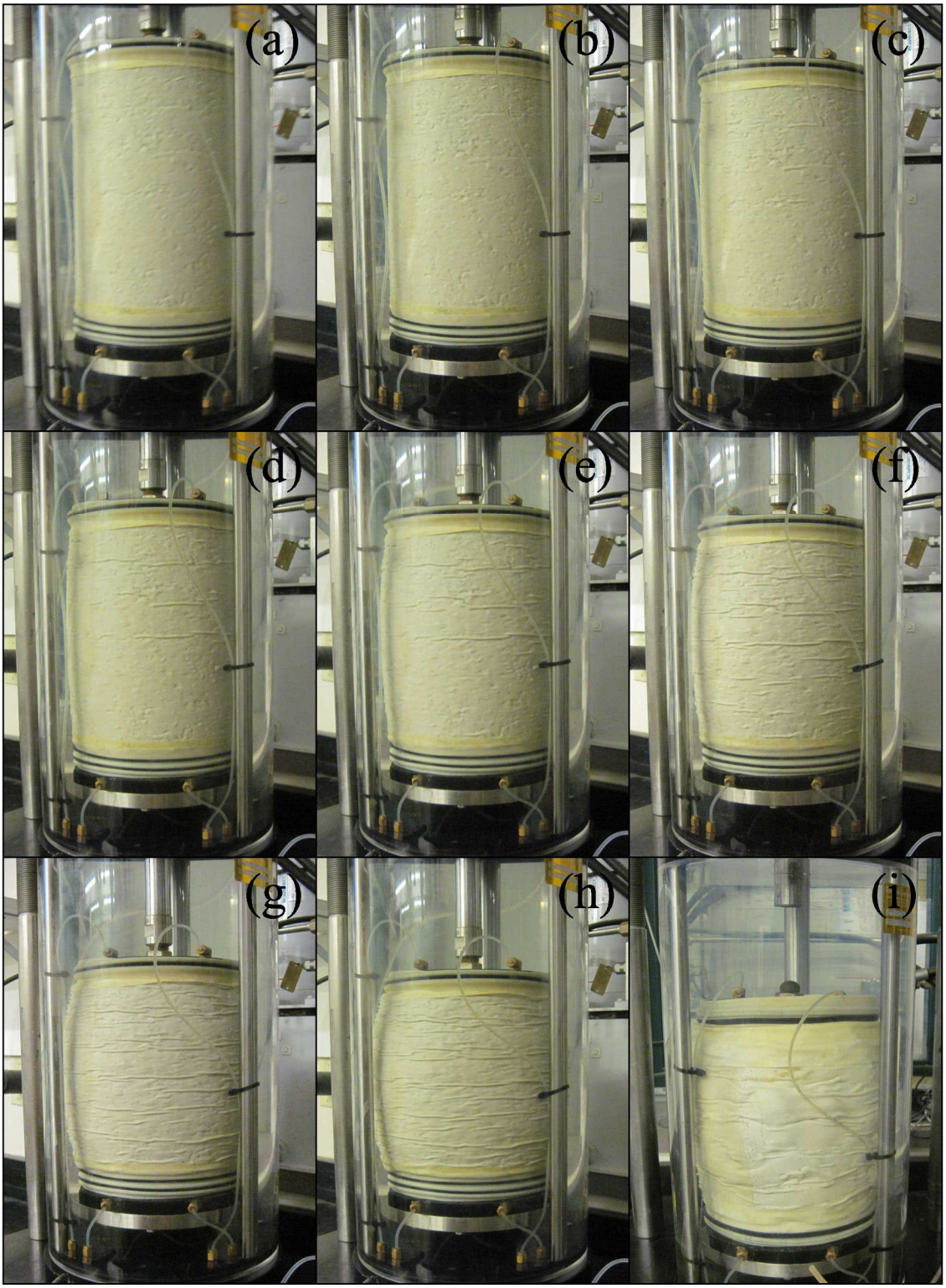

Figure D.8 6.7-mm ESR LSTX specimens during axisymmetric compression at ε_a increments of approximately (a) 0, (b) 4, (c) 8, (d) 12, (e) 16, (f) 24, (g) 28, (h) 32% for one 6.7-mm specimen and (i) 30% for one 19.0-mm specimen